To the Graduate Council:

I am submitting herewith a dissertation written by Preston P. Smith entitled "Ion Implantation Applications for Pitting Corrosion Inhibition - Tungsten Beam Implantation of Aluminum and Nitrogen Plasma Ion Implantation of 304L Stainless Steel." I have examined the final copy of this dissertation for form and content and recommend that it be accepted in partial fulfillment of the requirements for the degree of Doctor of Philosophy, with a major in Metallurgical Engineering.

R. A. Buchanan

R. A. Buchanan, Major Professor

We have read this dissertation
and recommend its acceptance:

Accepted for the Council:

Associate Vice Chancellor
and Dean of the Graduate School

ION IMPLANTATION APPLICATIONS FOR PITTING CORROSION INHIBITION - (TUNGSTEN BEAM IMPLANTATION OF ALUMINUM AND NITROGEN PLASMA ION IMPLANTATION OF 304L STAINLESS STEEL)

A Dissertation

Presented for the

Doctor of Philosophy

Degree

The University of Tennessee, Knoxville

Preston Paul Smith

May 1995

This dissertation is dedicated to my wife

Mia Wren Creasman Smith

for her patience, love, and understanding

ACKNOWLEDGMENTS

The author would like to acknowledge and express his genuine gratitude to the many people who have provided help and guidance throughout the pursuit of this degree. The major advisor of this research, Professor Ray A. Buchanan, was always available to the student, eager to provide assistance with any problem, and a genuine pleasure with whom to work. Professor Eugene E. Stansbury was an invaluable source of information and suggestions, who greatly augmented the quality of the work herein. Thanks also go out to Professor J. Reece Roth of the Department of Electrical and Computer Engineering for his support and insight into the field of plasma science. The author also appreciates Dr. Roth's careful analysis of this manuscript for accuracy and completeness. Professor Tony Pedraza gave generously of his time while serving on the committee, answering technical questions and providing a unique perspective on some of the technical details. Thanks are extended to Jim Williams of the Oak Ridge National Laboratory for his input and his aid in understanding the fundamentals of ion implantation and Rutherford backscattering, and to Dave Brasky and Cindy Arnold of the ORNL High Temperature Materials Laboratory for their help in characterizing materials used in this work.

The financial support provided by the Army Research Office under Contract No. DAAL 03-89-0125 was greatly appreciated, as was support from the University of Tennessee Center for Materials Processing. The additional financial support provided through a teaching assistantship by the Materials Science and Engineering Department, and its Head, Dr. Joe Spruiell, is gratefully acknowledged.

The author wishes to express his appreciation for his fellow graduate students in the Department of Materials Science and Engineering, and his colleagues in the MSE Corrosion Group. Specifically, David Johnson, Ping Li, Robert Perrin, Tim Newport, and Annette Kovacs will each be remembered for helping the author to maintain his sanity during some of the bleak hours which confront all graduate students.

The author is indebted to Sanjay Kamath, graduate student in the Plasma Science Laboratory, for his efforts in implanting the 304L stainless samples, and for his congenial attitude in the face of ongoing experimental difficulties.

The author would like to express his sincere gratitude to Sandy and Carla in the MSE office, Sancy and Betty in the Chemical Engineering office, Frank, Randy, and Ms. Cagle in Purchasing and Receiving, and the electronic and machine shop staffs.

Finally, a word of appreciation goes out to Joyce Creasman for her enthusiastic encouragement to begin this journey.

ABSTRACT

Ion implantation has been investigated to assess the effects of the implanted species on inhibiting the chloride induced pitting corrosion of common commercial alloys. Studies are described involving the application of an emerging technology, plasma ion implantation, to implant 304L stainless steel with nitrogen, as well as ion beam implantations of aluminum 1100 with tungsten. These surface modifications can potentially be very effective in enhancing corrosion resistance by producing non-equilibrium surface alloys and / or surface structural changes, and by conserving cost-prohibitive alloying elements. Many of the limitations of the ion beam implantation process may eventually be ameliorated by plasma ion implantation (PII), in which workpieces can be immersed in a plasma for simultaneous exposure of the entire surface. The focus of this research was to document alterations in the pitting behavior by both electrochemical and immersion techniques, and to characterize the resulting microstructure, corrosion mechanisms, and implanted species distribution.

Tungsten additions always enhance the passivity of Al, regardless of the substrate alloy or the applied dose (3 - 9 x 10^{16} ions/cm^2). Anodic polarization, potentiostatic, and immersion testing all indicate that the implanted tungsten acts

to significantly slow pitting propagation. This improvement can be traced primarily to oxide blisters which form on the surface during pitting.

Nitrogen ions have been successfully implanted into 304L stainless steel in a uniform microwave plasma. An increase in pitting potential of up to 700 mV was measured for relatively low doses. No improvement was noted for higher doses, indicating that nitrogen doses effective in improvement of wear properties may not be effective in enhancing localized corrosion resistance. Low accelerating potentials were successfully utilized to increase the N ion concentration in the near-surface region. The lateral dose uniformity on 304L specimens exposed to N PII has been greatly improved through successive modifications of the sample holder geometry.

TABLE OF CONTENTS

CHAPTER			PAGE
1.	INTRODUCTION		1
2.	LITERATURE REVIEW		3
	A.	Aluminum 1100	3
	B.	Aluminum Pitting Corrosion	5
	C.	304L Stainless Steel	9
	D.	Conventional Corrosion Resistant Surface Treatments	12
	E.	Ion Implantation	12
	F.	Ion Implantation for Corrosion Control	20
	G.	Nitrogen Implantation into Stainless Steel	26
	H.	Aluminum Corrosion Inhibition by Ion Implantation	29
	I.	Aluminum Pitting Resistance Improvements via Non-Equilibrium Alloying Additions	33
	J.	Pitting Resistance of W-Al Films	36
	K.	Proposed Mechanisms of Enhanced Passivity of Non-Equilibrium Aluminum Alloys	41
	L.	Aluminum Pitting and Oxide Blister Formation	50
	M.	Aluminum Pitting Corrosion Inhibitors	53
	N.	Plasma - the Fourth State of Matter	54
	O.	Plasma Ion Implantation	57
	P.	Auger Electron Spectroscopy	65
	Q.	Rutherford Backscattering Spectroscopy	70
	R.	Atomic Force Microscopy	73
3.	EXPERIMENTAL PROCEDURES		76
	A.	Materials	76
	B.	Ion Beam Implantation	79
	C.	Rutherford Backscattering Spectroscopy	80
	D.	Plasma Ion Implantation	80
	E.	Electrochemical Corrosion Testing	84
		i. Anodic Polarization	89
		ii. Amercoat Masking	93
		iii. Immersion Testing	95
	F.	Auger Electron Spectroscopy	97
	G.	Atomic Force Microscopy	98

4. RESULTS AND DISCUSSION 99

PART I - *Tungsten Ion Implantation of Aluminum 1100* 99

A. Electrochemical Polarization Testing 99
B. Immersion / Potentiostatic Testing 124
C. Microhardness Testing 147
D. Auger Electron Spectroscopy / Atomic Force Microscopy Testing 147

PART II - *Nitrogen Plasma Ion Implantation of 304L Stainless Steel* 179

A. Experimental Difficulties Associated with Non-Uniformity of PII Dose Distribution and 304L Crevicing Tendency 179
B. 304L Crevice Potential 180
C. 304L Pitting Potential with 20 kV Nitrogen 191
D. 304L Pitting Potential with Nitric Acid Passivation 197
E. 304L Pitting Potential with Manual Oxide Removal 205
F. 304L Pitting Potential with Potentiostatic Etching 213
G. 304L Pitting Potential with Modified PII Sample Holder 219
H. 304L Pitting Potential with Cathodic Cleaning Oxide Removal 225
I. 304L Anodic Polarization Summary 232
J. Characterization of Dose Distribution by RBS/Auger Analyses 238

5. CONCLUSIONS 249

PART I - *Tungsten Ion Implantation of Aluminum 1100* 249

PART II - *Nitrogen Plasma Ion Implantation of 304L Stainless Steel* 252

LIST OF REFERENCES 254

VITA 266

LIST OF TABLES

TABLE		PAGE
Table 1.	Compositions of Standard Austenitic Stainless Steels.	11
Table 2.	Pitting Resistance of Ion Implanted Aluminum.	30
Table 3.	Work Necessary to Remove Ion Pairs From Various Oxide Lattices.	42
Table 4.	Chemical Composition (w/o) of 304L Stainless Steel (Williams & Co., Inc.).	78
Table 5.	Effect of Test Variables on Electrochemical Properties of 60 kV W-implanted Al 1100.	145
Table 6.	Crevice Potentials of PII N 304L Stainless Steel in Deaerated 1 wt% NaCl.	183
Table 7.	Pitting Potentials of 304L Stainless Steel in Deaerated 1 wt% NaCl.	193
Table 8.	Pitting Potentials of PII N 304L Stainless Steel in Deaerated 1 wt% NaCl with Manual Oxide Removal.	207
Table 9.	Pitting Potentials of PII N 304L Stainless Steel in Deaerated 1 wt% NaCl after Potentiostatic Etching.	218
Table 10.	Pitting Potentials of PII N 304L Stainless Steel in Deaerated 1 wt% NaCl (Round Sample Holder).	223
Table 11.	Pitting Potentials of PII N 304L Stainless Steel in Deaerated 1 wt% NaCl after Cathodic Cleaning at -1259 mV (SHE) for 1 minute.	227

Table 12. Qualitative RBS Nitrogen Content of 1e17 PII N 304L Stainless Steel (2 cm x 2 cm square sample holder). 241

LIST OF FIGURES

FIGURE		PAGE
Figure 1.	Al 1100-H18 sheet, cold rolled. Secondary phase is $FeAl_3$ (1).	4
Figure 2.	Auger profile of the passive film formed on high purity Al held at -750 mV (SCE) in 0.1 M NaCl for 24 hours (7).	7
Figure 3.	Autocatalytic processes occurring in a corrosion pit.	8
Figure 4.	Anodic polarization curve of 99.99% Al in deaerated 0.1 MNaCl (8).	10
Figure 5.	Schematic representation of an ion implantation system with magnetic mass separation of beam constituents (14).	14
Figure 6.	Depth profile for ion implanted 280 keV Zr in Ti-6Al-4V.	17
Figure 7.	Depth profile of implanted ions showing Gaussian distribution, projected range, and standard deviation (20).	18
Figure 8.	Calculated depth profile synthesized by four separate implantations with varying doses and energies (20).	19
Figure 9.	Distribution of Cr ions and displacement defects in Al_2O_3 resulting from bombardment with 280 keV Cr ions (21).	21
Figure 10.	Schematic illustration of the cascade effect resulting from an impinging accelerated ion (22).	22

Figure 11.	Corrosion current as a function of time for unimplanted and N-implanted Ti-6Al-4V alloys during a corrosion wear test (25).	25
Figure 12.	The iron-nitrogen phase diagram (35).	27
Figure 13.	Coupons of Al 2014 after a variety of ion implantation treatments, followed by salt fog testing (52).	32
Figure 14.	The effect of average Mo content on pitting potential of thin cosputtered Al-Mo films (5).	34
Figure 15.	Pitting potentials of various Al alloy thin films in deaerated, pH 10, 0.1M NaCl as a function of concentration (57).	35
Figure 16.	Polarization curves for tungsten in citric acid + Na_2HPO_4 solutions (58).	37
Figure 17.	Pourbaix diagram for the W-H_2O system (3).	38
Figure 18.	The aluminum-tungsten phase diagram (35).	39
Figure 19.	Anodic polarization of Al-W in aerated 0.1M KCl (61).	40
Figure 20.	The pH dependence of the surface charge character of an oxide; positive ($pH < pH_{pzc}$), negative ($pH > pH_{pzc}$) (6).	43
Figure 21.	Pourbaix diagram for the Mo-H_2O system (3).	46
Figure 22.	Pourbaix diagram for the Cr-H_2O system (3).	47
Figure 23.	Pourbaix diagram for the Zr-H_2O system (3).	48
Figure 24.	Pourbaix diagram for the Ta-H_2O system (3).	49
Figure 25.	Schematic diagram of a blister (74).	51

Figure 26.	The potential of blister formation on Al, and the Al pitting potential as a function of the chloride concentration (74).	52
Figure 27.	RBS spectra for films produced in a tungstate inhibited solution (79).	55
Figure 28.	Schematic diagram of plasma source ion implantation apparatus(110).	58
Figure 29.	Dependence of plasma sheath ability to conform to surface contours on the contour size scale (110).	60
Figure 30.	Comparison of Conventional Beamline Ion Implantation and Plasma Ion Implantation (105).	61
Figure 31.	Auger profiles of 1018 and 304 steels implanted to 3 x 10^{17} ions/cm^2 nitrogen at 25 keV by (a) ion beam implantation, and (b) PII (84).	63
Figure 32.	Energy-level diagrams of (a) photoelectron and (b) Auger electron excitation (91).	67
Figure 33.	Principal Auger electron energies for each element (91).	68
Figure 34.	Comparison of Auger electron escape depth with emission depths of backscattered electrons and x-rays (91).	69
Figure 35.	Collision kinematics between a projectile atom m and a target atom M_2 (92).	71
Figure 36.	RBS spectrum of 2 MeV ^{4}He ions backscattered from a silicon crystal implanted with 1.2 x 10^{15} ions / cm^2 As at 250 keV (93).	72

Figure 37.	AFM with laser light detection system. Reflected beam position, and thus force on the sample, is kept constant by vertical sample movement (96).	75
Figure 38.	Schematic diagram of the University of Tennessee Microwave Plasma Facility for Plasma Ion Implantation (99).	81
Figure 39.	Pulsed voltage and current waveforms generated during N PII (99).	83
Figure 40.	Initial sample holder used for PII (99).	85
Figure 41.	Second sample holder used for PII (99).	86
Figure 42.	Third sample holder used for PII (99).	87
Figure 43.	Fourth sample holder used for PII (99).	88
Figure 44.	Schematic diagram of electrochemical polarization cell (100).	90
Figure 45.	Idealized electrochemical polarization curve for an active-passive alloy, showing active, passive, and pitting regions.	92
Figure 46.	Schematic diagram of the specimen holder used for corrosion testing (101).	94
Figure 47.	Schematic diagram of the immersion test cell (101).	96
Figure 48.	Microstructure of Al 1100 alloy, polished and unetched (200 x).	100
Figure 49.	Two examples of the anodic polarization of Al 1100 in aerated 1 wt% Na_2SO_4.	101
Figure 50.	Al 1100 in (A) deaerated 1 wt% Na_2SO_4 and (B) deaerated 1 wt% NaCl.	103

Figure 51.	Anodic polarization of Al 1100 in (A) deaerated 1 wt% Na_2SO_4 and (B) deaerated 1 wt% NaCl.	104
Figure 52.	Anodic polarization of W - (2 wt% ThO) in (A) deaerated 1 wt% NaCl and (B) deaerated 1 wt% Na_2SO_4.	106
Figure 53.	Anodic polarization in deaerated 1 wt% NaCl of (A) Al 1100, (B) Al 1100 - 60 kV 6.2 x 10^{15} W ions/cm^2, and (C) Al 1100 - 60 kV 1.0 x 10^{16} W ions/cm^2.	107
Figure 54.	Anodic polarization in deaerated 1 wt% NaCl of (A) Al 1100, (B) Al 1100 - 60 kV 6.2 x 10^{15} W ions/cm^2, (C) Al 1100 - 60 kV 1.0 x 10^{16} W ions/cm^2, and (D) Al 1100 - 60 kV 1.7 x 10^{16} W ions/cm^2.	108
Figure 55.	Rutherford backscattering spectroscopy profiles of three 60 kV tungsten ion implanted Al 1100 alloys.	110
Figure 56.	Anodic polarization in deaerated 1 wt% NaCl of (A) Al 1100, (B) W - 2 wt% ThO, and (C) Al 1100 - 60 kV 4.9 x 10^{16} W ions/cm^2.	111
Figure 57.	RBS profiles of Al 1100 - 60 kV 4.9 x 10^{16} W ions/cm^2 (A) prior to anodic polarization and (B) after anodic polarization, retention of 4.0 x 10^{16} W ions/cm^2.	113
Figure 58.	Anodic polarization in deaerated 1 wt% NaCl of (A) Al 1100, (B) Al 1100 - 60 kV 5.7 x 10^{16} W ions/cm^2, (C) Al 1100 - 60 kV 4.5 x 10^{16} W ions/cm^2.	115
Figure 59.	Oxide blisters formed during anodic polarization of Al 1100 implanted with 60 kV 4.9 x 10^{16} W ions/cm^2 (1000 x).	117

Figure 60.	Secondary (left) and backscattered (right) images of the same region of an Al 1100 alloy implanted with 60 kV 1.9 x 10^{16} W ions/cm^2 (1500 x).	117
Figure 61.	Oxide blisters formed on Al 1100 implanted with 60 kV 1.7 x 10^{16} W ions/cm^2 (500 x).	119
Figure 62.	Oxide blisters formed on Al 1100 implanted with 60 kV 1.7 x 10^{16} W ions/cm^2 (1750 x).	119
Figure 63.	Linear oxide blister stringers formed on Al 1100 implanted with 60 kV 1.7 x 10^{16} W ions/cm^2 (113 x).	120
Figure 64.	Pitting nucleated at a blister periphery of Al 1100 - 60 kV 7.0 x 10^{16} W ions/cm^2 (400 x).	120
Figure 65.	Oxide blister exhibiting underlying pit propagation.	122
Figure 66.	Blisters covering surface of Al 1100 alloy implanted with 60 kV 4.9 x 10^{16} W ions/cm^2 (50 x).	122
Figure 67.	Anodic polarization in aerated 1 wt% NaCl of (A) Al 1100, (B) Al 1100 - 60 kV 3.1 x 10^{16} W ions/cm^2, and (C) Al 1100 - 60 kV 9.0 x 10^{16} W ions/cm^2.	123
Figure 68.	Pitting on the surface of Al 1100 implanted with 60 kV 3.1 x 10^{16} W ions/cm^2, anodically polarized in aerated 1 wt% NaCl (21 x).	125
Figure 69.	Crystallographic attack within pits on the surface of Al 1100 implanted with 60 kV 3.1 x 10^{16} W ions/cm^2, anodically polarized in aerated 1 wt% NaCl (1470 x).	125
Figure 70.	Anodic polarization in deaerated 1 wt% NaCl of (A) 99.9999% Al (B) 99.9999% Al implanted with 60 kV 6.4 x 10^{16} W ions/cm^2.	126

Figure 71.	Oxide blisters formed on 99.9999 % Al implanted with 60 kV 6.4 x 10^{16} W ions/cm^2 during anodic polarization (100 x).	127
Figure 72.	Al 1100, potentiostatically held 50 mV above E_{corr} in aerated 1 wt% NaCl.	129
Figure 73.	(A) Al 1100 and (B) Al 1100 - 60 kV 4.1 x 10^{16} W ions/cm^2, potentiostatically held 50 mV above E_{corr} in aerated 1 wt% NaCl.	130
Figure 74.	Corrosion potentials of (A) Al 1100 and (B) Al 1100 - 60 kV 5.5 x 10^{16} W ions/cm^2, immersed in aerated 3.5 wt% NaCl.	131
Figure 75.	Schematic illustration of the decrease in corrosion potential with the onset of pitting. (A - passive anodic curve, B - cathodic curve, C - active anodic curve)	133
Figure 76.	Corrosion potentials of (A) Al 1100 - 60 kV 9.0 x 10^{16} W ions/cm^2, (B) Al 1100 - 60 kV 4.5 x 10^{16} W ions/cm^2, and (C) Al 1100, immersed in aerated 3.5 wt% NaCl.	134
Figure 77.	Large oxide blisters formed on Al 1100 - 60 kV 5.4 x 10^{16} W ions/cm^2 during immersion in aerated 3.5 wt% NaCl (52 x).	135
Figure 78.	Pitting nucleated beneath blister center on Al 1100 - 60 kV 5.4 x 10^{16} W ions/cm^2 during immersion in aerated 3.5 wt% NaCl (400 x).	136
Figure 79.	Fractured oxide blocking blister opening formed on Al 1100 - 60 kV 5.4 x 10^{16} W ions/cm^2 during immersion in aerated 3.5 wt% NaCl (491 x).	137
Figure 80.	Oxide blisters formed on unimplanted Al 1100 during immersion in aerated 3.5 wt% NaCl (100 x).	137

Figure 81.	Pitting formed on Al 1100 during immersion in aerated 3.5 wt% NaCl (509 x).	138
Figure 82.	Pitting formed around secondary $FeAl_3$ particles on Al 1100 during immersion in aerated 3.5 wt% NaCl (1000 x).	138
Figure 83.	Minute blistering formed beneath corrosion product on Al 1100 implanted with 60 kV 5.4×10^{16} W ions/cm^2 during immersion in aerated 3.5 wt% NaCl (5000 x).	140
Figure 84.	Aluminum oxide corrosion product precipitated on the surface of Al 1100 implanted with 60 kV 5.4×10^{16} W ions/cm^2 during immersion in aerated 3.5 wt% NaCl (50 x).	140
Figure 85.	EDS spectrum of corrosion product formed on the surface of Al 1100 implanted with 60 kV 5.4×10^{16} W ions/cm^2 during immersion in aerated 3.5 wt% NaCl.	141
Figure 86.	Anodic polarization of Al 1100 in deaerated (A) 1 wt% NaCl, (B) 1 wt% NaCl and 2.0 wt% Na_2WO_4, and (C) 1 wt% NaCl and 0.2 wt% Na_2WO_4.	143
Figure 87.	Extent of passive region for (1) Al 1100, deaerated, (2) 99.9999% Al, deaerated, and (3) Al 1100, aerated [(A) unimplanted, (B) W implanted].	146
Figure 88.	Hardness of Al 1100 as a function of implanted tungsten dose.	148
Figure 89.	Auger depth profile of Al 1100 implanted with 60 kV 9×10^{16} W ions/cm^2.	149

Figure 90.	Surface of Al 1100 implanted with 60 kV 4.5 x 10^{16} W ions/cm^2, after anodic polarization in deaerated 1 wt% NaCl. Boxes indicate locations of Auger depth profile generation.	151
Figure 91.	Auger depth profile generated through an oxide blister on Al 1100 implanted with 60 kV 4.5 x 10^{16} W ions/cm^2, after anodic polarization.	152
Figure 92.	Auger depth profile generated through the oxide matrix on Al 1100 implanted with 60 kV 4.5 x 10^{16} W ions/cm^2, after anodic polarization.	153
Figure 93.	AFM image of collapsed blisters on Al 1100 implanted with 60 kV 1.7 x 10^{16} W ions/cm^2.	155
Figure 94.	Three-dimensional AFM image of four adjoining blisters from Figure 93.	156
Figure 95.	High-magnification AFM image of blister in center of Figure 93.	157
Figure 96.	Al 1100 - 60 kV 1.7 x 10^{16} W ions/cm^2 in deaerated 1 wt% NaCl.	159
Figure 97.	Surface of Al 1100 implanted with 60 kV 5.5 x 10^{16} W ions/cm^2, after immersion in aerated 3.5 wt% NaCl. Boxes indicate locations of Auger depth profile generation.	161
Figure 98.	Auger depth profile generated through the corrosion product on Al 1100 implanted with 60 kV 5.5 x 10^{16} W ions/cm^2, after immersion in aerated 3.5 wt% NaCl.	162
Figure 99.	Auger depth profile generated through an oxide blister on Al 1100 implanted with 60 kV 5.5 x 10^{16} W ions/cm^2, after immersion in aerated 3.5 wt% NaCl.	163

Figure 100.	Auger depth profile generated through the matrix oxide on Al 1100 implanted with 60 kV 5.5 x 10^{16} W ions/cm^2, after immersion in aerated 3.5 wt% NaCl.	164
Figure 101.	Model illustrating corrosion mechanisms on tungsten implanted aluminum in a NaCl solution.	166
Figure 102.	Surface of Al 1100 implanted with 60 kV 5.5 x 10^{16} W ions/cm^2, after immersion in aerated 3.5 wt% NaCl. Surface Ar sputtered for 3 minutes.	171
Figure 103.	Surface of Al 1100 implanted with 60 kV 5.5 x 10^{16} W ions/cm^2, after immersion in aerated 3.5 wt% NaCl. Surface Ar sputtered for 8 minutes.	172
Figure 104.	Surface of Al 1100 implanted with 5.5 x 10^{16} W ions/cm^2, after immersion in aerated 3.5 wt% NaCl. Surface Ar sputtered for 20 minutes.	173
Figure 105.	Surface of Al 1100 implanted with 5.5 x 10^{16} W ions/cm^2, after immersion in aerated 3.5 wt% NaCl. Surface Ar sputtered for 25 minutes.	174
Figure 106.	Topographical surface line scans of AFM image from Figure 94.	176
Figure 107.	Topographical surface line scan of AFM image from Figure 95.	177
Figure 108.	Crevice corrosion potentials of 304L stainless steel in deaerated 1 wt% NaCl as a function of applied N plasma ion implantation dose.	182
Figure 109.	Anodic polarization in deaerated 1 wt% NaCl of (A) 304L and (B) 304L implanted with 5 x 10^{14} N ions/cm^2 at 20 kV.	184

Figure 110.	Anodic polarization in deaerated 1 wt% NaCl of (A) 304L and (B) 304L implanted with 7 x 10^{14} N ions/cm^2 at 10 kV.	185
Figure 111.	PROFILE code simulation of retained dose profile for 1 x 10^{18} ions/cm^2 N implanted into 304L stainless steel at 10 kV.	187
Figure 112.	PROFILE code simulation of retained dose profile for 1 x 10^{15} ions/cm^2 N implanted into 304L stainless steel at 10 kV.	189
Figure 113.	Discoloration pattern developed on 2 cm x 2 cm square sample holder during N PII.	190
Figure 114.	Pitting potentials of 304L stainless steel in deaerated 1 wt% NaCl as a function of applied N plasma ion implantation dose (20 kV implantation energy).	192
Figure 115.	Anodic polarization behavior of 304L PII 1 x 10^{17} N ions/cm^2 in deaerated 1 wt% NaCl.	195
Figure 116.	Two examples of the anodic polarization of 304L PII 20 kV 1 x 10^{15} N ions/cm^2 in deaerated 1 wt% NaCl.	196
Figure 117.	Discoloration pattern developed on 5.08 cm x 5.08 cm square sample holder during N PII.	199
Figure 118.	Breakdown potentials of 304L in deaerated 1 wt% NaCl after nitrogen implantation to 1x 10^{15} using the sample holder shown in Figure 41, and after applying the HNO_3 prepassivation treatment.	200
Figure 119.	Weight ratios of Fe and Cr to the total weight of cations in 304 and 316 oxide films as a function of surface treatment.	201

Figure 120.	Relationship between the pitting potential of 304 and 316 stainless steels in 3.5 wt% NaCl solution and the total amount Cr in the oxide.	202
Figure 121.	Anodic polarization behavior of (A) HNO_3-prepassivated PII 10 kV 1 x 10^{15} N ions/cm^2, and (B) HNO_3-prepassivated control 304L.	204
Figure 122.	Pitting potentials of 304L stainless steel in deaerated 1 wt% NaCl as a function of applied N plasma ion implantation dose at 10 kV, after HNO_3 prepassivation and manual oxide film removal.	206
Figure 123.	Anodic polarization of 304L in deaerated 1 wt% NaCl, after HNO_3 prepassivation and manual oxide film removal.	208
Figure 124.	Anodic polarization of 304L PII 10 kV 1 x 10^{18} N ions/cm^2 in deaerated 1 wt% NaCl, after HNO_3 prepassivation and manual oxide film removal.	210
Figure 125.	Anodic polarization of (A) 304L PII 10 kV 3 x 10^{14} N ions/cm^2 and (B) 304L PII 10 kV 7 x 10^{14} N ions/cm^2 in deaerated 1 wt% NaCl, after HNO_3 prepassivation and manual oxide film removal.	211
Figure 126.	Anodic polarization of 304L in deaerated 1 N H_2SO_4 and .01 M KSCN.	215
Figure 127.	Current density behavior of 304L PII 1 x 10^{15} N ions/cm^2 during potentiostatic etching in deaerated 1 N H_2SO_4 and .01 M KSCN at -104 mV (SHE).	216
Figure 128.	Anodic polarization behavior of 304L PII 10 kV 1 x 10^{15} N ions/cm^2 in deaerated 1 wt% NaCl after potentiostatic etching removal of 225 angstroms from the surface.	217

Figure 129.	Discoloration pattern developed on 8.35 cm diameter round sample holder during N PII.	221
Figure 130.	Pitting potentials of 304L stainless steel in deaerated 1 wt% NaCl as a function of applied N plasma ion implantation dose, after PII with large round sample holder (10 kV), HNO_3 prepassivation, and manual oxide film removal.	222
Figure 131.	Three examples of anodic polarization of 304L, plasma ion implanted with N, in deaerated 1 wt% NaCl, after PII with large round sample holder (10 kV), HNO_3 prepassivation and manual oxide film removal.	224
Figure 132.	Three examples of the increasing corrosion potential of prepassivated 304L alloys after cathodic polarization at -1259 mV (SHE) for 1 minute.	226
Figure 133.	Three examples of the corrosion potential increasing to a more active E_{corr} on prepassivated 304L alloys after cathodic polarization at -1509 mV (SHE) for 20 minutes.	229
Figure 134.	Comparison of breakdown potentials on 304L control and 304L PII N samples after cathodic cleaning at -1509 mV (SHE) for 20 minutes.	230
Figure 135.	Anodic polarization of (A) 304L control and (B) 304L PII 2 x 10^{15} N ions/cm^2 in deaerated 1 wt% NaCl after cathodic cleaning at -1509 mV (SHE) for 20 minutes.	231
Figure 136.	Change in the oxide film breakdown potential of 304L stainless steel due to nitrogen plasma ion implantation as a function of the applied dose.	233

Figure 137.	Anodic polarization of 304L PII 10 kV 5 x 10^{14} N ions/cm^2 in deaerated 1 wt% NaCl with potential reversal after reaching E_{1000}, showing large pitting hysteresis.	235
Figure 138.	Anodic polarization of 304 stainless steel in tap water illustrating oxygen evolution.	237
Figure 139.	RBS spectra from 304L implanted to a dose of 1 x 10^{17} N ions/cm^2 on the 2 cm x 2 cm sample holder.	239
Figure 140.	Magnification of the energy range containing N peak from RBS spectra in Figure 139.	240
Figure 141.	Auger depth profile of 304L implanted at 10 kV on round sample holder with a dose of 5 x 10^{15} N ions/cm^2.	243
Figure 142.	Auger nitrogen distribution on 304L implanted on round sample holder with a dose of 5 x 10^{15} N ions/cm^2. N content determined after sputtering surface for 1 minute.	245
Figure 143.	Chromium atom fraction (Cr / Cr + Fe + Ni) as determined by Auger spectroscopy as a function of depth on (A) control 304L with air formed oxide film, and (B) 304L, prepassivated in 50% HNO_3 for 30 minutes at 55°C.	246
Figure 144.	Chromium atom fraction (Cr / Cr + Fe + Ni) as determined by Auger spectroscopy as a function of depth on 304L PII 10 kV 1e15 N after prepassivation in 50% HNO_3 for 30 minutes at 55°C.	248

1. INTRODUCTION

Aluminum alloys and stainless steels are utilized extensively for their resistance to corrosion, which is a consequence of their ability to form an adherent, nonporous oxide film. However, each is also susceptible to pitting in chloride environments, an especially insidious form of corrosive attack due to its localized, and often unanticipated, nature. Aluminum is particularly vulnerable because it cannot be alloyed for anti-corrosive properties as a result of its limited solubility for traditional passivating species such as chromium and molybdenum. Surface modification treatments have traditionally been employed not only for enhanced resistance to corrosion, but also to improve hardness, wear, and other surface properties. Ion beam implantation is an emerging technology which has proven applications in each of these areas. However, its unit processing cost is still prohibitive for most manufactured goods. One of the primary operational restraints is the need for target manipulation due to the unidirectionality of the ion beam. Many of the costly and limiting aspects of ion beam implantation may be ameliorated by a related new technique (plasma ion implantation (PII)) in which workpieces can be immersed in a plasma for simultaneous implantation of the entire surface. Evidence exists from the work of other researchers that tungsten

in non-equilibrium solid solution with aluminum and nitrogen implanted into stainless steel both enhance the resistance of these alloys to localized corrosion.

The focus of the present research is to apply the emerging technology of PII to implant N into 304L ss, and to ion beam implant Al 1100 with W. Resulting alterations of the pitting behavior will be characterized both electrochemically and by immersion techniques. Analysis of metallurgical microstructure, corrosion mechanisms and implant distribution before and after corrosion will be performed using scanning electron microscopy, Rutherford backscattering spectroscopy, Auger electron spectroscopy, and atomic force microscopy.

2. LITERATURE REVIEW

Aluminum 1100

Aluminum alloys find broad areas of application due to the attractive combination of physical and mechanical properties inherent to Al. These include (1):

- low cost
- relative natural abundance
- low density
- high specific strength
- superior corrosion resistance
- non-toxicity
- high electrical conductivity
- high thermal conductivity
- good formability
- good castability
- amenability to surface finishing

Al 1100 is a commercially pure aluminum alloy whose nominal composition is 99.00 Al (minimum), 0.12 Cu, and the balance Fe. Its microstructure in the cold rolled condition is shown in Figure 1, where the secondary phase is $FeAl_3$.

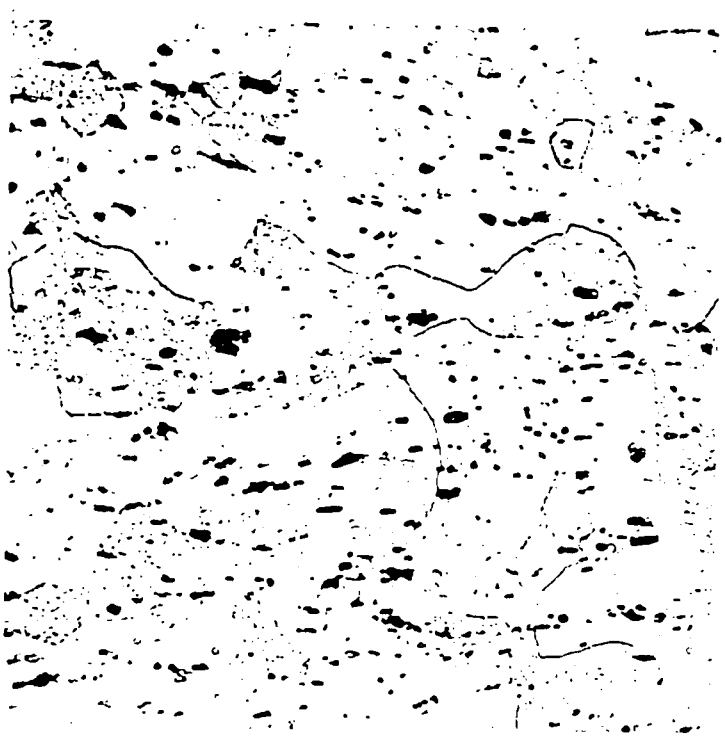

Figure 1. Al 1100-H18 sheet, cold rolled. Secondary phase is $FeAl_3$ (1).

Aluminum Pitting Corrosion

Aluminum owes its corrosion resistance to its highly reactive nature, which results in the formation of a passive film. The air formed film is Al_2O_3, but the oxide formed during anodic polarization is dependent upon the solution chemistry (2). This oxide is soluble in both acidic and basic solutions, but is insoluble and very protective between pH 4 and 9 (3). However, exposure to environments containing aggressive anions, such as chlorides, can cause aluminum to undergo a localized corrosion process such as pitting. Pitting corrosion results from the localized, sporadic dissolution of the oxide film of a passivated metal.

The pitting process is generally accepted to involve a sequence of four reaction steps (4):

- adsorption of anions onto the oxide surface
- chemical reaction of anions with aluminum oxide ions or with precipitated aluminum hydroxide
- oxide film thinning by dissolution
- direct attack of underlying metal

Many recent non-equilibrium Al alloying studies herald reduction of the adsorption step as the key to delaying pit nucleation (5,6). When aluminum is immersed in a chloride solution, there is competition among chloride ions, hydroxyl ions, and water to become adsorbed onto the oxide surface. XPS and Auger spectroscopic analyses of aluminum oxides find little evidence of chloride

incorporated into the film at the freely corroding potential, below the pitting potential. However, Figure 2 (7) is representative of the chloride content of an aluminum film held near the pitting potential. Most studies indicate that the Cl^- is present at this potential, but is restricted to the outer 15 to 20 angstroms.

Another key role in the initiation of pits on aluminum is played by preexisting oxide flaws. Al passive films contain defects that result primarily from segregation phase boundaries (such as $FeAl_3$) or mechanical flaws such as surface scratches or stress induced microcracks. These inhomogeneities interfere with oxide growth above them, and also in the surrounding area. Pitting initiates at these sites and either propagates or repassivates, depending upon the solution conditions within the pit.

Once an aggressive solution chemistry is achieved within the pit, the dissolution process is rapid and autocatalytic. As seen in Figure 3, in which a metal M is being pitted by an aerated chloride solution, the anodic process in the pit is being supported on the surrounding surface by the reduction of oxygen.

$$M \dashrightarrow M^+ + e^-$$
$$O_2 + 2\,H_2O + 4e^- \dashrightarrow 4\,OH^-$$

This assumes that the oxide film M_mO_n is conductive. The cathodic processes occur in the pit for an insulating oxide such as Al_2O_3. The increased metal

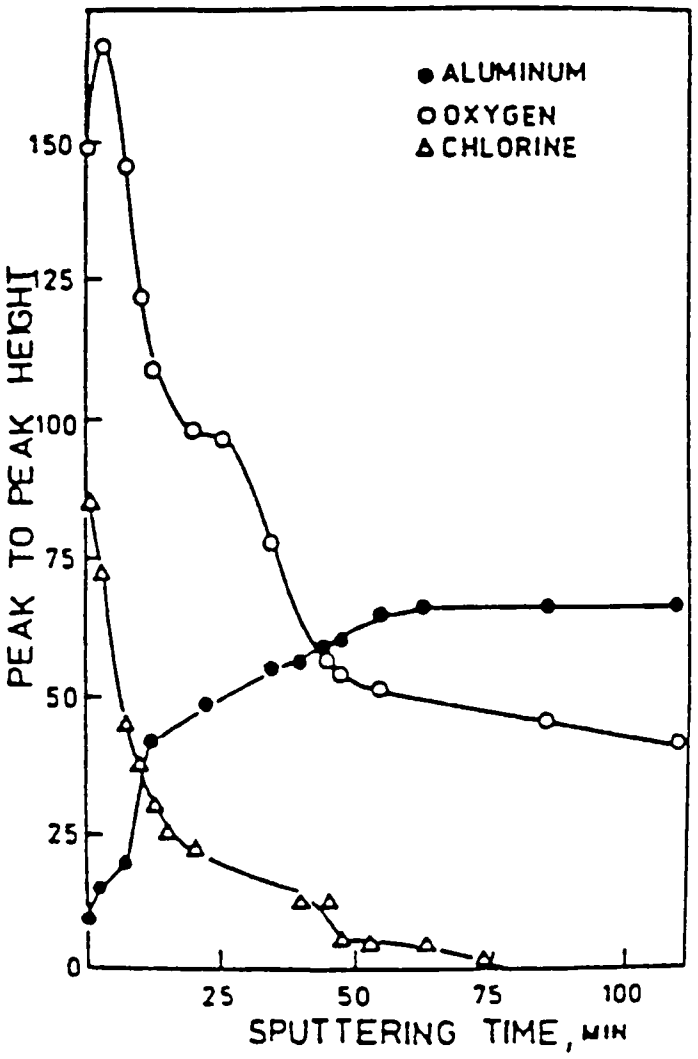

Figure 2. Auger profile of the passive film formed on high purity Al held at -750 mV (SCE) in 0.1 M NaCl for 24 hours (7).

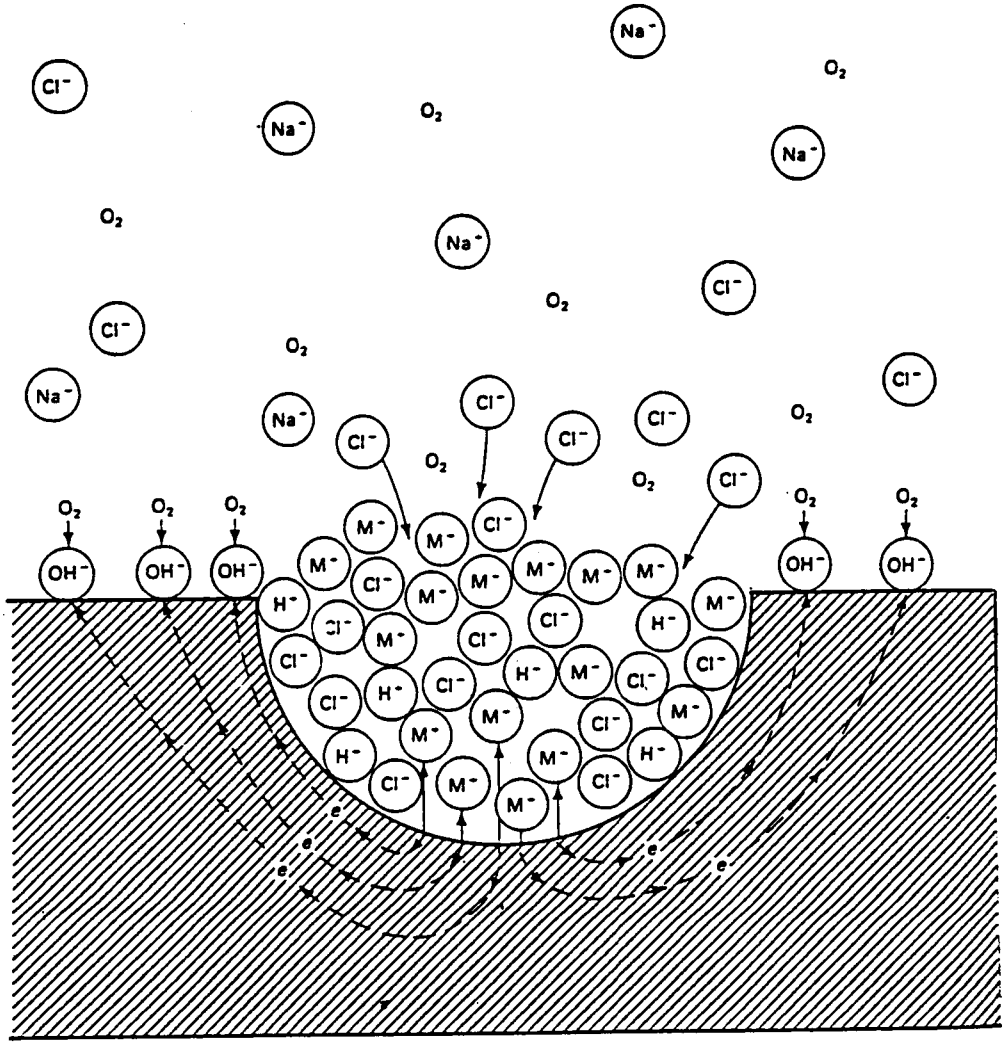

Figure 3. Autocatalytic processes occurring in a corrosion pit.

concentration in the pit attracts chloride ions and decreases the local pH by metal hydrolysis.

$$M^+ + Cl^- + H_2O \rightarrow MOH + H^+Cl^-$$

The corrosion rate then accelerates as the pH continues to decrease. A typical anodic polarization curve of aluminum in an NaCl solution is shown in Figure 4 (8). If the electrolyte contains a high concentration of inactive ions, the chloride ions are transport limited and the pit will repassivate with corrosion products. Anodic polarization will then show current oscillations, but no stable pits will form.

304L Stainless Steel

Stainless steels have customarily been classified as any alloy steel containing at least 10 - 12 % Cr (9). The chromium content, along with other alloying additions such as copper, aluminum, silicon, nickel, and molybdenum, increases the base material's resistance to corrosion and / or oxidation. As a result of composition and processing, the microstructure of stainless steels can be martensitic, ferritic, austenitic, precipitation hardened, or duplex. 304L is an austenitic stainless steel whose composition is given in Table 1 (1). The L designation refers to a reduced carbon content relative to the standard 304 alloy.

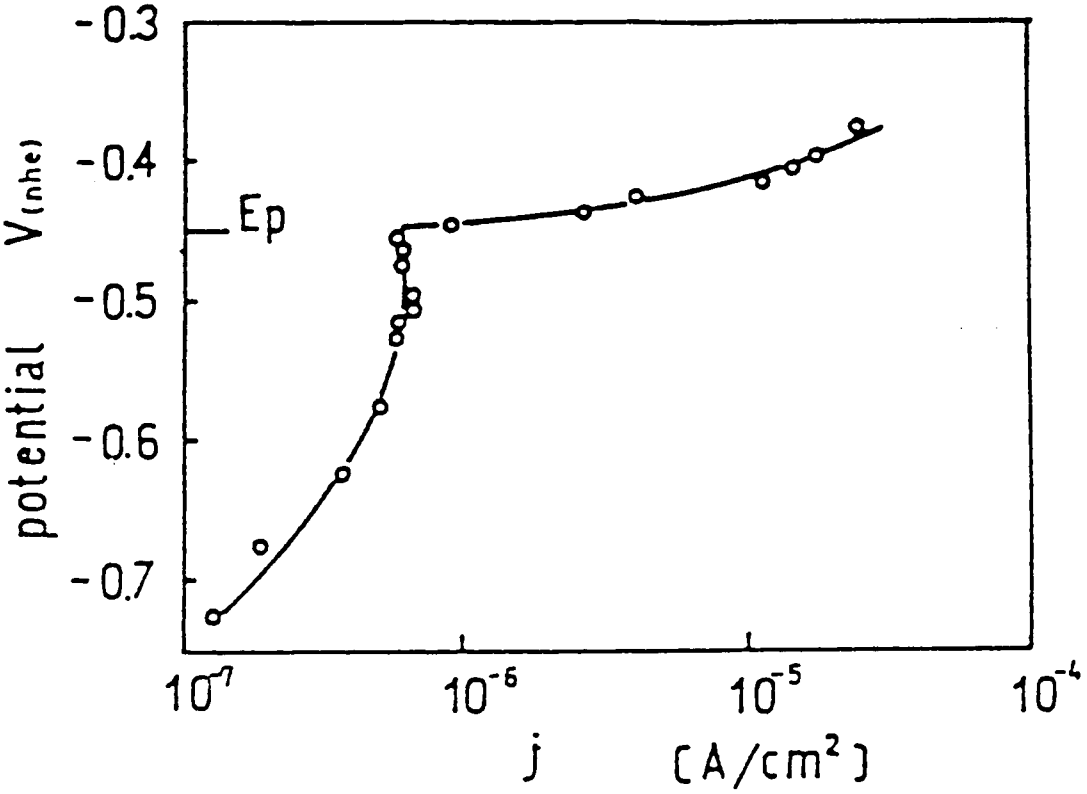

Figure 4. Anodic polarization curve of 99.99% Al in deaerated 0.1 M NaCl (8).

Table 1 Compositions of Standard Austenitic Stainless Steels

Common designation	Composition(a), % C	Mn	Si	Cr	Ni	P	S	Others
201	0.15	5.5-7.5	1.00	16.0-18.0	3.5-5.5	0.06	0.03	0.25 N
202	0.15	7.5-10.0	1.00	17.0-19.0	4.0-6.0	0.06	0.03	0.25 N
205	0.12-0.25	14.0-15.5	1.00	16.0-18.0	1.0-1.75	0.06	0.03	0.32-0.40 N
Nitronic 50, 22-13-5	0.06	4.0-6.0	1.00	20.5-23.5	11.5-13.5	0.04	0.03	1.5-3.0 Mo; 0.2-0.4 N; 0.1-0.3 Nb; 0.1-0.3 V
Tenelon (XM-31)	0.12	14.0-16.0	0.3-1.0	17.0-18.5	1.00	0.045	0.03	0.35 N min
Cryogenic Tenelon (XM-14)	0.12	14.0-16.0	1.00	17.0-19.0	5.0-6.0	0.06	0.03	0.35-0.50 N
216 (XM-17)	0.08	7.5-9.0	1.00	17.5-22.0	5.0-7.0	0.045	0.03	2.0-3.0 Mo; 0.25-0.50 N
216L	0.03	7.5-9.0	1.00	17.5-22.0	5.0-7.0	0.045	0.03	2.0-3.0 Mo; 0.25-0.50 N
Nitronic 60	0.10	7.0-9.0	3.5-4.5	16.0-18.0	8.0-9.0	0.06	0.03	0.08-0.18N
Nitronic 40, 21-6-9	0.08	8.0-10.0	1.00	19.0-21.5	5.5-7.5	0.06	0.03	0.15-0.40 N
Nitronic 33, 18-3-12	0.08	11.50-14.50	1.00	17.0-19.0	2.25-3.75	0.060	0.030	0.20-0.40 N
Nitronic 32, 18-2-12	0.15	11.0-14.0	1.0	16.5-19.0	0.5-2.5	0.06	0.03	0.20-0.45 N
18-18 Plus	0.15	17.0-19.0	1.00	17.5-19.0	...	0.045	0.03	0.75-1.25 Mo; 0.75-1.25 Cu; 0.4-0.6 N
301	0.15	2.00	1.00	16.0-18.0	6.0-8.0	0.045	0.03	...
302	0.15	2.00	1.00	17.0-19.0	8.0-10.0	0.045	0.03	...
302B	0.15	2.00	2.0-3.0	17.0-19.0	8.0-10.0	0.045	0.03	...
303	0.15	2.00	1.00	17.0-19.0	8.0-10.0	0.20	0.15 min	0.6 Mo (optional)
303 Plus X (XM-5)	0.15	2.5-4.5	1.00	17.0-19.0	7.0-10.0	0.20	0.25 min	...
303Se	0.15	2.00	1.00	17.0-19.0	8.0-10.0	0.20	0.06	0.15 min Se
303 Al-Modified	0.15	2.00	1.00	17.0-19.0	8.0-10.0	0.05	0.11-0.16	0.40-0.60 Mo; 0.60-1.00 Al
304	0.08	2.00	1.00	18.0-20.0	8.0-10.5	0.045	0.03	0.10 N
304L	0.03	2.00	1.00	18.0-20.0	8.0-12.0	0.045	0.03	0.10 N
304H	0.04-0.10	2.00	1.00	18.0-20.0	8.0-10.5	0.045	0.03	...
18-9-LW	0.10	2.00	1.00	17.0-19.0	8.0-10.0	0.045	0.03	3.0-4.0 Cu
304N	0.08	2.00	1.00	18.0-20.0	8.0-10.5	0.045	0.03	0.10-0.16 N
304HN	0.08	2.00	1.00	18.0-20.0	8.0-10.5	0.045	0.03	0.16-0.30 N
304LN	0.03	2.00	1.00	18.0-20.0	8.0-12.0	0.045	0.03	0.10-0.16 N
305	0.12	2.00	1.00	17.0-19.0	10.5-13.0	0.045	0.03	...
308	0.08	2.00	1.00	19.0-21.0	10.0-12.0	0.045	0.03	...
253MA	0.10	0.80	1.40-2.00	20.0-22.0	10.0-12.0	0.040	0.030	0.03-0.08 Ce; 0.14-0.20 N
309	0.20	2.00	1.00	22.0-24.0	12.0-15.0	0.045	0.03	...
309S	0.08	2.00	1.00	22.0-24.0	12.0-15.0	0.045	0.03	...
309Cb	0.08	2.00	1.00	22.0-24.0	12.0-16.0	0.045	0.03	10 × %C min, 1.10 max (Nb+Ta); 0.10 N
310	0.25	2.00	1.50	24.0-26.0	19.0-22.0	0.045	0.03	...
310S	0.08	2.00	1.50	24.0-26.0	19.0-22.0	0.045	0.03	...
310Cb	0.08	2.00	1.50	24.0-26.0	19.0-22.0	0.045	0.030	10 × %C min, 1.10 max (Nb+Ta); 0.10 N
254 SMO	0.02	1.00	0.80	19.5-20.5	17.5-18.5	0.030	0.010	6.00-6.50 Mo; 0.50-1.00 Cu; 0.18-0.22 N

It is considered to be a basic stainless steel with mid-range corrosion resistance by stainless standards which has not been alloyed for increased strength (10). 304L is typically used in food processing and processing of mild corrodents.

Conventional Corrosion Resistant Surface Treatments

The earliest method for retarding metallic surface degradation was by paint application, a practice that is still the most widely used on manufactured products. Other common industrial practices include galvanizing, electroplating, anodizing, electroless plating, vacuum deposition, and sputtering (11). Each of these treatments is affected to some degree by several limitations, such as: lack of uniform coverage at surface irregularities, dimensional changes, cleanliness problems, and particularly coating delamination.

Ion Implantation

The near surface modification of materials by the direct application of ion beams is an outgrowth of semiconductor technology, where it has gained general acceptance as a superior alternative to doping by thermal diffusion (12). The non-equilibrium nature of the process can produce compositions and structures unattainable by conventional methods. The chemistry and / or structure of the target material surface can be reproducibly transformed through the creation of

alloy layers, metastable phases or amorphous regions by the injection of highly accelerated ionic species. Applications of this process have proved fruitful in such diverse areas as corrosion, tribology, and fatigue of metallic substrates, ceramic fracture toughness, and metallic-polymeric bonding. A schematic drawing of a typical ion beam implanter (Fig 5) illustrates the essential operating components. The material to be implanted, which can be almost any element that can be vaporized and ionized into the plasma state under vacuum (13), can be introduced into the ion source in gaseous or solid form. Solid feed materials are heated in order to provide an adequate vapor pressure. A heated filament in the ion source generates electrons which ionize the gas to form a plasma. The ions are extracted by a negatively biased grid located near the plasma boundary. Upon extraction and acceleration into a unidirectional ion beam, magnetic separation of specific species or isotopes can be accomplished before implantation under vacuum into the target material. The ion beam is directed toward the workpiece by a series of electrostatic and magnetic lenses which determine the area on the target to be implanted. The ion beam current can be integrated to calculate the fluence in ions / cm^2. End-line accelerating energies generally vary between 25 and 400 keV (14). The advantages of surface modification by the direct application of ion beams over other forms of surface coatings include (15,16):

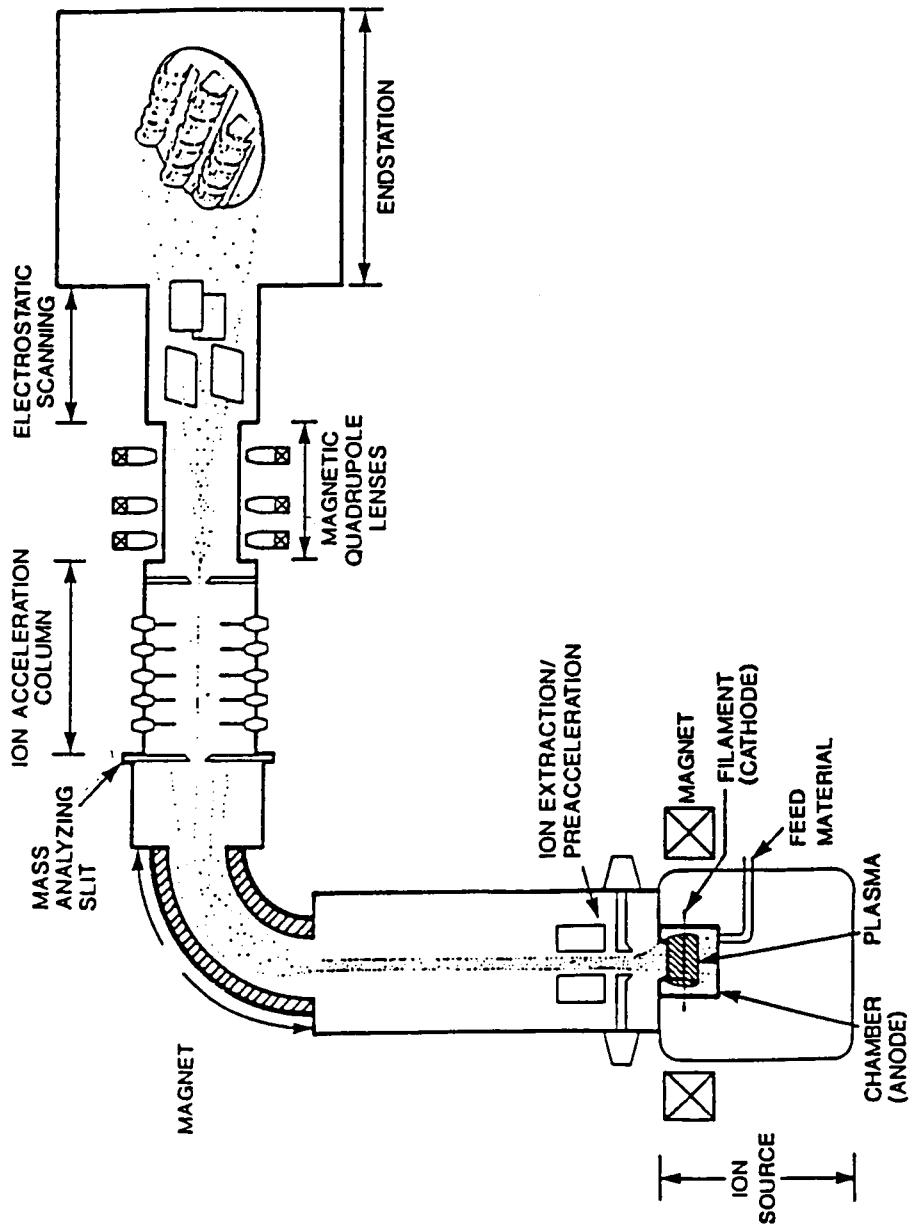

Figure 5. Schematic representation of an ion implantation system with magnetic mass separation of beam constituents (14).

- potential for production of non-equilibrium surface alloys
- conservation of scarce or expensive alloying elements
- possible structure amorphization by radiation damage
- excellent lateral dose uniformity
- avoidance of coating delamination due to lack of an interface
- concentration distribution may be tailored to satisfy need
- low temperature process
- negligible dimensional changes
- cleanliness of vacuum process

The versatility of this technology has led to a number of related techniques such as ion beam sputtering, ion beam mixing and stitching, ion beam assisted deposition, and plasma ion implantation.

However, besides the cost intensive nature of equipment and operation of the implanters (approximately $\$400/m^2$ (14)), widespread use of this technique has been limited for reasons that include (13, 17):

- lack of coverage uniformity on target material contours (line-of-sight process)
- target heat generation (up to $500^{\circ}C$) due to the high energy input (typically 2 W / cm^2)
- thinness of the implanted region
- substrate inclusions may prevent dose uniformity
- in-service temperatures may lead to undesirable diffusional changes
- only small workpieces can be accommodated in most target chambers
- batch processing required due to vacuum conditions

The concentration distribution or depth profile of the implanted species is dependent upon the atomic number of the substrate and the implant, as well as the

accelerating voltage. Prior to implantation, a model of the projectile-ion / host nuclear and electronic interactions (i.e., TRIM (18)) can be utilized to predict the ensuing dose distribution (Fig. 6 (14)). Nuclear, or Coulombic, energy transfers result from the elastic electrostatic repulsion between the incident and lattice nuclei, while inelastic electronic scattering arises from ionic interactions with the target electrons (19). Assuming that sputtering is not excessive, a nearly Gaussian ion distribution generally results during implantation at a constant accelerating potential (Fig. 7) (20). More complex depth profiles may be achieved through successive implantations which vary in ion energy and dose (Fig. 8) (20).

Sputtering loss of substrate layers can become quite significant for certain combinations of implantation parameters (i. e., large fluences of heavy elements), possibly leading to the sputtering rate equaling the implantation rate and attainment of a saturation condition. The sputtering rate is dependent upon (14) substrate and ion composition, metallurgical structure and chemical bonding, beam energy, and incident beam angle.

Finally, the structural modifications of the near-surface layers should not be neglected in favor of compositional changes when analyzing the effect of ion

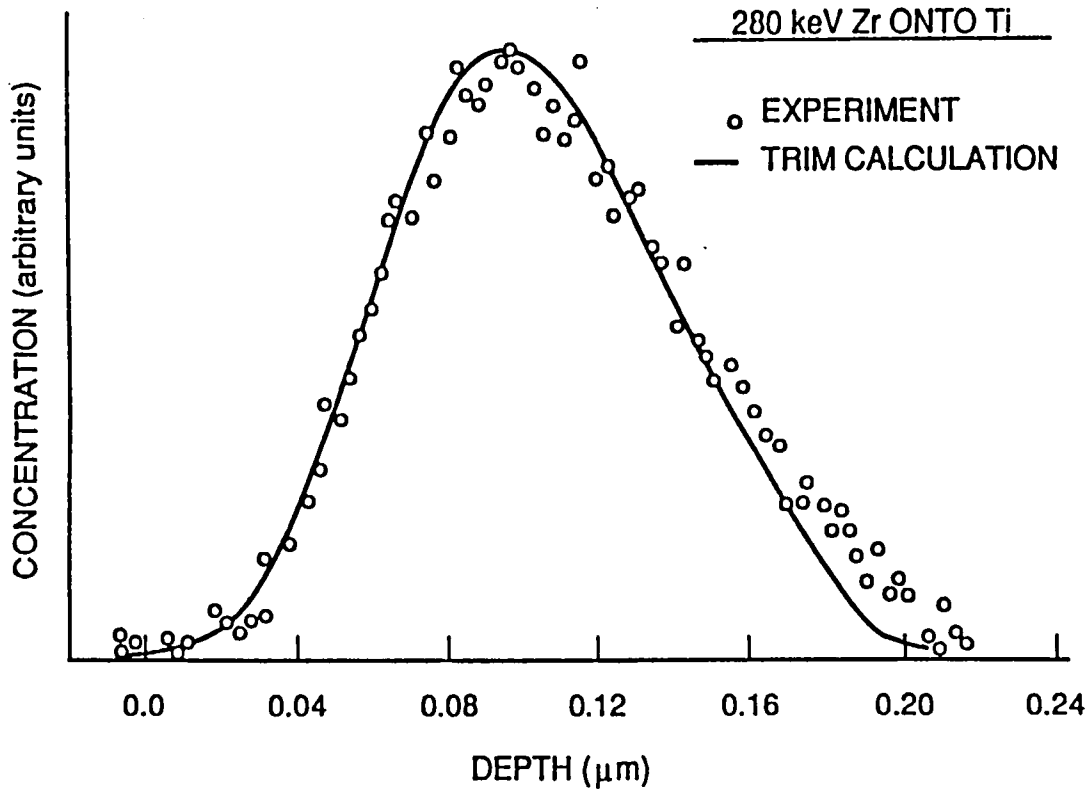

Figure 6. Depth profile for ion implanted 280 keV Zr in Ti-6Al-4V. Experimental determination of depth distribution by RBS is compared with that derived from a TRIM calculation (14).

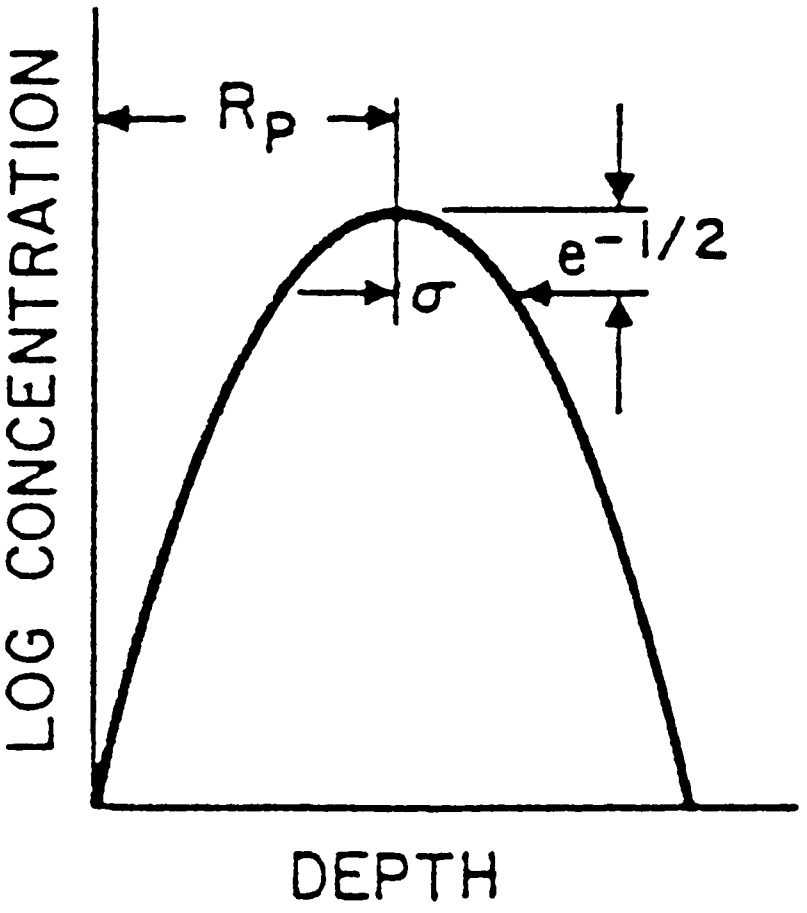

Figure 7. Depth profile of implanted ions showing Gaussian distribution, projected range, and standard deviation (20).

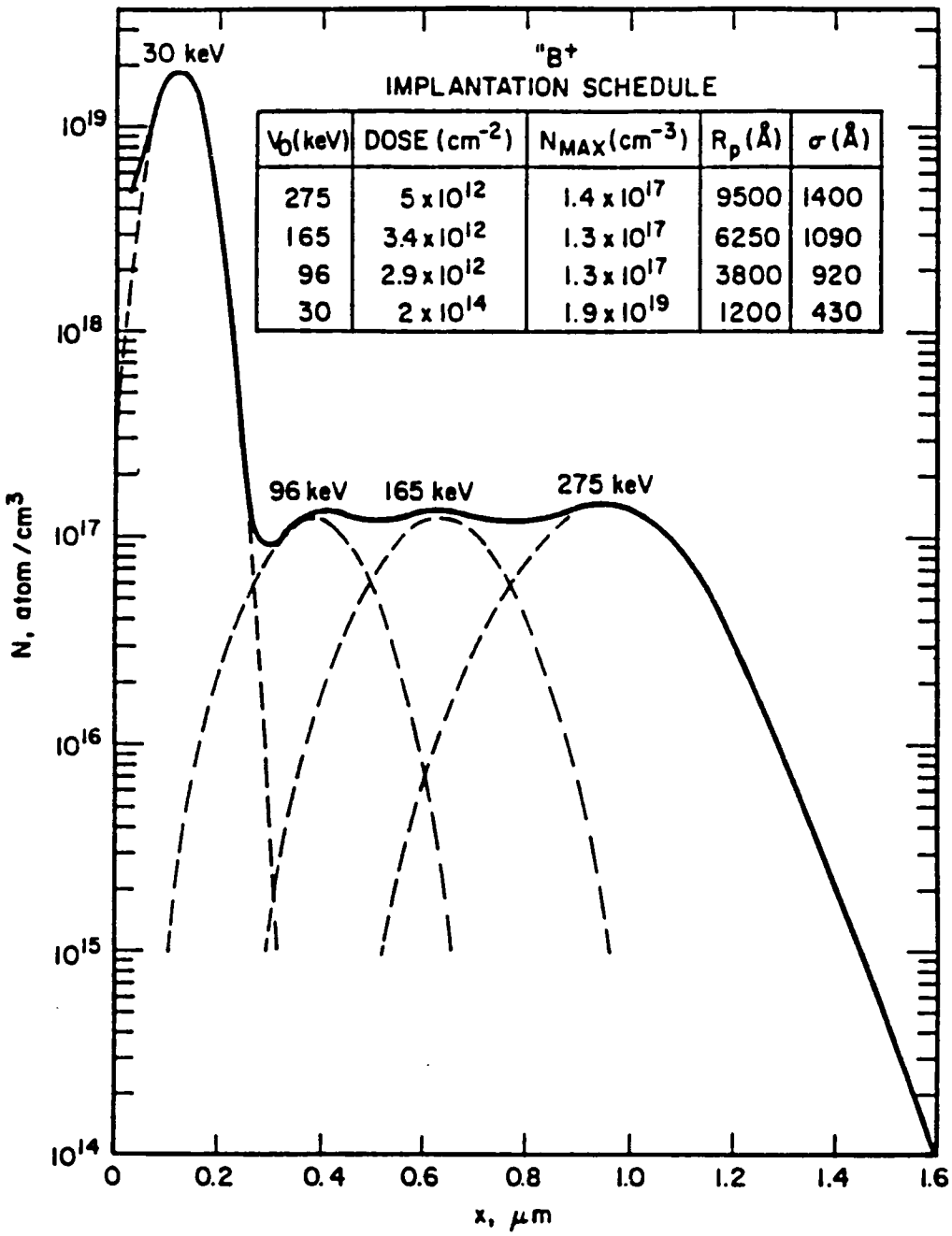

Figure 8. Calculated depth profile synthesized by four separate implantations with varying doses and energies (20).

bombardment. As seen in Figure 9 (21) for the implantation of Cr into Al_2O_3, the relative intensity of displacement events involving lattice sites can dwarf the number of implanted ions. This result can be traced to the cascade effect in which a single implanted ion may displace many atoms from their original positions (Fig. 10) (22). These defect formations along with the presence of implanted ions result in expansion of the near surface region and a biaxial residual compressive stress. These residual stresses can modify the hardness and wear properties of the implanted material.

Ion Implantation for Corrosion Control

The main thrust of materials science research efforts into ion implantation effects upon the surface properties of metals has been in mitigating friction and wear. However, as is the case for tribological mechanisms, aqueous corrosion is essentially a surface phenomenon, and ion beam modifications have also resulted in various successful applications of this technology to enhancing resistance to various forms of metallic corrosion. Cost effectiveness is of great importance in corrosion control. Many alloying elements that promote passivity or slow the rate of anodic or cathodic reactions are also prohibitively expensive. Ion implantation holds the promise of a surface treatment that requires locating these elements only in the near-surface regions where they are most effective. Also,

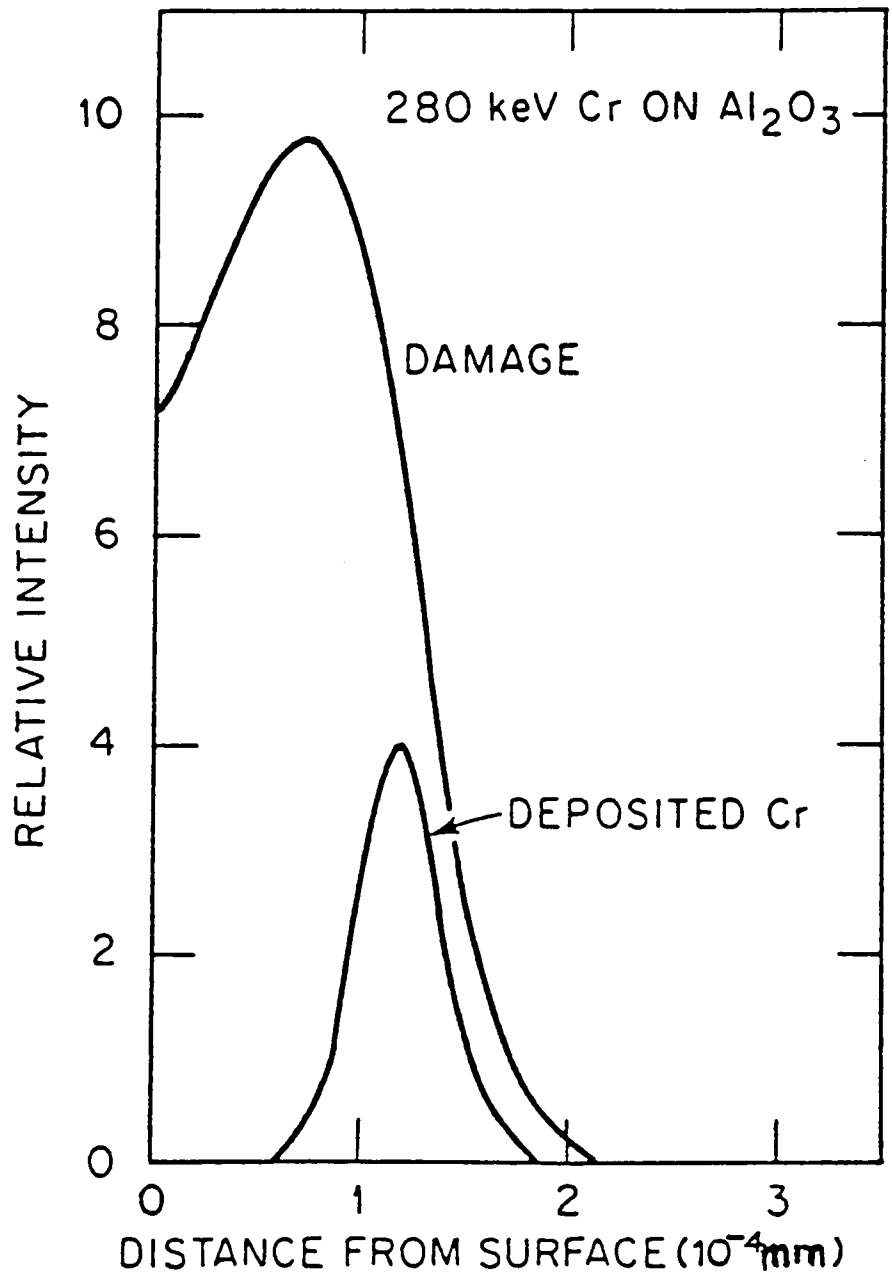

Figure 9. Distribution of Cr ions and displacement defects in Al_2O_3 resulting from bombardment with 280 keV Cr ions (21).

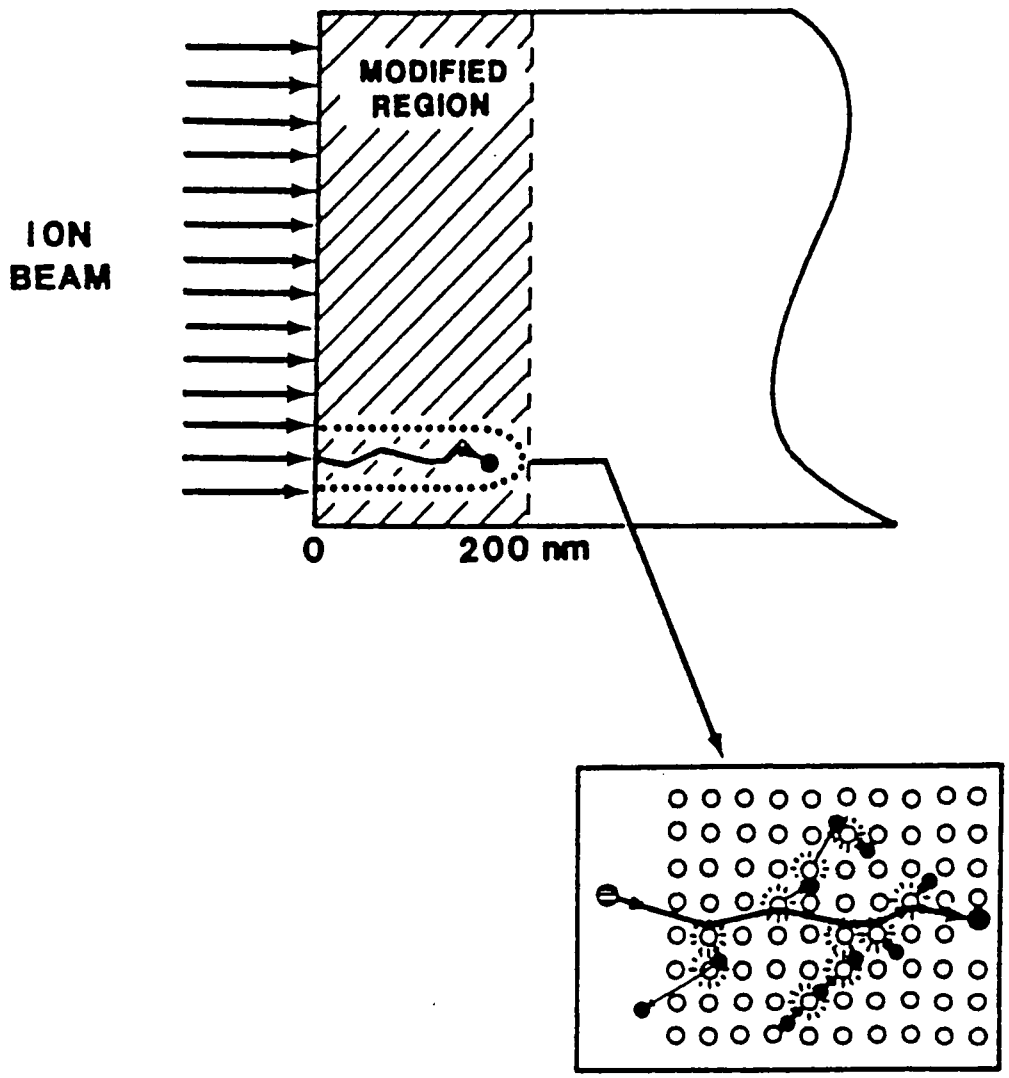

Figure 10. Schematic illustration of the cascade effect resulting from an impinging accelerated ion (22).

new non-equilibrium compositions offer possible improvements in the corrosion resistance of a variety of materials. Solid solutions of elements which are normally immiscible can be fabricated. This is an important advantage since conventional alloys which are not single phase are susceptible to local galvanic attack at phase boundaries.

Much previous work involving the implantation of noble elements into commercial alloys has indicated that the defect structure resulting from radiation damage usually has a negligible effect on the subsequent corrosion properties. However, if the surface is made highly amorphous, the corrosion rate may decrease since this region can act as a diffusion barrier (21). Amorphized surfaces can also result in elimination of surface defects such as crevices and grain boundaries that can nucleate localized breakdown of passivity (23). Nevertheless, most of the beneficial properties noted in corrosion studies of ion implanted metals have been attributed to the chemical, or alloying, effect. Mechanisms for enhanced corrosion resistance by alloying additions via high energy ion beam application include (24):

- passivity promotion by lowering the critical current density and / or the passivation potential
- passivity promotion by stimulating cathodic kinetics
- increased resistance to localized passive film breakdown
- cathodic poisoning

- decreased active corrosion rate by surface ennoblement

For example, an iron surface implanted with 5.3 atom % Cr was found to have essentially the same corrosion resistance as a conventional stainless alloy of the same composition (21). Many other examples exist of the successful transfer of the corrosion properties of a bulk alloyed material to the surface layers by the ion implantation technique. Other ion implantation applications include:

- additions of nitrogen to Ti-6Al-4V surgical alloy decrease the rate of corrosive wear (Fig. 11) (25)
- additions of lead to iron lower its active corrosion rate and increases its resistance to pitting
- additions of tantalum to iron increase its passive behavior (26)
- additions of palladium to titanium shift the corrosion potential into the passive range (27)
- additions of copper to iron act as a cathodic poison by lowering the hydrogen exchange current density (28)
- additions of nitrogen to steels have met with mixed results in enhancing passivity

The susceptibility of steels to pitting in chloride solutions has motivated their implantation with highly passivating species. For example, the pitting potential of 52100 martensitic steel in deaerated 0.01 M NaCl is increased by 970 mV following tantalum implantation, and 600 mV after the implantation of chromium (29). Similar results have been obtained for these species when implanted into pure iron (19).

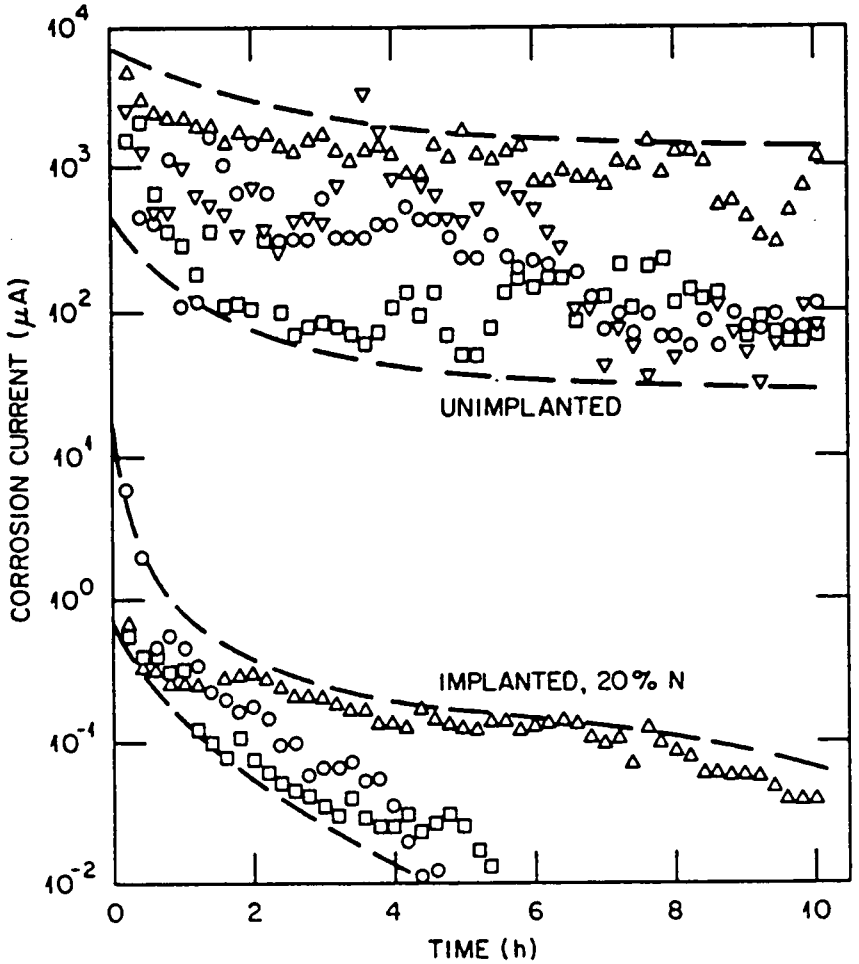

Figure 11. Corrosion current as a function of time for unimplanted and N-implanted Ti-6Al-4V alloys during a corrosion wear test (25).

The primary concern about using the implantation process for corrosion mitigation is that the surface layer be of sufficient thickness so as to not be penetrated during the normal operating lifetime of the material. This has led to adoption of related technologies that result in a thicker coating, such as ion beam assisted deposition (IBAD).

Nitrogen Implantation into Stainless Steel

Additions of nitrogen to austenitic stainless steels, originally investigated as an inexpensive austenite stabilizer, have been utilized historically to increase the fracture toughness and yield strength of these alloys. More recent efforts have shown that high-dose nitrogen implantation or nitriding results in improved wear characteristics, with the greatest enhancement of tribological properties occurring for a nitrogen dose exceeding 1×10^{17} ions/cm^2 (30). In addition, equilibrium amounts of nitrogen (below 1 at. %) in high Cr, Mo stainless steels increase their resistance to several forms of corrosion, including pitting and crevice corrosion (31,32), sensitization (33), and uniform attack in certain acidic and basic solutions (34). However, just as for the α-phase solubility limit of an Fe-C alloy (Fig. 12) (35), nitrogen content in solid solution in the bulk γ-alloy is restricted

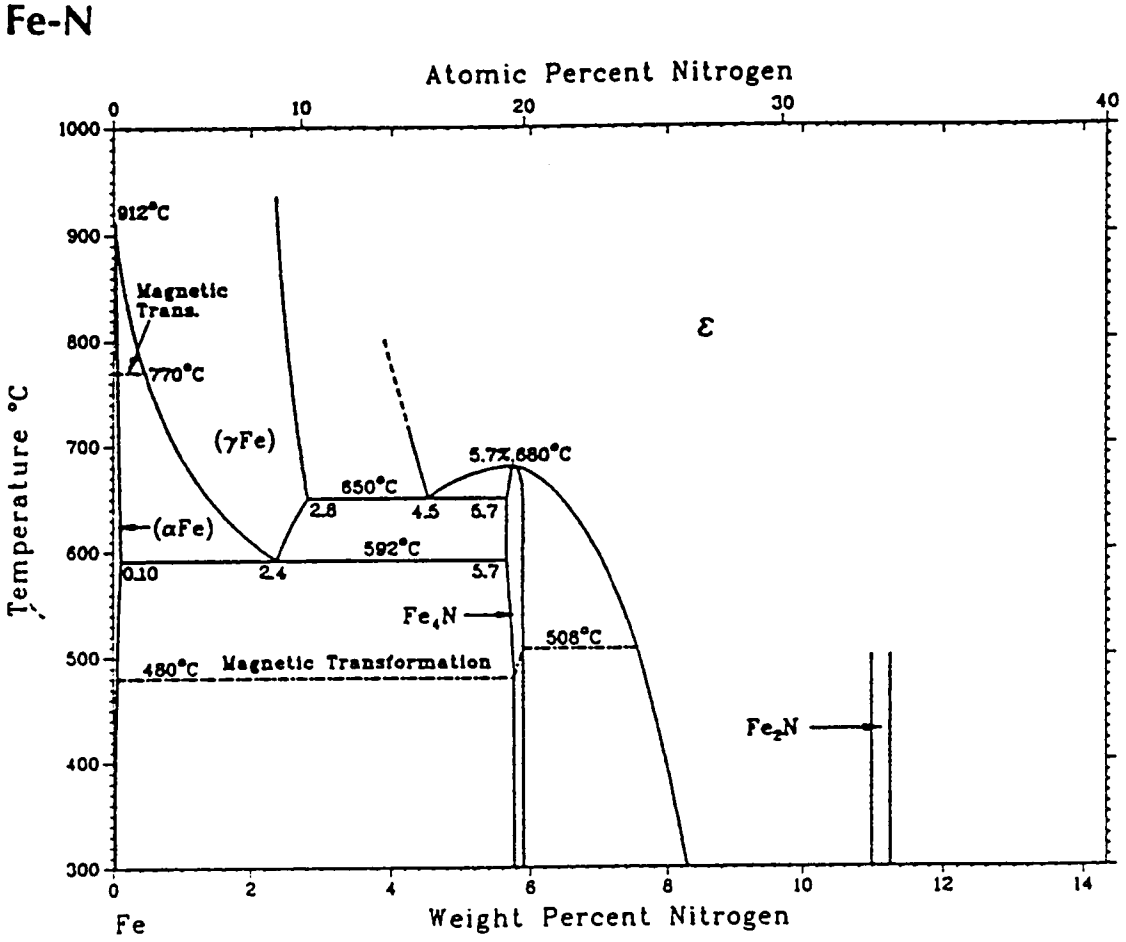

Figure 12. The iron-nitrogen phase diagram (35).

due to limited solubility, and nitride formation and sensitization may result if the solubility limit is exceeded. Evidence also exists that crevice corrosion susceptibility increases for equilibrium nitrogen contents above 1 at. % due to chromium nitride formation (36). Stainless steel passivity is in large part due to the presence of chromium in the passive film. If excessive nitride formation ties up the alloyed Cr content, the inherent 304L passivity is lost.

In order to further improve the resistance of austenitic stainless steels to the above types of corrosion, non-equilibrium techniques must be explored. Sputtered film (37) and ion beam implantation (38-40) treatments have resulted in decreased active corrosion rates in deaerated sulfate and borate solutions (37), and acidic solutions (38-40). Lower passive current densities also were noted in the acidic environments (39,40). However, these results do not address the primary corrosion problem of localized passive-film breakdown (pitting and crevice corrosion) in chloride solutions. A plasma nitriding treatment (41) has been used to demonstrate that a low-alloy steel (4140) containing 7 wt. % chromium-nitride at and near the surface results in an expanded pH-potential domain for stabilization of passivity. The pitting potential was raised from +400 to +1000 mV (SHE) in an electrolyte of near neutral pH = 8 and 1 wt. % NaCl. The application of nitrogen ion implantation, and more specifically, nitrogen plasma ion implantation, to the problem of austenitic 304L stainless steel and its

susceptibility to pitting corrosion, may further enhance its ability to effectively passivate in halide environments beyond that seen for conventional nitrogen-alloying conditions.

The exact mechanism of nitrogen-induced passivation is still uncertain. Proposed mechanisms include anodic dissolution inhibition by N (42,43); acidic pit neutralization via NH^{4+} production (41,44); radiation damage stimulated diffusion and oxidation (39); reduced surface catalytic activity for the hydrogen cathodic reaction (37); and N-Cr clustering which increases the Cr content in the passive film (45,46).

Aluminum Corrosion Inhibition by Ion Implantation

Solid solution alloying additions to aluminum for improved corrosion resistance are restricted due to its limited solubility for passivating species such as chromium and molybdenum. Ion implantation of a variety of species has been applied to Al above equilibrium concentrations in an attempt to enhance its resistance to pitting corrosion in chloride containing solutions. Table 2 summarizes results from several authors. The most applicable comparison of pitting resistance among alloys is the potential at which pitting commences in an anodic polarization test (E_p). ΔE_p refers to the change in E_p in millivolts with

Table 2. Pitting Resistance of Ion Implanted Aluminum

Al Alloy	Implant	Dose (ions / cm^2)	Solution	ΔE_p (mV)	Reference
99.99 %	Mo	2×10^{17}	d 1000ppm NaCl	200	47
99.99 %	Mo	12 a/o at surface	d 0.1 M NaCl	155	48
99.99 %	Si	12 a/o at surface	d 0.1 M NaCl	450	48
99.99 %	Nb	12 a/o at surface	d 0.1 M NaCl	115	48
99.99 %	Zr	12 a/o at surface	d 0.1 M NaCl	290	48
99.99 %	Cr	12 a/o at surface	d 0.1 M NaCl	135	48
99.99 %	Ta	4×10^{16}	d 0.1 M NaCl	175	49
Al 1100	N	1×10^{17}	a 3.5 w/o NaCl	115	50
Al 1100	Ti	5×10^{17}	a 3.5 w/o NaCl	95	50
Al 1100	V	1×10^{17}	a 3.5 w/o NaCl	70	50
99.999 %	Mo & Cr	$4 - 8 \times 10^{16}$	d 0.1 M NaCl	115	51

respect to the unimplanted aluminum material. However, this value is dependent not only on the composition of the base material, but also on the implanted dose and its distribution, and the makeup of the test solution. This makes direct comparison of pitting potential increases for the various species implanted by various researchers difficult at best. Some of the most significant enhancements of pitting resistance seem to occur with the implantation of elements which are well known passivating additions to stainless steel. An example of a known steel passivating species imparting corrosion resistance to aluminum is shown in Figure 13 (52). A Cr-implanted Al 2014 alloy shows no pit development in a salt spray test (ASTM B 117-73), while the unimplanted specimen and other implants undergo severe corrosion. The most surprising result from Table 2 is the moderate pitting inhibition imparted by N_2 implantation, especially in light of the aggressive solution utilized. Other authors have noted the tendency for N_2 to inhibit pit growth (52,53); and given the relative ease of using N_2 as a source material, more extensive studies of this effect would seem warranted. Aluminum is among the most susceptible of metals to localized corrosion in chloride environments, and it is therefore not surprising that incorporating a wide variety of non-equilibrium species into the surface of the material provides for an increase in resistance to pitting.

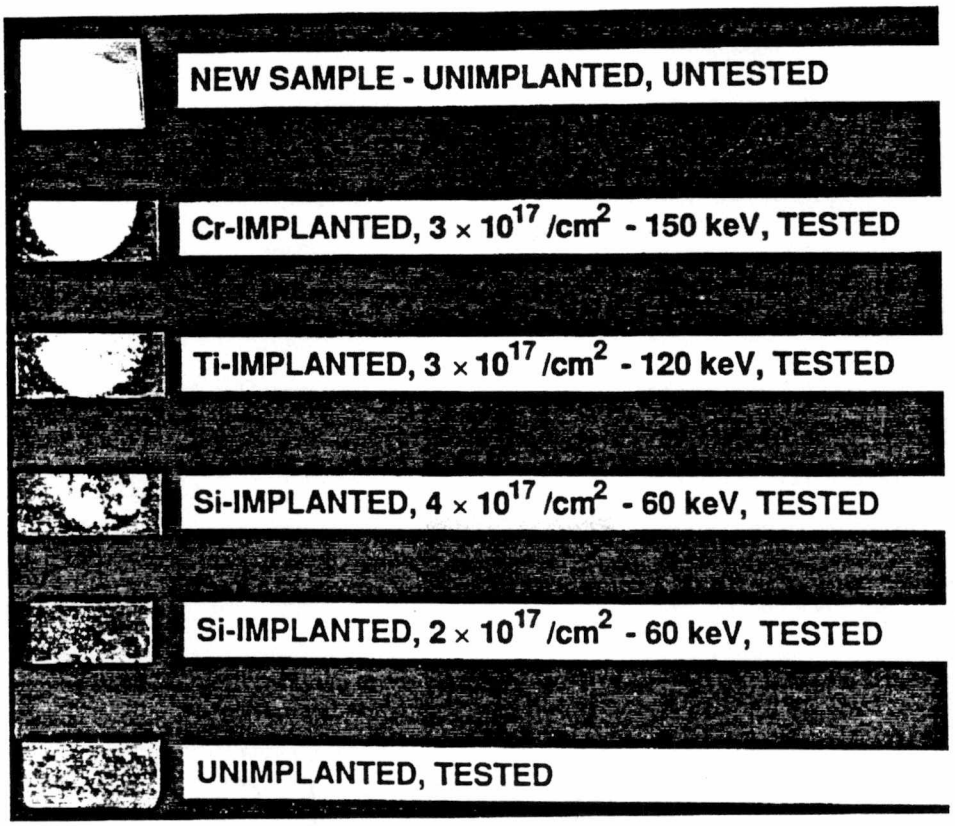

Figure 13. Coupons of Al 2014 after a variety of ion implantation treatments, followed by salt fog testing (52).

Aluminum Pitting Resistance Improvements Via Non-Equilibrium Alloying Additions

In addition to ion beam implantation, other non-equilibrium techniques, such as rapid solidification and co-sputtered thin films, have been employed to enhance the pitting resistance of aluminum alloys. Melt-spun ribbons of Al-4Ti and Al-12Ti, when pulverized and extruded into billets, exhibit a two order of magnitude decrease in corrosion current density when compared to Al 7075-T73 (54). These compositions also show a greater resistance to pitting in a 3.5 wt. % NaCl solution than does Al-8Fe-2Mo. Melt-spun ribbons of Al-11Er (55) also demonstrate elevated pitting potentials in an aggressive chloride solution.

The most beneficial of the increases in localized corrosion resistance are shown by thin films of aluminum co-sputtered with a variety of transition elements onto a silicon single-crystal wafer. The wafers are cooled to liquid nitrogen temperatures in order to suppress the formation of precipitates, which, if formed, lead to preferential pit nucleation at these sites. As seen in Figure 14 (5), solid solution molybdenum additions increase the breakdown potential in deaerated 0.1 N KCl. E_{corr} is also elevated by 520 mV and the passive current density is decreased by half (56). Similarly, Al films containing Mo, Nb, Ta, Ti, and Cr each exhibited elevated pitting potentials (Fig. 15) (57).

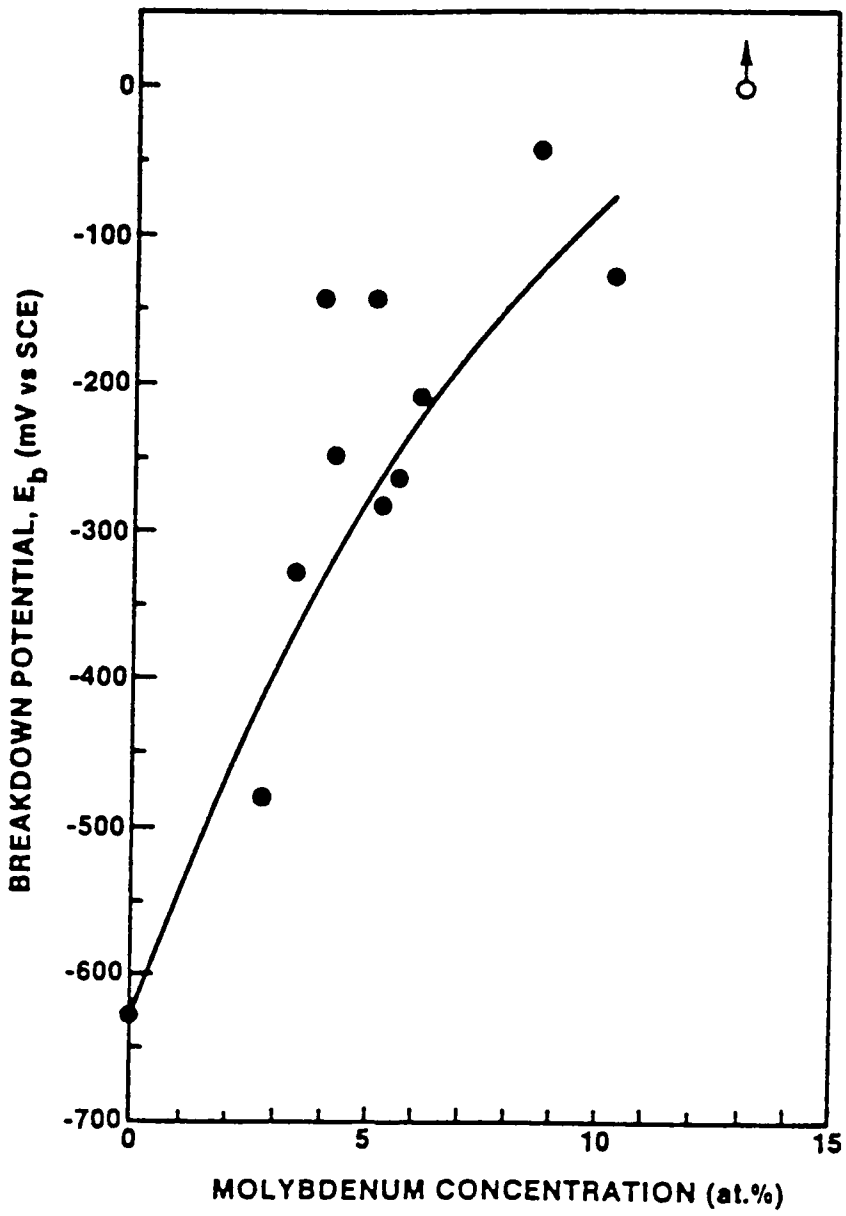

Figure 14. The effect of average Mo content on pitting potential of thin cosputtered Al-Mo films (5).

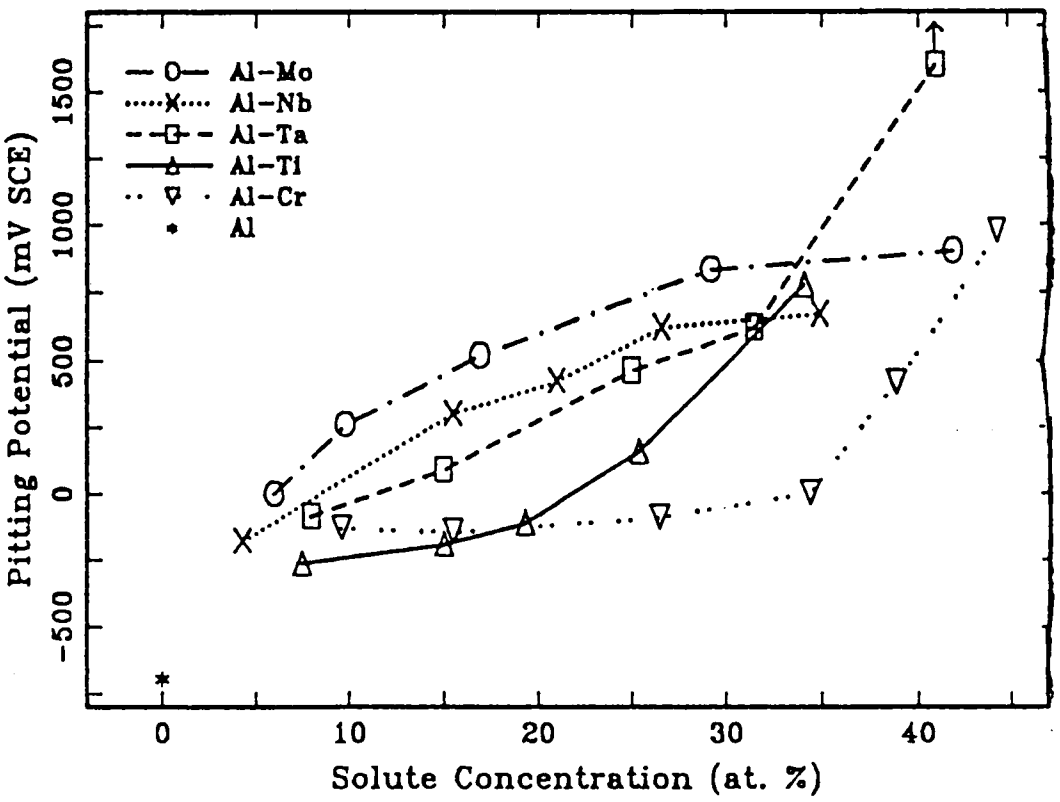

Figure 15. Pitting potentials of various Al alloy thin films in deaerated, pH 10, 0.1M NaCl as a function of concentration (57).

Pitting Resistance Of W-Al Films

Tungsten lies in the same column of the periodic table as the highly passivating species chromium and molybdenum, and it is therefore not surprising that W is not easily activated in solution. Anodic curves that are typical of the W response to polarization are seen in Figure 16 (58). In acidic solutions the passive region extends as high as 110 V before oxygen evolution commences, indicating the formation of a highly insulating oxide film. The W Pourbaix diagram (Fig. 17) (3) illustrates its tendency to passivate in acidic and neutral environments. In alkaline solutions dissolution occurs with the formation of WO_4^{2-} ions.

Tungsten is another transition element that has limited solubility in aluminum (Fig. 18) (35) and which increases the resistance to pitting of Al when cosputtered into a thin film. W alloying additions have previously been shown to enhance the passivity of stainless steels by stabilizing the oxide and increasing its adhesion to the metal (59,60). As shown in Figure 19 (61), the pitting potential of Al-W films in aerated 0.1 M KCl increases dramatically with tungsten content. For 10.3 % additions, E_p is elevated to 2600 mV above the unimplanted value. These films retain a portion of this pitting resistance even after precipitation during heat treatment at 400°C, where E_p remains 700 mV above the control

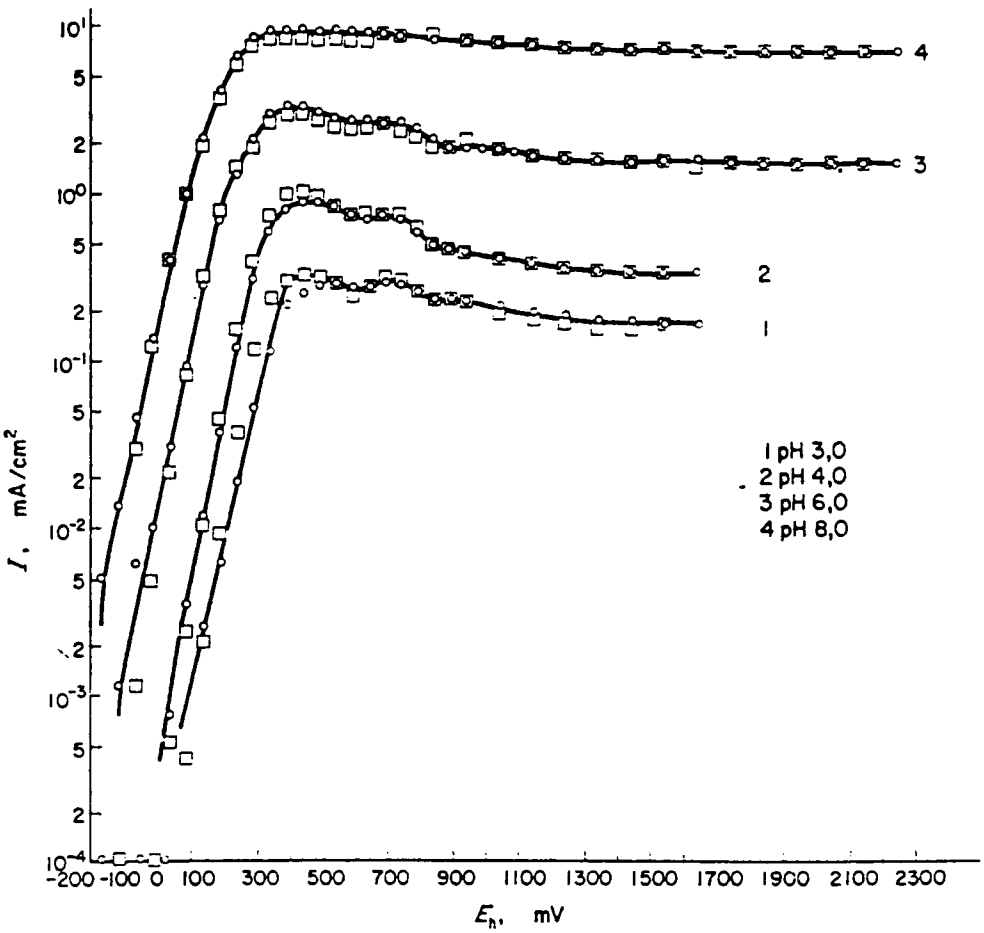

Figure 16. Polarization curves for tungsten in citric acid + Na_2HPO_4 solutions (58).

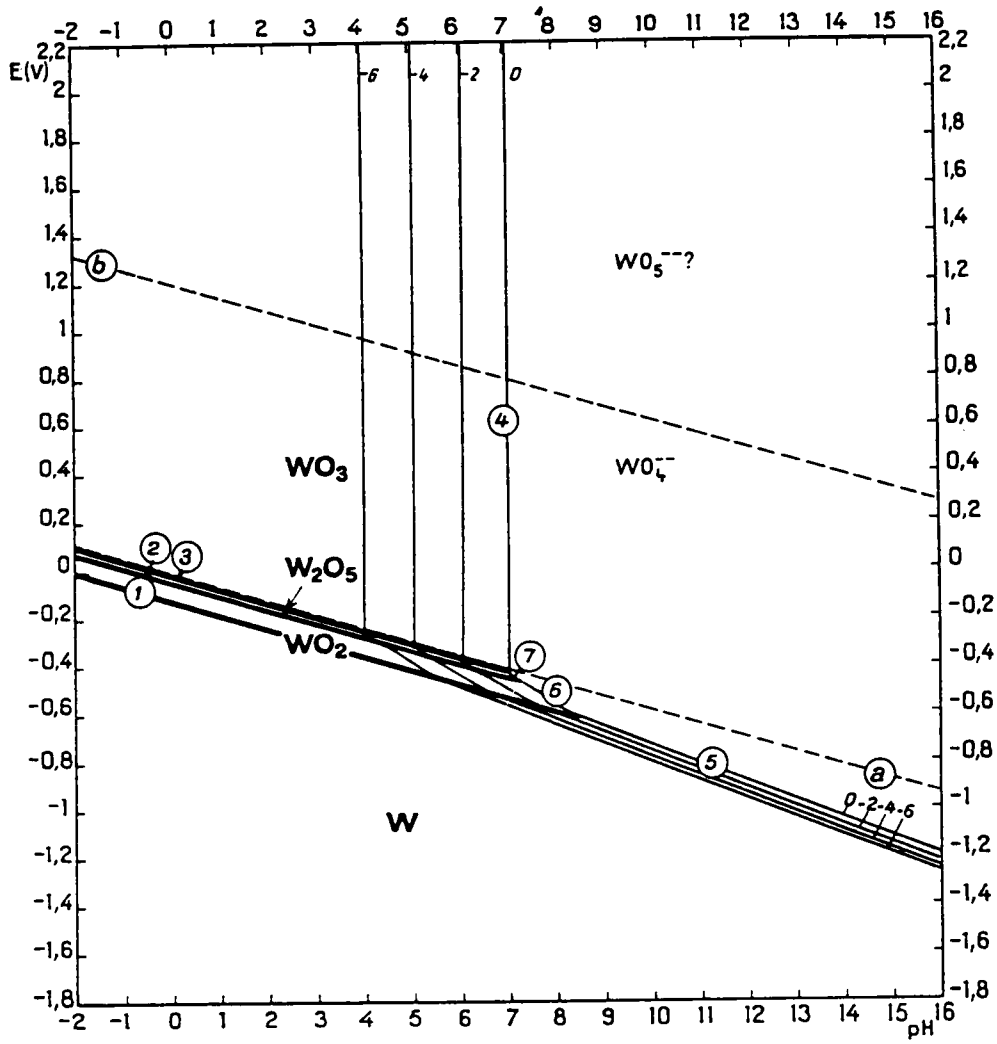

Figure 17. Pourbaix diagram for the W-H_2O system (3).

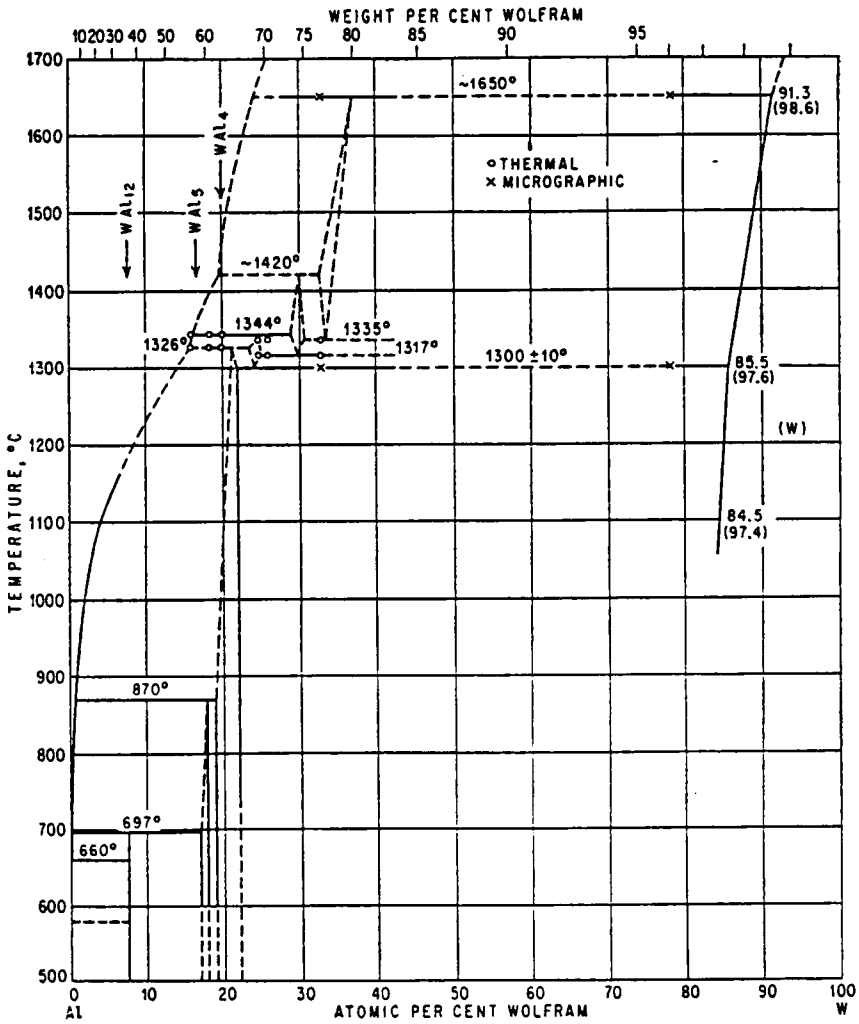

Figure 18. The aluminum-tungsten phase diagram (35).

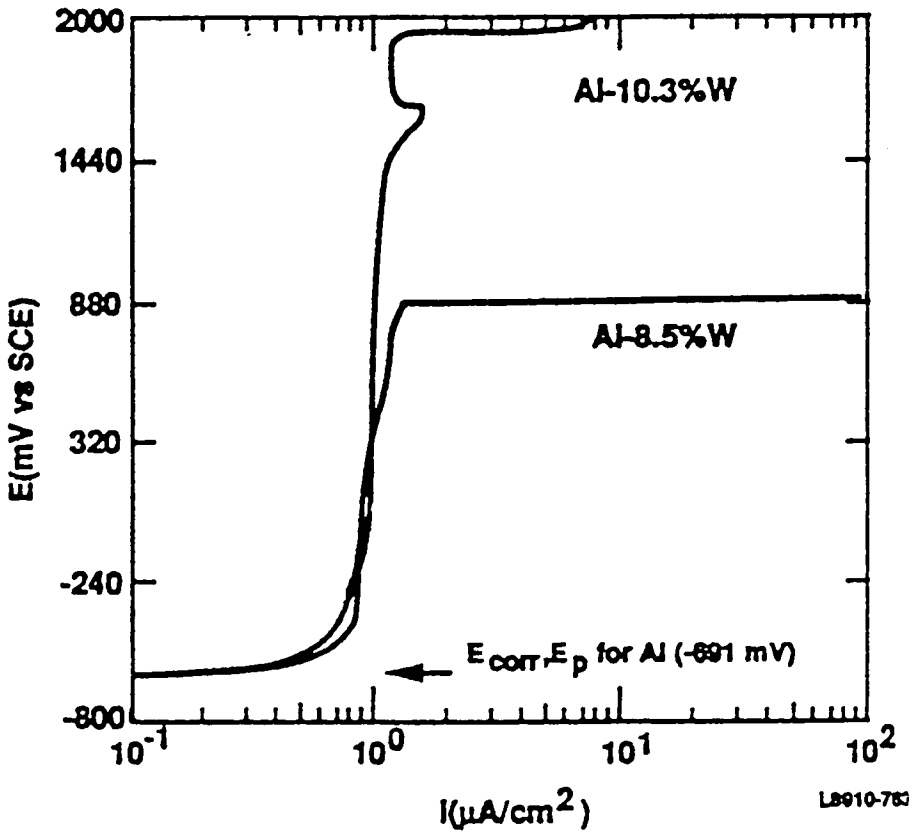

Figure 19. Anodic polarization of Al-W in aerated 0.1M KCl (61).

value (62). Al-W films have also been shown to be highly corrosion resistant in deaerated 1 M HCl (63).

Proposed Mechanisms of Enhanced Passivity of Non-Equilibrium Aluminum Alloys

An early author traced the relative passivity of Ta, Mo, W etc. in solutions containing Cl^- ions to the protective basic chloride films that form on these metals (64). Another related the work necessary to remove an ion pair from the oxide, W_L, to its corrosion tendency in chloride solutions (65). As seen in Table 3, the passivating species have large W_L values, with tungsten and molybdenum possessing the largest values.

Recent consideration has been given to the pH of zero charge of various oxides, and its relationship to Al pit nucleation in chloride solutions (66). The pH of zero charge of an oxide, pH_{pzc}, is the solution pH at which a given oxide has no net charge. As seen in Figure 20, when the $pH < pH_{pzc}$, the oxide has a net positive charge, and anions such as Cl^- are attracted to the surface. Conversely, when the $pH > pH_{pzc}$, cations are drawn to the surface. The pH_{pzc} varies with the type of metallic oxide and is a function of (6):

- cationic charge
- surface stoichiometry

Table 3 Work Necessary to Remove Ion Pairs From Various Oxide Lattices

Ion pair	W_L, kcal
$Fe^{3+}—O^{-2}$	724
$Cr^{3+}—O^{-2}$	727
$Al^{3+}—O^{2-}$	763
$Zr^{4+}—O^{2-}$	910
$Ti^{4+}—O^{2-}$	951
$Ta^{5+}—O^{2-}$	1189
$Mo^{6+}—O^{2-}$	1461
$W^{6+}—O^{2-}$	1461

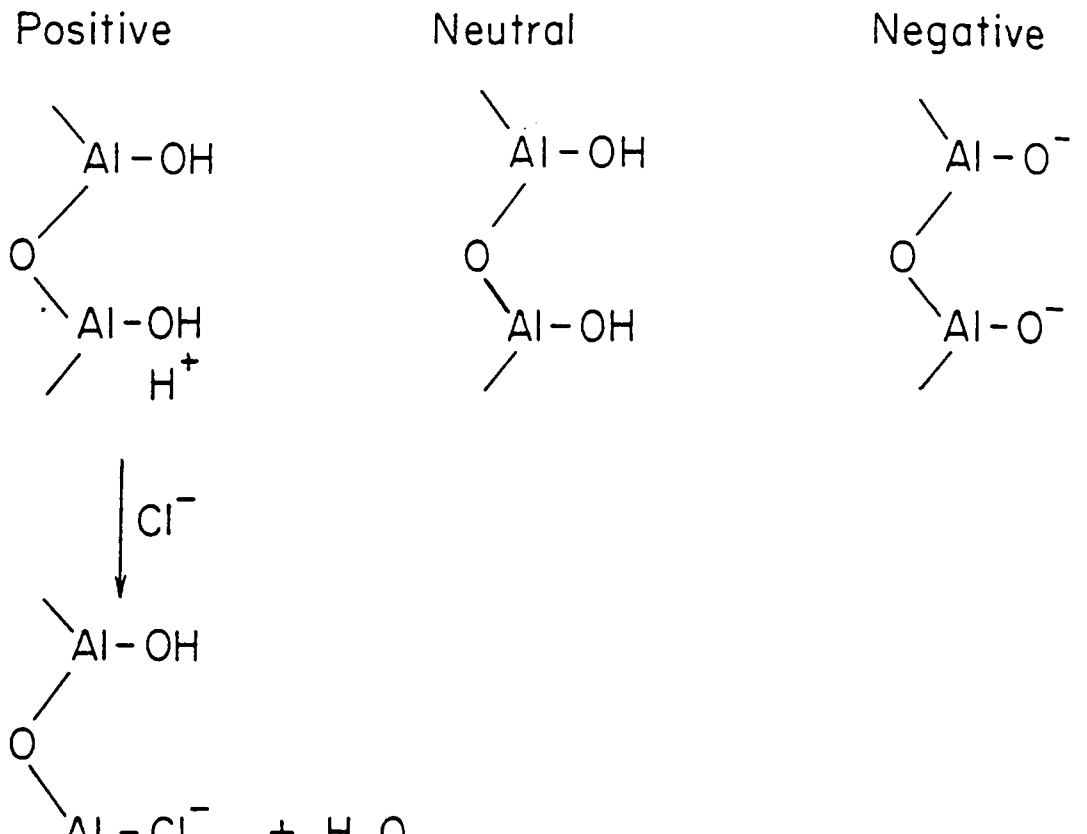

Figure 20. The pH dependence of the surface charge character of an oxide; positive ($pH < pH_{pzc}$), negative ($pH > pH_{pzc}$) (6).

- degree of surface hydration
- oxide semiconducting properties
- crystal structure
- defect structure
- ratio of bonds exposed to solution to filled bonds
- difference in acidic and basic dissociation constants of surface hydroxyl groups
- impurity content

When ionic species whose oxides are characterized by $pH_{pzc} < pH_{pzc,Al}$ (Ta, Ti, Zr) are implanted into aluminum the resulting structure has a higher pitting potential. These additions, when incorporated in the aluminum oxide, act to repel Cl^- ions from the surface due to the more highly electronegative nature of their oxides. XPS analyses (5,67,68) and a reflection-extended x-ray absorption fine-structure spectroscopic analysis (68) have shown that transition elements implanted into aluminum often are incorporated into the oxide structure. Chloride ion adsorption is thought to be the first step in the breakdown of an oxide which leads to pit nucleation. Lack of Cl^- access to the oxide surface delays the onset of pitting, and is manifested by a higher pitting potential. Conversely, implanted ions whose oxides have a higher pH_{pzc} than Al (Mg, Zn) tend to lower its pitting potential. In addition to this electrostatic repulsion model, it has also been proposed that these additions enhance passivity by modification of the oxide structure (69) or by an oxidized solute barrier layer mechanism (67).

Tungsten implanted aluminum shows no evidence of oxide solute enrichment in neutral pH solutions, yet produces the most elevated pitting potential of all transition element implanted alloys. This has led to the proposal of an alternative model for implant induced passivation (70-72). All passive films are thought to contain defects such as cracks and flaws that exist above grain boundaries, surface dislocations, or other inhomogeneities. Therefore, upon immersion into a chloride containing solution, occluded cells form in these defects, their pH decreases by metal ion hydrolysis, and pitting will commence if the passive film in the cell is soluble at this lower pH value. When metallic Al dissolution begins in implanted alloys of Mo, Cr, Zr, W, and Ta, the surface exposed to the solution becomes enriched in solute. Although the Pourbaix diagrams for Mo, Cr, and Zr do not indicate passivity at low pH (Figs. 21-23) (3), these elements do have lower solubility than Al at pH = 0. Therefore, they tend to moderately enhance aluminum passivity. W and Ta can passivate at low pH values (Figs. 17 and 24), and they tend to dramatically enhance aluminum passivity. Solute enrichment of the oxide has been noted at neutral pH for additions of Mo, Cr, Ta, and Zr but not for W. This, as seen from the respective Pourbaix diagrams, is a result of the solubility of tungsten and the oxide stability of the remaining elements at neutral pH.

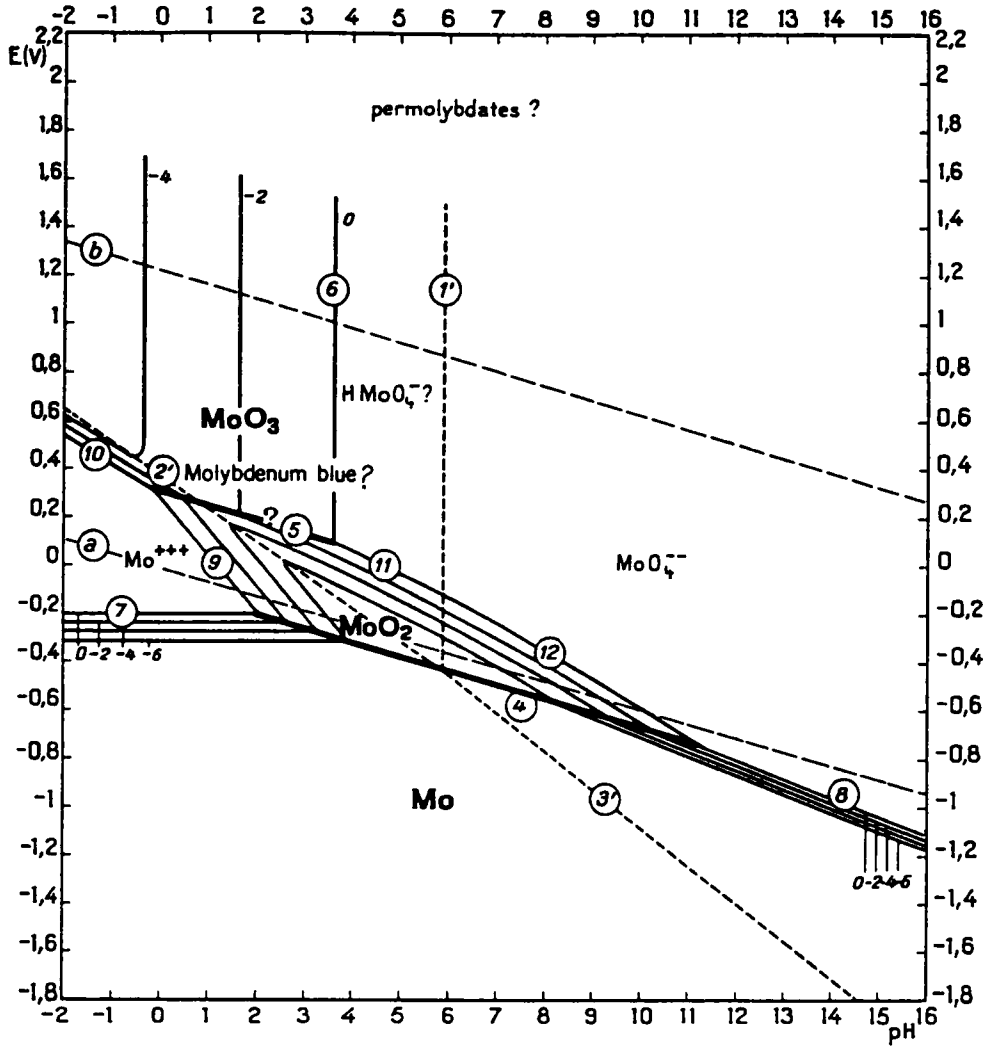

Figure 21. Pourbaix diagram for the Mo-H_2O system (3).

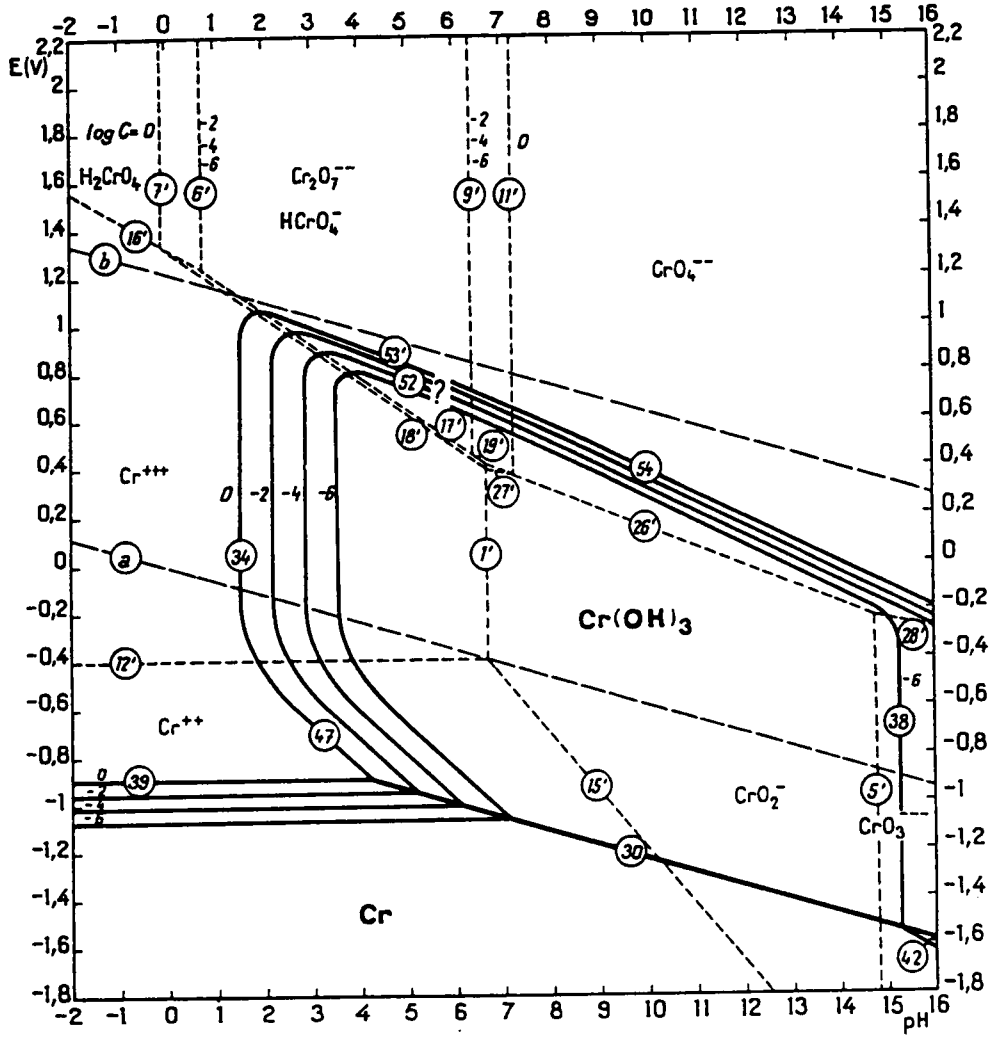

Figure 22. Pourbaix diagram for the Cr-H_2O system (3).

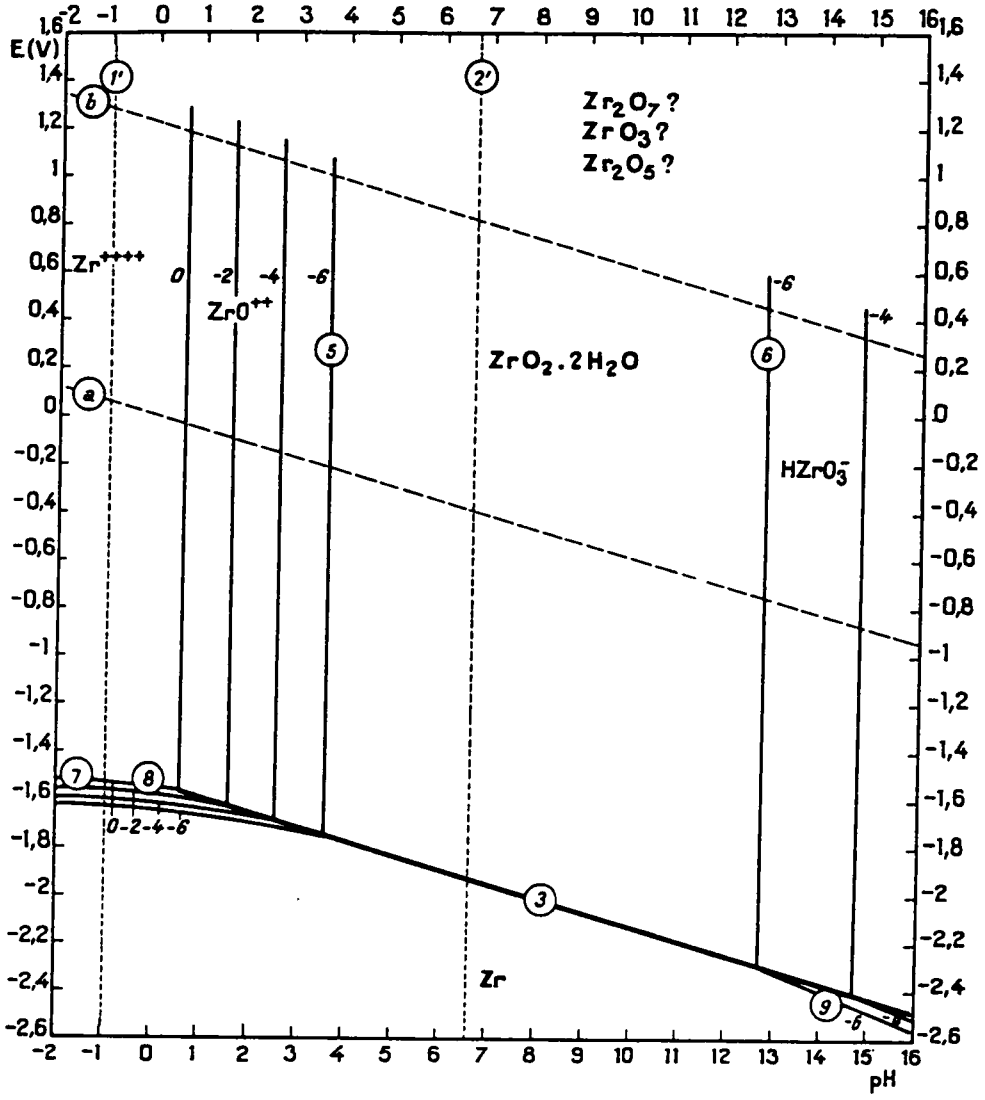

Figure 23. Pourbaix diagram for the Zr-H_2O system (3).

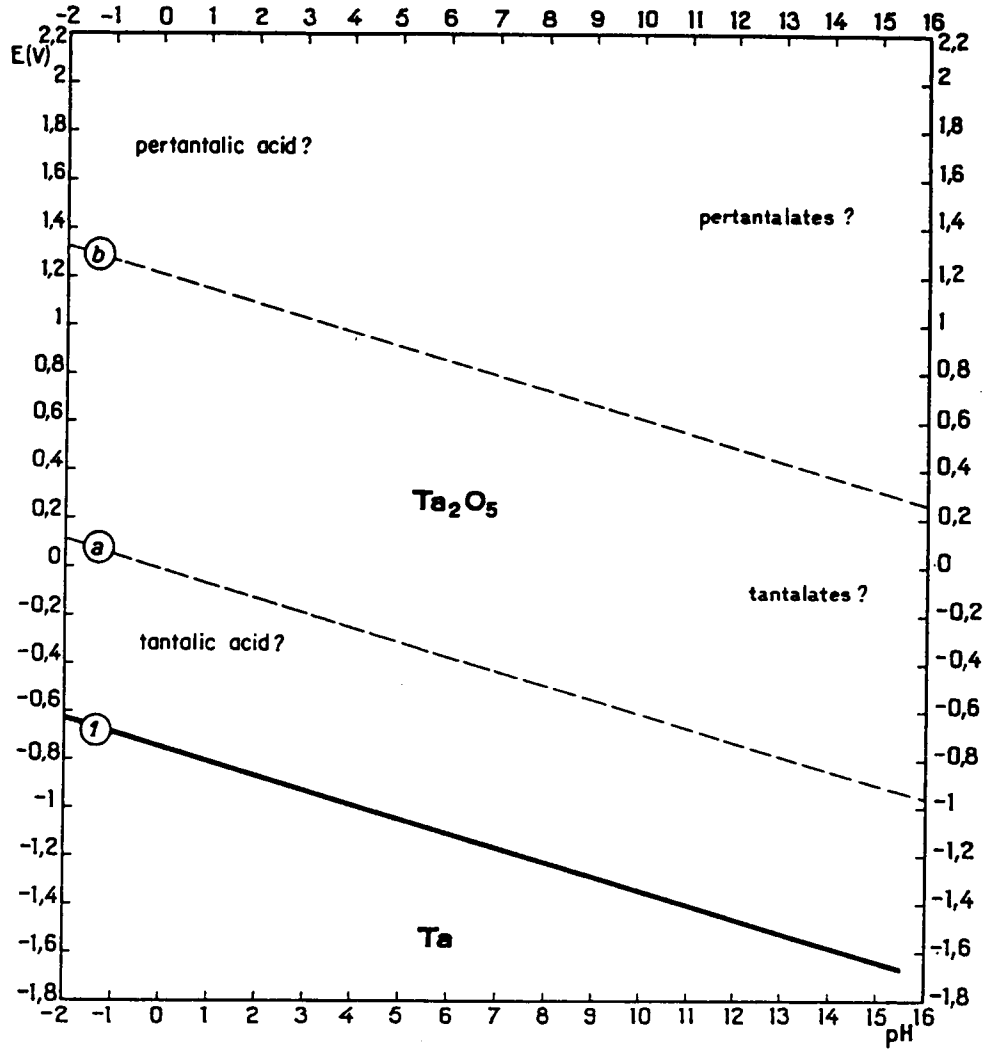

Figure 24. Pourbaix diagram for the Ta-H_2O system (3).

Aluminum Pitting and Oxide Blister Formation

Oxide blistering above the pitting potential, as a precursor step in the pit propagation on Al under anodic polarization in chloride solutions, was originally identified by Bargeron and Givens (73,74). Ingress of Cl^- and H_2O through the film to the bare metal surface leads to an aluminum - chloride - water reaction that produces hydrogen gas in the occluded cell. The gas pressure escalates until the oxide film blisters outward from the metal surface. This is shown schematically in Figure 25 (74). Eventually, as the gas pressure increases, the blister or the surrounding oxide is ruptured locally and the exposed metal surface is vulnerable to rapid pit propagation. Direct comparisons of the potentials at which blister growth commences with the electrochemically measured pitting potentials show that, for a variety of chloride concentrations, they are equivalent (Fig. 26). These authors present indirect indications that blistering may be a general step in the pit propagation process for aluminum alloys; however, all direct microstructural evidence has been gathered from anodic polarization of anodized specimens. The ability of the oxide to deform and withstand the pressure of the developing H_2 gas is directly related to its thickness. Natishan et al. (75) found that pure Al ion implanted with Cr, Si, Zr, and Nb exhibited similar blistering after anodic polarization in deaerated 0.1 M NaCl. Each of

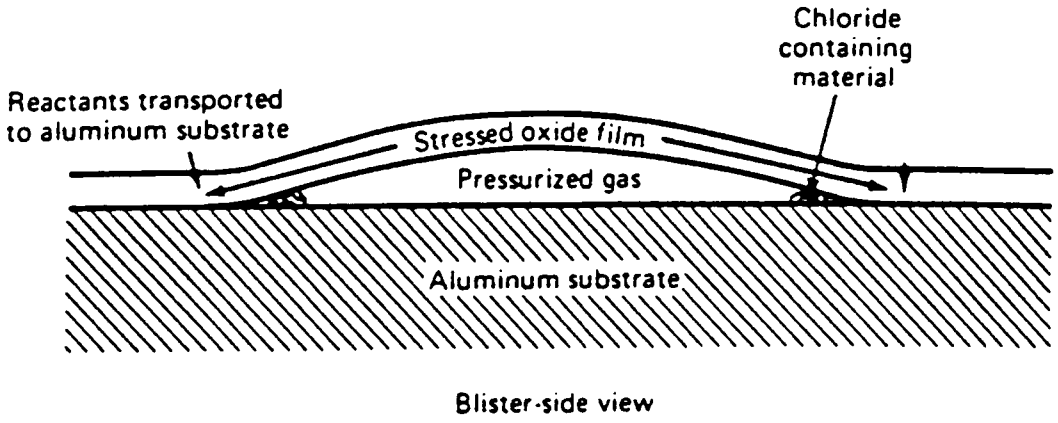

Figure 25. Schematic diagram of a blister (74).

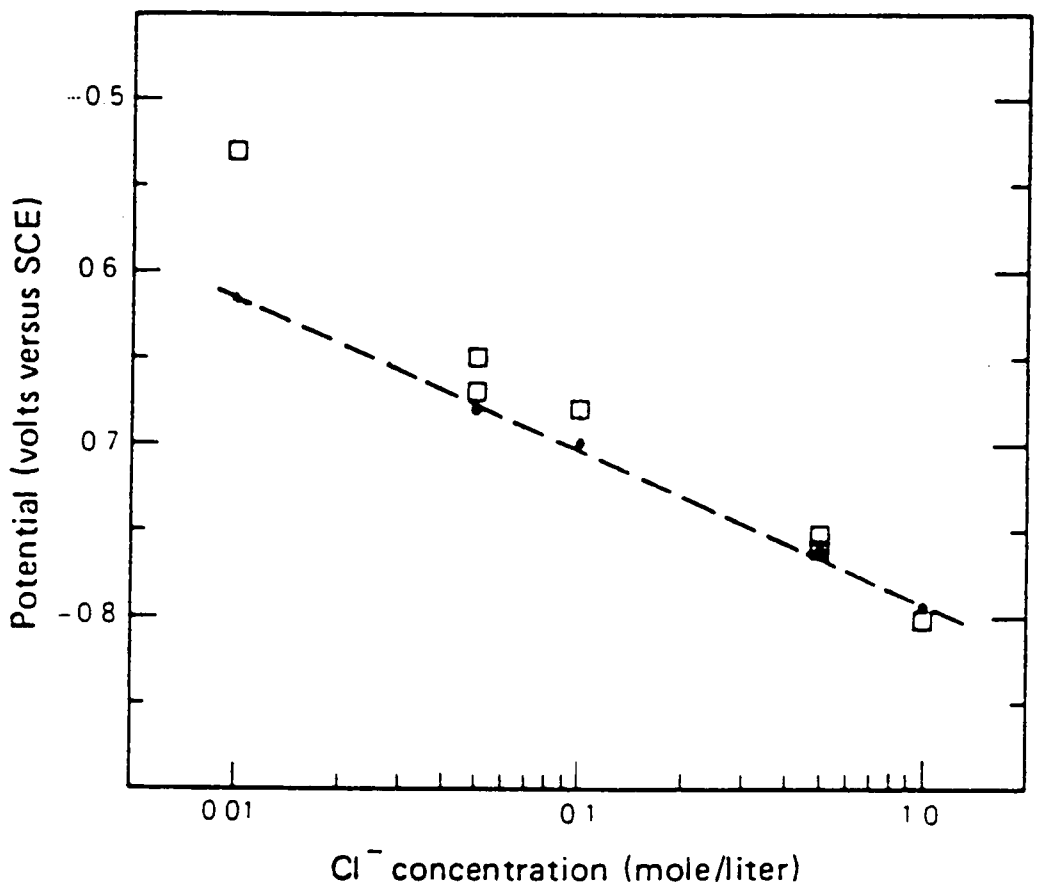

Figure 26. The potential of blister formation (●) on Al, and the Al pitting potential (□) as a function of the chloride concentration (74).

these surface treatments also resulted in an increase in the pitting potential. The increase in E_p was linked to blister formation and attributed to an improvement of the mechanical integrity of the oxide by the implantation process. Possible oxide strengthening mechanisms include altering the surface charge or changing the transport properties. Ruptures of the stressed oxide film occurred primarily at the center of the blisters for the ion implanted specimens. The resulting pits propagated directly beneath the center of the blisters. Conversely, for the anodized specimens, ruptures were exclusively associated with the peripheries of the growing blistered regions. The anodic current density gradually increases from 10^{-2} μA / cm^2 to 1.0 μA / cm^2 during blister growth. Upon rupture, it increases suddenly to 10^2 to 10^3 μA / cm^2.

Aluminum Pitting Corrosion Inhibitors

Non-aggressive species in solution with halide ions can act as corrosion inhibition agents. For aluminum and its alloys, examples include (76,77): sulfates, nitrates, chromates, acetates, benzoates, citrates, phosphates, molybdates, tungstates, and tartrates. The mechanism by which inhibition occurs is anion dependent. Chromate and phosphate prevent Cl^- access by adsorbing on the Al passive film (78), while nitrate and sulfate promote passivation. Molybdate, phosphate and tungstate form precipitates on the oxide surface, but only in the

presence of dissolved oxygen (77). A Rutherford backscattering spectroscopy analysis of films grown on Al in a solution containing tungstate ions (79) indicates that W is a major oxide component (Fig. 27). From the distinct Al ledge, one can deduce that the film is initially a tungsten oxide. After exposure times of 20 minutes or more, Al edge broadening and W peak spreading indicate that an aluminum hydrate is forming which incorporates the tungstate ions.

Plasma - the Fourth State of Matter

A plasma is a partially or fully ionized, approximately electrically neutral gas consisting of electrons, ions, and neutral atoms or molecules, which is capable of responding to electric and magnetic fields. If energy is added to a solid material, it will first undergo a transition into the liquid state, then into the gaseous state, and finally into a plasma state. For this reason, plasma can be considered to be the fourth state of matter. On an atomistic scale, a plasma is a complex mix of active species, which may include (80) ions, electrons, photons, radicals, sputtered ions, sputtered neutrals, background neutrals, atomic states, molecular fragments, electronically excited species, and vibrationally excited molecules. This complexity of active species is the primary reason that plasma-surface interactions are poorly understood scientifically. Attempts to perform plasma processing of materials (such as surface modification) require a multidisciplinary

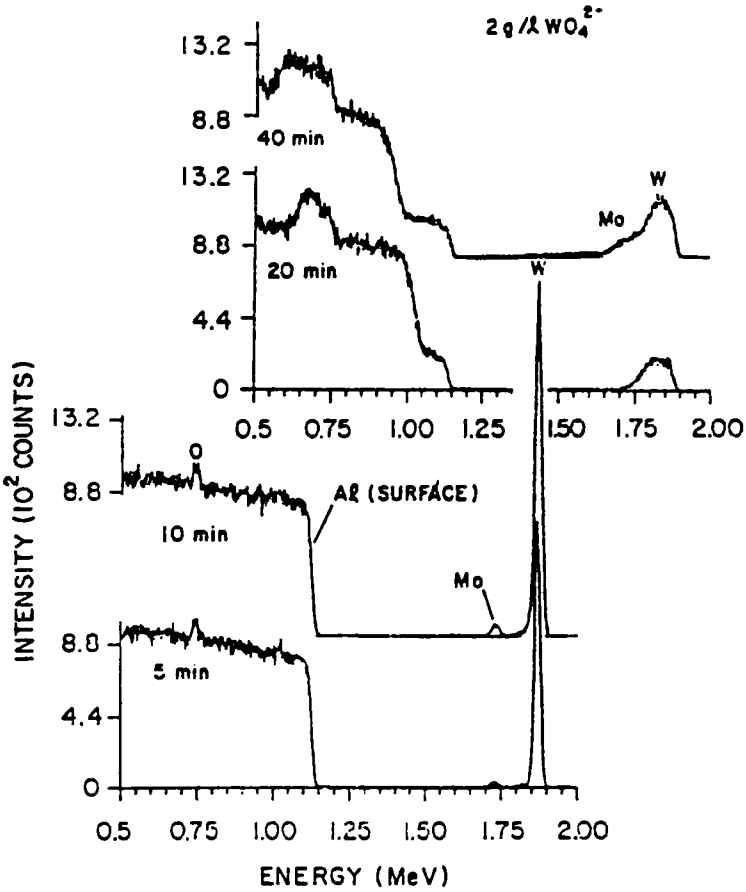

Figure 27. RBS spectra for films produced in a tungstate inhibited solution (79).

approach in which it is necessary to combine elements of electrodynamics, plasma science, surface science, computer science, and industrial process control. This background is necessary to regulate the plasma conditions and excitation methods which are utilized (81). A simultaneous awareness of elements of materials science is needed to comprehend the structural modifications and material properties resulting from such processing. In spite of the technological difficulties, plasma applications are increasing at an ever expanding rate. The industrial motivation for this was expressed succinctly by a Panel on Plasma Processing of Materials authorized by the National Research Council's Commission on Physical Sciences, Mathematics, and Applications (81):

"This pervasive use of plasmas in modern technology is a result of the range of parameters that can be accessed and that is inaccessible by any other means. No other medium can provide gas temperatures or energy densities as high as those of plasmas; no other medium can excite atomic and molecular species to radiate as efficiently; no other medium can be arranged to provide comparable transient and non-equilibrium conditions.

In materials processing, opportunity lies in the fact that a highly excited medium can be obtained with no physical or chemical counterpart accessible in the natural environment. Plasmas can therefore alter the natural pathways through which chemical systems evolve from one stable state to another and can thus enable production of novel materials.

The diversity of applications of plasma-based systems used to process materials is matched by the diversity of plasma conditions, geometries, and excitation methods."

Current industrial uses of plasmas include heating and melting (arc melting, plasma welding, plasma spray); particle production (ions and neutrals); and ion bombardment (plasma nitriding, physical vapor deposition).

Plasma Ion Implantation

The inherent disadvantages associated with ion beam implantation were discussed previously, and included the high cost of equipment and operation of the implanters, the poor uniformity of coverage on target material contours due to the line-of-sight nature of the process, and the fact that only relatively small workpieces (app. 10 cm) can be accommodated in most target chambers. Commercial ion implantation systems require a manipulator stage to rotate the target into the ion beam to ensure uniformity of coverage. In order to eliminate these practical difficulties, researchers at the University of Wisconsin-Madison developed the plasma ion implantation technique (PII) (82). In PII, the target material is placed in the plasma (Fig. 28), as opposed to extracting ions from a plasma and accelerating them towards the specimen. A highly negative bias, V_0, is applied to the target with respect to the walls of the plasma chamber. The applied potential must also be pulsed on a microsecond time scale to avoid quenching the plasma, and to limit the heat flux to the surface. Quenching can occur when the implantation rate of positive ions is higher than their rate of

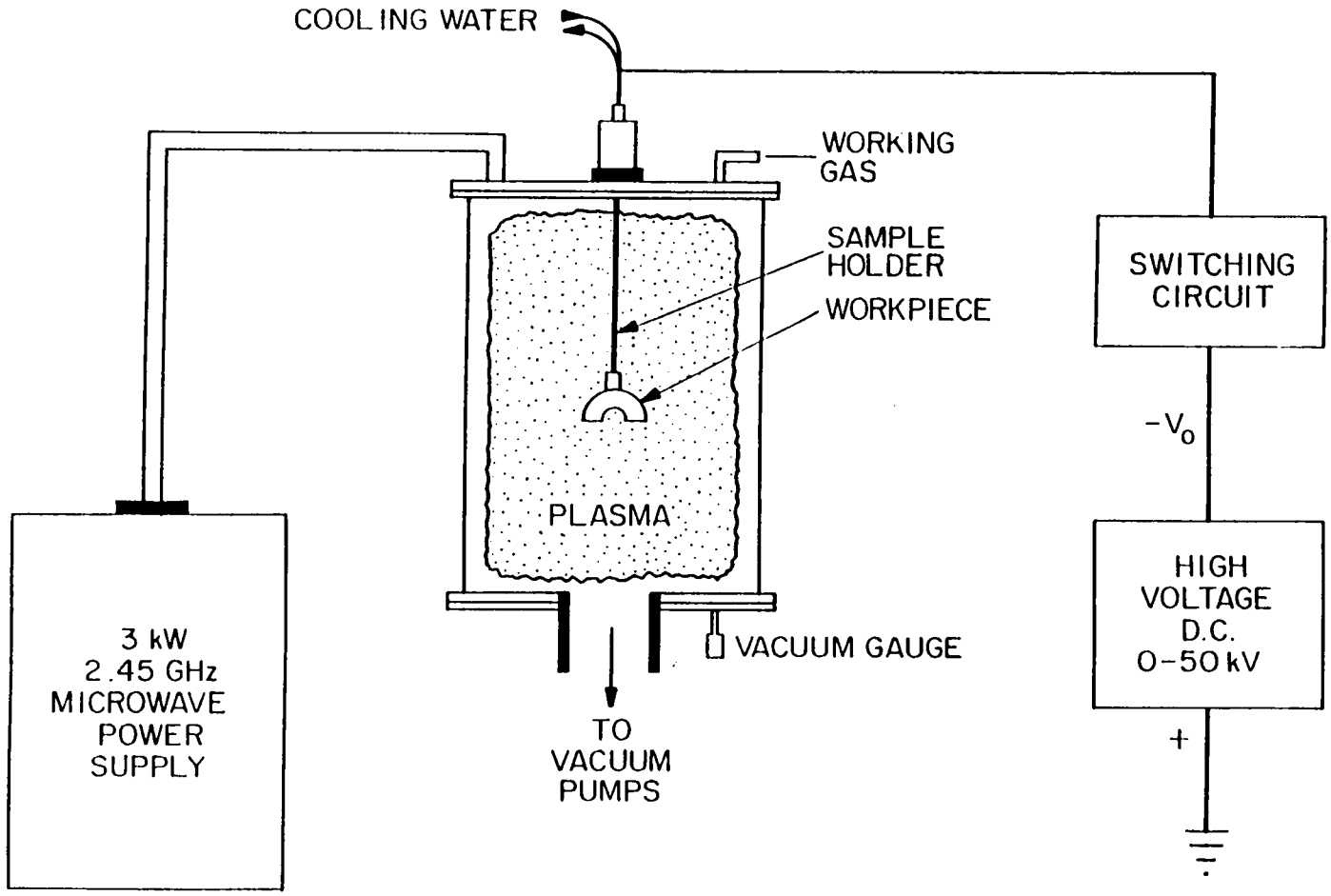

Figure 28. Schematic diagram of plasma source ion implantation apparatus (110).

generation, as can happen in small-volume plasmas. The positively charged ions in the plasma are accelerated towards the workpiece and are uniformly implanted into the surface with an equivalent energy of V_0 eV. Implantation energies as high as 150 kV have been achieved (87). Any surface in contact with a plasma will form a sheath region in which charge quasineutrality is violated in order to shield the plasma from applied electric fields (83). Ions are accelerated normal to this sheath, which ideally conforms to the target surface contours, promotes uniform dose distribution, and eliminates sputtering from implantation at oblique angles of incidence. However, as seen in Figure 29, this is only true if the surface contour scale R is larger than the sheath thickness S. Another PII limitation is the absence of any mass analyzing system. This creates the possibility that undesirable species, present due to vacuum system limitations, may also be implanted. A schematic comparison of ion beam implantation technology and the PII process is shown in Figure 30. The simple immersion in the plasma makes it a simpler and more cost effective technology than conventional line-of-sight beam implantation. As of August 1993, there were twenty organizations (thirteen in the USA, including the University of Tennessee) actively researching potential applications of the PII technology.

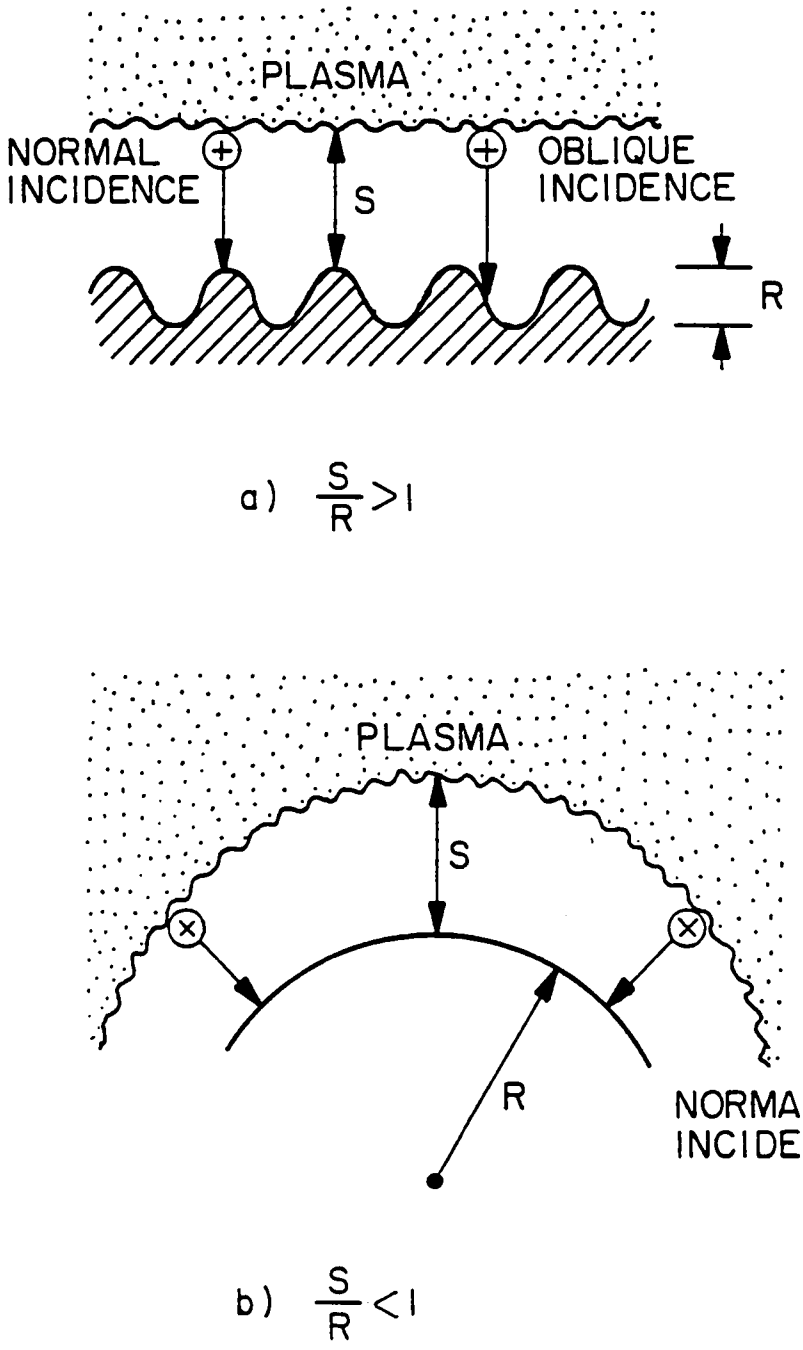

Figure 29. Dependence of plasma sheath ability to conform to surface contours on the contour size scale (110).

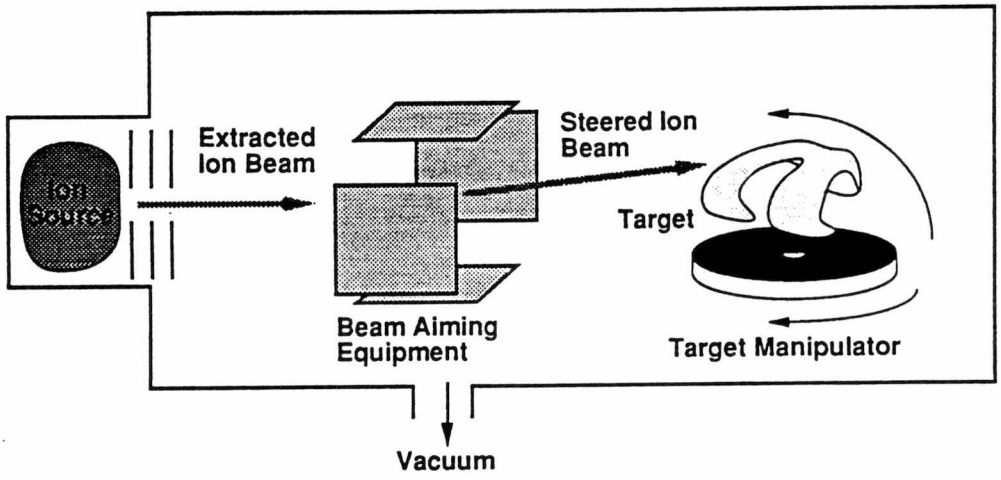

Conventional Beamline Implantation

- Line-of-sight process
- Beamline aiming and target manipulation are required for uniform implantation of all target surfaces

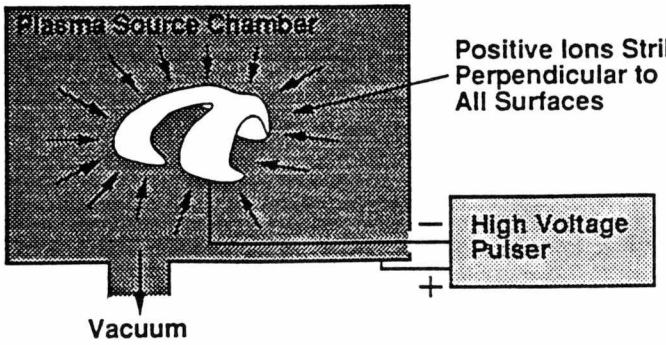

Plasma Source Ion Implantation

- Plasma sheath surrounds target
- Ions bombard all surfaces of target without beam aiming or target manipulation

Figure 30. Comparison of Conventional Beamline Ion Implantation and Plasma Ion Implantation (99).

Plasma ion implantation produces equivalent dose distributions to those that result from ion beam implantation at a comparable energy. Both a carbon steel, AISI 1018, and a stainless steel, AISI 304, were processed by PII and IBI using N^+ ions at 25 keV and a total dose of 3×10^{17} ions / cm^2 (84). Figure 31 shows Auger depth profiles generated for each. The nitrogen distributions are very similar for both the carbon and stainless steels. It is also noted that the carbon levels in each alloy are greatly reduced in the plasma process. This is attributed to a cleaning effect that results from the sputtering of low energy ions between the high voltage pulses.

PII has discernible advantages over the related technique of ion plating (85). This process involves immersing a workpiece in a plasma and using an applied voltage to modify the near surface composition of the target. However, the accelerating potential is insufficient to allow ions to penetrate substantially into the substrate structure. Instead, this process produces only a surface coating which is susceptible to delamination.

Although plasma ion implantation was patented in 1987, by August 1993 considerable work had been completed in materials modification using this

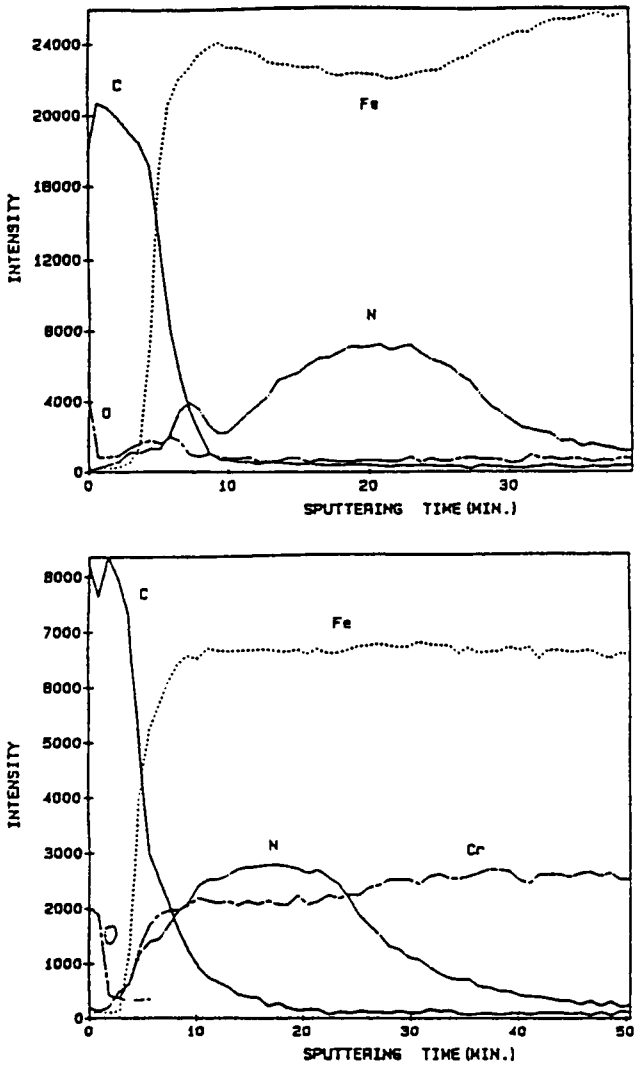

(a)

Figure 31. Auger profiles of 1018 and 304 steels implanted to 3 x 10^{17} ions/cm^2 nitrogen at 25 keV by (a) ion beam implantation, and (b) PII (84).

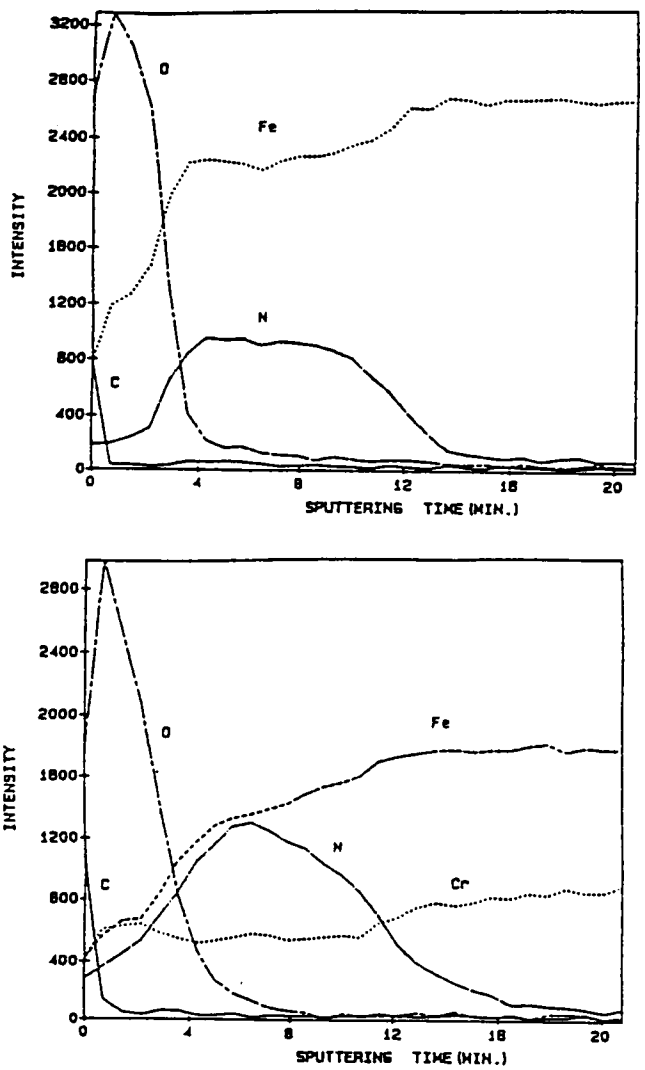

(b)

Figure 31 (cont.). Auger profiles of 1018 and 304 steels implanted to 3 x 10^{17} ions/cm^2 nitrogen at 25 keV by (b) PII (84).

developing technology, primarily in the wear of nitrogen implanted surfaces. Other applications include:

- corrosive wear of Cr-Mo PII-IBED austenitic stainless steels (86)
- TiN and CrN PII-IBED coatings produced on AISI 52100 steel (87)
- PII-IBED of W, Pt, Cr, TiN, TaN, and CrN coatings (88)
- corrosion resistance of N PII Aluminum (89,111)
- BF_3 PII into Si for fabrication of shallow P^+ / N junctions (90)
- hardness of C PII (methane or acetylene) specimens (88)

Auger Electron Spectroscopy *

The distribution of implanted species during the ion implantation process affects the substrate surface properties. Characterizing this distribution by traditional methods such as energy dispersive spectroscopy and x-ray diffraction is made difficult by the shallowness of the modified region and the much greater penetration depth of these tools. Auger electron spectroscopy (AES) is a powerful instrument for analyzing an ion implanted surface, since it allows analysis of compositions in the outer 1 to 3 nanometers of a solid specimen. The technique, using an electron beam as a probing source, derives surface chemistry information from analysis of Auger electrons emitted form the surface. These Auger electrons are produced whenever incident radiation, in the form of electrons, ions, photons, or neutral atoms, interacts with target atoms with an

* much of this discussion is paraphrased from A. Joshi (reference 91).

energy which exceeds that necessary to remove an inner shell electron from the atom (Fig. 32). This core hole leaves the atom in an unstable state and an electron will immediately drop from a higher energy level into this gap. A by-product of this de-excitation is either an x-ray or an Auger electron. Obviously, generation of an Auger electron requires the participation of at least three electrons, which excludes hydrogen and helium from detection by AES. The energy of the Auger electron depends on the element from which it is ejected, thus allowing for its identification. A chart of the principal Auger electron energies, including the transitions from the various electron levels (KLL, LMM, etc.), is shown in Figure 33. Auger electrons have a short mean free path within the specimen, and cannot travel more than several atomic layers without losing their characteristic energy. Therefore, only those emitted from the very near surface region will be detected, with an energy identified with the composition of the target material. The extent of this region is termed the escape depth, and is extremely shallow in comparison with other characterization tools, as seen in Figure 34. Compositional profiling as a function of depth can be performed by progressive sputtering of the surface. However, the accuracy of the quantitative analysis is generally limited to $\pm$30 %.

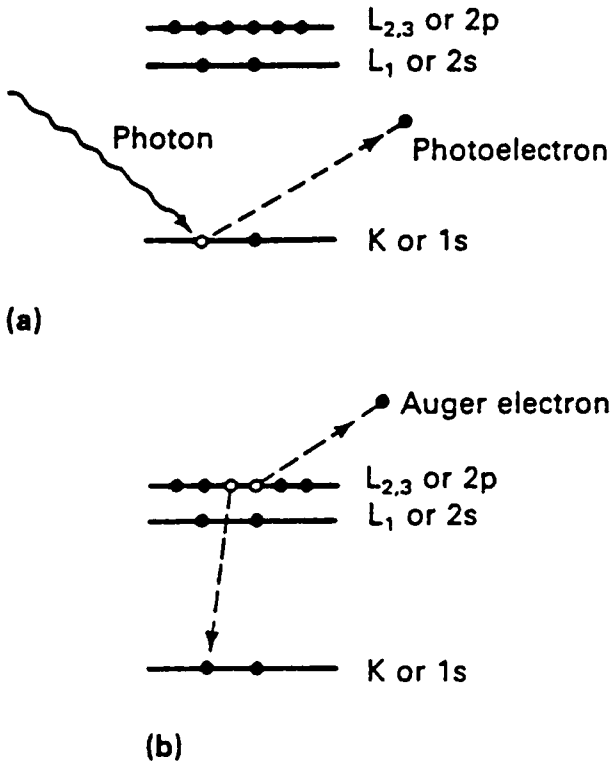

Figure 32. Energy-level diagrams of (a) photoelectron and (b) Auger electron excitation (91).

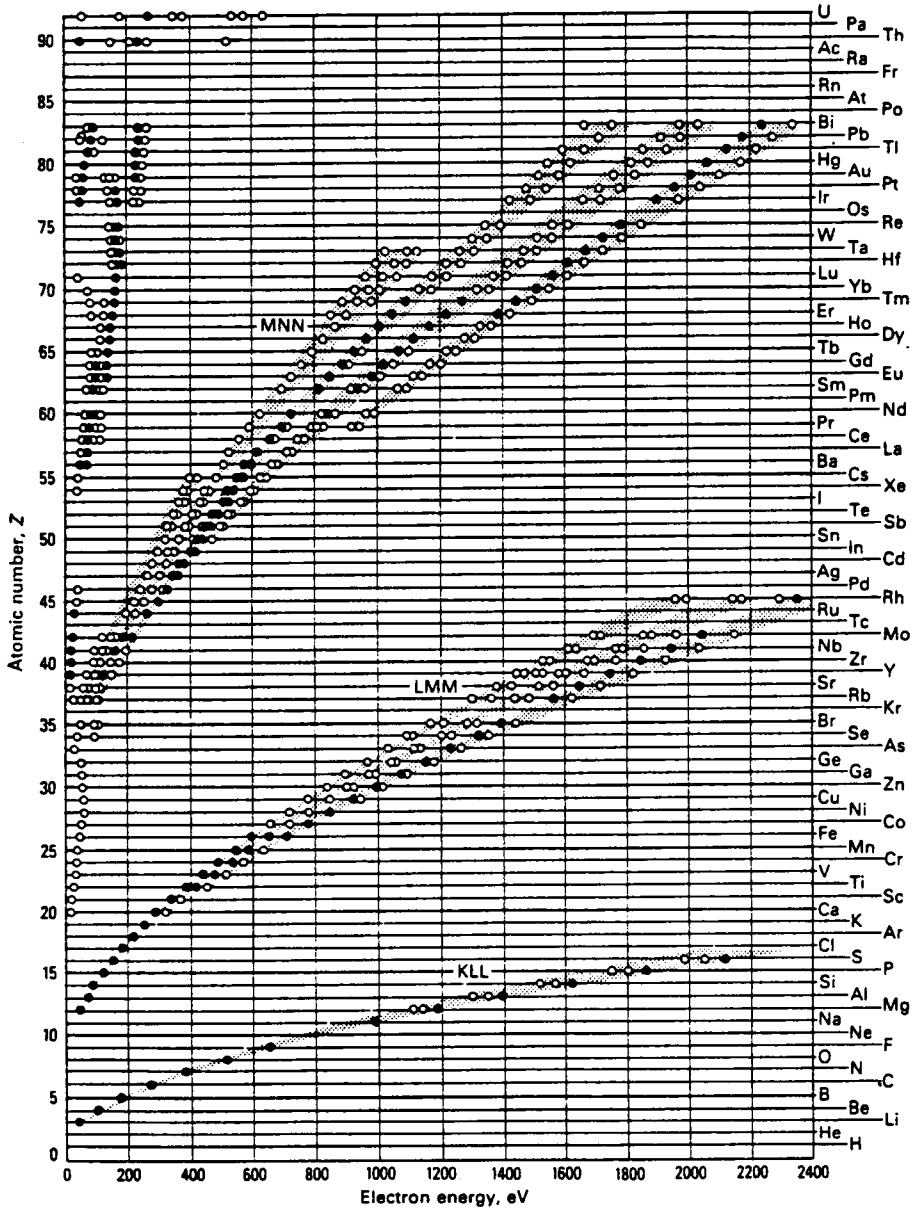

Figure 33. Principal Auger electron energies for each element (91).

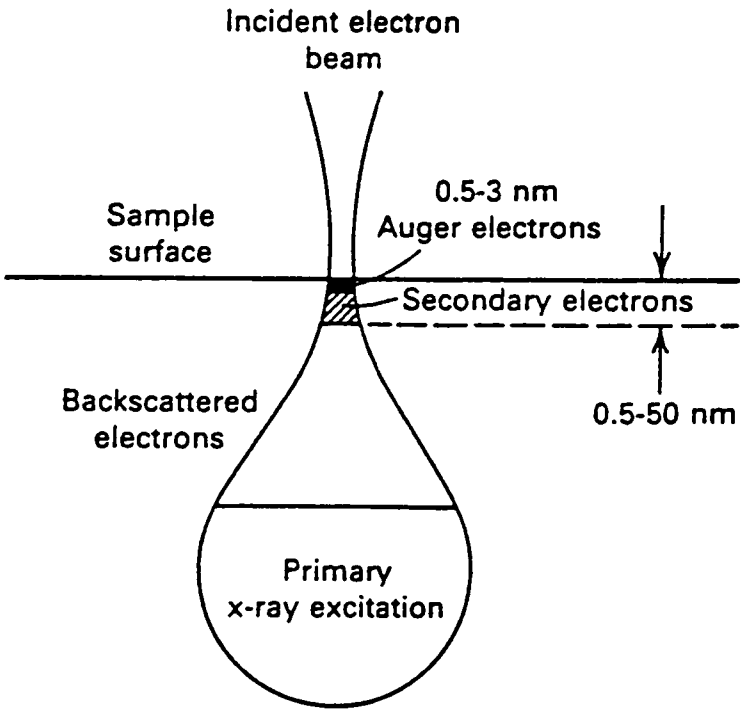

Figure 34. Comparison of Auger electron escape depth with emission depths of backscattered electrons and x-rays (91).

Rutherford Backscattering Spectroscopy*

The Rutherford backscattering spectroscopy (RBS) technique is often utilized to calculate the depth profile of ion implanted species without layer removal by ion sputtering or chemical stripping. It is a simple quantitative technique in which a monoenergetic and collimated ion beam (typically 2.0 MeV He^+) is directed at the implanted surface, and the ions backscattered from the target are energy analyzed. From the ion energies detected, the mass of the target elements can be determined by assuming elastic collisions and utilizing the law of conservation of momentum (Fig. 35). An ion scattered from a heavy element has more energy than one backscattered from a lighter element. If the ion traverses the material for some distance before being backscattered, it will have lost some of its kinetic energy to inelastic interactions with the substrate atoms. The inelastic "stopping power" of the substrate arises from ionic interactions with the target electrons. These energy losses can be detected in the energy spectrum and the depth of the backscattering element can be determined. Therefore, in the case of RBS of an ion implanted surface, the depth profile can be determined from this energy broadening. An RBS spectrum from arsenic-implanted silicon is shown in Figure 36. From the As peak, one can determine the maximum concentration, the total

---

* from Thompson and Lichter (reference 19), W. K. Chu (reference 92), and Chu, Mayer, and Nicolet (reference 93).

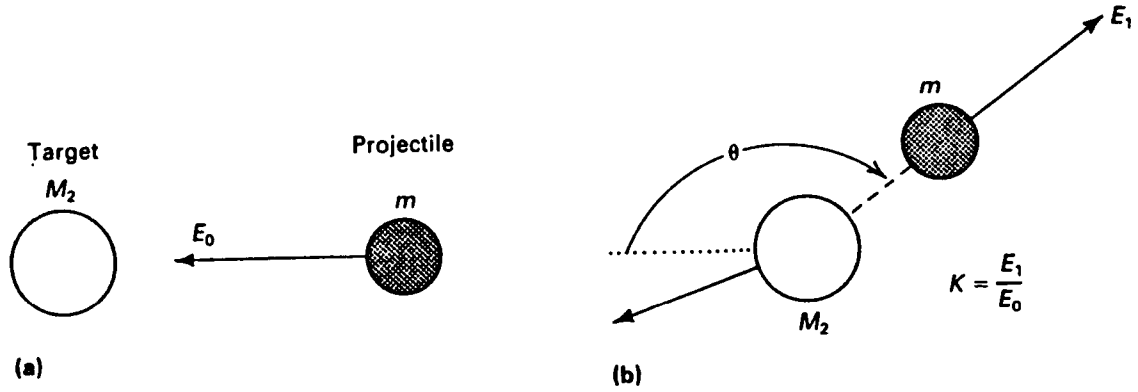

Figure 35. Collision kinematics between a projectile atom m and a target atom M_2 (92).

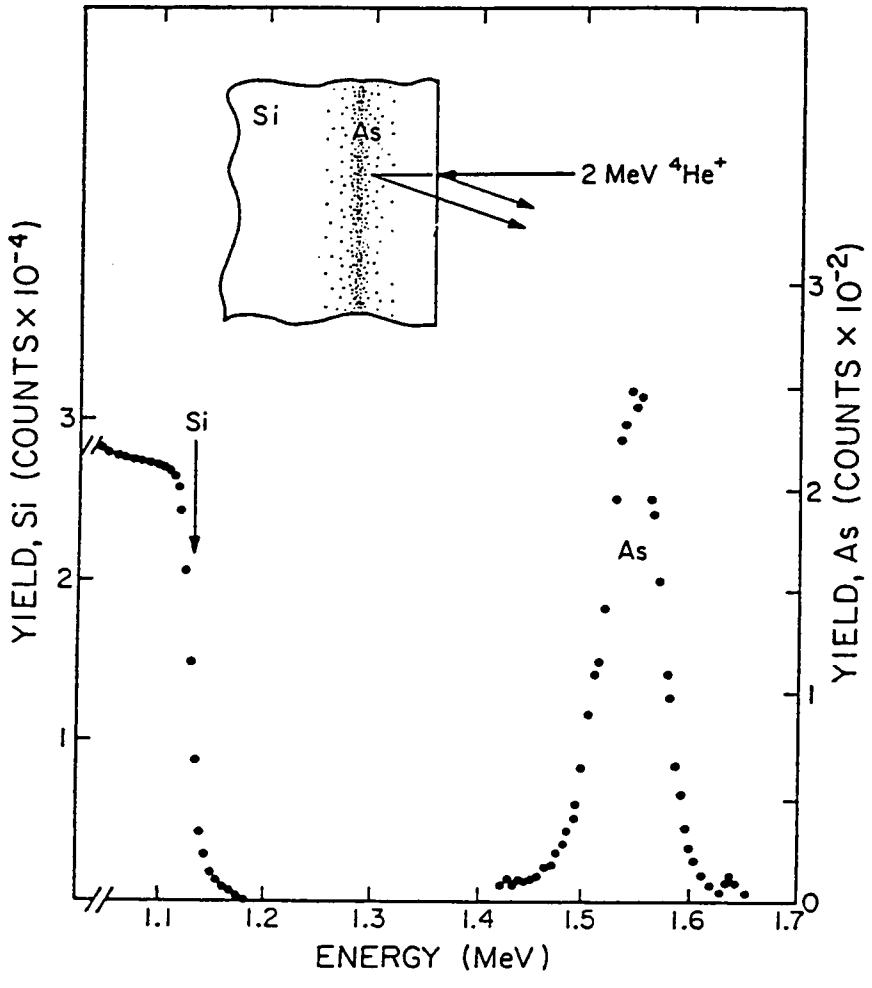

Figure 36. RBS spectrum of 2 MeV ^{4}He ions backscattered from a silicon crystal implanted with 1.2 x 10^{15} ions / cm^2 As at 250 keV (93).

dose, and the depth profile. Some limitations of this technique include poor lateral resolution (typically 1 mm^2), poor mass resolution for high Z elements such as Au, Pt, and W, and poor sensitivity to low Z elements contained within heavier substrates. It is also less sensitive than other methods such as neutron activation and secondary ion mass spectroscopy.

Atomic Force Microscopy

Scanning tunneling microscopy, invented in 1982 by Binnig and Rohrer, provides for surface characterization at an atomic level. This method is based on the principle of quantum mechanical tunneling of electrons between two electrodes under an applied electric field (94). Topographical images are created by scanning an atomically sharp stylus across a surface. Scanning movement is produced by mounting either the tip or the specimen on piezoelectric ceramics which move in the x,y, and z directions under the influence of applied electric fields. A constant current is maintained between the tip and surface by applying a potential through a feedback control unit, which forces the tip to keep a fixed separation distance from the specimen. With proper tip preparation, spatial resolution of 1 angstrom can be achieved.

Atomic force microscopy (AFM) is a related technique which allows, in addition, probing of the surface of nonconducting materials (95). In AFM analysis, the probe tip is attached to a flexible microfabricated cantilever, the deflection of which is usually measured by optical methods (Fig. 37) (96). A constant force is maintained between the surfaces by moving the sample up and down such that the reflected light beam is always in an identical position. AFM imaging has been documented for corrosion processes (97) including an in situ analysis of localized corrosion near Fe inclusions in an Al alloy (98).

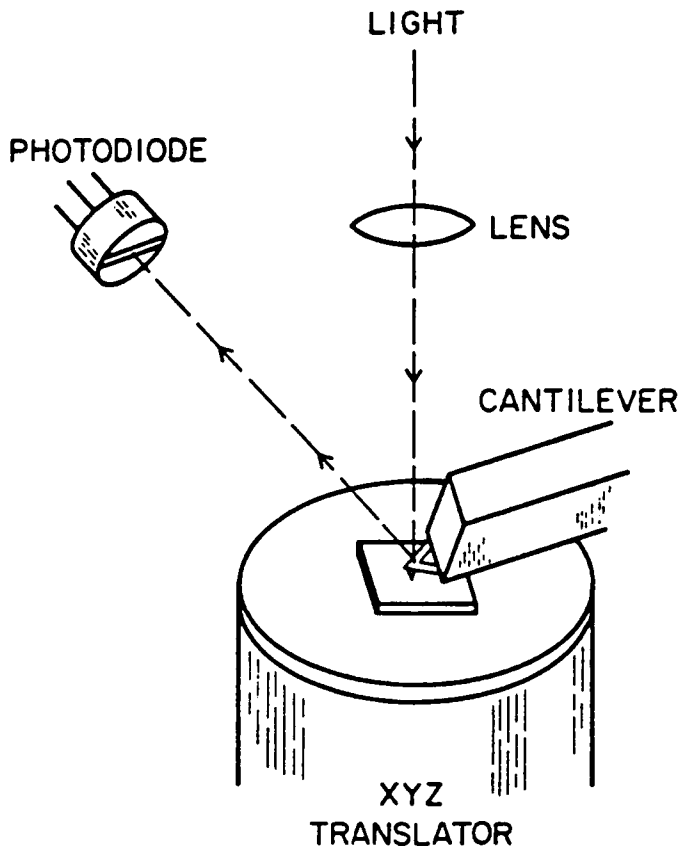

Figure 37. AFM with laser light detection system. Reflected beam position, and thus force on the sample, is kept constant by vertical sample movement (96).

3. EXPERIMENTAL PROCEDURES

The objective of the present research is to apply the emerging technology of PII to implant N into 304L ss, and to ion beam implant Al 1100 with W. Resulting alterations of the pitting behavior will be characterized both electrochemically and by immersion techniques. Analysis of metallurgical microstructure, corrosion mechanisms and implant distribution before and after corrosion will be performed using scanning electron microscopy, Rutherford backscattering spectroscopy, Auger electron spectroscopy, and atomic force microscopy.

Materials

Commercial grade wrought Al 1100 samples were cut to a thickness of approximately 0.32 cm (1/8") from an annealed 2.54 cm (1") diameter bar. Each specimen was ground and automatically polished by the Oak Ridge National Laboratory metallography group using a colloidal silica suspension. These samples were used for all ion implanted Al 1100 results.

Commercial grade wrought Al 1100 samples were cut from 0.3175 cm (1/8") sheet into 2.0 x 2.0 cm squares. Each specimen was ground using a series of successively finer SiC papers, and automatically polished in the UTK MSE

metallography lab using a colloidal silica suspension. These samples were used for all unimplanted control Al 1100 results, except where indicated. Separate Al 1100 source materials were used for the unimplanted and implanted specimens to conserve the limited supply of the larger diameter bar stock.

High purity 99.9999% Al was obtained in bar form from Cominco Electronic Materials - Cominco Products, Inc. of Spokane, Wash. (HPM 4721, Lot 245-E). Samples of approximate dimensions 2.0 cm x 1.5 cm x 0.1 cm were machined from this stock, and ground and polished (UTK MSE) using a colloidal silica suspension. These samples were used for all high purity aluminum tests, both ion implanted and control.

304L stainless steel samples of certified chemical composition (Table 4) were machined from 0.16 cm plate into 2.0 x 2.0 cm squares. Two screw holes (size 256) were machined in diagonal corners for mounting onto a PII sample holder. Each specimen was ground and polished with 9 μm diamond paste and 1 μm alumina slurry. These samples were used for the initial nitrogen PII implantations.

Table 4 Chemical Composition (w/o) of 304L Stainless Steel (Williams & Co., Inc.)

C	P	Si	Ni	Cu	Mn	S	Cr	Mo	Fe
0.026	0.031	0.42	9.18	0.07	1.75	0.016	18.50	0.27	Bal

304L stainless steel from this same stock material was machined into circular samples of diameter 2.56 cm. Two screw holes (size 256) were again machined into opposite edges for PII mounting. Each specimen was ground with a series of fine SiC papers through 2400 grit. These samples were used for later nitrogen PII implantations. All metallographic specimens were cleaned with methanol after polishing and stored in air tight containers.

Ion Beam Implantation

Ion beam implantation was performed at the Surface Modification and Characterization (SMAC) Facility in the Solid State Division of the Oak Ridge National Laboratory (ORNL). SMAC provides advanced processing and characterization techniques for alteration and analysis of the near surface properties of a wide range of materials including: ion implantation doping, ion beam deposition, ion beam and laser mixing, and pulsed vacuum laser annealing.

Polished samples were mounted onto three sides of a four sided block sample holder, with the fourth side used for beam calibration. W ions were generated by sputtering from the tungsten filament of a Freeman source in an analyzed beam Eaton 10-80 system. Where indicated, the target was cooled by providing a liquid nitrogen heat sink internal to the sample holder. Implantations were

performed using accelerating voltages of 60 and 90 kV, and doses ranged from 7.0×10^{15} to 9.0×10^{16} ions / cm^2.

Rutherford Backscattering Spectroscopy

Rutherford backscattering spectroscopy (RBS) was performed on W ion beam implanted Al 1100 at SMAC-ORNL using 2 MeV He in a Van de Graff particle accelerator. A scattering angle of approximately 160° was employed for each analysis along with a normal angle of incidence.

Plasma Ion Implantation*

Nitrogen implantation into 304L stainless steel was achieved via Plasma Ion Implantation in the UTK Microwave Plasma Facility (Fig. 38) (115-122), which is capable of generating a large volume (206 liter) uniform plasma of density 6×10^{16} electrons / m^3 with 2.45 GHz microwave power. The operating plasma utilized a nitrogen pressure of 40-45 mTorr, a pulse repetition frequency of 0.1 to 30 Hz, and a pulse width of 20 μs. All specimens were implanted at a voltage of either 10 or 20 kV, and the dose varied from 10^{14} to 10^{18} ions / cm^2. The highly negative DC voltages are applied by a DC power supply capable of 1 amp steady

* bibliographical sources - S. G. Kamath (reference 99), P. F. Keebler (reference 112), and P. D. Spence (reference 113)

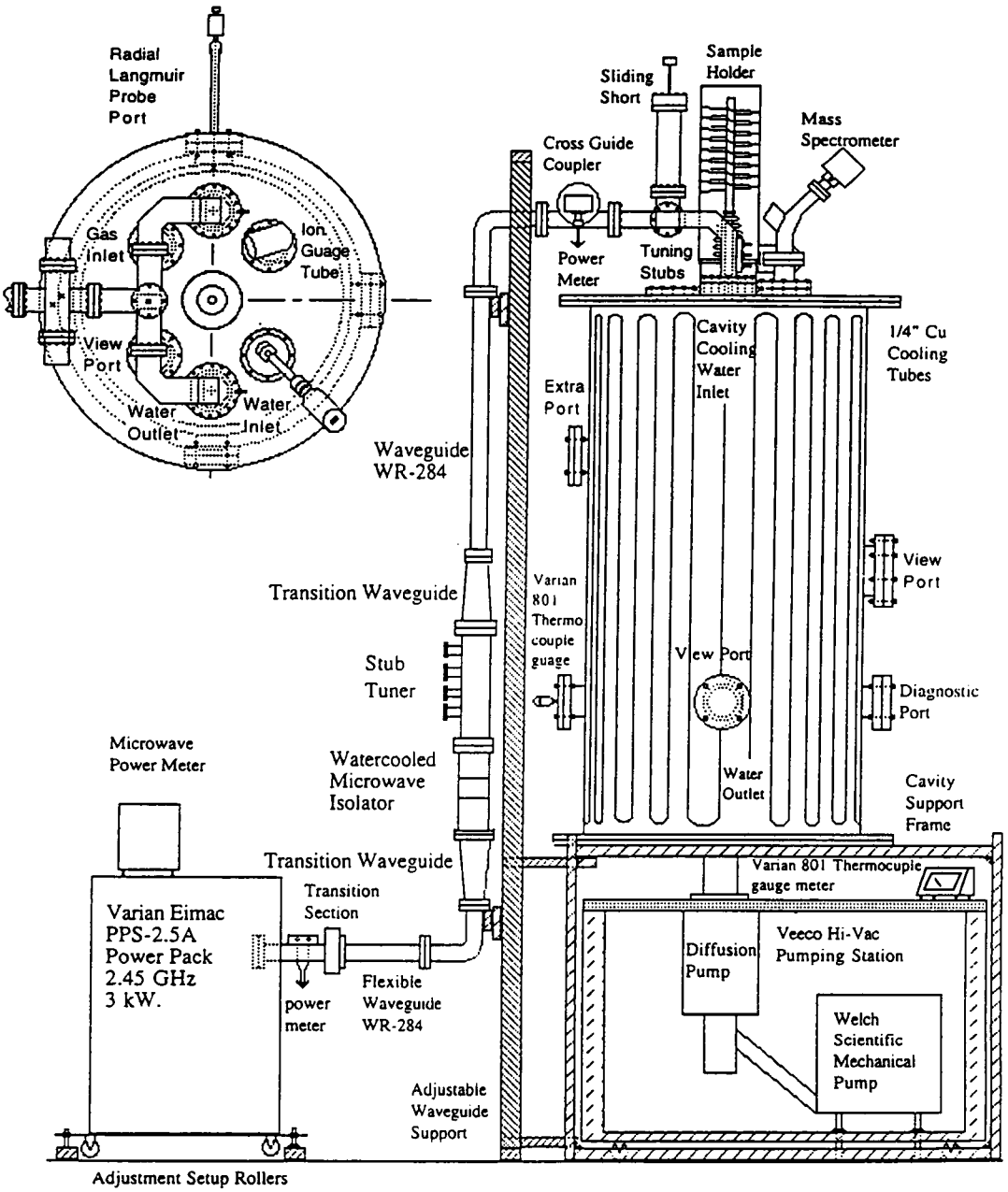

Figure 38. Schematic diagram of the University of Tennessee Microwave Plasma Facility for Plasma Ion Implantation (99).

state up to 50 kV DC. The rapid pulses are made possible by a custom made switching circuit (112,114) capable of producing pulses of current from 5 to more than 250 μs in length, with a repetition rate of 0.1 to 5000 Hz. Ions were delivered to the sample during each pulse, and pulsing was continued until the required dose was achieved.

Oscilloscope traces illustrating the manner in which the pulsed voltage and current waveforms vary with time for a workpiece inserted into a nitrogen plasma are shown in Figure 39. The shape of these waveforms is characteristic of plasma ion implantation performed in this facility. Such waveforms have been observed in other large volume, high number density PII apparatus which also implant samples without significant ion depletion. The current waveform rises for a duration of 1-2 μs, a characteristic time limited by the capacitance of the sample holder and the switching circuit. After peaking for approximately 5 μs, the current approaches an asymptotic, non-zero value before the pulse is terminated, which strongly suggests that the plasma sheath surrounding the workpiece reaches a steady state thickness in about ten microseconds. This waveform is used to calculate the implanted dose after compensating for the secondary electron emission coefficient appropriate to the implant material and to the implantation energy.

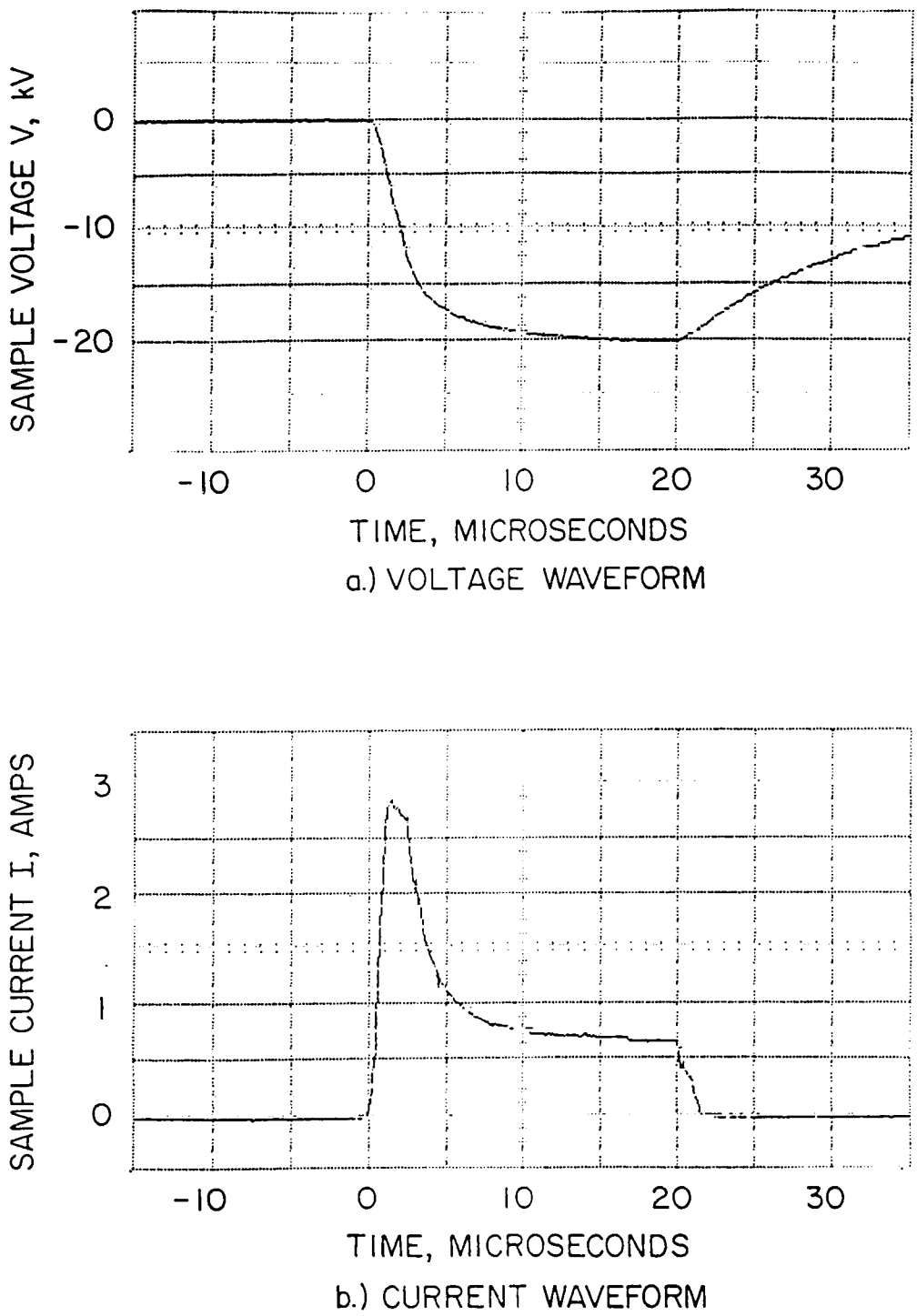

Figure 39. Pulsed voltage and current waveforms generated during N PII (99).

Four different sample holder geometries were tested in an effort to improve lateral nitrogen implant uniformity. Their backing plates' individual dimensions were:

- A square plate of 2 .0 x 2.0 cm^2 area (Fig. 40)
- A square plate 5.08 x 5.08 cm^2 area (Fig. 41)
- A circular plate 8.377 cm in diameter (Fig. 42)
- A circular plate 4.445 cm in diameter (Fig. 43)

The latter two each contained recesses for mounting polished specimens flush with the sample holder backing plate.

Electrochemical Corrosion Testing

All corrosion measurements were performed in the Corrosion Laboratory of the Materials Science and Engineering Department, UTK. The primary purpose was to measure the pitting corrosion resistance of ion implanted and control materials. The UTK MSE Corrosion Laboratory, working primarily in cooperation with the ORNL-SMAC facility, has compiled a significant work history in investigating the corrosion inhibition of ion-implanted alloys (123-136).

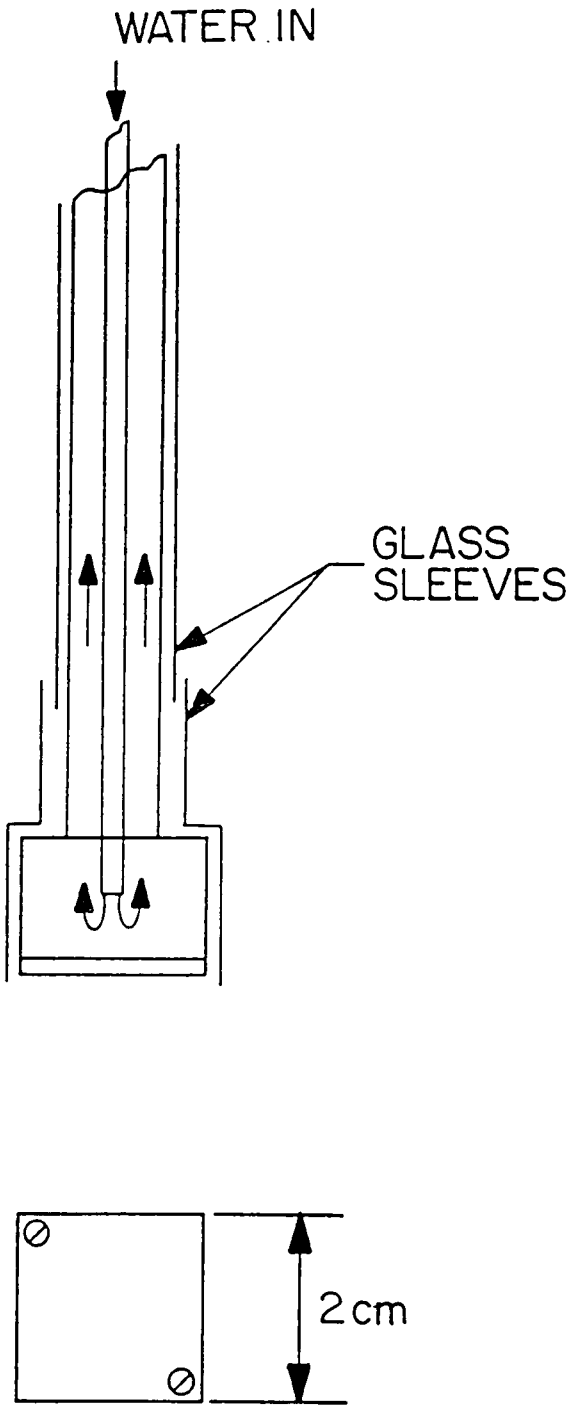

Figure 40. Initial sample holder used for PII (99).

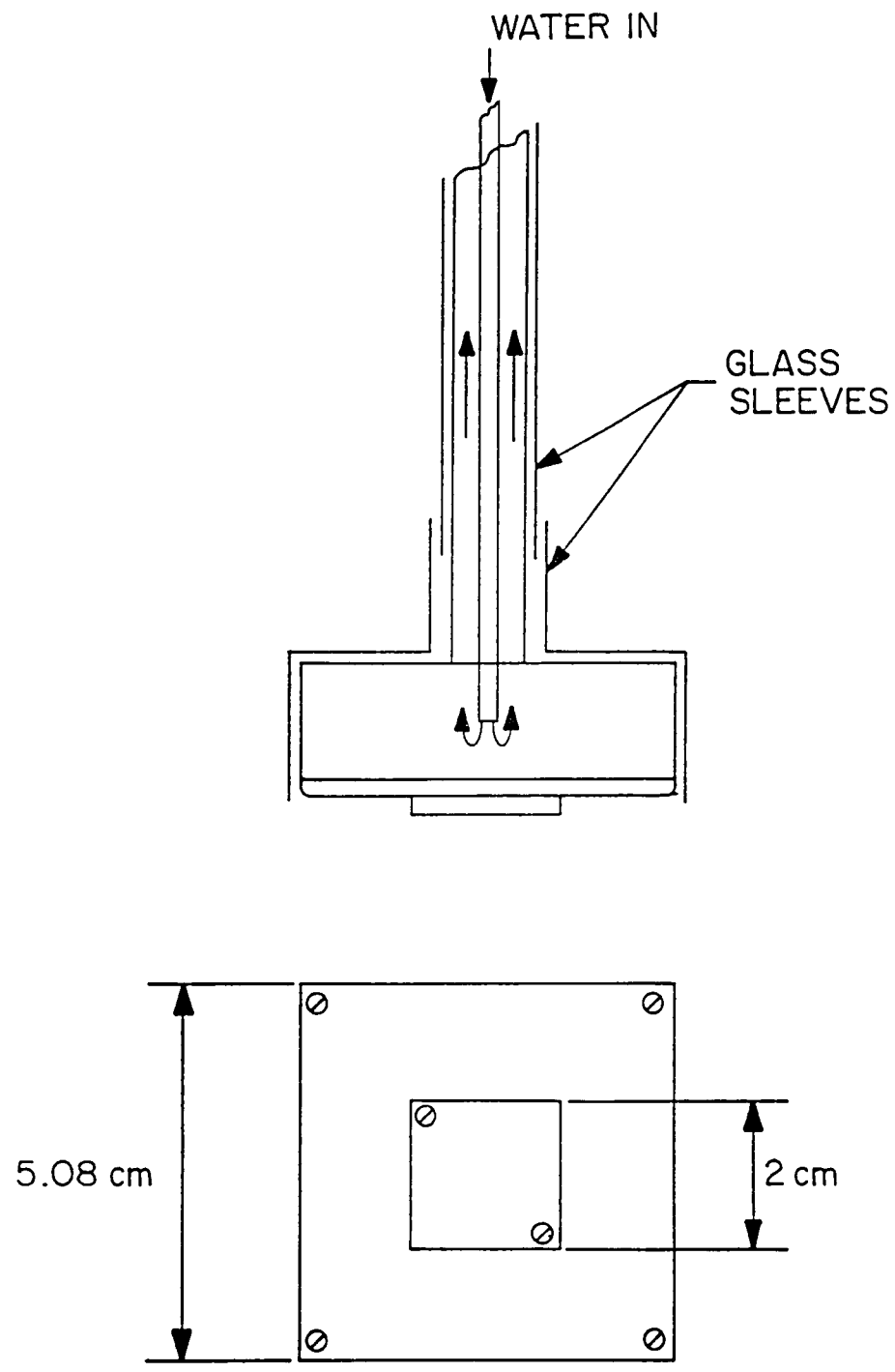

Figure 41. Second sample holder used for PII (99).

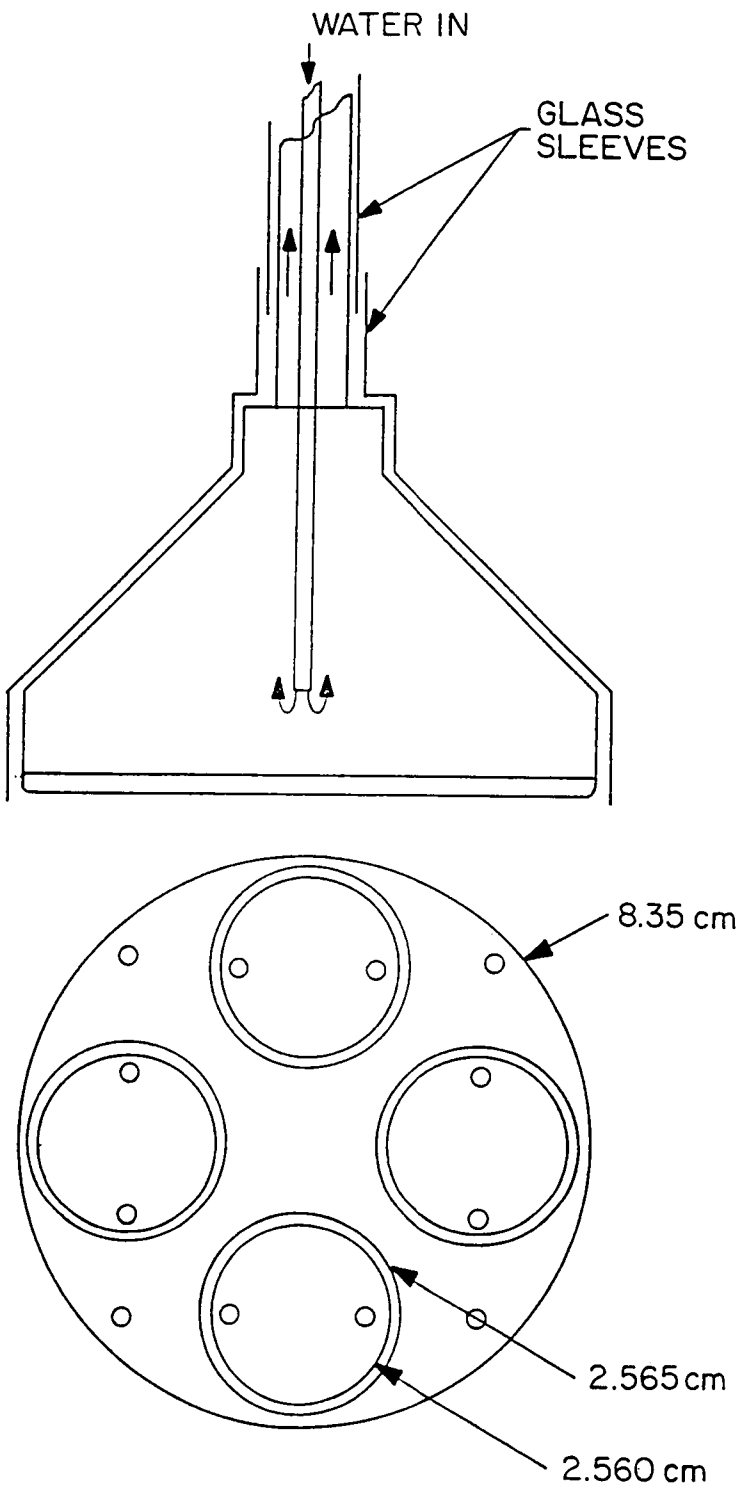

Figure 42. Third sample holder used for PII (99).

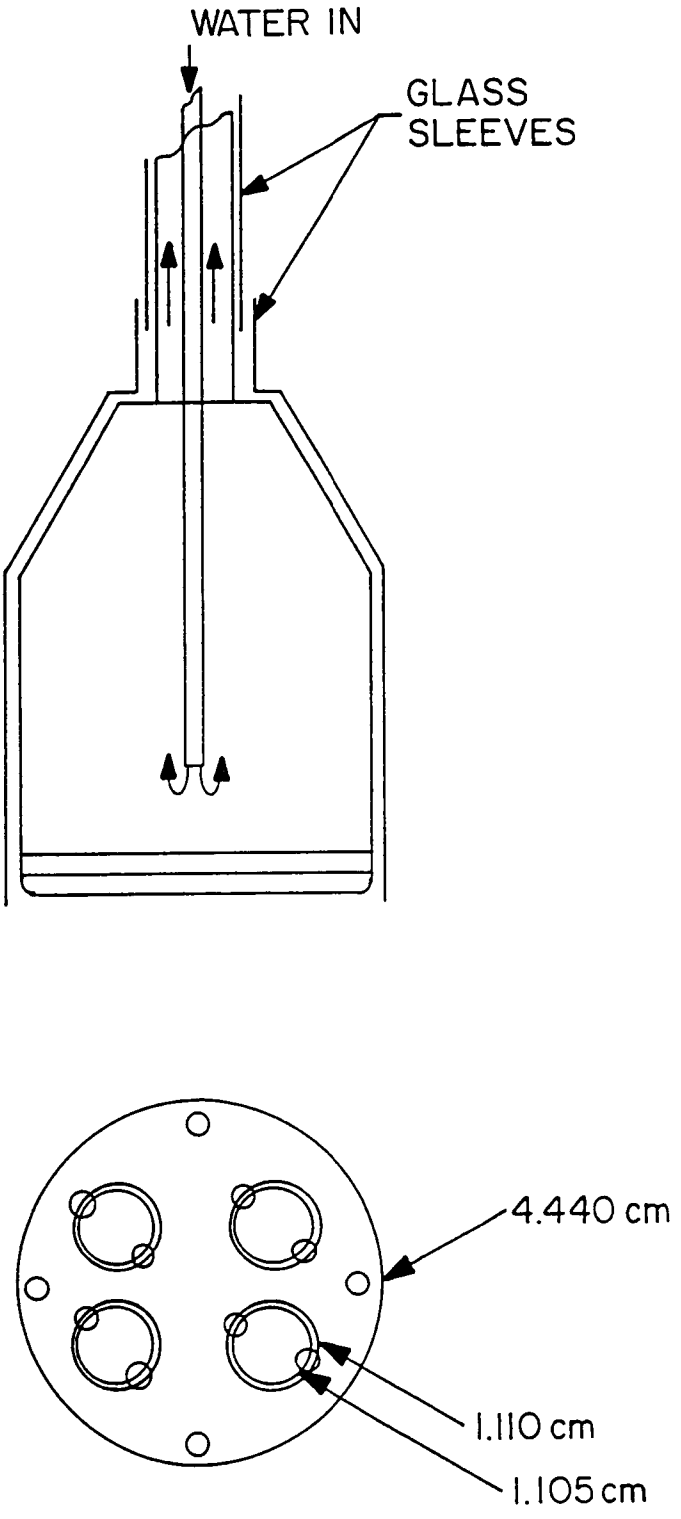

Figure 43. Fourth sample holder used for PII (99).

Anodic Polarization

The primary electrochemical test utilized to ascertain the modified localized corrosion behavior of ion implanted materials was anodic polarization (AP). All AP curves were determined with an EG&G Princeton Applied Research Model 273 potentiostat/galvanostat. Process control and data retrieval were executed by an EG&G Model 342 Softcorr Corrosion software package running on an Epson Equity III+ microcomputer.

A schematic of the polarization cell is shown in Figure 44 (100). A 2 liter Pyrex vessel was covered by a PVC plate containing holes for the working, Pt counter, and reference electrode holders, and also for the gas sparger, gas outlet, and thermometer. PVC fittings were used to securely hold each device in the desired position. The test cell was isolated from the environment by compressing an O-ring between the PVC plate and the cell flange with brass screws. The reference electrode was either saturated silver/silver-chloride contained in a capillary tipped glass tube or a standard commercial saturated calomel electrode. All Ag/AgCl electrodes were checked for accuracy against a standard calomel electrode prior to testing. All potentials were later converted to the standard hydrogen scale (SHE). Nitrogen deaeration of the test electrolyte was performed for at least 30 minutes before any experimental work was initiated. The specimen was lowered

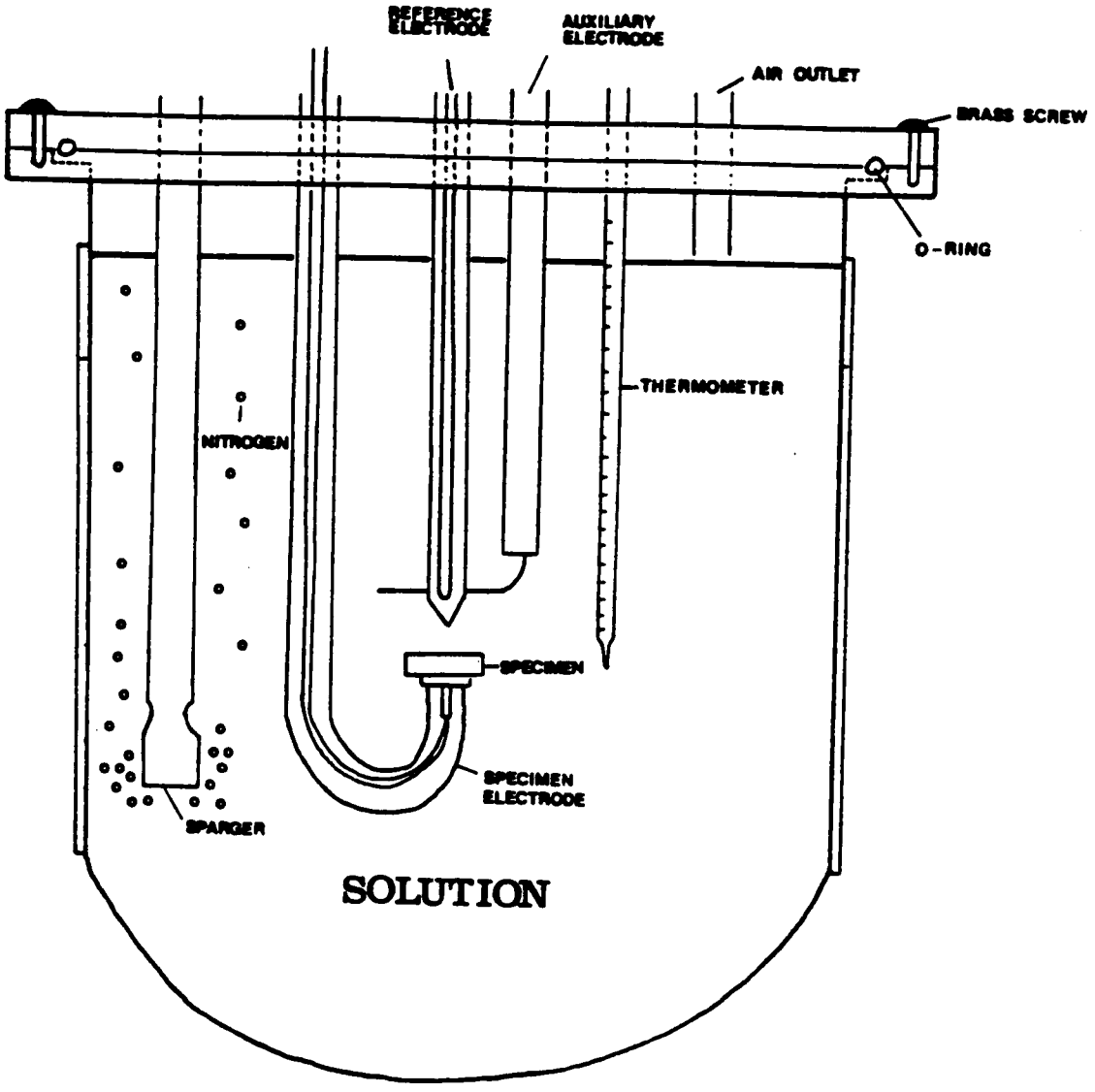

Figure 44. Schematic diagram of electrochemical polarization cell (100).

into the solution after completion of this deaeration, and immediately before initiating the open circuit potential test. Sparging of the solution was continued for the duration of all electrochemically testing. The test solution was deaerated 1 wt% [0.171 M] NaCl in 1.6 liters of doubly distilled water, unless otherwise indicated. All electrochemical measurements were performed at 25°C.

Prior to all anodic polarization scans, the open circuit corrosion potential (E_{corr}) of the specimen was monitored for at least 30 minutes. The E_{corr} vs. time behavior monitors changes in the metal surface reactions with the electrolyte after immersion into the solution.

After solution deaeration and stabilization of E_{corr}, the potential of the alloy was scanned in the noble direction at a constant rate of 0.6 V / hr, beginning 50 to 100 mV below E_{corr}. After scanning through the corrosion potential, passive region, and past the pitting potential, the direction of the potential scan was reversed when the pitting current density reached 10^3 μA / cm^2. An idealized AP curve of a passive metal that undergoes pitting is shown schematically in Figure 45. The pitting potential (E_{pit}) was determined as that potential in the passive region where a rapid increase was noted in the anodic current density. Upon removal from the test solution, the specimen surface was examined by light and

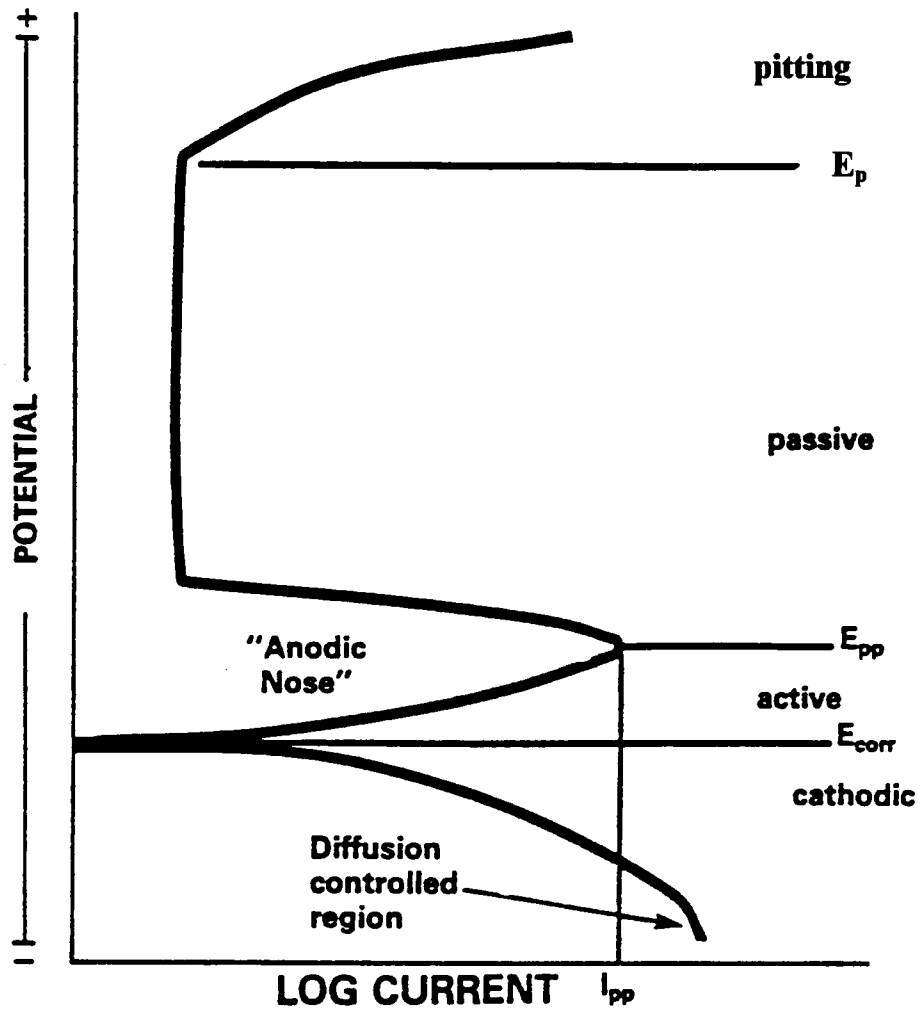

Figure 45. Idealized electrochemical polarization curve for an active-passive alloy, showing active, passive, and pitting regions.

scanning electron microscopy for evidence of localized corrosion. Pitting size, density, and morphology were noted where applicable. Another electrochemical test employed in this study was potentiostatically holding implanted and control specimens +50 mV above their respective corrosion potentials and monitoring the resulting corrosion rates. This resulted in an accelerated simulation of their corrosion rates in the aerated condition.

In order to preserve the implanted surfaces, a specially-constructed polytetrafluoroethylene sample holder was utilized for all corrosion experiments (Fig 46) (101). The sample-holder / sample contact area is minimized by sharpening the contact edges so that the crevicing geometry is minimized. The sample holder threads were wrapped in Teflon tape in order to prevent electrolyte seepage into the working electrode.

Amercoat Masking

Stainless steels and aluminum alloys are both susceptible not only to pitting, but to all forms of localized corrosion. This can manifest itself as an artificially high passive current density (102) or as an artificially low and inconsistent pitting potential value (103) during an anodic polarization test. Therefore, several precautions were employed to ensure that crevice corrosion at the metal/non-

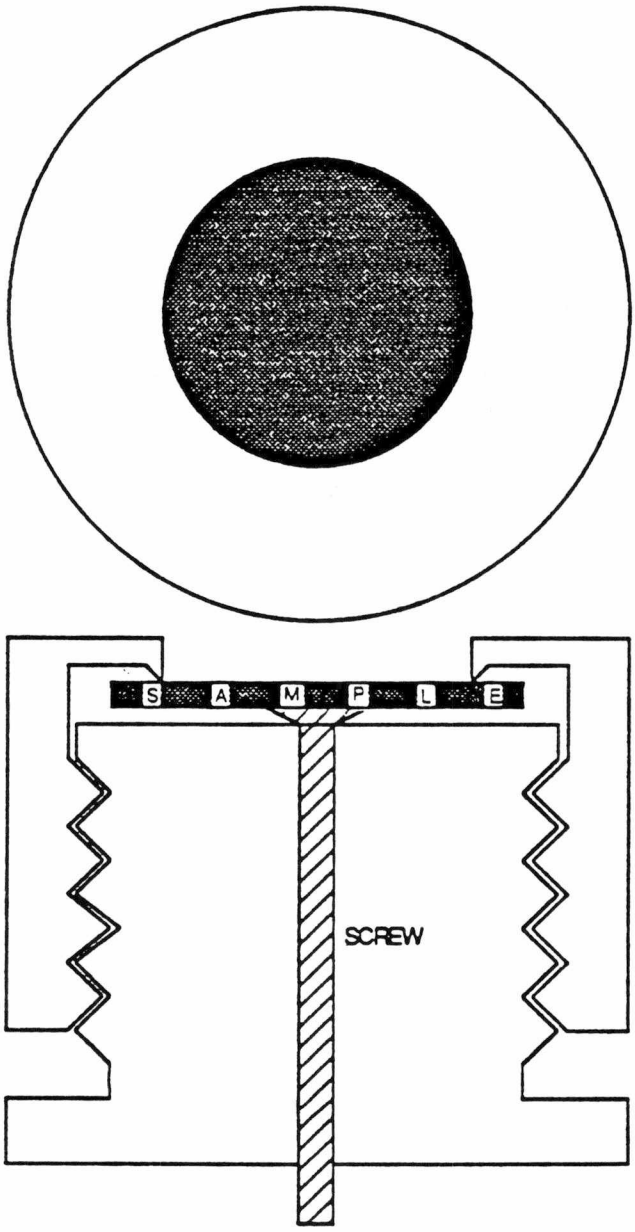

Figure 46. Schematic diagram of the specimen holder used for corrosion testing (101).

metal interface was eliminated, and a true pitting potential was measured. After implantation, the specimen surface was masked off with Amercoat 90 epoxy paint (Ameron Co., Brea, CA) leaving a 0.1-0.6 cm^2 exposed window. Typical industrial applications of this epoxy are for protection of steel and concrete exposed to corrosive chemicals and harsh weathering. In addition, the 304L surfaces were prepassivated in 50% HNO_3 + 50% H_2O at 55°C for 30 minutes prior to application of the epoxy coating. Due to the highly oxidizing nature of nitric acid, the free corrosion potential of 304L in this solution is well above the passivation potential. Immediately before immersion into the test electrolyte, the sample was manually repolished with a light application of 1 μm diamond paste, or was cathodically cleaned for several minutes in the test solution. This ensured removal of the passive film within the exposed window, but allowed the film to remain at the epoxy/metal interface to protect against crevice corrosion.

Immersion Testing

A similar 2 liter Pyrex container was used for immersion testing. The solution was aerated 3.5 % NaCl. Changes in open circuit potential with time for each specimen were monitored for the duration of each experiment. Data recording was automated and recorded by the use of a Samsung S330 microcomputer. Up to three working electrodes were contained within each cell, as shown in Figure

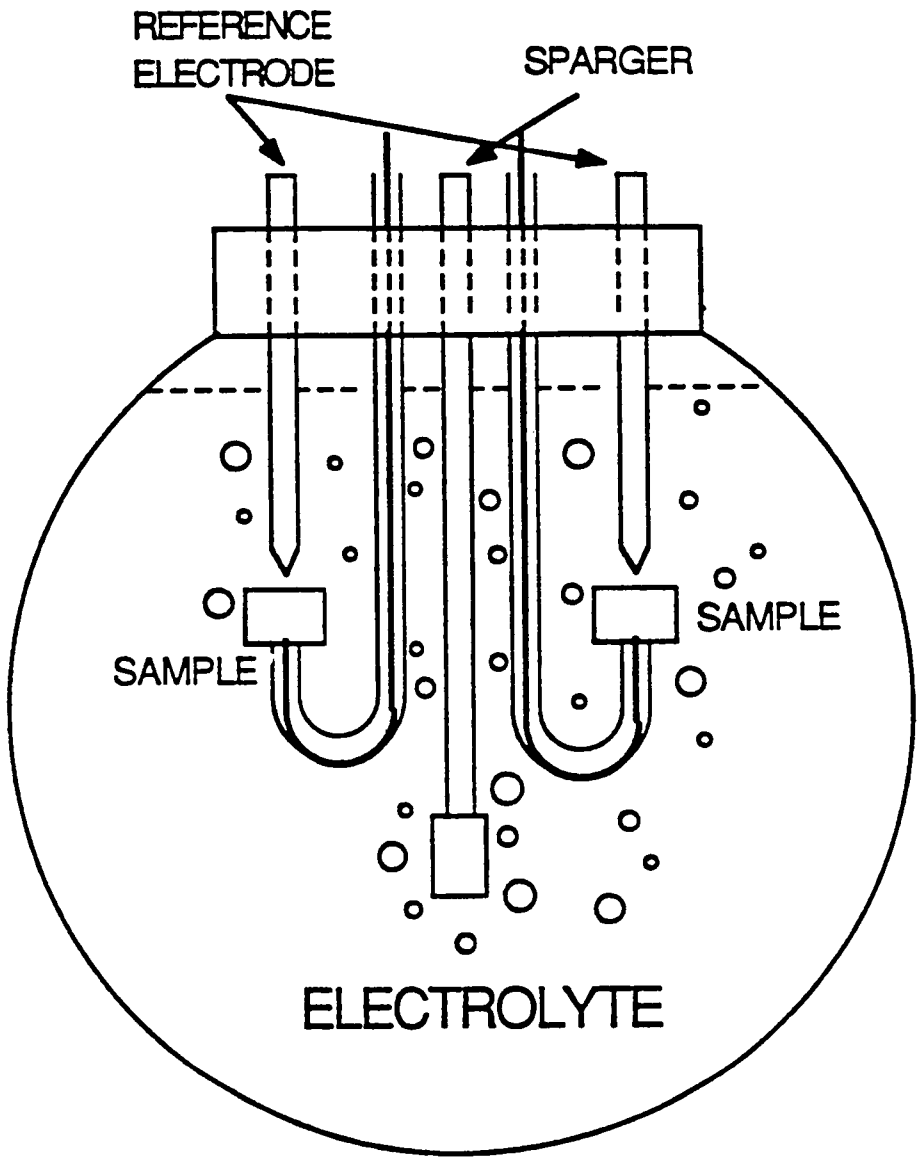

Figure 47. Schematic diagram of the immersion test cell (101).

47. Immersion tests were also carried out on nitrogen implanted 304L ss in ferric chloride and potassium permanganate solutions.

Auger Electron Spectroscopy

Chemical surface examination of implanted and electrochemically tested specimens by Auger electron spectroscopy was performed at the High Temperature Materials Laboratory (HTML) of the Oak Ridge National Laboratory. A Phi 660 Scanning Auger Microprobe (SAM) equipped with a Lab 6 filament and DASH software / hardware upgrade was used. The operating pressure was approximately 2 x 10^{-9} torr for each analysis. To optimize sputtering (3.5 keV Ar), the sample was tilted to an angle of 30° with respect to the beam. The beam current was 20 nA and the beam size was limited to a 0.25 μm spot radius by utilizing a 16 mil aperture. A low accelerating energy of 2 keV was used to minimize charging from the insulating Al_2O_3 oxide layer. Quantitative results were assumed to be $\pm$ 5 atomic percent since standards were not used for calibration. Profiling was automated by multiplex analysis of different elements, but peak locations were rechecked manually as a function of sputtering depth. A Mitsubishi CP210U color printer was used to capture an SEM image of the surface areas of inquiry.

Atomic Force Microscopy

A Topometrix TMX 2000 atomic force microprobe equipped with Topometrix SPM v3.04 software was used in the contact mode at HTML. Vibrational isolation was achieved by using a pneumatic isolation table for system support. Output photographs of surface topography was captured by a Kodak ColorEase Dye Sublimation Color Printer, which provides ultra-high resolution. The surfaces were scanned with a silicon nitride pyramid-shaped tip. Surface feature heights were measured by laser reflection focused on the center of an array of four photo cells.

4. RESULTS AND DISCUSSION

Part I - Tungsten Ion Implantation of Aluminum 1100

Electrochemical Polarization Testing

The Al 1100 microstructure is shown in Figure 48. The specimen was ground, polished, and ultrasonically cleaned, but unetched prior to optical examination at 200 x magnification. The size, number, and distribution of secondary $FeAl_3$ particles shown is not atypical for this alloy. The inherent passivity of aluminum can be demonstrated by polarization in an aerated 1 wt. % Na_2SO_4 solution (Fig. 49). The form of the anodic and cathodic curves, as well as the magnitude of the passive current density (30-40 $\mu A / cm^2$), is consistent between two separate runs in this electrolyte. However, the E_{corr} values differ by 161 mV. This illustrates the sensitive dependence of an alloy's electrochemical properties on test variables such as the degree of solution aeration / deaeration, accuracy of solute concentrations, and alloy surface conditions.

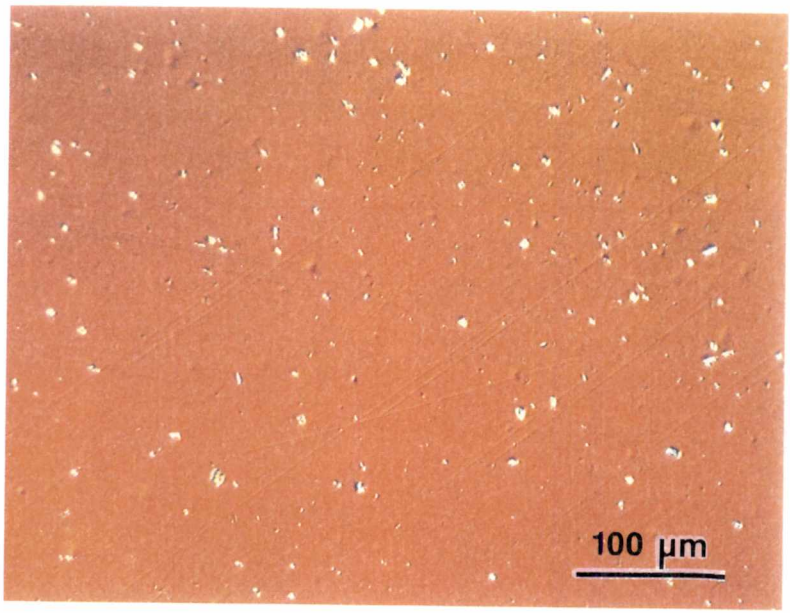

Figure 48. Microstructure of Al 1100 alloy, polished and unetched (200 x).

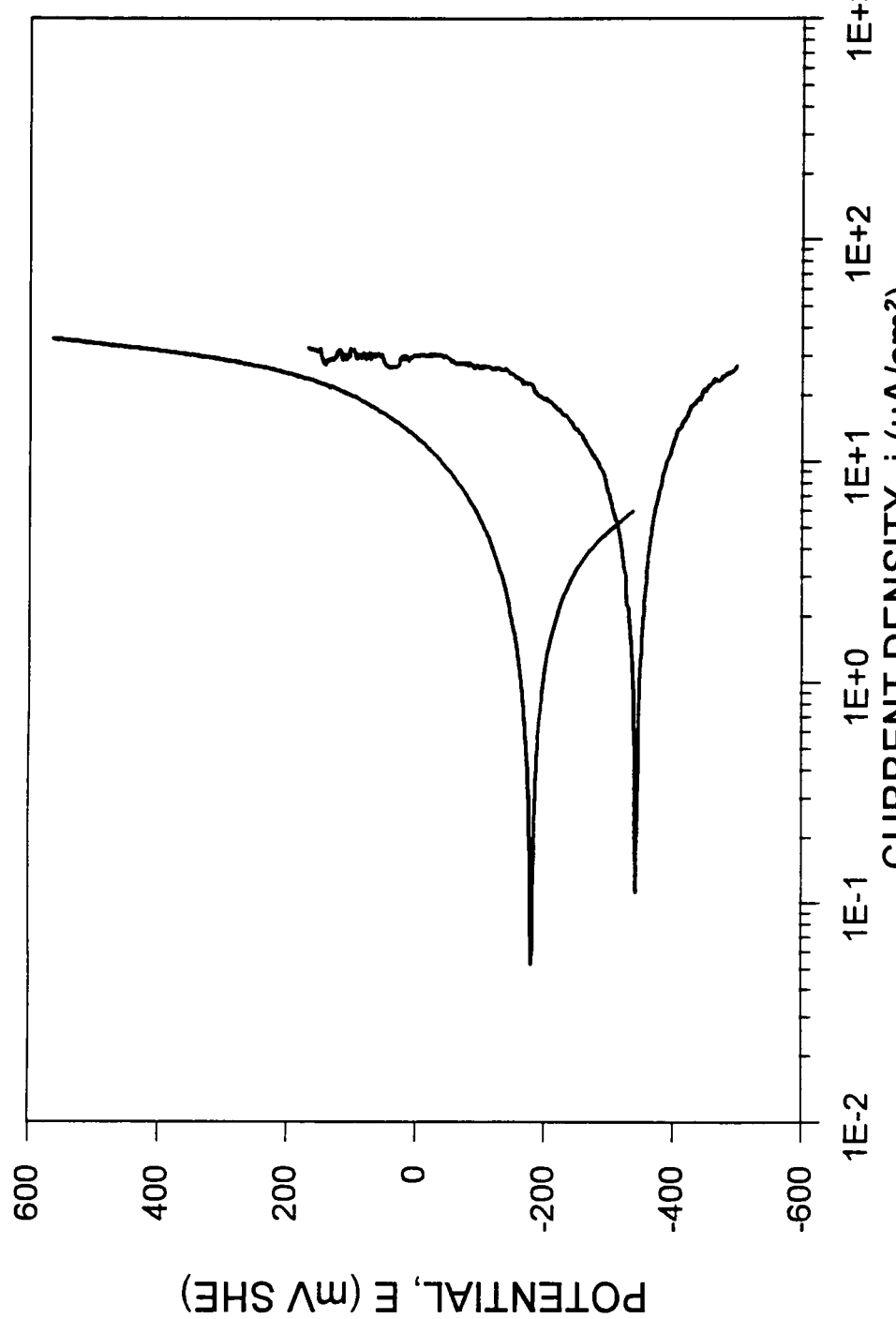

Figure 49. Two examples of the anodic polarization of Al 1100 in aerated 1 wt% Na_2SO_4.

Upon deaerating the sodium sulfate solution, Al 1100 exhibits a lower passive current density that increases with potential (Fig. 50). Also shown is the alloy behavior in a deaerated 1 wt. % NaCl solution. A very limited range of passivity (65 mV) is seen before pit propagation proceeds rapidly at the pitting potential of -432 mV (SHE). Comparison of the anodic polarization of Al 1100 in the sulfate and chloride solutions clearly demonstrates the deleterious effect of the chloride ion on the stability of the aluminum oxide film.

The proximity of the pitting potential (E_p) of Al 1100 to both the passivating potential (E_{pass}) and corrosion potential (E_{corr}) in the chloride containing environment is seen in Figure 51. The anodic loops, not typically observed during anodic polarization of aluminum alloys due to their extremely rapid passivation, were produced by a combination of an initial cathodic treatment, for the purpose of oxide removal, and the application of a rapid scan rate. The application of the cathodic potential causes the reduction of hydrogen ions (or water) on the surface, which raises the local pH and dissolves the amphoteric aluminum oxide film. The specimens were potentiostatically held at -1604 mV (SHE) for 30 minutes prior to scanning in the anodic direction at a rate of 3.0 mV / sec. The difference between the passivating potential (-516 mV) and the

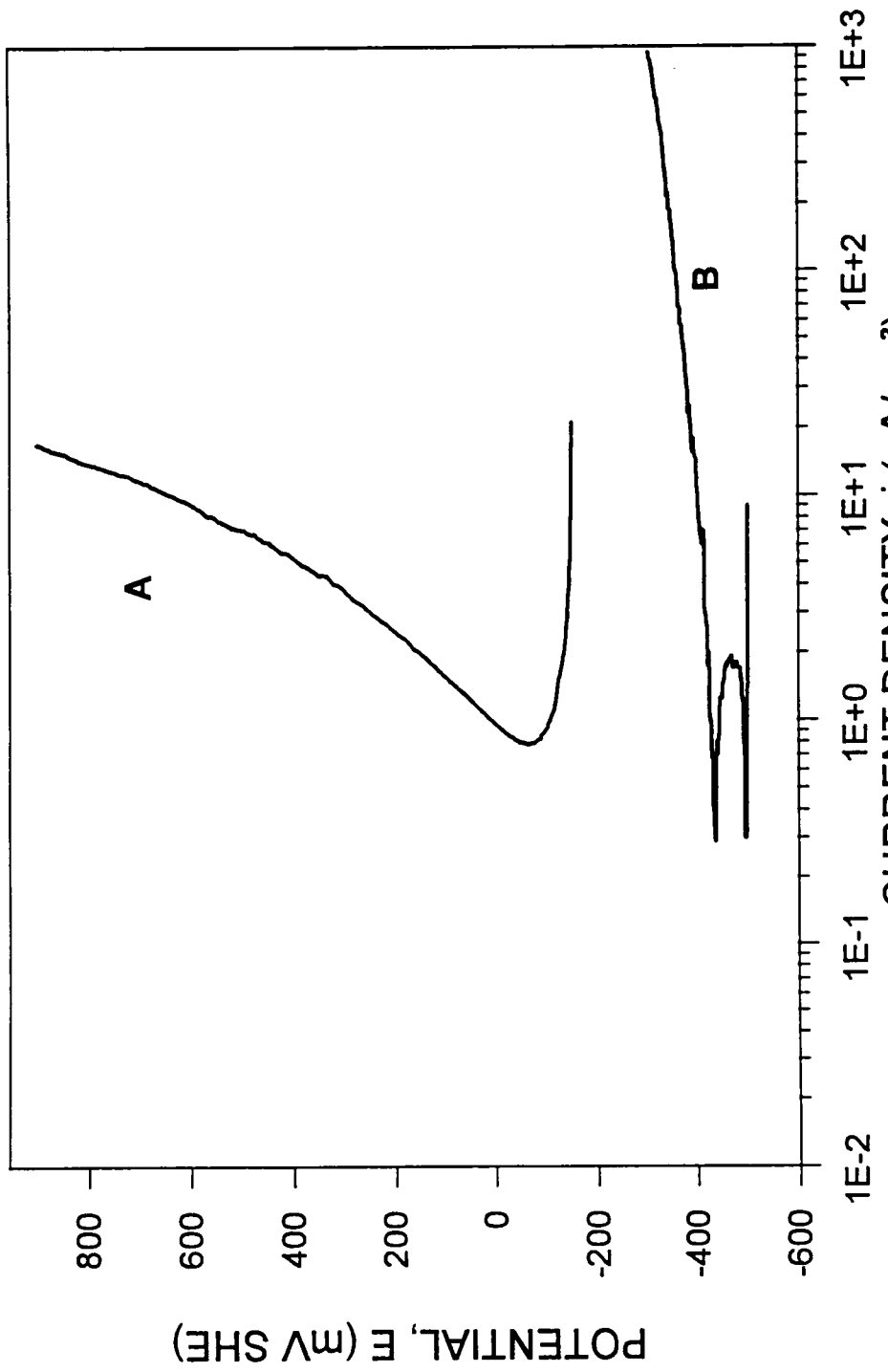

Figure 50. Al 1100 in (A) deaerated 1 wt% Na_2SO_4 and (B) deaerated 1 wt% NaCl.

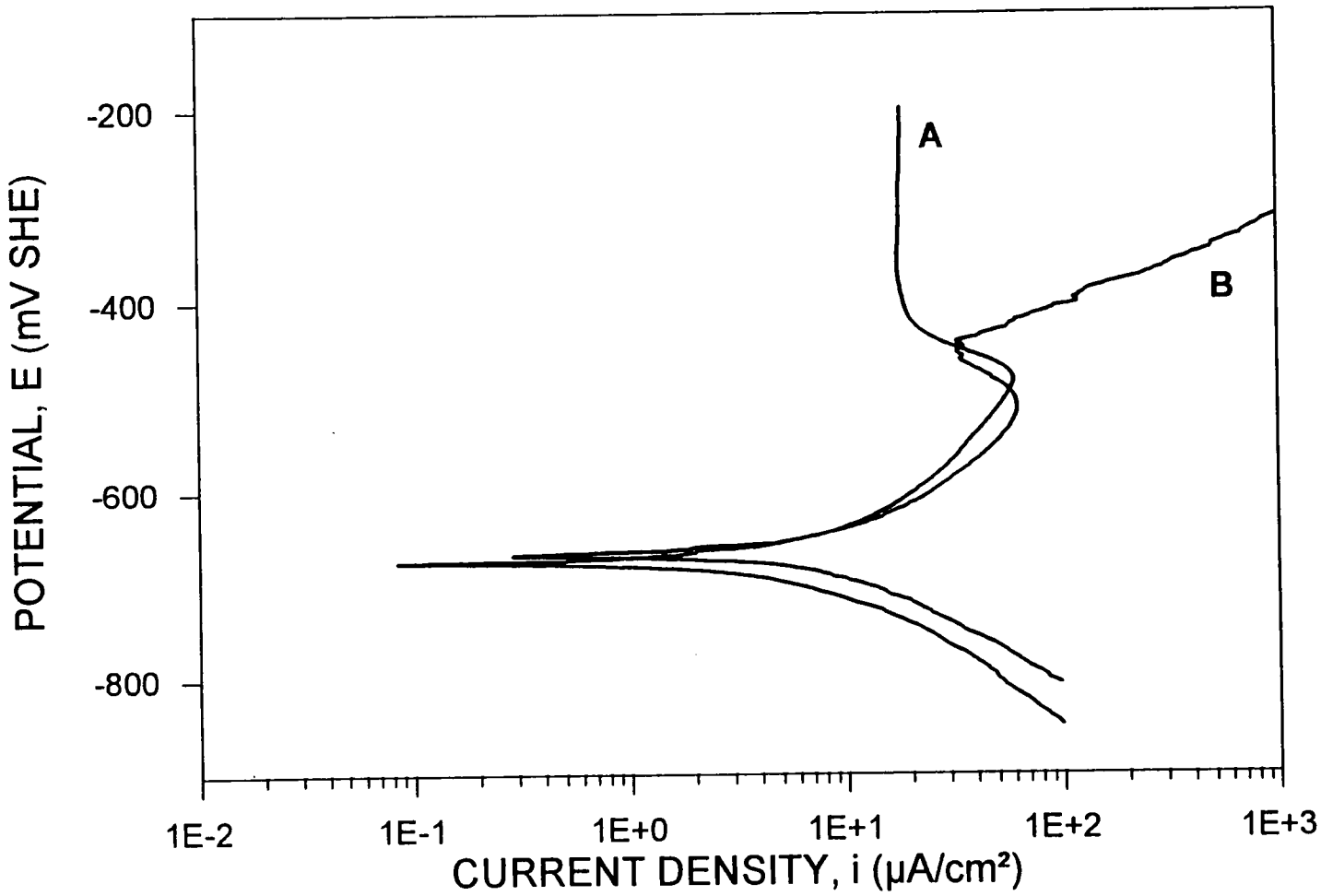

Figure 51. Anodic polarization of Al 1100 in (A) deaerated 1 wt% Na_2SO_4 and (B) deaerated 1 wt% NaCl. Scan rate = 3.0 mV / sec after cathodic polarization at -1604 mV (SHE) for 30 minutes.

pitting potential (-440 mV) is only 76 mV, a range of passivity that may be somewhat artificially extended as a result of the accelerated scan rate.

Anodic polarization behaviors of tungsten - (2 wt. % ThO) in the deaerated chloride and sulfate solutions are shown in Figure 52. In both solutions, the passive state continues to be stable to extremely high potentials (> 2000 mV SHE). The effect of the ThO addition to the specimen is seemingly insignificant electrochemically since these curves are similar to results from previous tests on pure W (Figure 16). The resistance to chloride induced breakdown of the tungsten oxide is shown by the surprising result that the passive current density in the Na_2SO_4 solution (500 $\mu A / cm^2$) exceeds that in the NaCl solution (100 $\mu A / cm^2$). Therefore, tungsten holds great promise for activating pit inhibition on aluminum if it can be incorporated into the material by a non-equilibrium technique such as ion implantation.

Tungsten implantation doses of 10^{16} ions / cm^2 or less do not significantly modify the polarization behavior of Al 1100 in deaerated 1 wt. % NaCl. Figure 53 shows that applied doses of 6.2×10^{15} and 1.0×10^{16} result in no elevation of the pitting potential, with the pitting current density of each corresponding very closely to the control behavior. However, as seen in Figure 54, when the amount

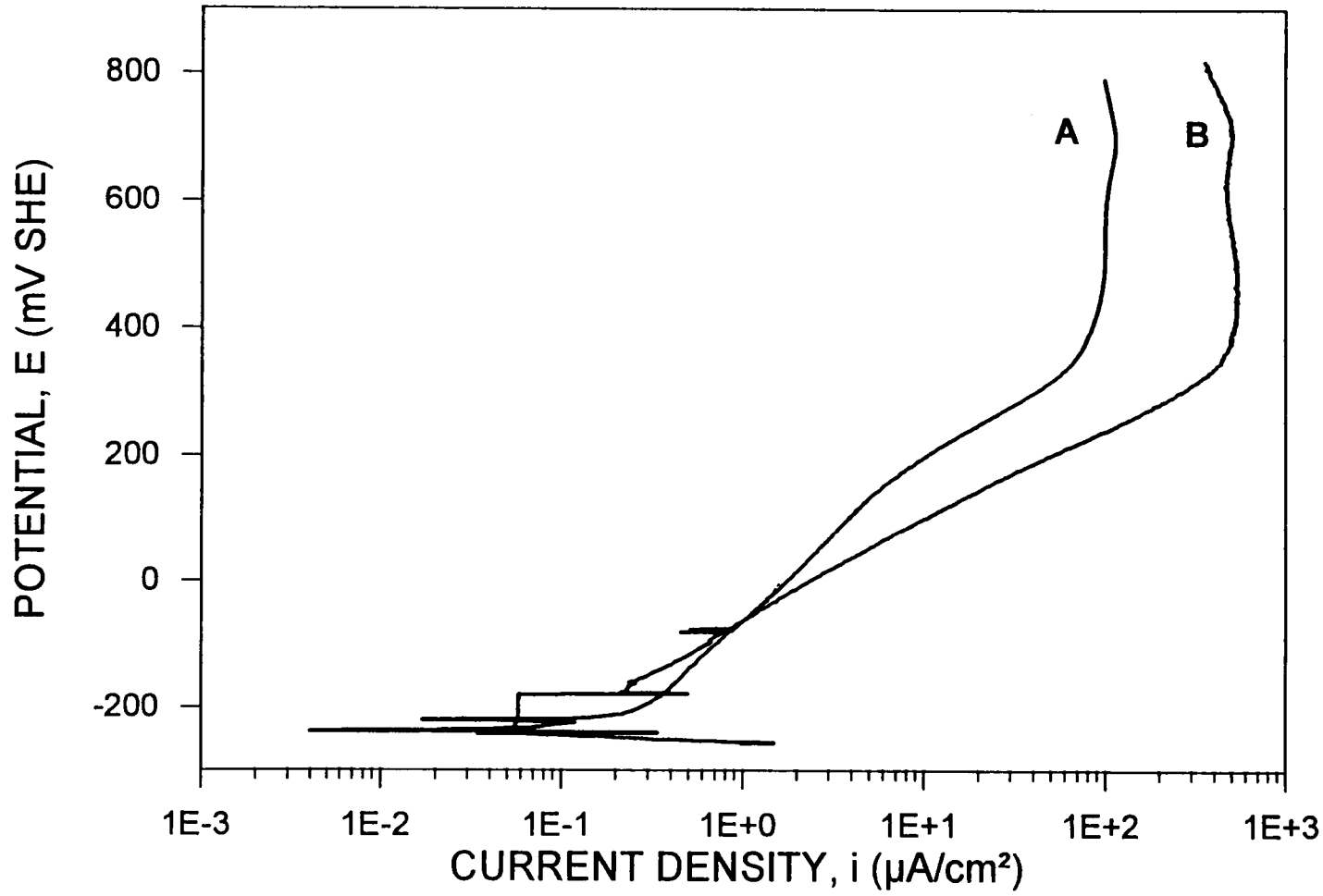

Figure 52. Anodic polarization of W - (2 wt% ThO) in (A) deaerated 1 wt% NaCl and (B) deaerated 1 wt% Na_2SO_4.

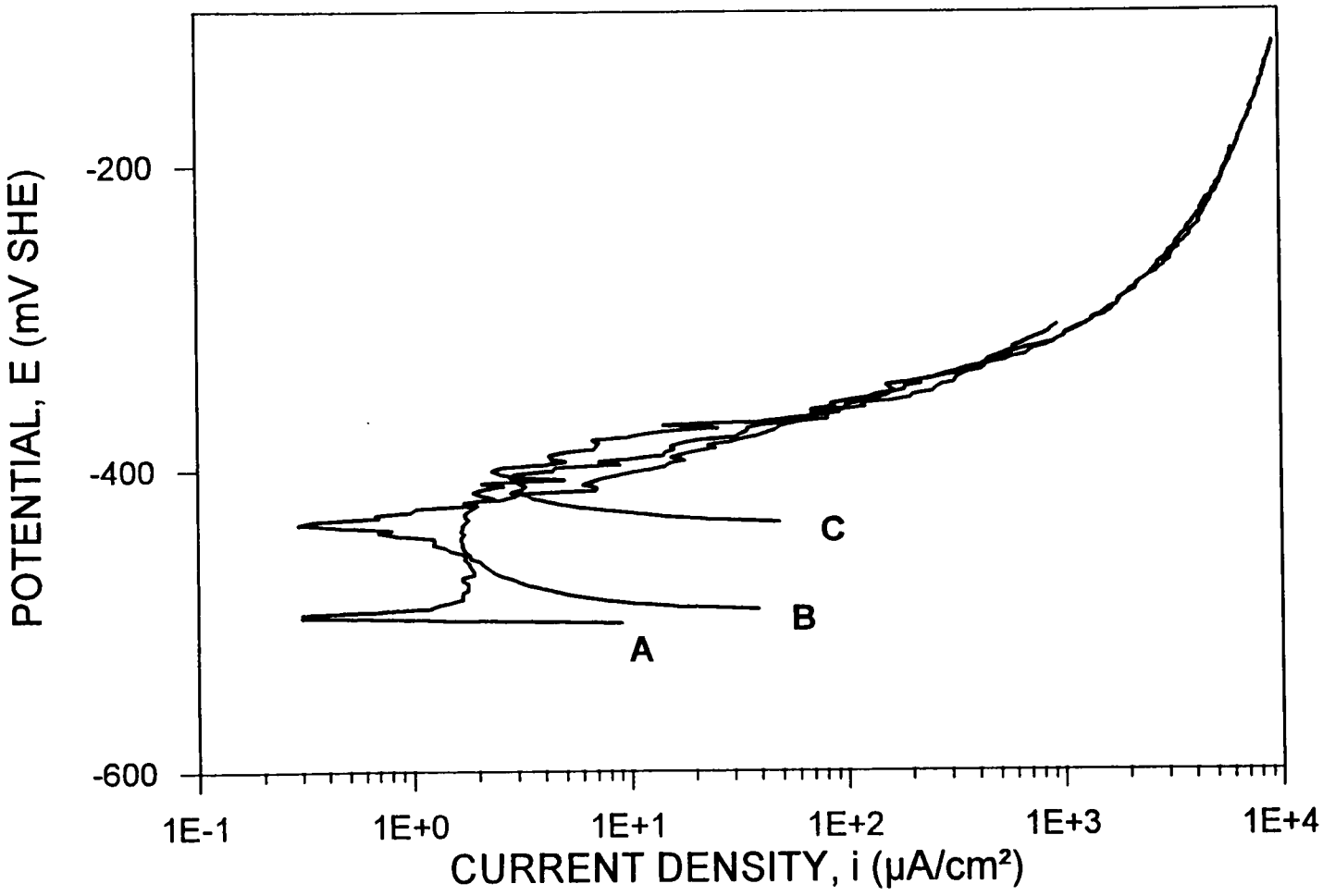

Figure 53. Anodic polarization in deaerated 1 wt% NaCl of (A) Al 1100, (B) Al 1100 - 60 kV 6.2 x 10^{15} W ions/cm^2, and (C) Al 1100 - 60 kV 1.0 x 10^{16} W ions/cm^2.

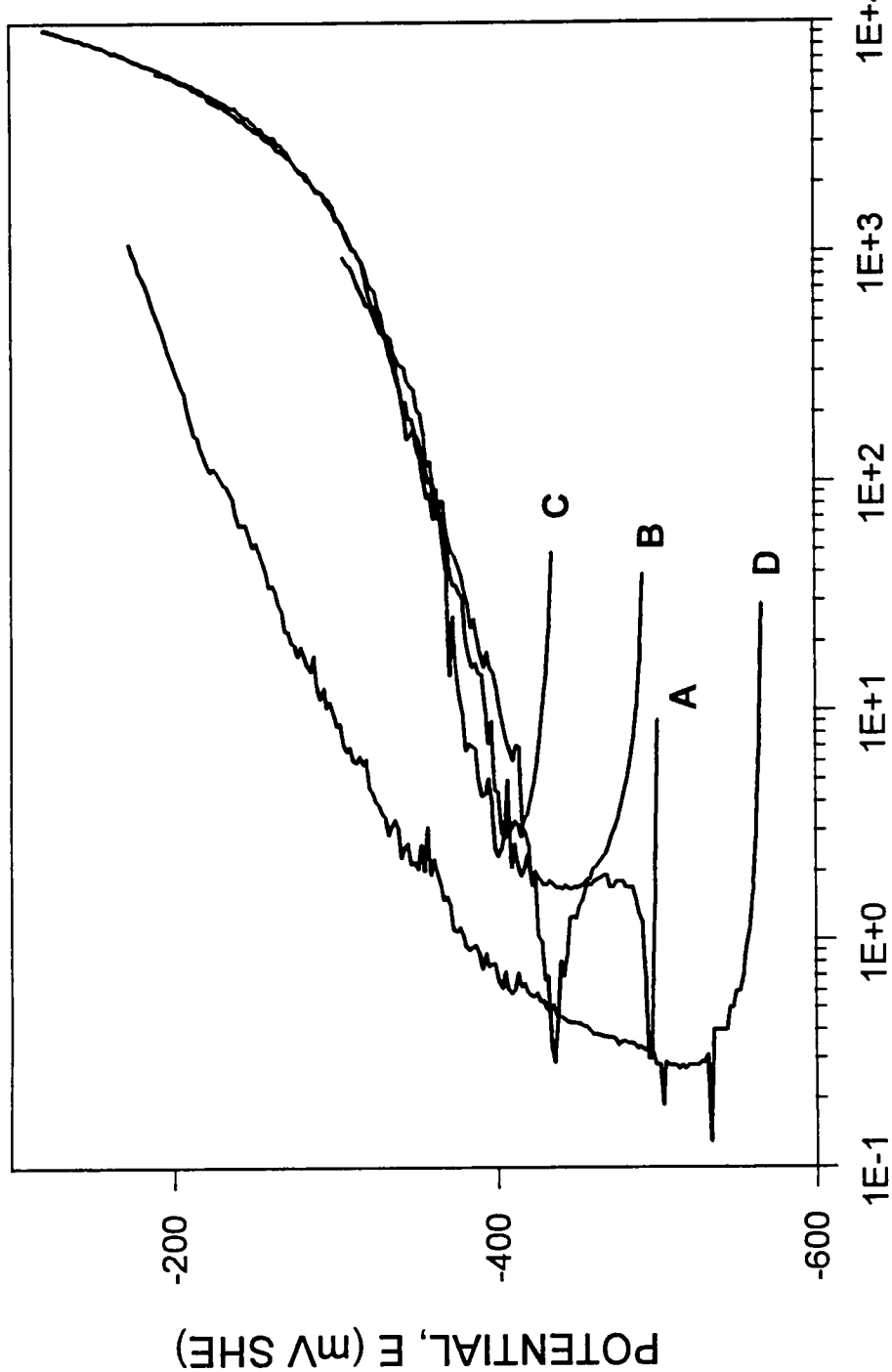

Figure 54. Anodic polarization in deaerated 1 wt% NaCl of (A) Al 1100, (B) Al 1100 - 60 kV 6.2×10^{15} W ions/cm^2, (C) Al 1100 - 60 kV 1.0×10^{16} W ions/cm^2, and (D) Al 1100 - 60 kV 1.7×10^{16} W ions/cm^2.

of implanted W is increased to 1.7 x 10^{16} ions / cm^2, an increase in passivity is observed. This expanded passive region is partially constituted by a slight rise in E_p. Since a distinct rapid current increase is not seen for this specimen, exact interpretation of the true pitting potential is difficult. However, another standard for comparison of a material's resistance to pit formation and propagation is the potential at which the pitting current density reaches 1000 μA / cm^2 (E_{1000}). A tungsten dose of 1.7 x 10^{16} ions / cm^2 increases E_{1000} from -304 mV (SHE) to -173 mV (SHE). The RBS profile for this alloy is revealed in Figure 55, along with those for the two lower dose specimens. They are typical of profiles for all of the W ion implantations, featuring a Gaussian distribution due to the application of a single implantation energy, and a penetration depth of approximately 1000 angstroms.

A further increase in the implanted dose to 4.9 x 10^{16} W ions / cm^2 resulted in a dramatic enhancement of the alloy's pitting resistance during polarization in 1 wt. % NaCl. Figure 56 illustrates that a very stable passive state was maintained by this specimen up to a breakdown potential of +1806 mV. The tungsten and aluminum alloy standards are also plotted in this figure for comparison. The passive range extends to approximately 1500 mV above the corrosion potential as contrasted with less than a 100 mV passive region in the unimplanted control.

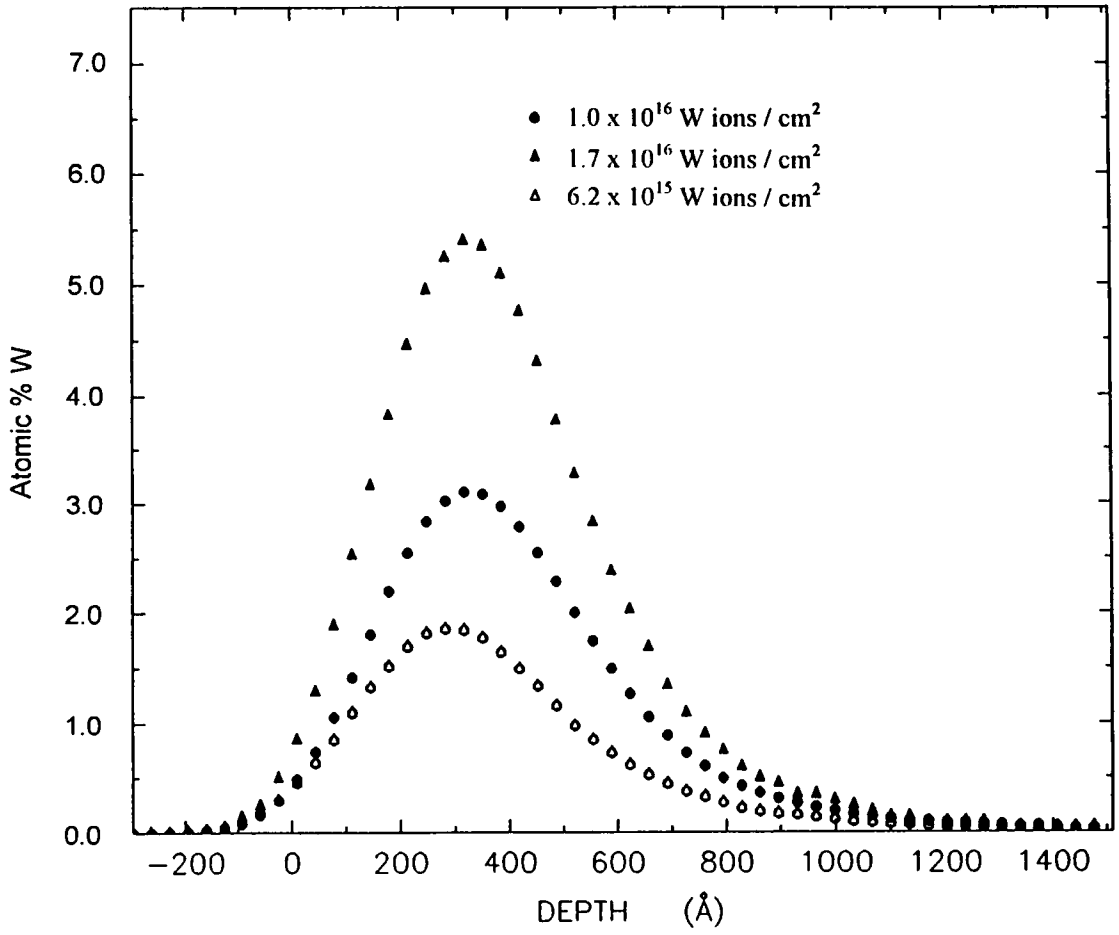

Figure 55. Rutherford backscattering spectroscopy profiles of three 60 kV tungsten ion implanted Al 1100 alloys.

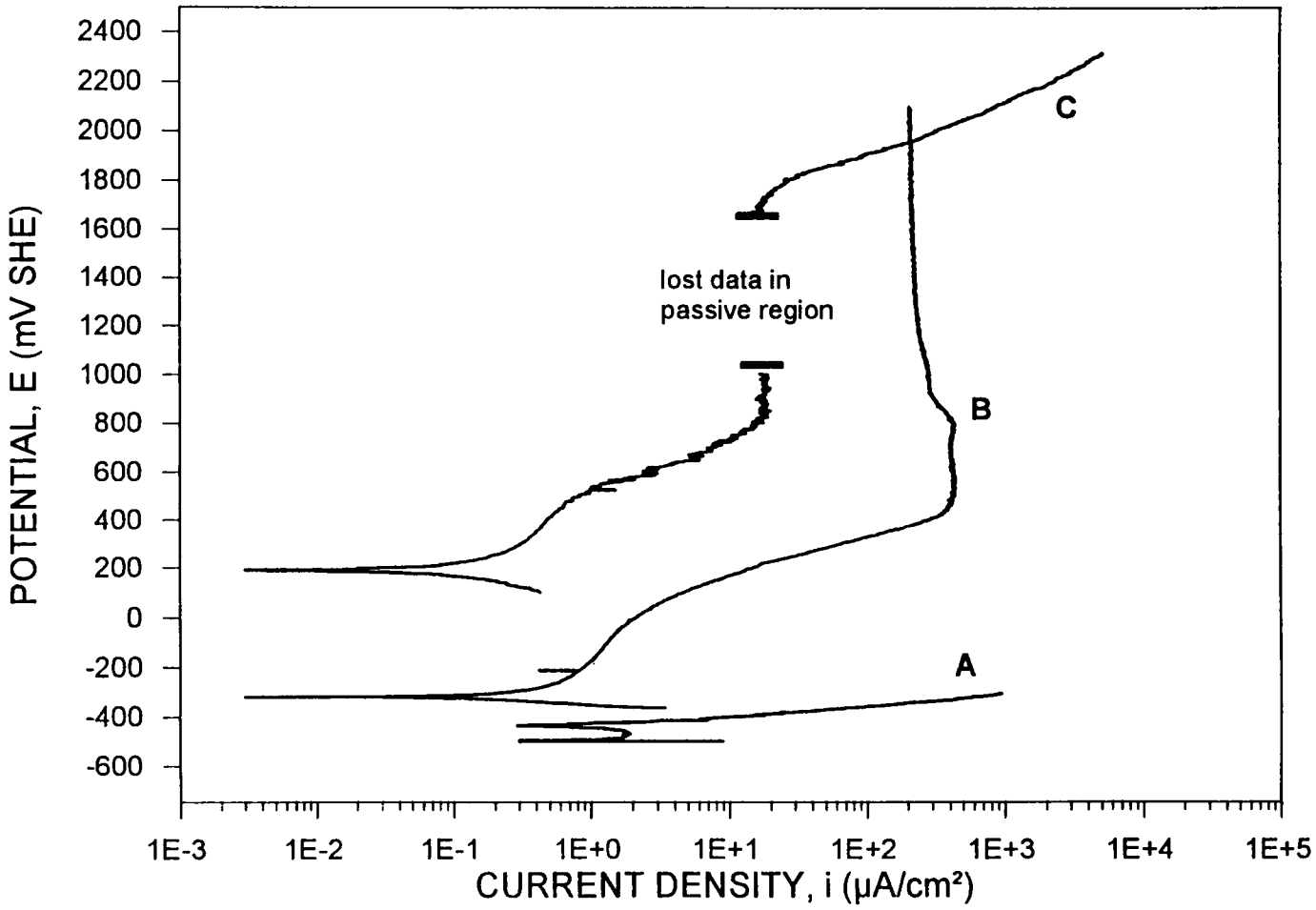

Figure 56. Anodic polarization in deaerated 1 wt% NaCl of (A) Al 1100, (B) W - 2 wt% ThO, and (C) Al 1100 - 60 kV 4.9 x 10^{16} W ions/cm^2.

Furthermore, the passive current density is approximately 20 μA / cm^2, and surprisingly, is significantly lower than that of the W alloy. Finally, E_{corr} is increased by 688 mV, a significant improvement in general corrosion resistance because of the corresponding decrease in the active current density. This pitting potential and passive current density are similar to those reported by Shaw et al. (62) for thin sputtered Al-W films. Therefore, it is possible to extrapolate the W-Al thin film results to a bulk aluminum alloy using ion implantation. The RBS profiles of this specimen before and after completion of anodic polarization (Fig. 57) reveal that the retained dose decreases from 4.85 x 10^{16} to 4.00 x 10^{16} ions / cm^2 during the passivation / pitting processes. This is a retention of only 79 % of the original dose, indicating that W dissolution occurs in the passive state. This dislodged tungsten enters the solution since no W buildup near the surface is detected in any of the post-corrosion-testing spectra, and previous results (72) indicate that it is not incorporated into the passive film at this pH. This is unsurprising in light of the solubility of tungsten oxide at neutral pH. The majority of the implanted tungsten remains in the aluminum lattice after scanning through both the prolonged passive region and pit formation. This can be understood by a Faraday's law calculation of the corrosion penetration rate during the polarization test. A corrosion penetration of approximately 350 angstroms is calculated from integration of the total charge passed during anodic polarization

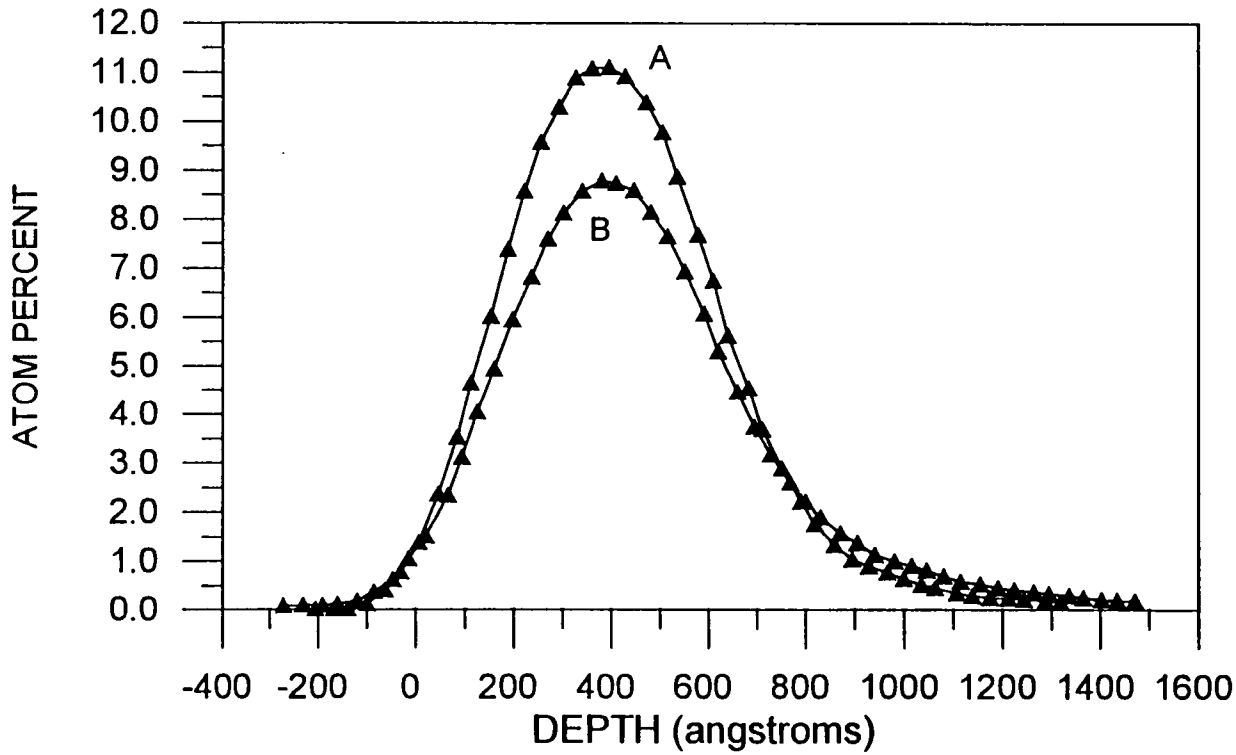

Figure 57. RBS profiles of Al 1100 - 60 kV 4.9 x 10^{16} W ions/cm^2 (A) prior to anodic polarization and (B) after anodic polarization, retention of 4.0 x 10^{16} W ions/cm^2.

between E_{corr} and E_p, and Figure 57 indicates that the W peak is at least 400 angstroms below the surface. Therefore, the majority of the implanted species is seen to be unaffected during the anodic polarization test.

Attempts to duplicate this behavior were unsuccessful. However, multiple exposures of similarly treated alloys did consistently result in increases in the range of passivity (Fig. 58). The pitting potential is increased by a minimum of 223 mV. Also, the potential at which the pitting current density reaches 10^3 μA / cm^2 (E_{1000}) is delayed from -304 mV (SHE) to approximately +200 mV (SHE), which is a significant increase in the material's resistance to pit propagation. In addition, the passive current density is decreased. Implantation doses ranging from 3 x 10^{16} to 9 x 10^{16} ions / cm^2 at an accelerating energy of 60 kV imparted such beneficial properties.

Wide variations in the measured pitting potential for a given implanted dose illustrates limitations of the ion implantation process. Since passive alloys such as aluminum are attacked at the points of least resistance on the surface, uniformity of W coverage is essential. Substrate inclusions, such as the large number of $FeAl_3$ particles present in Al 1100, are known to limit dose uniformity. Ion implantation has been applied successfully in many studies in

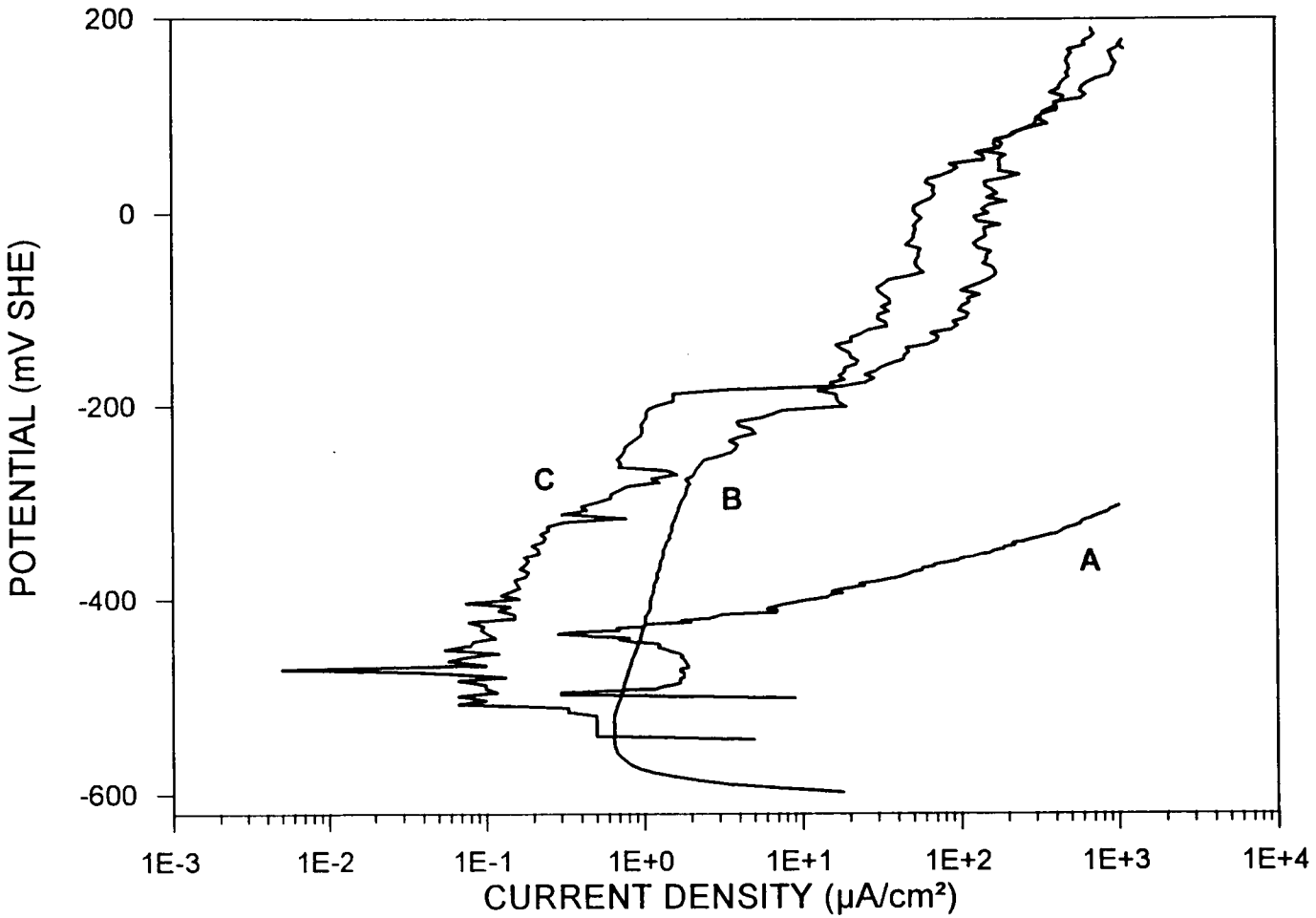

Figure 58. Anodic polarization in deaerated 1 wt% NaCl of (A) Al 1100, (B) Al 1100 - 60 kV 5.7 x 10^{16} W ions/cm^2, (C) Al 1100 - 60 kV 4.5 x 10^{16} W ions/cm^2.

improving tribological properties, while corrosion improvements are more elusive. This follows from wear being a measure of an average surface property, while pitting corrosion is a measure of the resistance of the "weakest link" on the surface. The thinness of the implanted layer also leaves the surface vulnerable to premature failure as a result of any mechanical abrasion during material handling or cleaning. An additional source of error in this study arises from the application of cathodic cleaning to some of the alloy surfaces prior to anodic polarization. Lin and Hebert (110) have pointed out that prior cathodic polarization can cause Al to become more susceptible to pitting during subsequent anodic polarization. This results in a variable which was not sufficiently controlled during this experimental work.

Each polarization test concluded after the pitting potential was exceeded and the pitting corrosion current density subsequently reached 1000 $\mu A / cm^2$ (at E_{1000}). Analysis of the corroded surfaces of unimplanted specimens indicated that pitting occurs at a number of sites on the exposed area in a non-crystallographic, semi-hemispherical manner with no unusual characteristics. In contrast, the corroded surfaces of all W ion implanted specimens featured circular blisters in the oxide film formed during polarization (Fig. 59). Comparison of backscattered and secondary SEM images of the same region (Fig. 60) of one microstructure

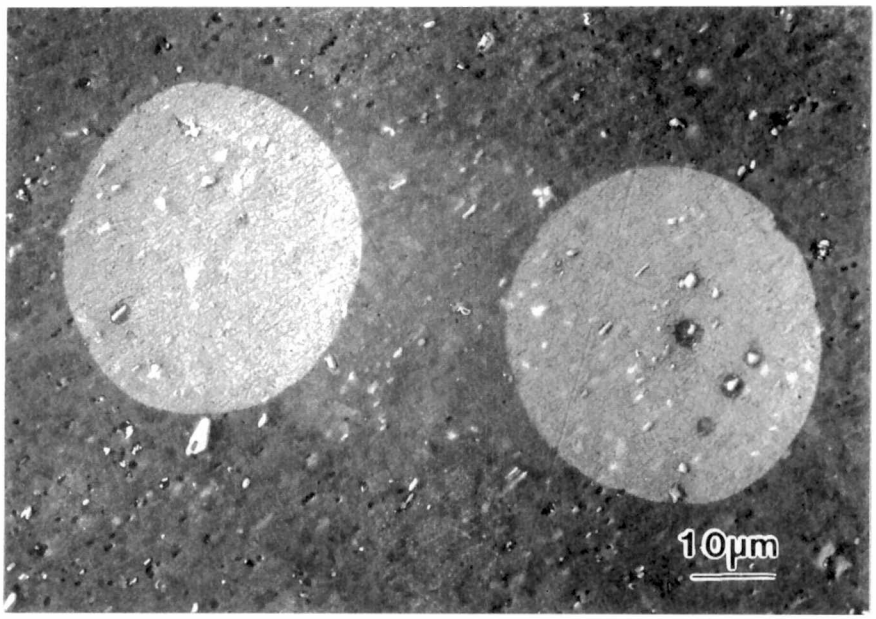

Figure 59. Oxide blisters formed during anodic polarization of Al 1100 implanted with 60 kV 4.9 x 10^{16} W ions/cm^2 (1000 x).

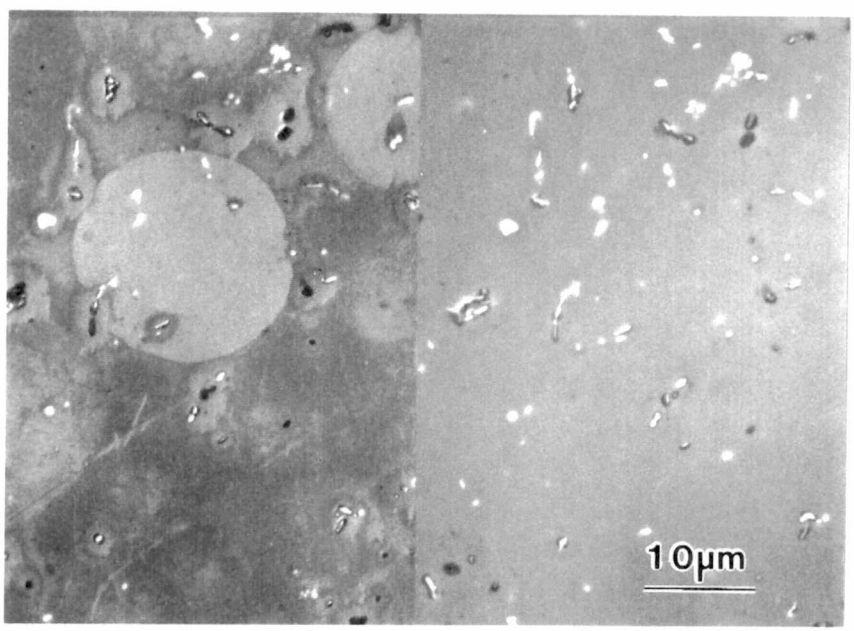

Figure 60. Secondary (left) and backscattered (right) images of the same region of an Al 1100 alloy implanted with 60 kV 1.9 x 10^{16} W ions/cm^2 (1500 x).

reveals that blisters are evident only in the secondary mode, which confirms that they are a surface phenomenon.

The relationship between the morphology of the blistered regions and the location of the ensuing pit nucleation is dependent on both the experimental conditions (i.e. polarization vs. immersion) and the degree of passivity inherent to the alloy surface. The surface of an Al 1100 specimen implanted with a dose of 1.7×10^{16} W ions / cm^2 at 60 kV is depicted in Figure 61 after polarization testing. A higher magnification (1750 x) of the same surface is shown in Figure 62. This specimen, which displayed only a slight increase in E_p relative to the unimplanted alloy, is inundated with small pits. However, they have formed almost exclusively outside of the blistered regions at the secondary $FeAl_3$ particles. Therefore, in the case of a minimally pit resistant surface, although oxide blisters do form, they are disassociated from the pitting process other than to protect the underlying Al-$FeAl_3$ interfaces from becoming pit nucleation sites. An interesting aspect of the blistering morphology on this sample can be seen in Figure 63. At each of the indicated points, two adjacent blisters have stressed the intermediate oxide sufficiently enough to separate it from the metal, resulting in a linear stringer of three overlapping blisters.

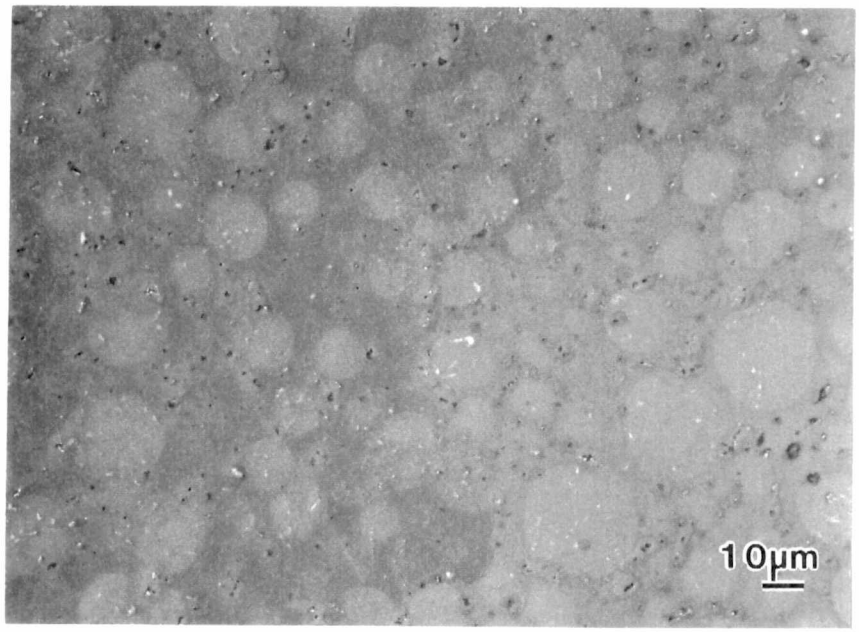

Figure 61. Oxide blisters formed on Al 1100 implanted with 60 kV 1.7 x 10^{16} W ions/cm^2 (500 x).

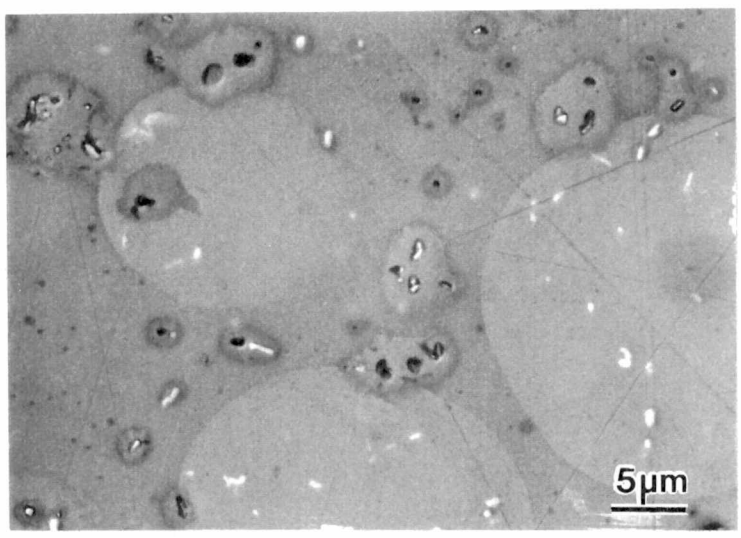

Figure 62. Oxide blisters formed on Al 1100 implanted with 60 kV 1.7 x 10^{16} W ions/cm^2 (1750 x).

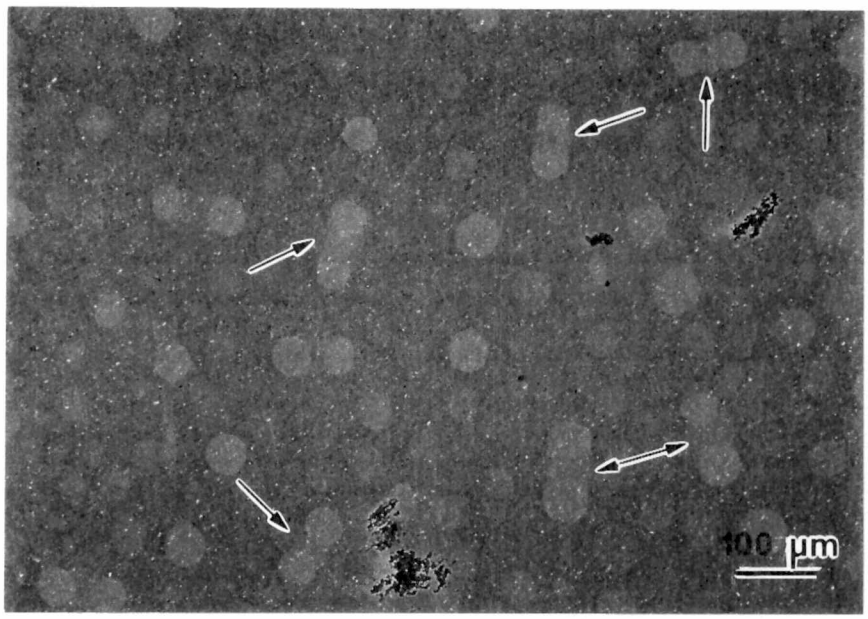

Figure 63. Linear oxide blister stringers formed on Al 1100 implanted with 60 kV 1.7 x 10^{16} W ions/cm^2 (113 x).

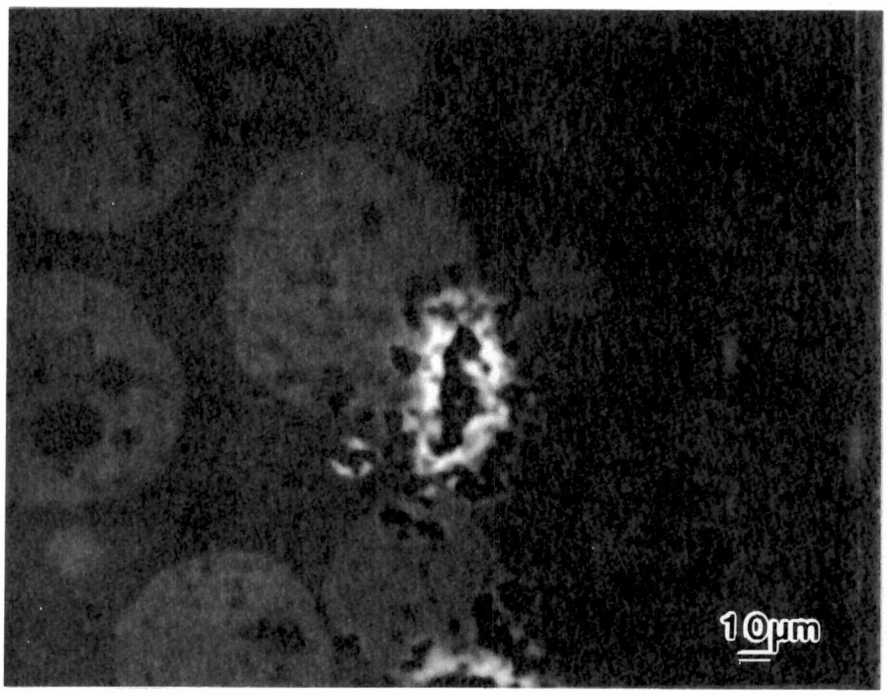

Figure 64. Pitting nucleated at a blister periphery of Al 1100 - 60 kV 7.0 x 10^{16} W ions/cm^2 (400 x).

Pictured in Figure 64 is an Al 1100 - 7.0 x 10^{16} W sample in which a pit has grown laterally away from a blistered region, although the nucleation site seems to be centered at the blister periphery. This is the most likely region for an oxide blister rupture and the ensuing pit formation since it is the region of highest stress. This blister / pit arrangement is seen after anodic polarization in the chloride environment of alloys which exhibit elevated pitting potentials. Figure 65 shows the edge of a very large pit that propagated away from the blistered region, but also partially tunneled into the underlying metal. The circumference of the blistered anodic film can still be seen between the indicated points. Large blisters were ubiquitous on this highly pit resistant specimen, with their surface area covering the majority of the exposed region (Fig 66).

Anodic polarization tests in aerated 1 wt. % NaCl were also performed. Al 1100 pits spontaneously in the aerated chloride solution. However, a moderate passive region featuring an extremely low passive current density (0.02 - 0.04 $\mu A / cm^2$) is imparted by W implantation, as seen in Figure 67. The pitting potential is increased by 130 mV relative to an E_{corr} of -410 mV (SHE). Again, the resistance to propagation of nucleated pits is enhanced by the implanted tungsten, as seen in the delay in reaching i_{1000} after surpassing the pitting potential. The pitting morphology, however, contrasts with the blister formation seen in the

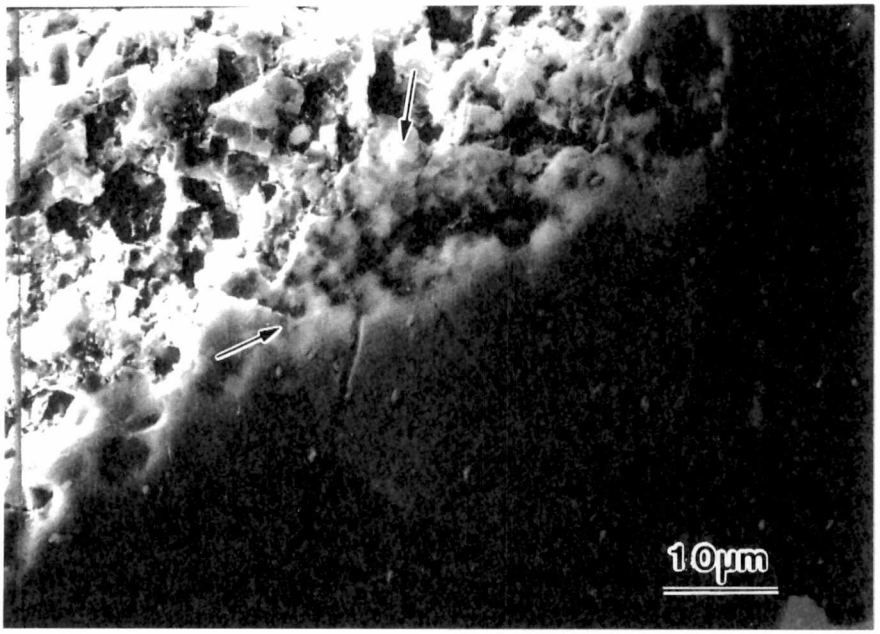

Figure 65. Oxide blister exhibiting underlying pit propagation. Periphery of blister can be seen between indicated points. (Al 1100 - 60 kV 4.9 x 10^{16} W ions/cm^2) (1500 x).

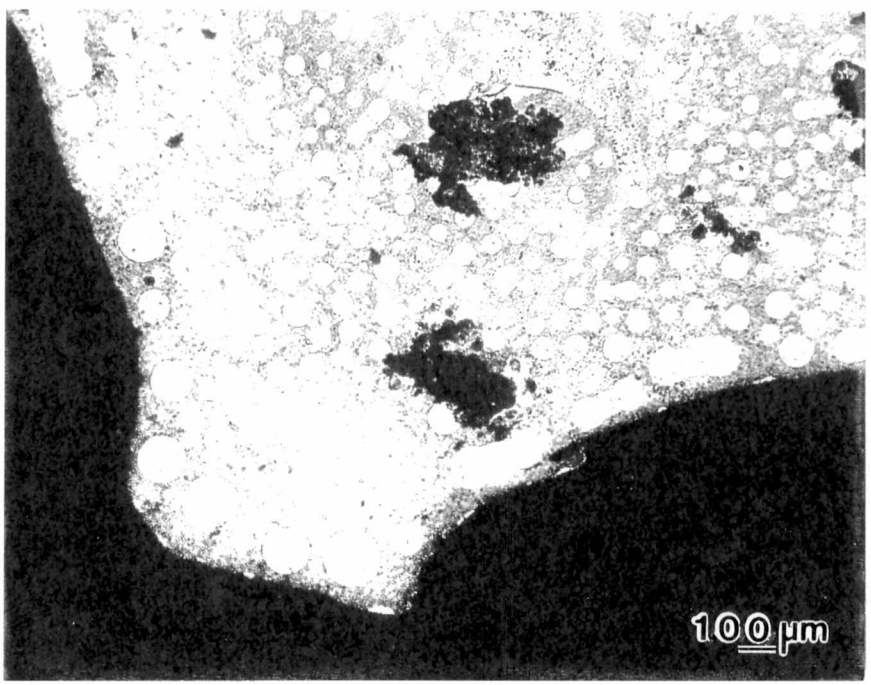

Figure 66. Blisters covering surface of Al 1100 alloy implanted with 60 kV 4.9 x 10^{16} W ions/cm^2 (50 x).

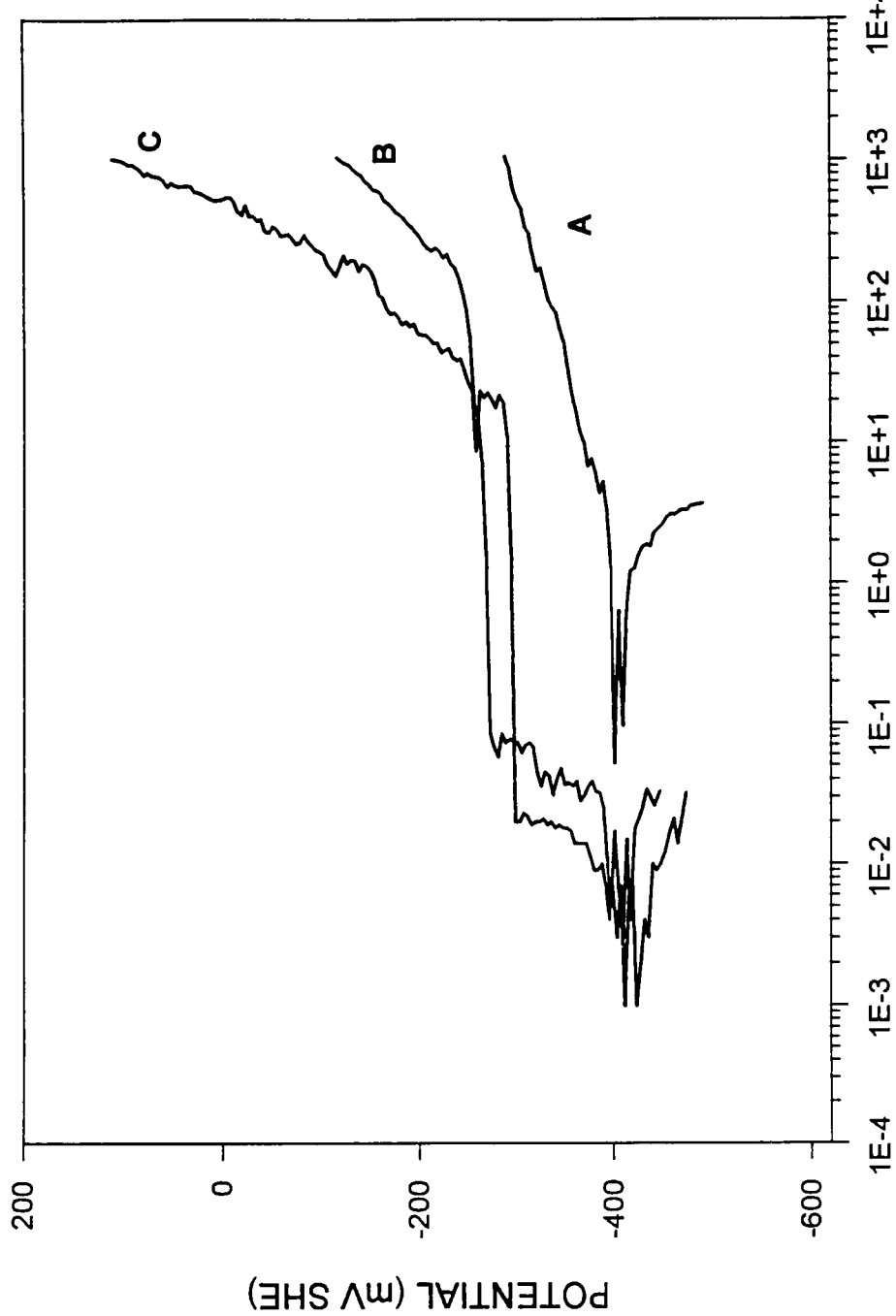

Figure 67. Anodic polarization in aerated 1 wt% NaCl of (A) Al 1100, (B) Al 1100 - 60 kV 3.1×10^{16} W ions/cm^2, and (C) Al 1100 - 60 kV 9.0×10^{16} W ions/cm^2.

deaerated condition. As shown in Figures 68 and 69, no blisters form in the oxide and the pitting is crystallographic. This generally occurs during the dissolution of aluminum at low pitting current densities and low applied potentials (2), which concurs with the abundant number of large pits that are seen in Figure 68.

A limited number of implantations also were applied to high purity (99.9999%) Al in the deaerated condition, with similar results. While the unimplanted material pits readily at E_{corr}, the W addition purveys an extensive passive region (345 mV) with a moderate increase in pitting potential (141 mV) (Fig. 70). Blisters cover the exposed surface after polarization (Fig. 71), but their relationship to the pitting sites remained unclear.

Immersion / Potentiostatic Testing

Confirmation of the anodic polarization results was sought through application of potentiostatic and conventional immersion techniques. One accelerated test of a material's corrosion resistance involves placing the working electrode under potentiostatic control a fixed number of mV above the corrosion potential. The resulting current density is monitored as a function of time, allowing for direct comparison of the corrosion response of different materials to the solution.

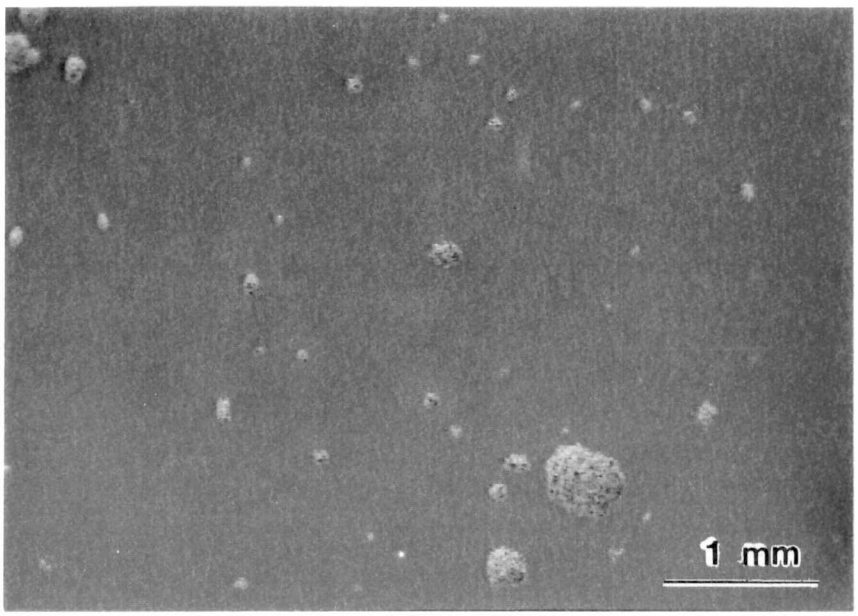

Figure 68. Pitting on the surface of Al 1100 implanted with 60 kV 3.1 x 10^{16} W ions/cm^2, anodically polarized in aerated 1 wt% NaCl (21 x).

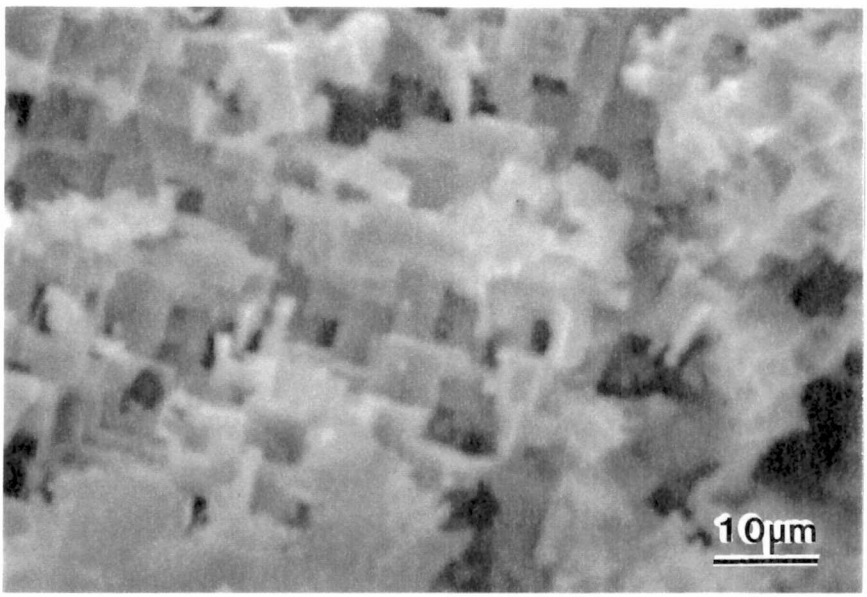

Figure 69. Crystallographic attack within pits on the surface of Al 1100 implanted with 60 kV 3.1 x 10^{16} W ions/cm^2, anodically polarized in aerated 1 wt% NaCl (1470 x).

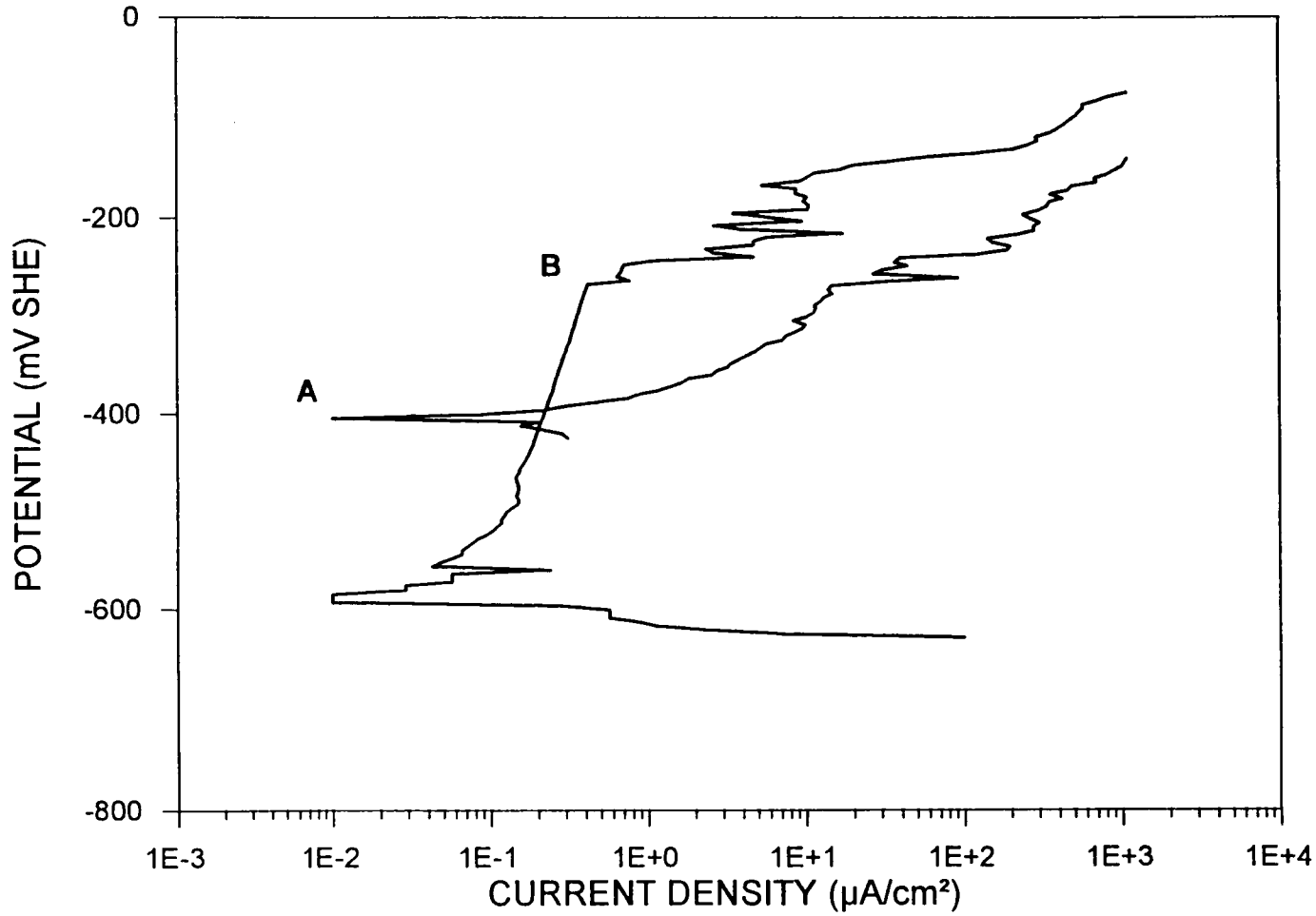

Figure 70. Anodic polarization in deaerated 1 wt% NaCl of (A) 99.9999% Al (B) 99.9999% Al implanted with 60 kV 6.4 x 10^{16} W ions/cm^2.

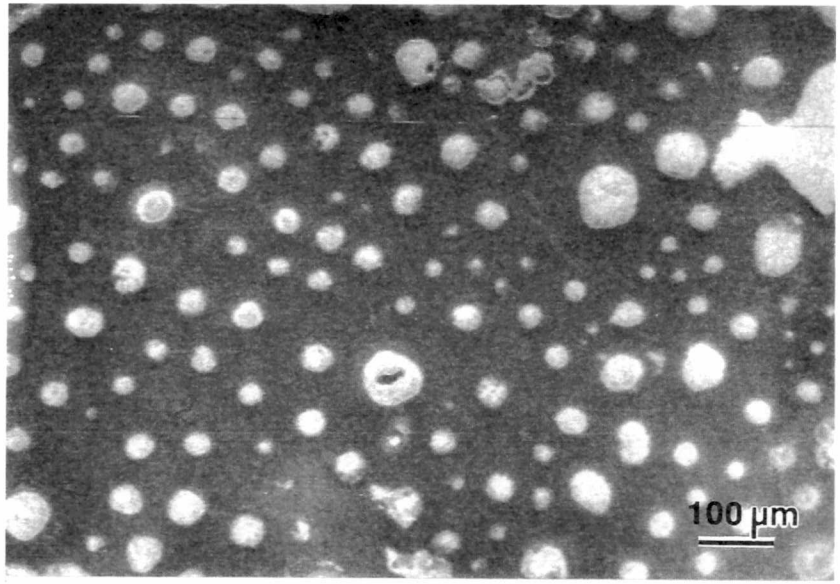

Figure 71. Oxide blisters formed on 99.9999 % Al implanted with 60 kV 6.4 x 10^{16} W ions/cm^2 during anodic polarization (100 x).

Implanted and control specimens were each held +50 mV above E_{corr} in aerated 1 wt. % NaCl. As seen in Figure 72, the unimplanted Al 1100 alloy exhibits an incubation time of 1100 seconds prior to pit nucleation, signified by the change in slope (di / dt) at this time value. This point is interpreted as the transition from a quasi-stable passive current to an accelerating pitting current. This behavior is typical of a material with minimal inherent resistance to pitting. Figure 73 reveals the response of an Al 1100 alloy implanted with 60 kV 4.1 x 10^{16} W ions / cm^2 to the same test. Although the implanted specimen does not produce a low, steady current density indicative of passivity for an extended period, it does exhibit a large capacity for inhibiting pit growth. The rate of pitting current density increase is lowered by more than an order of magnitude after implantation:

$$(di / dt)_{control} = 0.21\ \mu A / cm^2 / s$$

$$(di / dt)_{implant} = 0.01\ \mu A / cm^2 / s$$

An alternate method for monitoring the development of localized corrosion is to observe the E_{corr} fluctuations of a freely corroding sample during a long term immersion experiment. A trace of the corrosion potential of an Al 1100 implant (5.5 x 10^{16} W) and a corresponding control during an immersion test in aerated 3.5 wt. % NaCl (Fig. 74) shows that, after approximately 45 hours in solution,

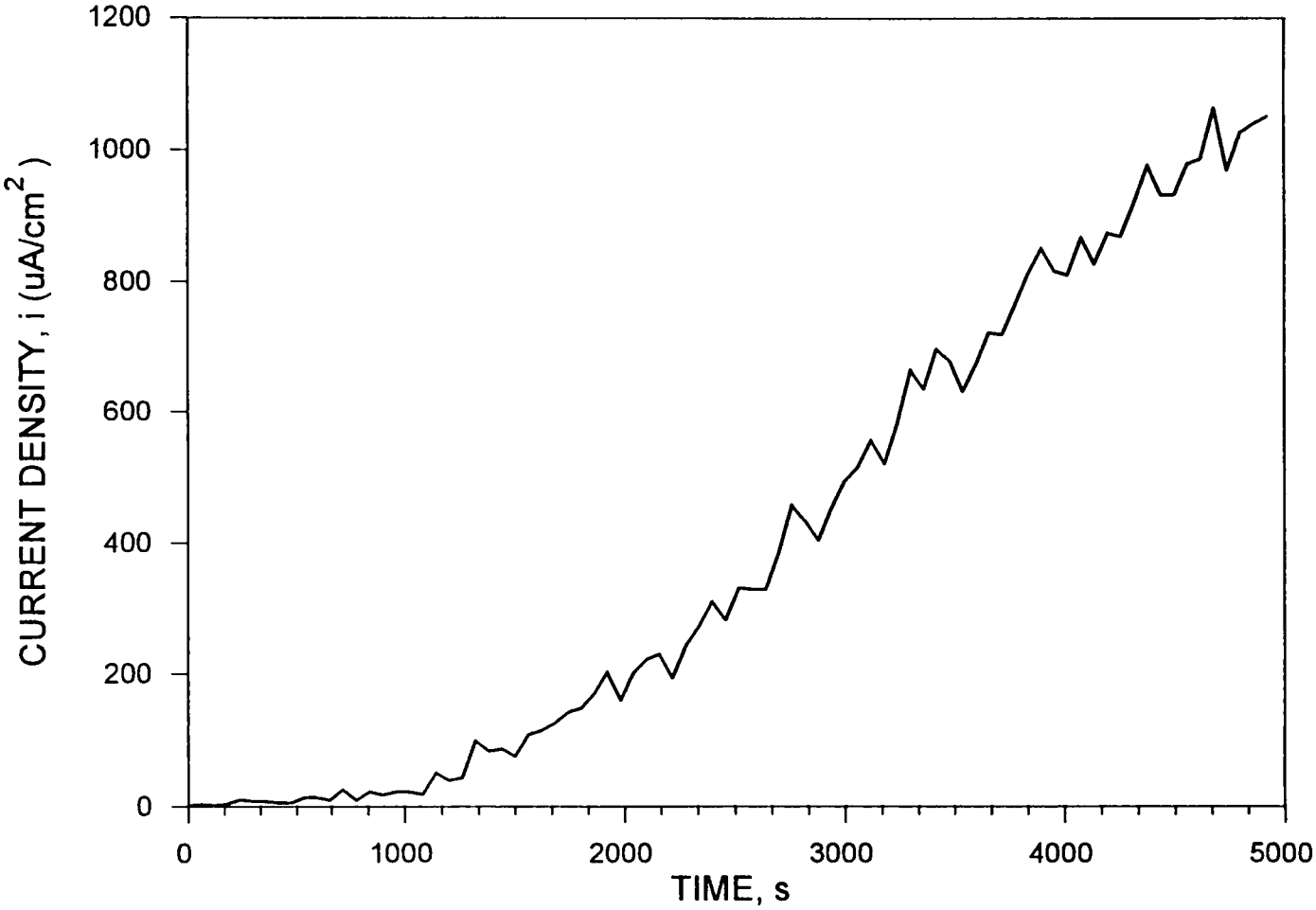

Figure 72. Al 1100, potentiostatically held 50 mV above E_{corr} in aerated 1 wt% NaCl.

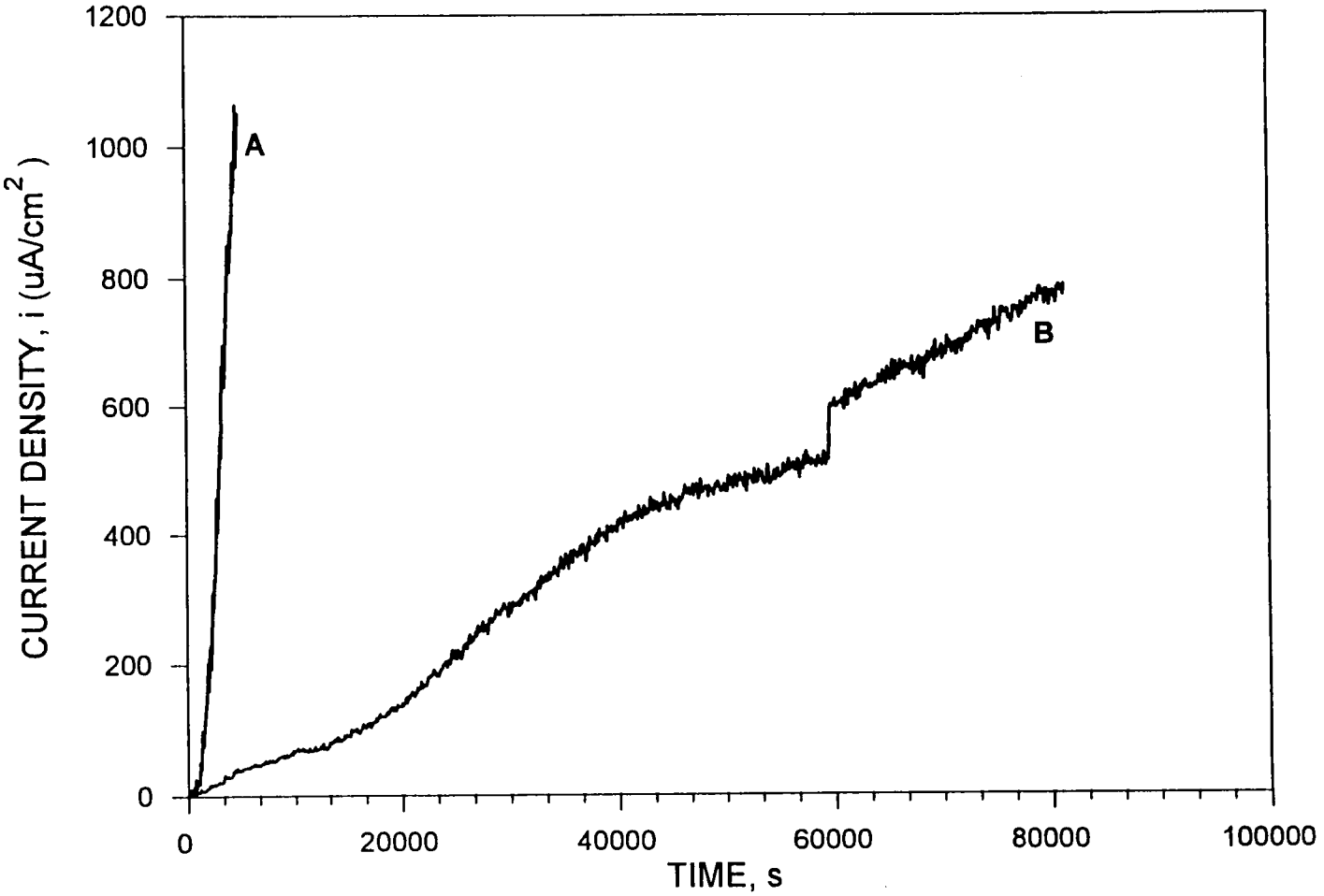

Figure 73. (A) Al 1100 and (B) Al 1100 - 60 kV 4.1 x 10^{16} W ions/cm^2, potentiostatically held 50 mV above E_{corr} in aerated 1 wt% NaCl.

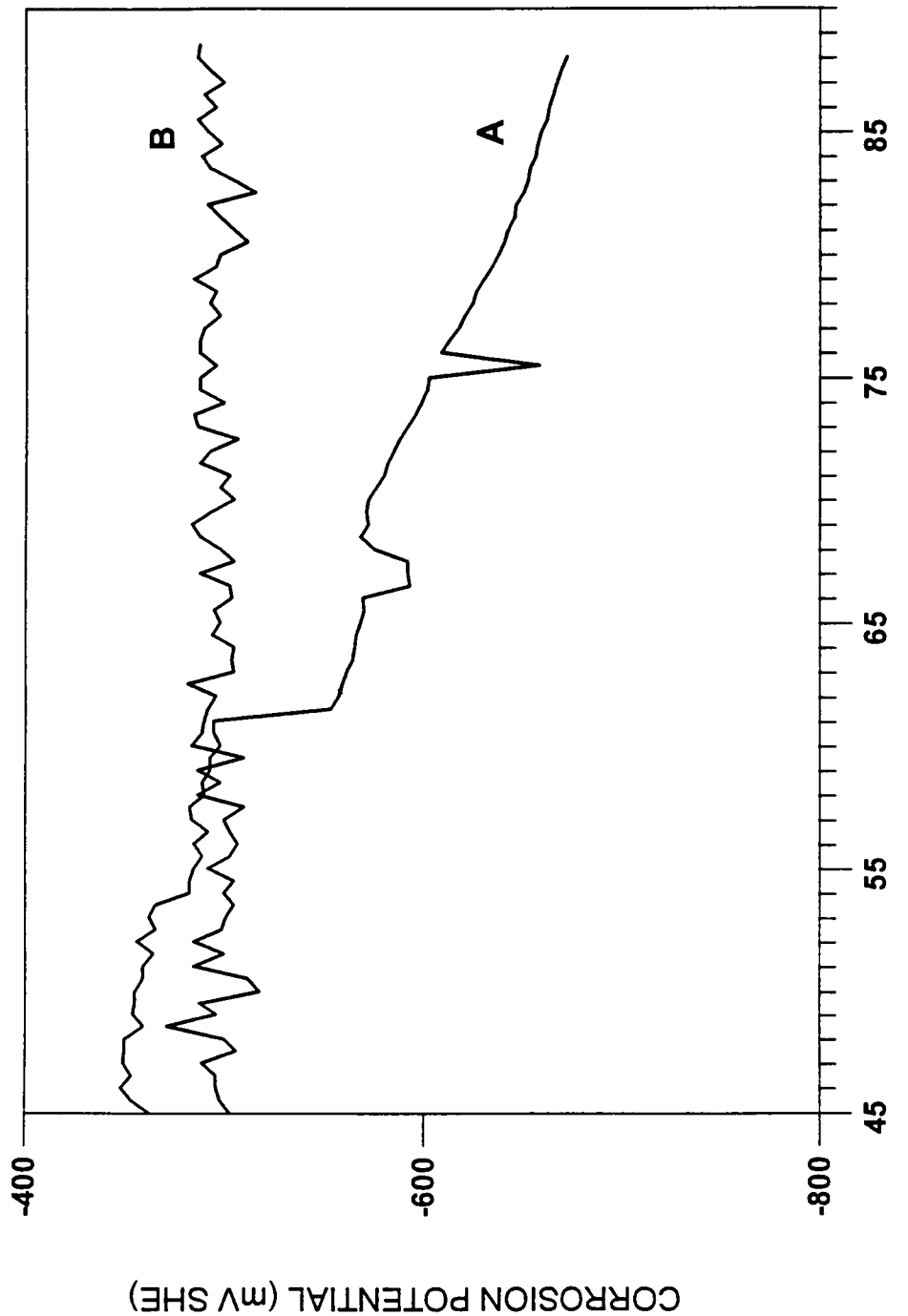

Figure 74. Corrosion potentials of (A) Al 1100 and (B) Al 1100 - 60 kV 5.5 x 10^{16} W ions/cm^2, immersed in aerated 3.5 wt% NaCl.

the unimplanted specimen displays a continuous drop in potential. Upon commencement of pitting, the surface consists of both active and passive areas; and as shown schematically in Figure 75, the surface potential should drop to some mixed potential between the passive and active states. This indicates that, for the unimplanted material, the majority of the corrosion current is being produced within active pitting sites after 45 hours of immersion. The W-implant exhibits a relatively steady E_{corr} value for the duration of the test. This is indicative of a relatively small proportion of the corrosion current arising from active pits, a fact verified by the small number and size of pits present on the exposed surface relative to the control. This procedure was repeated with two tungsten ion implanted Al 1100 specimens (4.5×10^{16} and 9×10^{16} W @ 60 kV) and one control. Again, each implanted sample demonstrated a relatively stable E_{corr} value for the duration of the test (Fig. 76), which in this case was extended to 280 hours of immersion. This stability in potential is in sharp contrast with the control, which again shows a continuous potential drop. In this case, pitting is delayed until after approximately 160 hours of immersion. Results of immersion testing supported the evidence gathered from anodic polarization that the implanted W ions act to delay pit propagation.

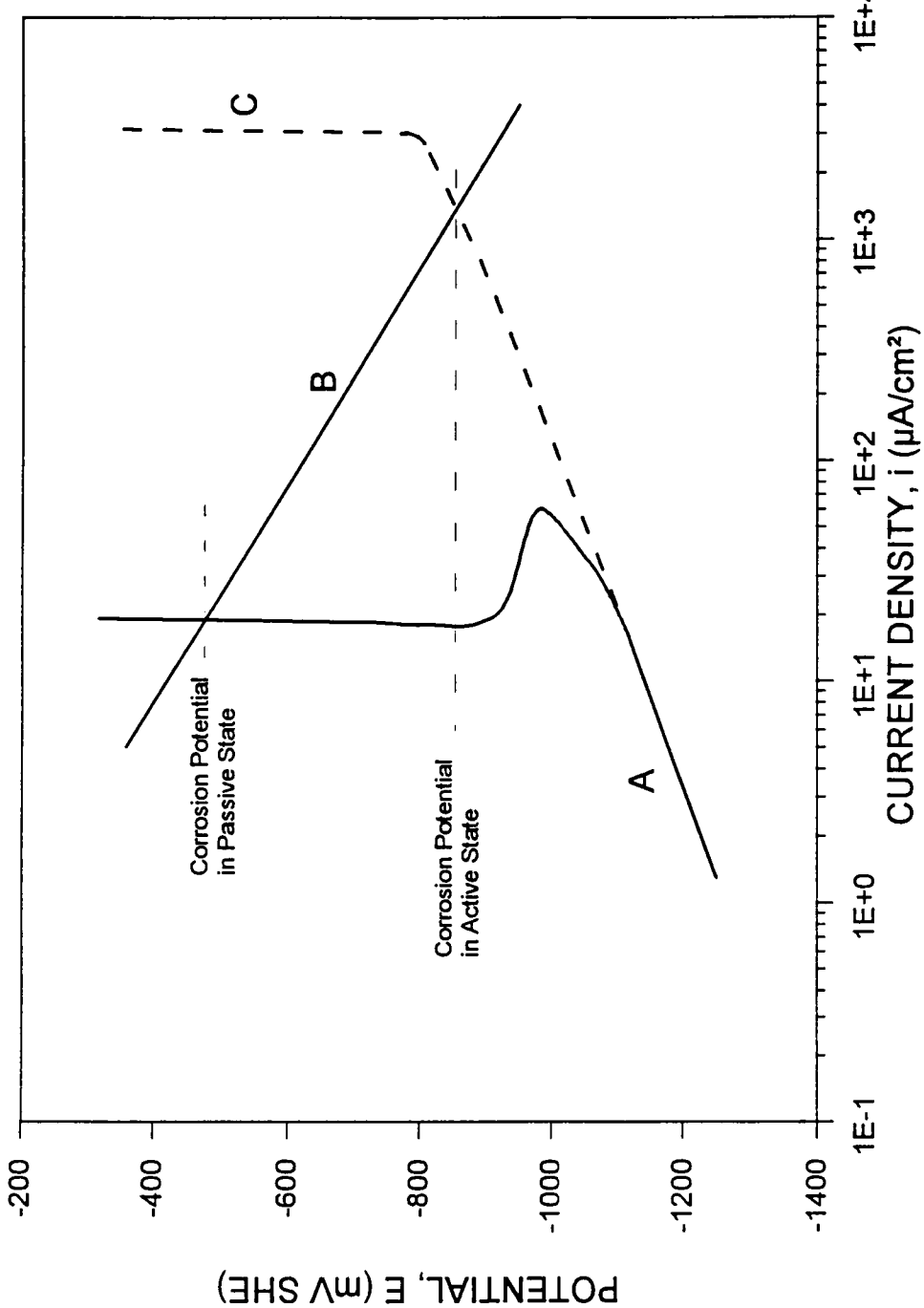

Figure 75. Schematic illustration of the decrease in corrosion potential with the onset of pitting. (A - passive anodic curve, B - cathodic curve, C - active anodic curve)

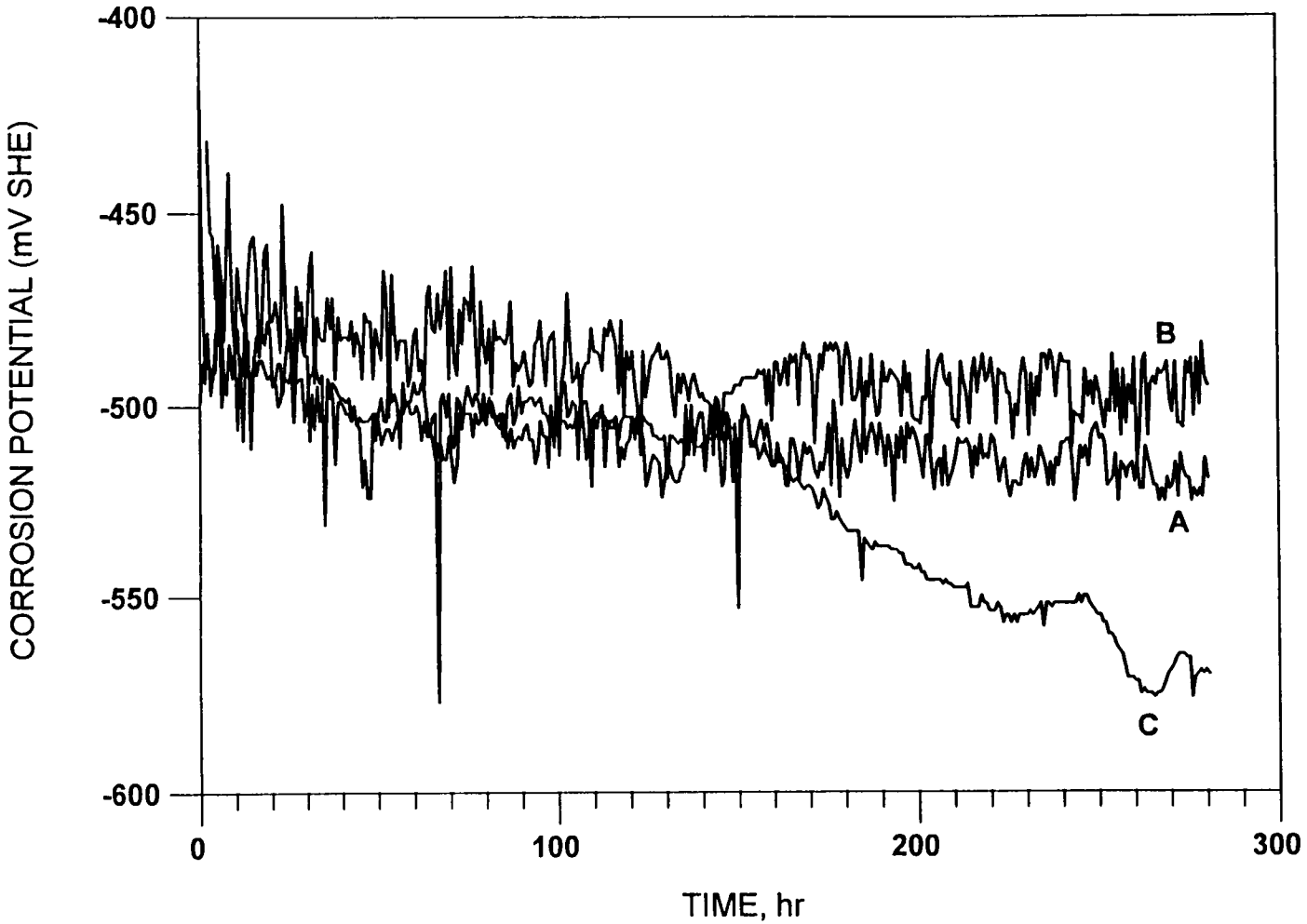

Figure 76. Corrosion potentials of (A) Al 1100 - 60 kV 9.0 x 10^{16} W ions/cm^2, (B) Al 1100 - 60 kV 4.5 x 10^{16} W ions/cm^2, and (C) Al 1100, immersed in aerated 3.5 wt% NaCl.

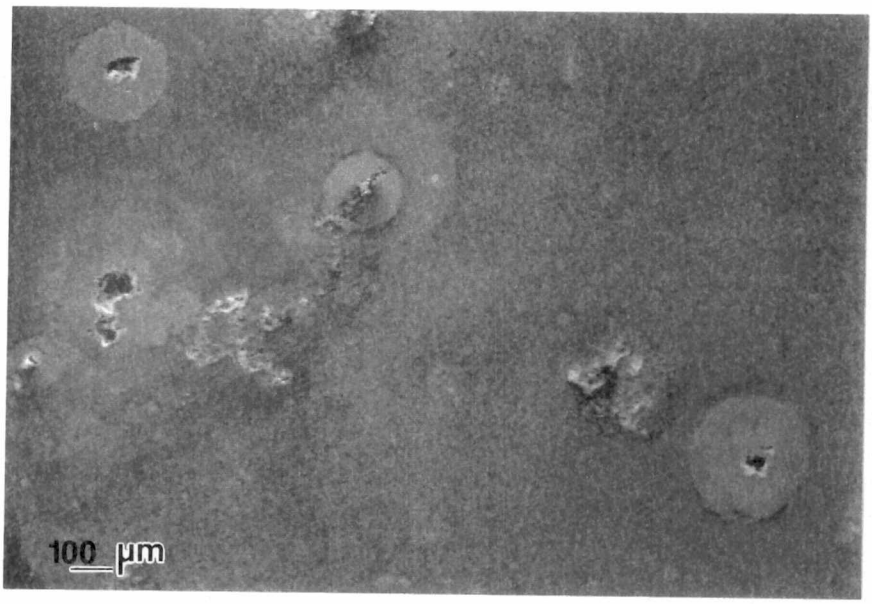

Figure 77. Large oxide blisters formed on Al 1100 - 60 kV 5.4 x 10^{16} W ions/cm^2 during immersion in aerated 3.5 wt% NaCl (52 x).

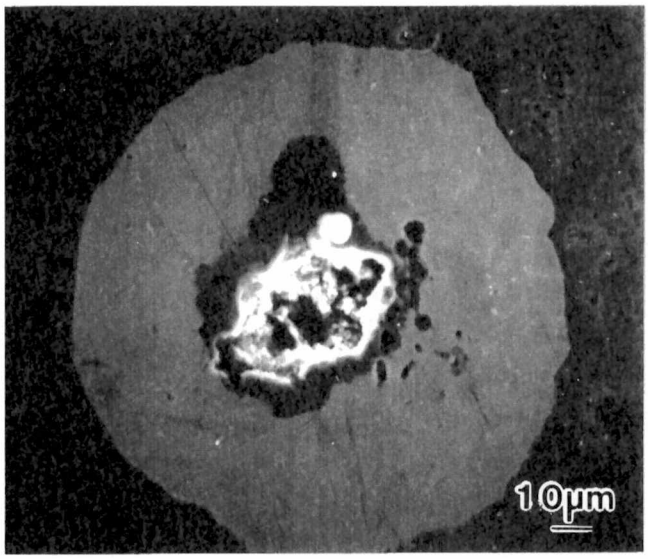

Figure 78. Pitting nucleated beneath blister center on Al 1100 - 60 kV 5.4 x 10^{16} W ions/cm^2 during immersion in aerated 3.5 wt% NaCl (400 x).

Blisters formed during immersion in the aerated 1 wt. % NaCl solution are shown in Figure 77. This is the first microstructural evidence presented of Al oxide blistering during an unaccelerated (non-potentiostatically controlled) immersion test. This spontaneous blister formation bolsters the speculation that their formation may be a normal precursor to Al pitting, and not an artifact of the anodic polarization process. The location of the pit nucleation sites that formed during immersion (Fig. 78), in contrast with anodic polarization results, was in the center of the broken blisters. Figure 79 shows an example of a blister containing large cracks and fractured oxide blocking an opening in the film. Edge ruptures have previously been associated with anodized films (74), while center ruptures have been seen on ion-implanted surfaces (48), both under anodic polarization. The blisters also grew to a much larger diameter (up to 250 μm) during the long term immersion in the electrolyte than was seen during the rapid polarization test (20-50 μm).

The development of large, unruptured blisters on unimplanted Al 1100 during immersion during the extended 280 hour test is shown in Figure 80. A large number of small pits covered the specimen, as shown in Figures 81 and 82. However, as with the low W dose anodically polarized samples, the pits were not associated with the blisters but with the secondary $FeAl_3$ particles. This test

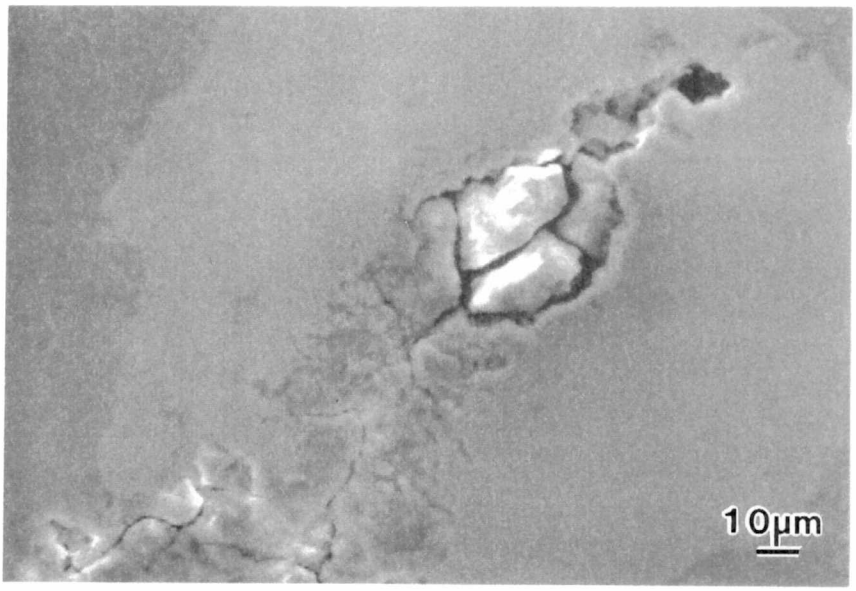

Figure 79. Fractured oxide blocking blister opening formed on Al 1100 - 60 kV 5.4 x 10^{16} W ions/cm^2 during immersion in aerated 3.5 wt% NaCl (491 x).

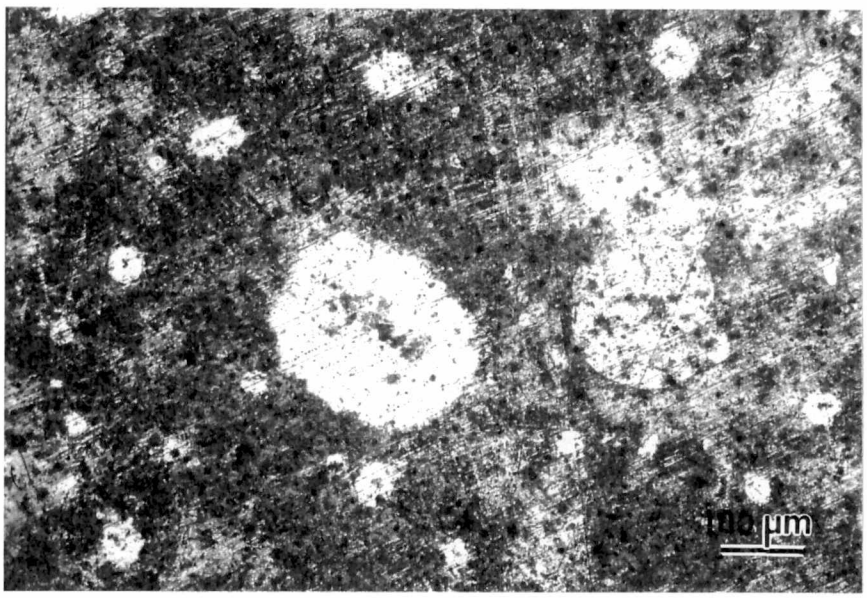

Figure 80. Oxide blisters formed on unimplanted Al 1100 during immersion in aerated 3.5 wt% NaCl (100 x).

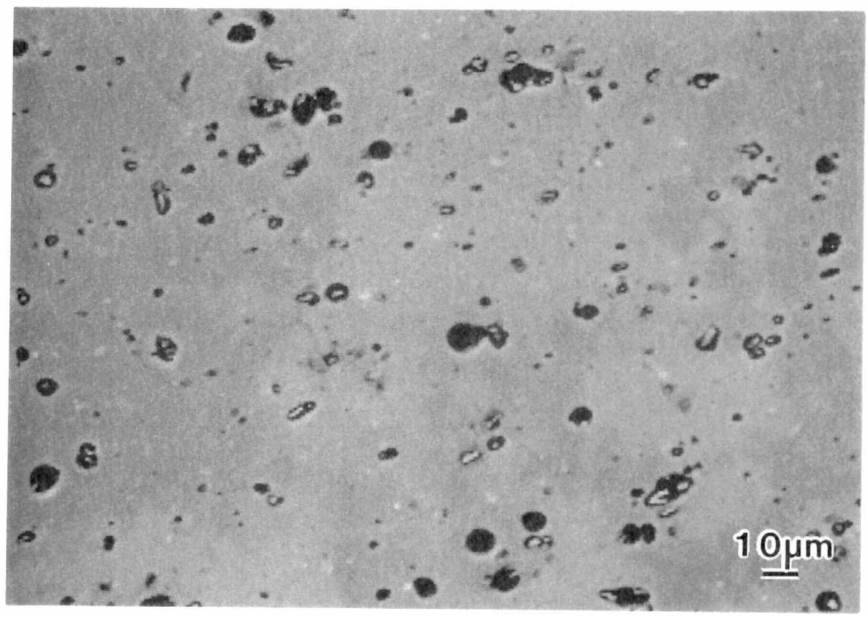

Figure 81. Pitting formed on Al 1100 during immersion in aerated 3.5 wt% NaCl (509 x).

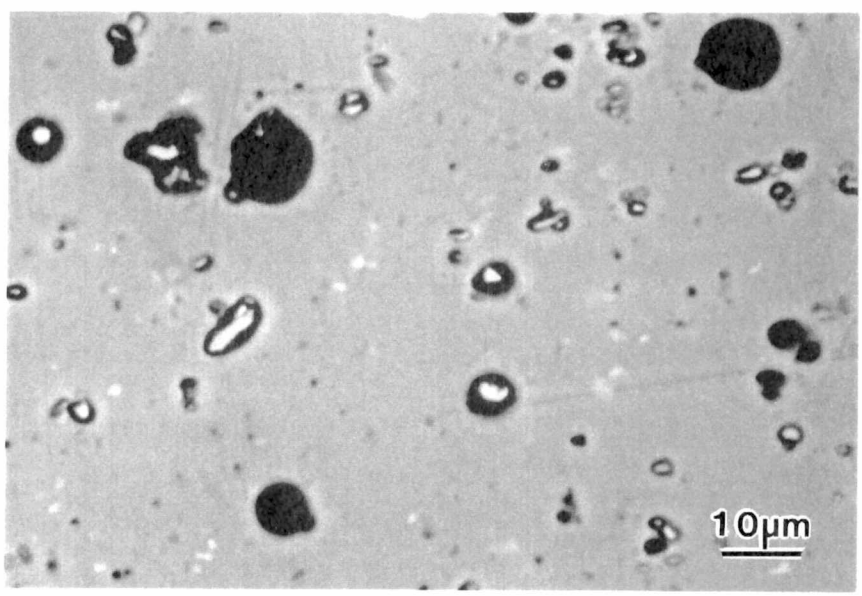

Figure 82. Pitting formed around secondary $FeAl_3$ particles on Al 1100 during immersion in aerated 3.5 wt% NaCl(1000 x).

result validates the hypothesis of Bargeron and Givens concerning the possibility of blister formation on non-anodized Al films in Cl^- environments (74).

While only a few large blisters with associated pits formed on the tungsten implanted surfaces during immersion, a greater number of very small diameter (1 - 10 μm) blisters were generated (Fig. 83), each showing extensive cracking. The significance of these minute regions is that the cracked oxide would have led to underlying metal dissolution and extensive pitting in the absence of a repassivating corrosion product which formed on the tungsten implanted alloys. When removed from the chloride solution, the specimen surface was covered with the thick corrosion product (Fig. 84) determined by EDS to contain primarily Al, with no discernible W present (Fig. 85). As expected, a great deal of chloride is also present, along with a trace amount of silicon, a common impurity in Al alloys. This product did not form on the unimplanted material in the same test. It presumably precipitates from the solution on the implanted material. The small size and number of pits, along with the electrochemical data, indicated that this precipitate acts to repassivate the broken blisters and slow pitting significantly. Both this micrograph and those of the larger blisters were taken after the removal of the precipitate by swabbing the surface gently with methanol.

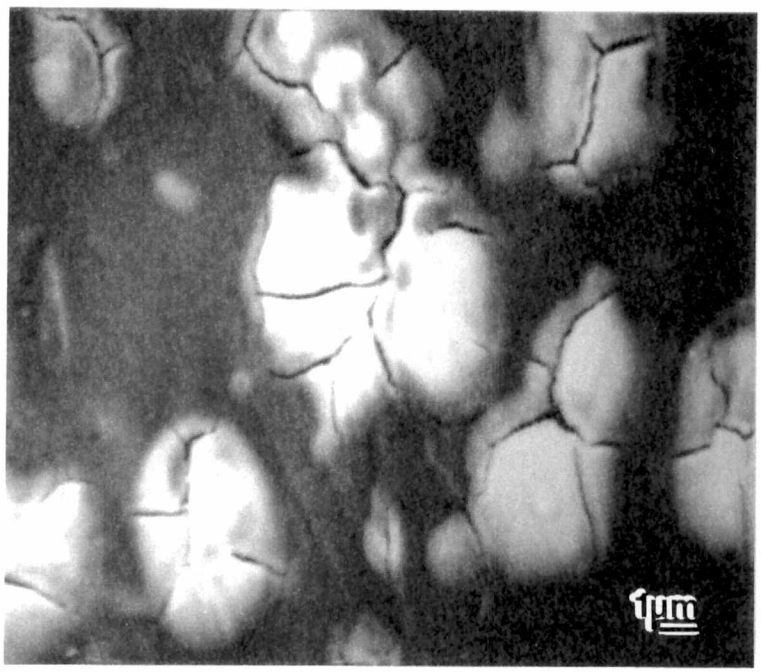

Figure 83. Minute blistering formed beneath corrosion product on Al 1100 implanted with 60 kV 5.4 x 10^{16} W ions/cm^2 during immersion in aerated 3.5 wt% NaCl (5000 x).

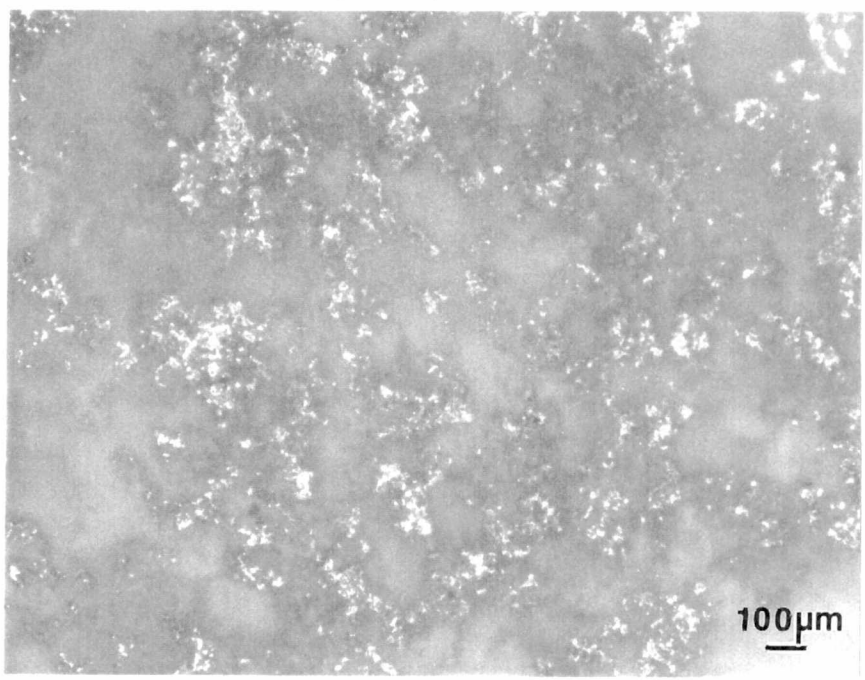

Figure 84. Aluminum oxide corrosion product precipitated on the surface of Al 1100 implanted with 60 kV 5.4 x 10^{16} W ions/cm^2 during immersion in aerated 3.5 wt% NaCl (50 x).

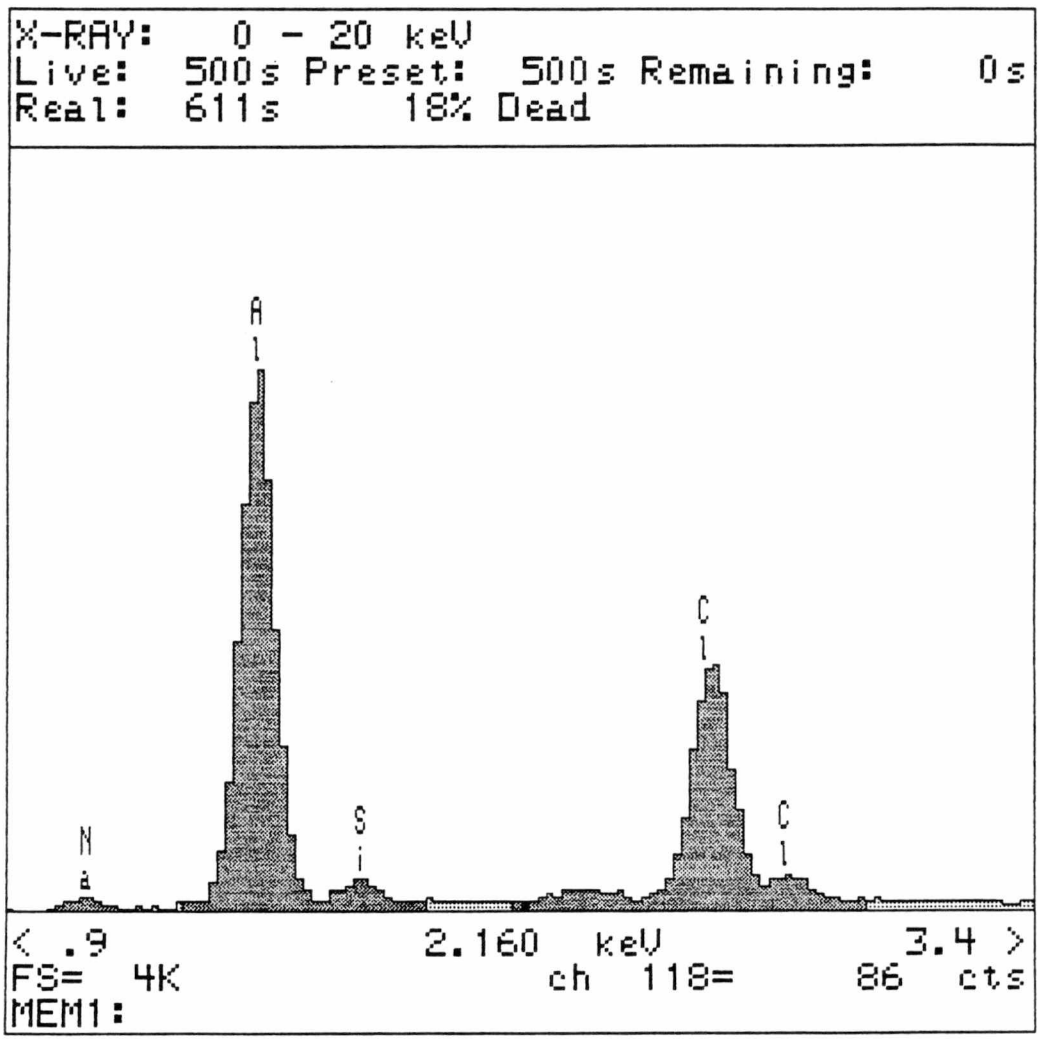

Figure 85. EDS spectrum of corrosion product formed on the surface of Al 1100 implanted with 60 kV 5.4 x 10^{16} W ions/cm^2 during immersion in aerated 3.5 wt% NaCl.

Additional experimental work was undertaken in an attempt to understand the role of the tungsten species once it enters the chloride solution. Tungstate ions (WO_4^{2-}) previously have been utilized to inhibit the accelerated dissolution of aluminum (76,77), including inhibition in aggressive Cl^- environments (104). Our investigations indicated that an extended range of passivity and a higher pitting potential can be achieved in deaerated 1 wt. % NaCl with additions of 0.2 - 2.0 w/o Na_2WO_4 [0.0068 - 0.068 M] to the electrolyte (Fig. 86). A precipitate film similar to that seen on the W-ion-implanted immersion specimens formed around pitted areas. Anodic polarization of a platinum surface in the same electrolyte did not result in any precipitation. As noted previously, EDS results from the W-implanted specimens showed the corrosion product to be almost solely Al-based, indicating that the W species catalyzes the formation of an aluminum oxide precipitate. An RBS analysis (79) of aluminum oxide formation indicated that precipitate films formed in tungstate solutions are initially composed of tungstate, but after a short exposure time, unimpeded growth of aluminum-hydrate begins. Therefore, during immersion, the implanted W not only promotes blister formation, but during dissolution the tungsten species in solution works to repassivate the corroding surface by an Al precipitation reaction. Anodic polarization of W-implanted specimens showed no visual evidence of such a reaction, possibly due to the accelerated nature of these tests

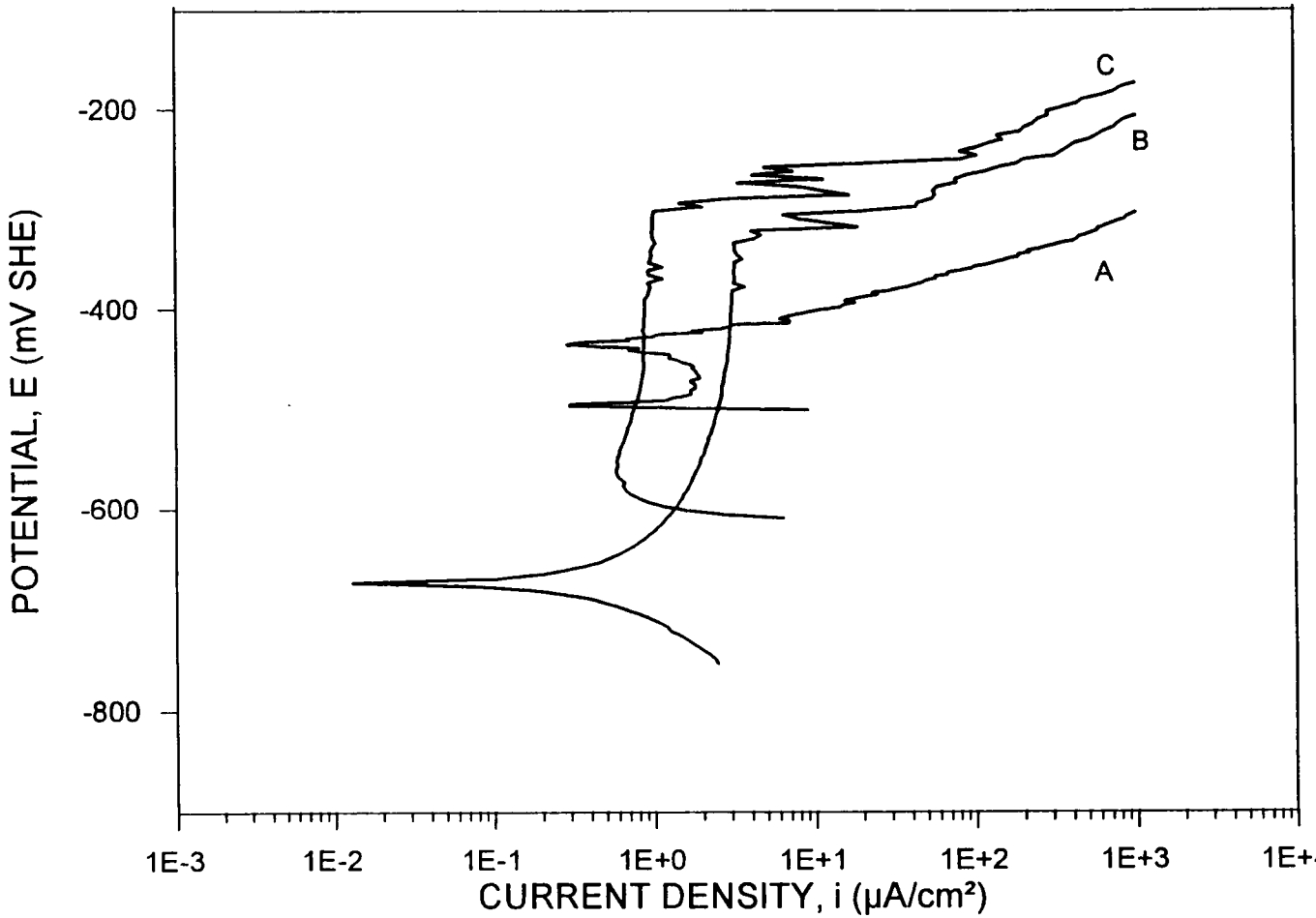

Figure 86. Anodic polarization of Al 1100 in deaerated (A) 1 wt% NaCl, (B) 1 wt% NaCl and 2.0 wt% Na_2WO_4, and (C) 1 wt% NaCl and 0.2 wt% Na_2WO_4.

or to the difference in aeration between the two experimental conditions (immersion aerated, polarization deaerated). However, electrochemical data does indicate a significant increase in resistance to pit propagation as evidenced by the delay in reaching E_{1000} after exceeding E_p (Figs. 58, 67).

Despite the variety of material and solution conditions (Table 5) utilized during electrochemical testing, the pitting resistance of Al 1100 is enhanced by W implantation. As seen in Figure 87, under all experimental conditions the alloy's range of passivity is expanded, but to varying degrees. Results of previous testing (74) showed that during blister formation, i_{pass} gradually increased from 0.03 to 1.0 $\mu A / cm^2$, while after rupture the pitting current density was greater than 100 $\mu A / cm^2$. Similar current densities were seen in the current work.

Proposed mechanisms (70,72) for the passivity of the W-Al thin films center around the stability of the tungsten oxide in the low pH environment of an active pit. This may be an alternative explanation for the sporadic pit growth which occurred during polarization testing of W-implanted bulk Al; however, the passivity enhancements are more directly correlated with oxide blistering and precipitate film formation. If indeed the strength and / or ductility of the oxide is

Table 5

Effect of Test Variables on Electrochemical Properties of 60 kV W-implanted Al 1100

Alloy	Aeration	Implanted Dose ions / cm^2	E_{corr} mV SHE	E_p mV SHE	E_{1000} mV SHE	i_{pass} $\mu A / cm^2$
Al 1100	deaerated	-----	-496	-432	-304	2.0
Al 1100	deaerated	4.9×10^{16}	+192	+1806	+2114	20.0
Al 1100	deaerated	5.7×10^{16}	-558	-209	+171	1.0
Al 1100	deaerated	4.5×10^{16}	-472	-180	+250	0.5
99.9999 % Al	deaerated	-----	-405	-405	-149	-----
99.9999 % Al	deaerated	6.4×10^{16}	-589	-244	-76	0.3
Al 1100	aerated	-----	-410	-410	-290	-----
Al 1100	aerated	3.1×10^{16}	-410	-270	-118	0.04
Al 1100	aerated	9.0×10^{16}	-412	-292	+104	0.02

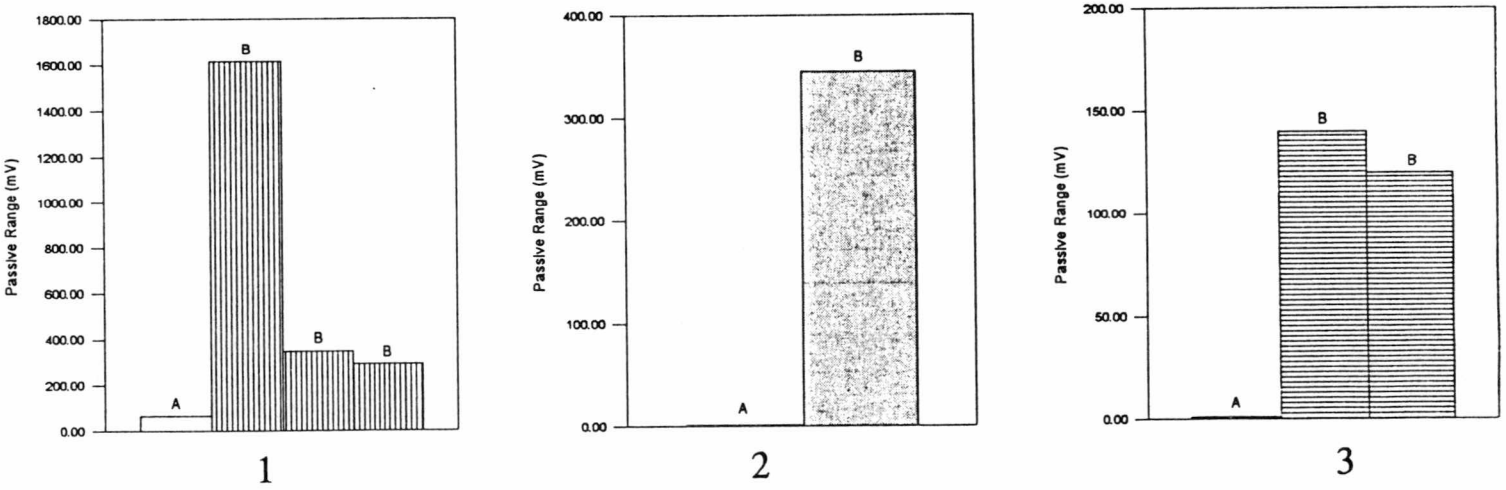

Figure 87. Extent of passive region for (1) Al 1100, deaerated, (2) 99.9999% Al, deaerated, and (3) Al 1100, aerated [(A) unimplanted, (B) W implanted].

enhanced by the implanted species, its access to available ions, as determined by the W dose and distribution, would determine the degree of improved passivity.

Microhardness Testing

Microhardness measurements were performed using a LECO M-400-G1 hardness tester with a Vickers indenter and a 25 g load. As shown in Figure 88, the hardness of Al 1100 does not increase with tungsten content. However, this can be attributed to the shallow implantation depth in comparison to the depth of the hardness impression. While all W doses were restricted to within 1000 angstroms of the surface, the indenter penetrates several orders of magnitude deeper into the material, even with a light load of 25 g. Therefore, it is unlikely that the thin implanted layer can affect the microhardness reading to a significant degree, and no conclusion can be drawn as to the effect of tungsten implantation on the hardness of Al 1100.

Auger Electron Spectroscopy / Atomic Force Microscopy Testing

The Auger compositional depth profile of an Al 1100 specimen implanted with 60 kV 9 x 10^{16} W ions / cm^2 is shown in Figure 89. The tungsten peaks at some depth below the surface and decreases to zero concentration after approximately 5 minutes sputtering time. RBS analyses of this and other implanted samples

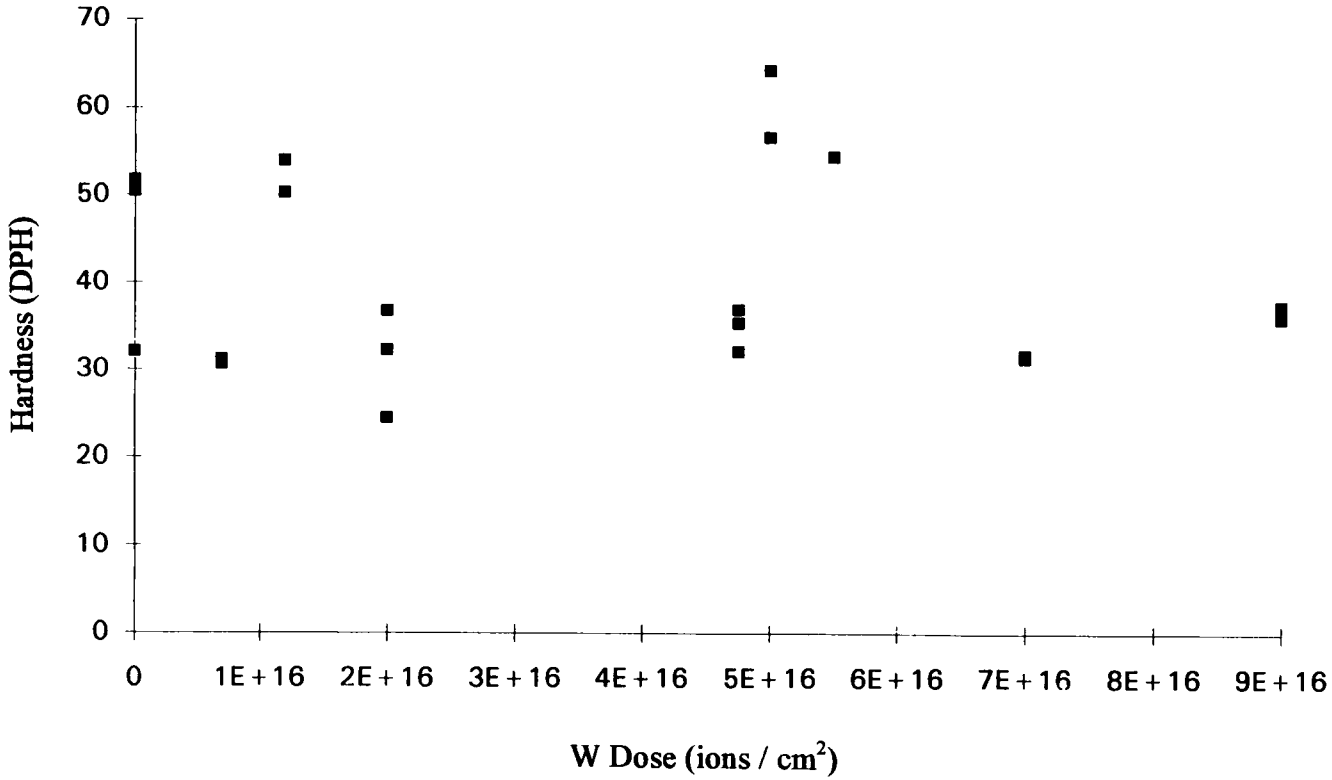

Figure 88. Hardness of Al 1100 as a function of implanted tungsten dose.

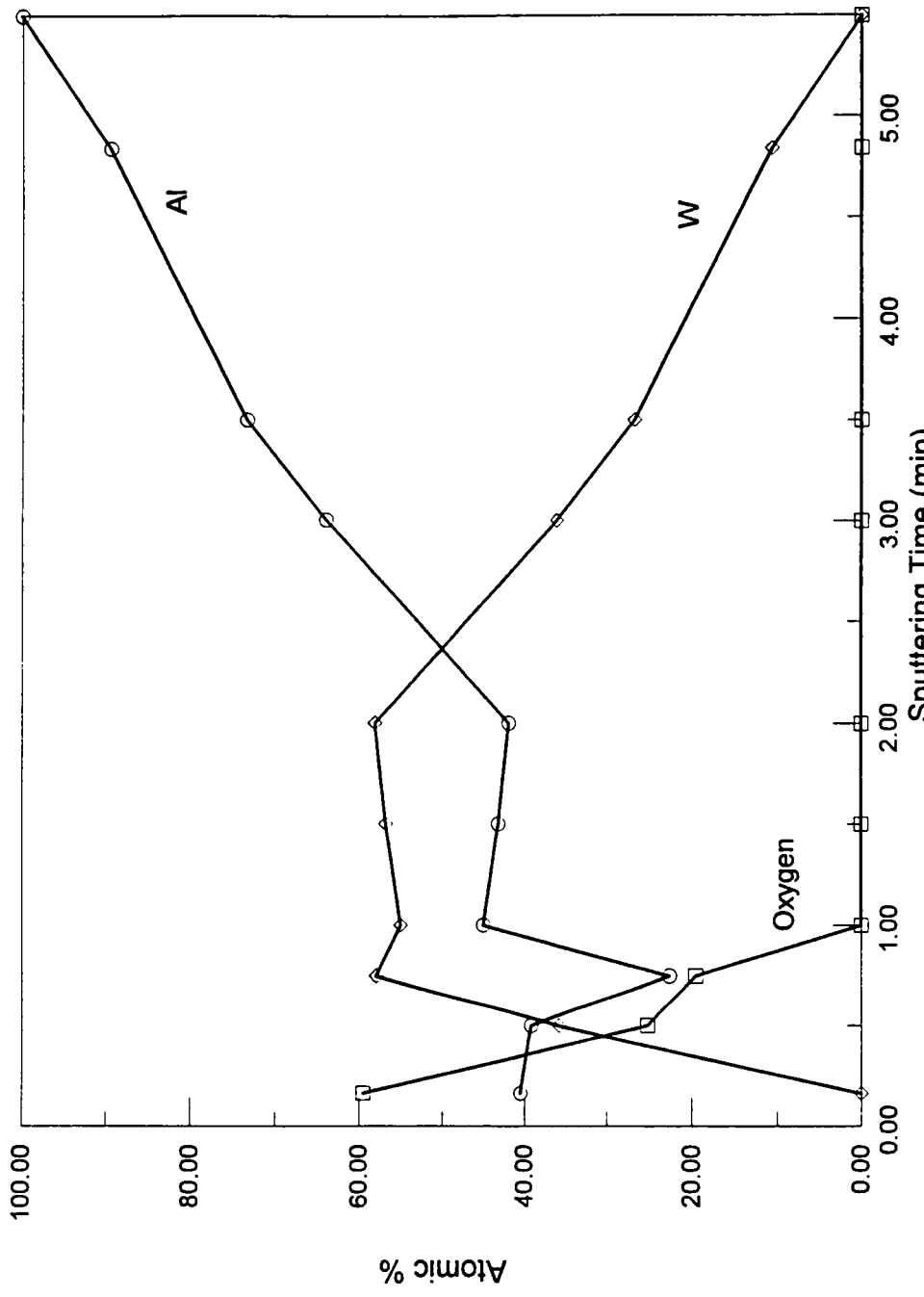

Figure 89. Auger depth profile of Al 1100 implanted with 60 kV 9 x 10^{16} W ions/cm^2.

indicate that the depth of ion penetration is limited to 1000-1100 angstroms, and is not a strong function of dose. One minute of sputtering time is therefore equivalent to the removal of 200 ($\pm$ 30) angstroms of material. The surface of the alloy is 60 atomic percent oxygen and 40 atomic percent aluminum, the exact stoichiometry expected for an air formed Al oxide layer. However, this degree of quantitative accuracy does not apply to the W concentrations detected by the Auger depth profiles. The elemental sensitivity factor, an empirical number by which the raw data is multiplied for each element, is extremely high for tungsten. This can lead to erroneously high detection levels. However, this source of error is constant for all depths on all analyzed samples and semi-quantitative comparisons of W concentration levels are still valid.

Post-anodic polarization Auger analysis was carried out on a 60 kV 4.5 x 10^{16} W implanted Al 1100 surface, which is shown in Figure 90. The depth profile through and under an oxide blister (Fig. 91) was generated from area 1. A representative profile from the non-blistered oxide (Fig. 92), hereafter referred to as the matrix, was taken from area 2. In each of these spectra, the metallic aluminum species could be differentiated from the oxide form by a slight Auger electron energy shift. The oxygen content and the oxidized Al content conform closely in an approximate 3:2 ratio. The metal / oxide interface is taken to be

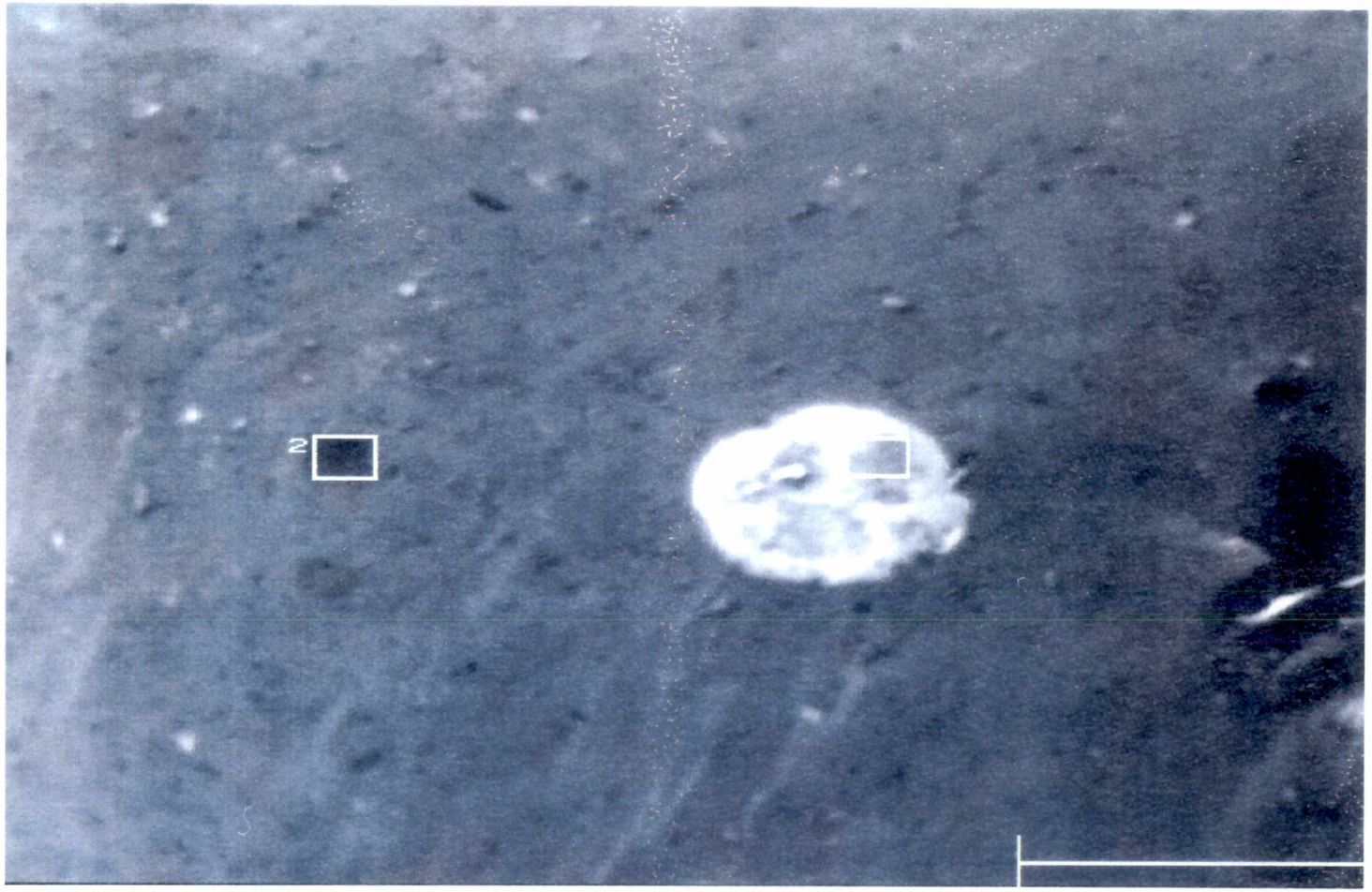

Figure 90. Surface of Al 1100 implanted with 60 kV 4.5 x 10^{16} W ions/cm^2, after anodic polarization in deaerated 1 wt% NaCl. Boxes indicate locations of Auger depth profile generation.

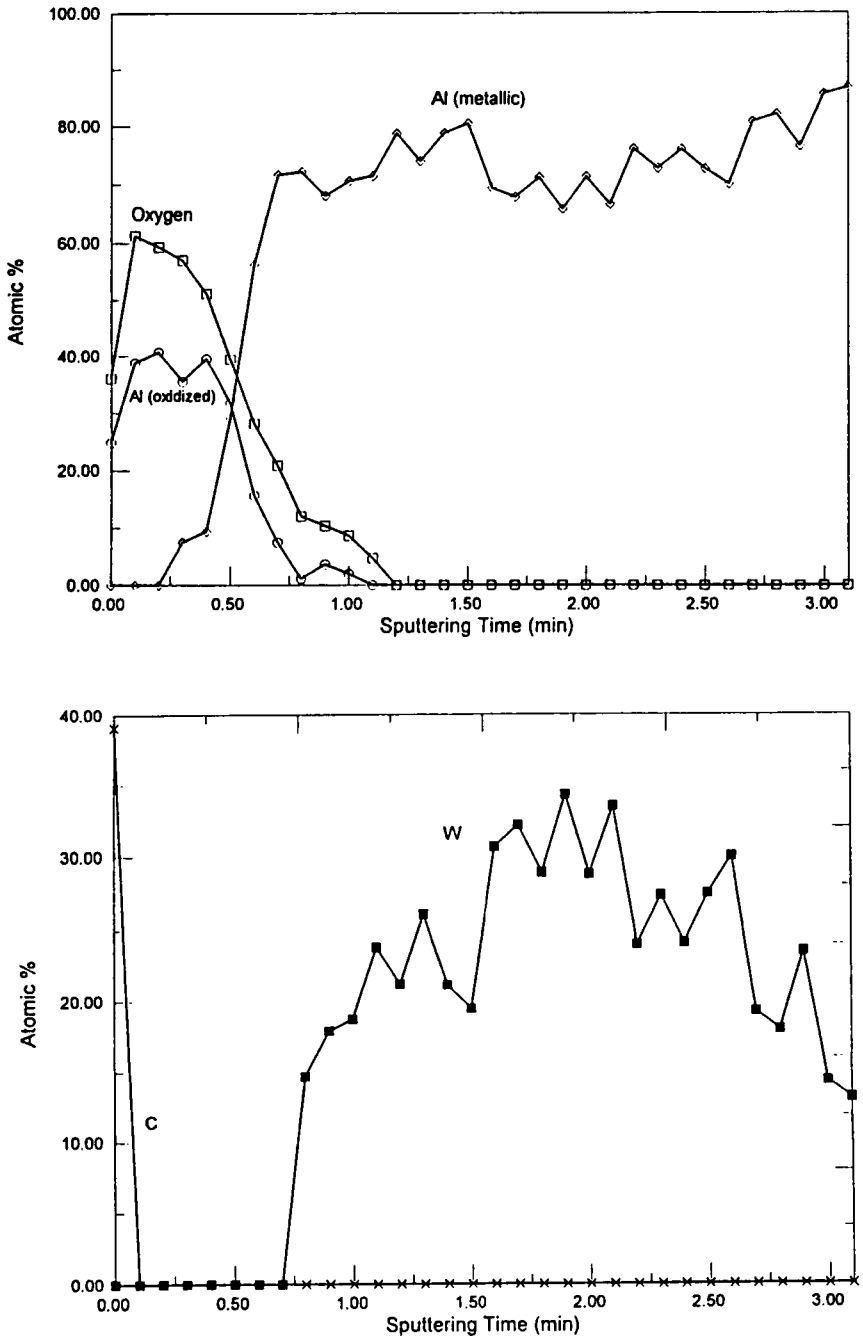

Figure 91. Auger depth profile generated through an oxide blister on Al 1100 implanted with 60 kV 4.5 x 10^{16} W ions/cm^2, after anodic polarization.

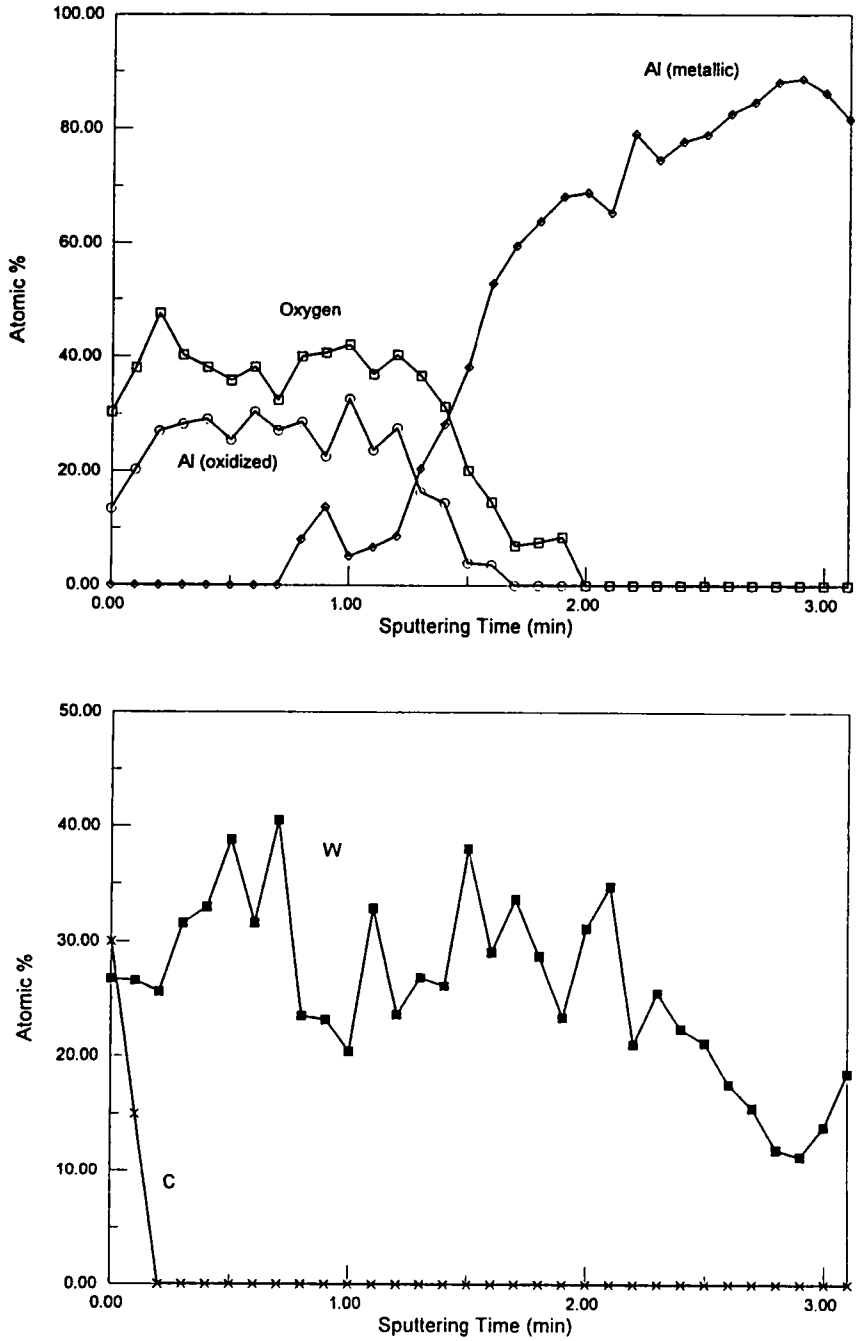

Figure 92. Auger depth profile generated through the oxide matrix on Al 1100 implanted with 60 kV 4.5 x 10^{16} W ions/cm^2, after anodic polarization.

located at the point where the metallic Al content surpasses the oxidized Al content.

The oxide comprising the blister is penetrated by sputtering after only 0.51 minutes, in contrast with the 1.28 minutes of the matrix oxide. These correspond to oxide thicknesses of approximately 100 and 250 angstroms, respectively. This discrepancy can be traced to the shorter time that the blistered region is in contact with the metal surface. After the oxide is forced away from the surface by the developing gas pressure, it no longer has access to further anodic reaction, and thereby cannot increase in thickness. After rupture, the blistered oxide collapses back onto the metallic surface. Since this oxide is much thinner than on the non-blistered regions, a depression will result on the post-corrosion surface topography. The depressions in the oxide created by collapsed blisters were detected by atomic force microscopy as indicated in Figure 93. Five blisters can be seen on the surface of the specimen, which was analyzed after anodic polarization following implantation with 60 kV 1.7×10^{16} W ions / cm^2. A three dimensional view of the area containing four adjoining blisters is shown in Figure 94, while Figure 95 is a higher magnification of the blister in the center of Figure 93.

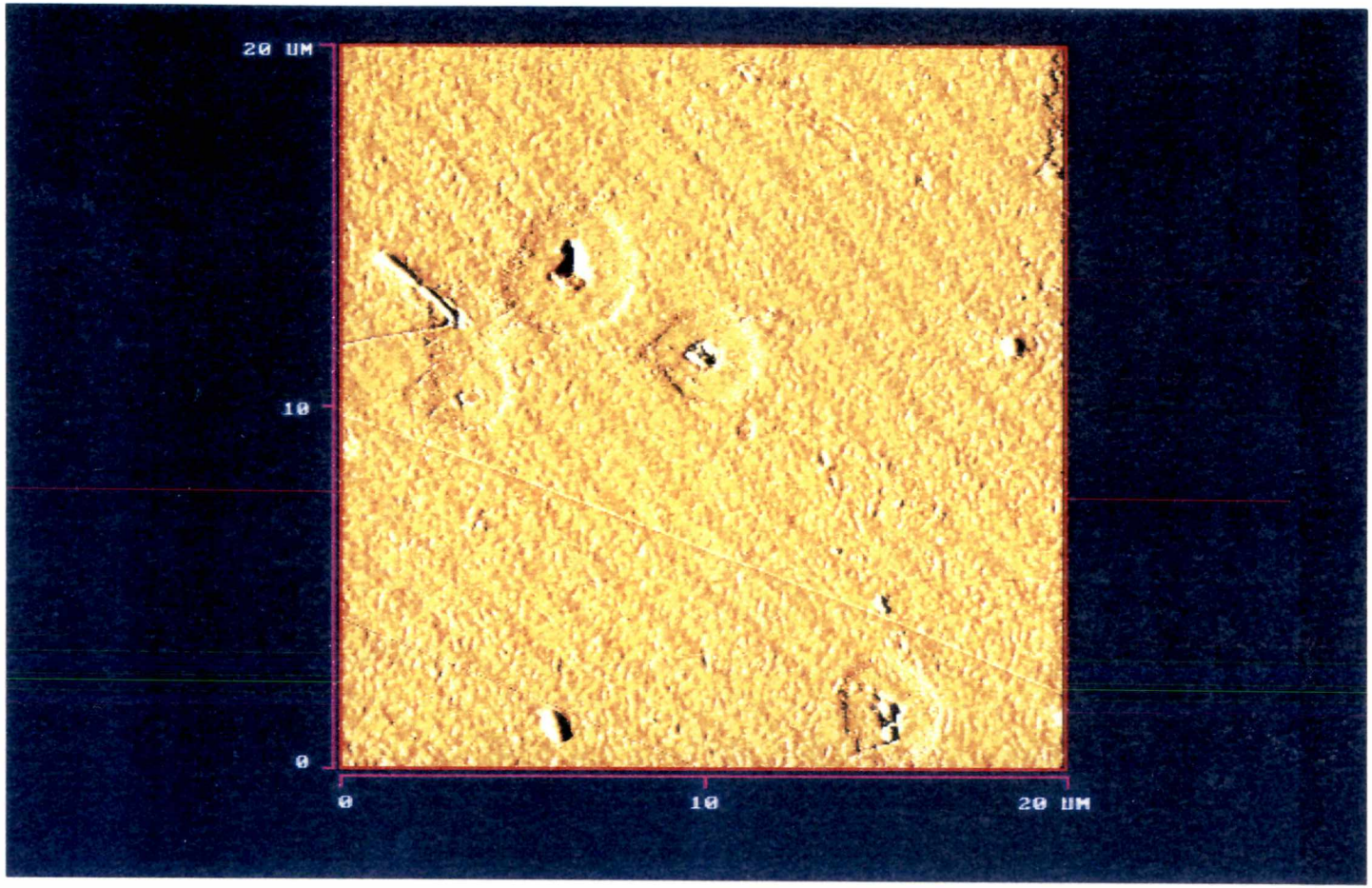

Figure 93. AFM image of collapsed blisters on Al 1100 implanted with 60 kV 1.7 x 10^{16} W ions/cm^2.

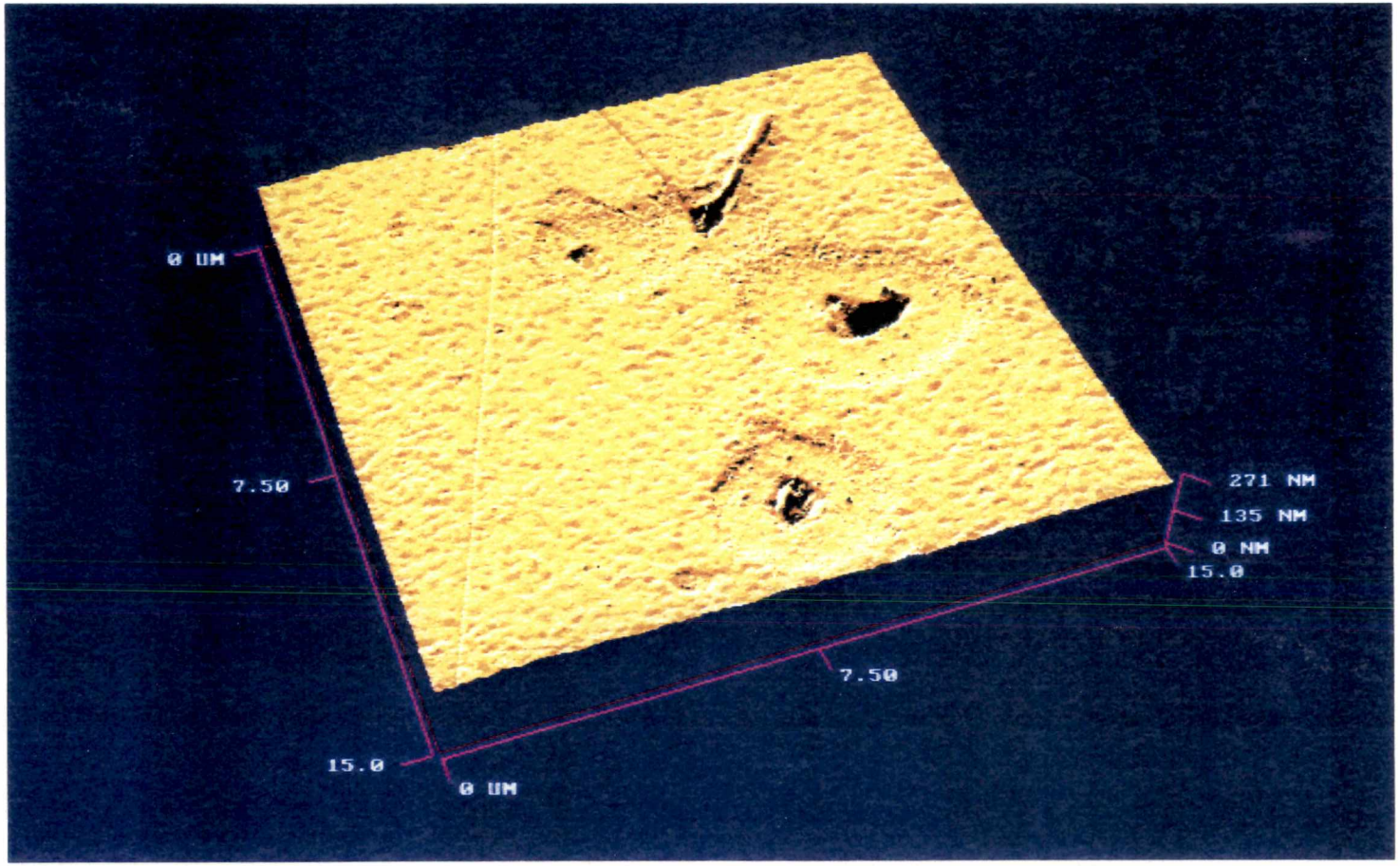

Figure 94. Three-dimensional AFM image of four adjoining blisters from Figure 93.

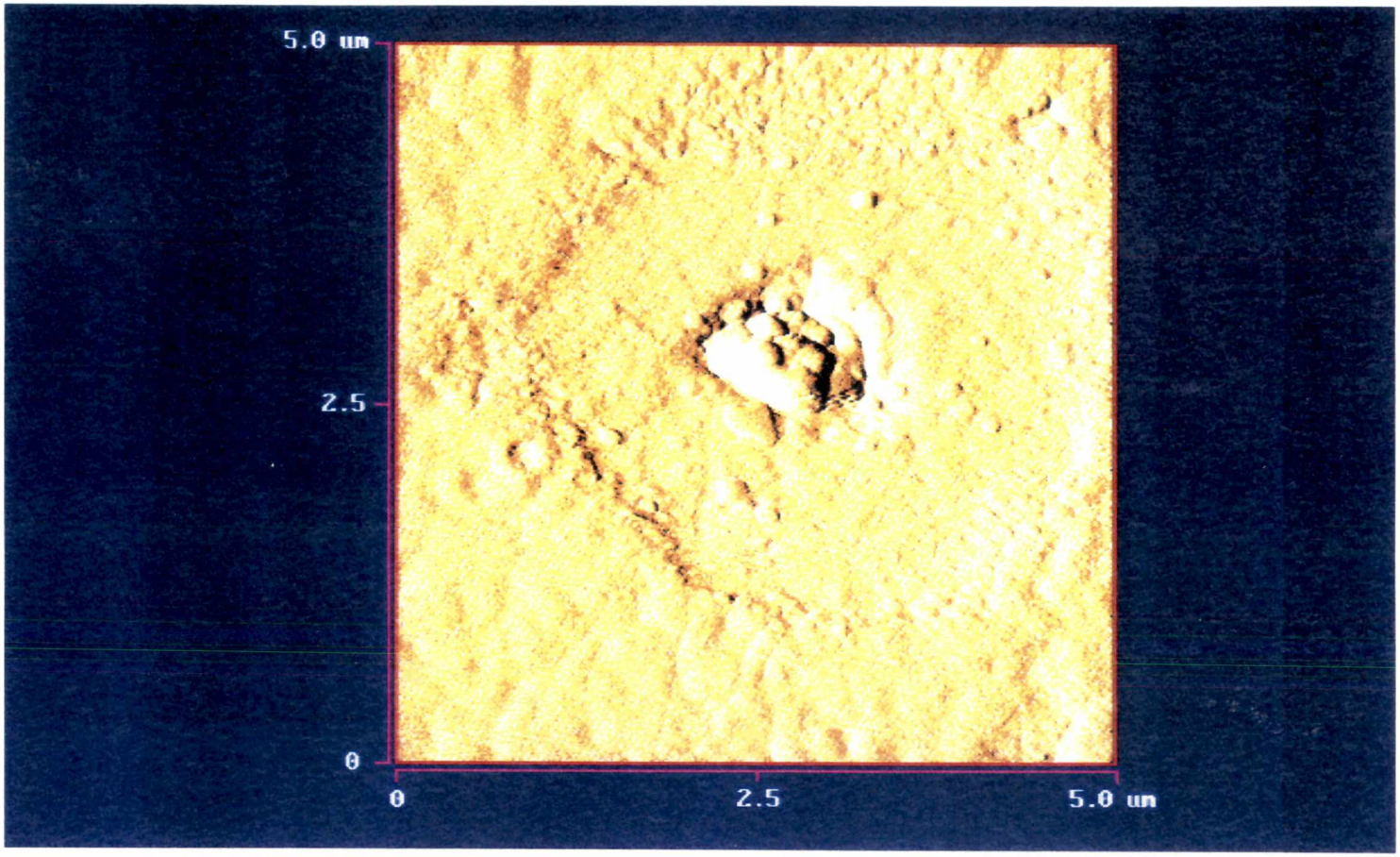

Figure 95. High-magnification AFM image of blister in center of Figure 93.

If the rate of growth of the oxide is not a strong function of potential, it is possible to determine the potential at which the blister formed. Since the blister is (0.51 / 1.28=) 40 % as thick as of the matrix, the potential of blister formation, E_{bl}, is :

$$E_{bl} = E_{corr} + (0.40 * (E_{1000} - E_{corr})) = -581 + (0.40 * ((-9)-(-581)))$$

$$= -352 \text{ mV (SHE)}$$

The pitting potential for this alloy is taken from the polarization curve (Fig. 96) as the potential at which a change in slope is seen at approximately -375 mV. These potentials are close enough to confirm the conclusion of Bargeron and Givens (74) that the blisters form at the pitting potential. This calculation neglects the thickness of the film present prior to polarization, but inclusion of this variable would shift E_{bl} to a lower potential, closer still to E_p. This lends further credence to the conclusion that the primary beneficial effect of the blisters on the corrosion behavior is to slow pitting propagation, not to inhibit pit nucleation.

Comparison of the W profiles from the anodically polarized specimen (Figs. 91b and 92b) reveals that, although tungsten is still present in the underlying metal, no tungsten is found in the blister oxide. The non-blistered oxide, on the other hand, exhibits a W presence in the metal which continues into the oxide layer.

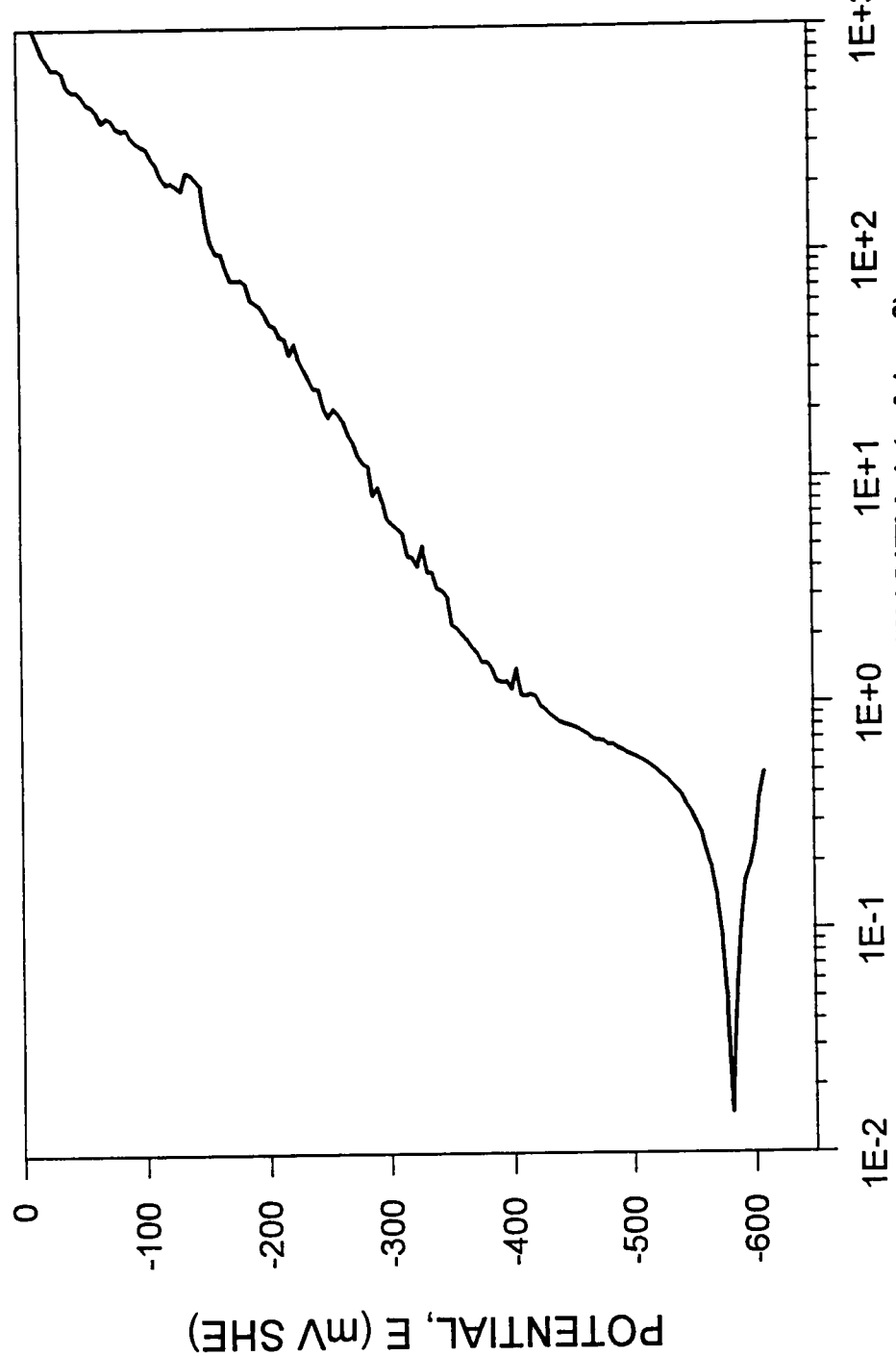

Figure 96. Al 1100 - 60 kV 1.7 x 10^{16} W ions/cm^2 in deaerated 1 wt% NaCl.

Since the O and oxidized Al curves trace each other, and noting the solubility of tungsten oxide at neutral pH, the W incorporated into the film may not be in an oxidized state. The absence of W in the blister indicates that it is either not incorporated at lower potentials, or there was insufficient tungsten implanted into the near surface regions to be incorporated in the first oxide layers formed at potentials near E_{corr}. While Natishan et al. (75) reported finding implanted species in the oxide layer via XPS after polarization and pitting in deaerated 0.1 M NaCl, no W was found in the blister oxide in the present study under polarization or immersion conditions. Therefore, it is difficult to claim, as those authors have, that the implanted species increases E_p by promoting blister formation by improving the mechanical properties of the oxide.

Post-immersion Auger analysis was carried out on a 60 kV 5.5 x 10^{16} W implanted Al 1100 surface, which is shown in Figure 97. A profile of the corrosion product that lies adjacent to the pit opening (Fig. 98) was taken from area 1, while the depth profile through and under an oxide blister (Fig. 99) was generated from area 2. A representative profile from the non-blistered oxide (Fig. 100) was taken from area 3. The corrosion product is a thick, non-uniform formation of aluminum oxide which most likely formed as a consequence of pit metal dissolution following blister rupture.

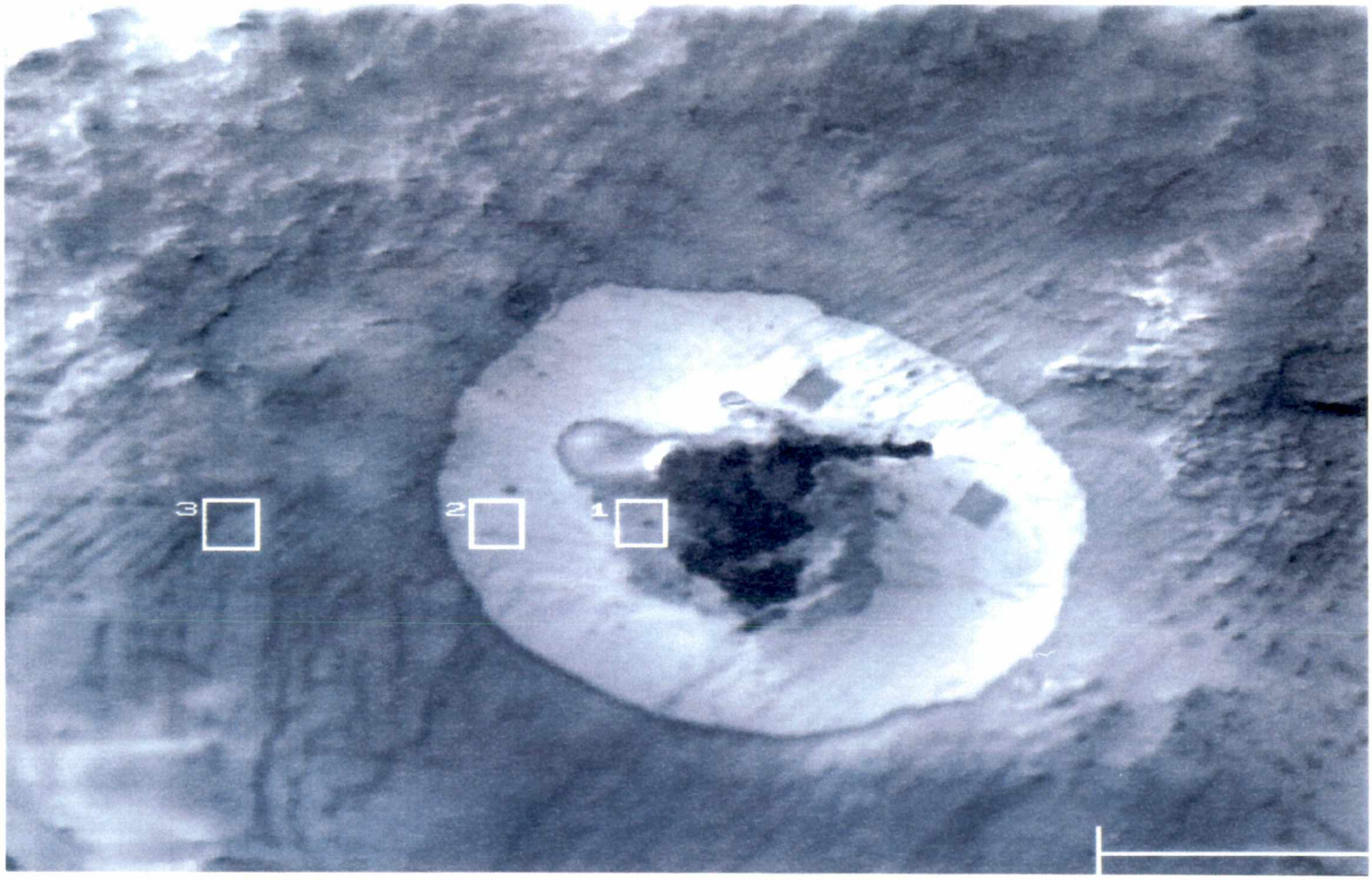

Figure 97. Surface of Al 1100 implanted with 60 kV 5.5 x 10^{16} W ions/cm^2, after immersion in aerated 3.5 wt% NaCl. Boxes indicate locations of Auger depth profile generation.

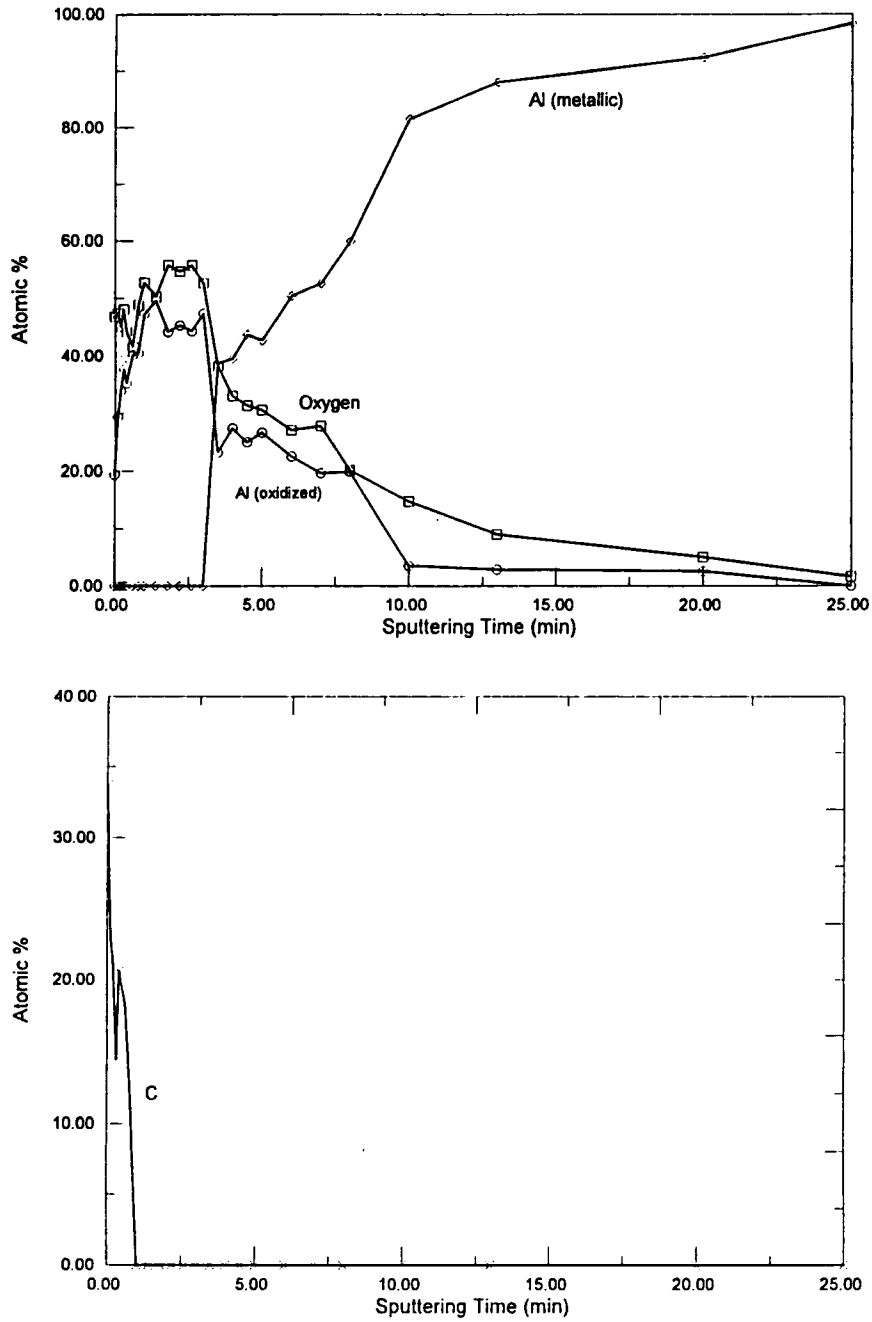

Figure 98. Auger depth profile generated through the corrosion product on Al 1100 implanted with 60 kV 5.5 x 10^{16} W ions/cm^2, after immersion in aerated 3.5 wt% NaCl.

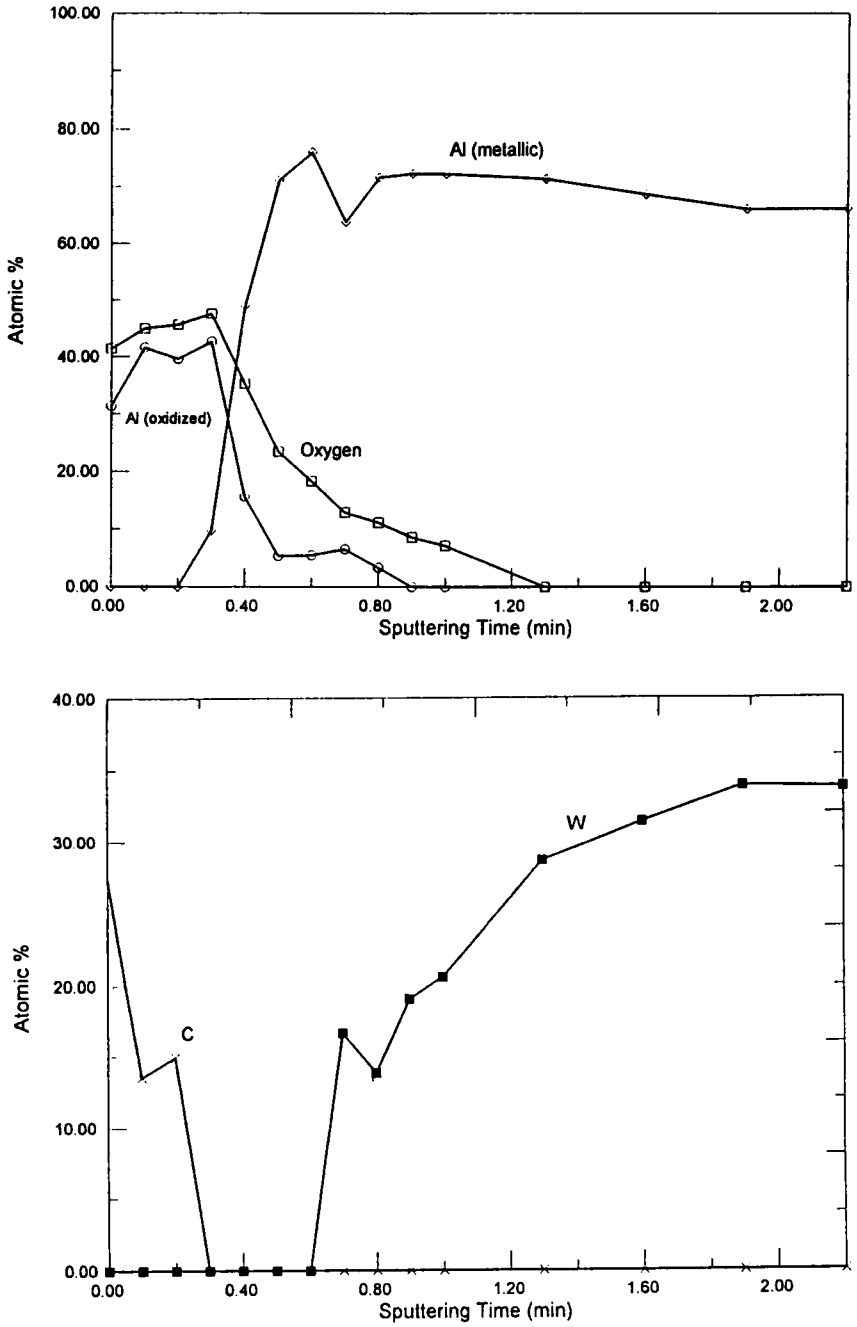

Figure 99. Auger depth profile generated through an oxide blister on Al 1100 implanted with 60 kV 5.5 x 10^{16} W ions/cm^2, after immersion in aerated 3.5 wt% NaCl.

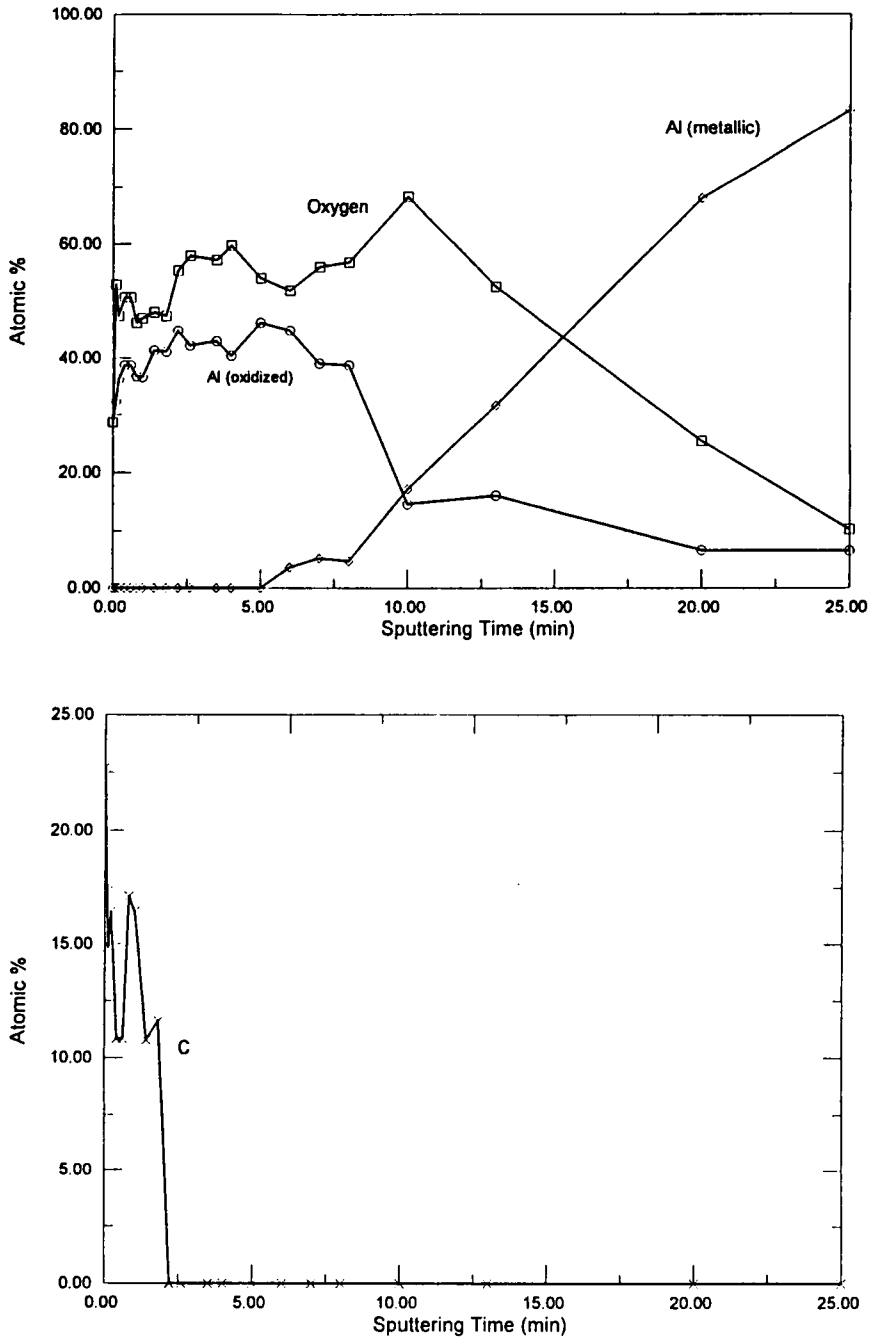

Figure 100. Auger depth profile generated through the matrix oxide on Al 1100 implanted with 60 kV 5.5 x 10^{16} W ions/cm^2, after immersion in aerated 3.5 wt% NaCl.

The oxide comprising the blister is penetrated by sputtering after only 0.36 minutes, in contrast with the 9.9 minutes of the non-blistered oxide. These correspond to oxide thicknesses of approximately 70 and 2000 angstroms, respectively. This blister thickness is smaller than that seen under anodic polarization conditions and much smaller than the matrix oxide, indicating that the blister forms very early in the immersion process.

An oxide thickness of 2000 angstroms indicates that significant reaction has occurred during the 88 hours of immersion. The lack of W in the non-blistered oxide depth profile (Fig. 100) attests to the dissolution of sufficient base metal to remove all of the implanted tungsten from this region. This stands in contrast to the seemingly unaffected W profile (Fig. 99) which retains its distinctive Gaussian shape in the material underlying the blister. The only other possible rationalizations for this W presence is the diffusion of the species from non-blistered areas, or migration inwards as dissolution beneath the blister proceeds. However, neither a driving force nor a mechanism for these explanations is plausible. Therefore, the following model, as illustrated in Figure 101, is proposed for the corrosion of Al implanted with W during immersion in a chloride containing solution.

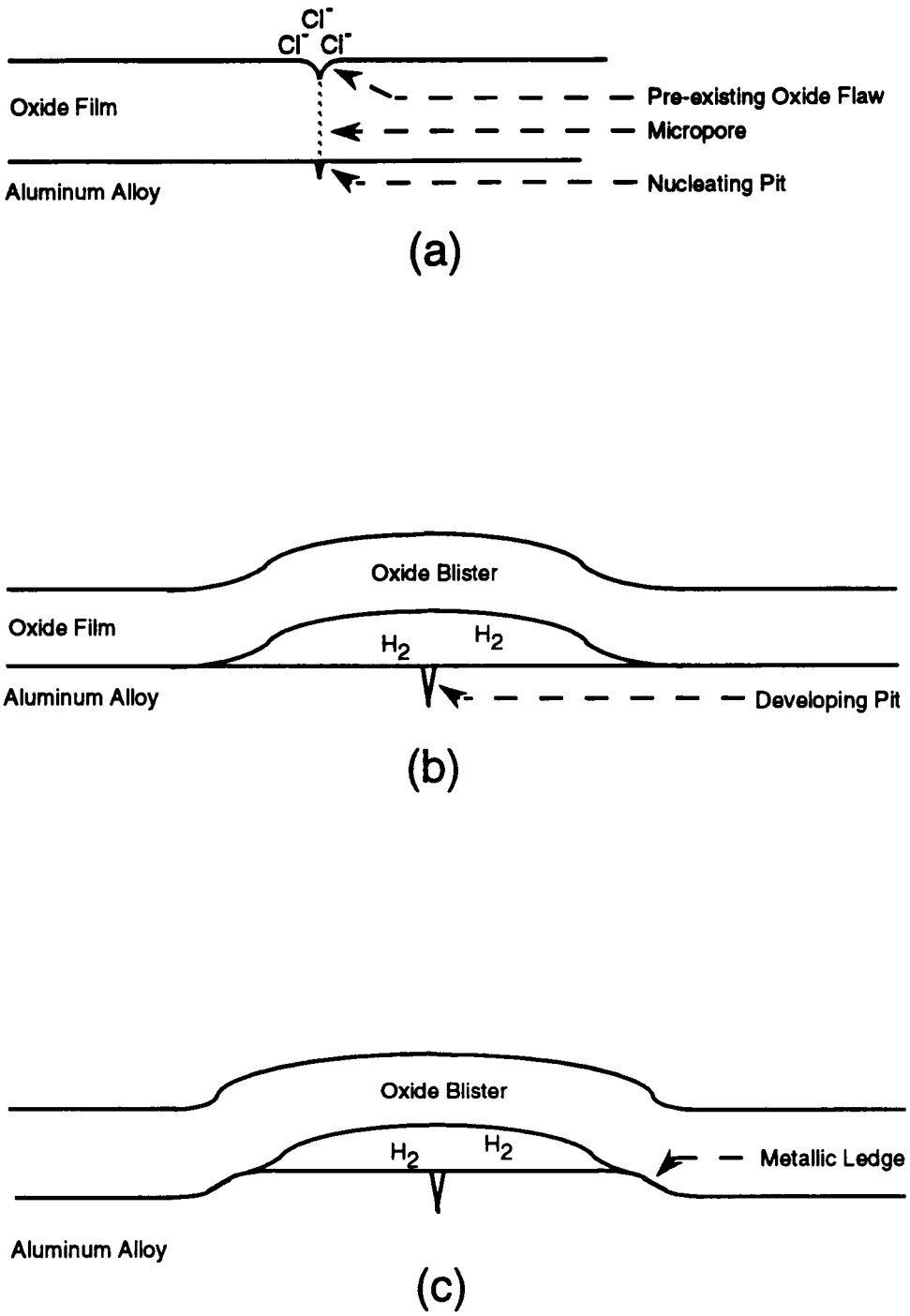

Figure 101. Model illustrating corrosion mechanisms on tungsten implanted aluminum in a NaCl solution.

In the initial stages of immersion, chloride ions adsorb onto the oxide surface and cause rapid film degradation at preexisting oxide flaws (Fig. 101a). Al 1100, which contains a large volume fraction of a secondary phase ($FeAl_3$), provides an abundant number of oxide imperfections at the phase boundaries. The film breakdown may take the form of micropore formation through which H_2O and Cl^- can penetrate. As the underlying aluminum metal is exposed to these species, rapid dissolution occurs that takes the form of pit nucleation. Hydrogen gas evolution begins with the onset of pitting beneath the oxide layer (107). Its formation can be attributed to one of two types of reactions. The first possibility is the creation of an aluminum chloride intermediate, followed by an aluminum chloride - water reaction (74). A more likely scenario involves direct H_2 generation from the chloride-activated reaction of aluminum metal and water. Anions such as chloride, bromide, and iodide are known to activate Al, so that it decomposes H_2O. Depending on whether the end product is an oxide or hydroxide, the pertinent reactions are (108):

$$2\ Al + 6\ H_2O = 2\ Al(OH)_3 + 3\ H_2$$

$$2\ Al + 3\ H_20 = 3\ H_2 + Al_2O_3$$

Due to the highly insulating nature of aluminum oxide, the cathodic reaction may also occur at the pit site during immersion, increasing the rate of localized hydrogen gas production.

If the oxide flaws through which the H_2O and Cl^- reactants migrate are not of significant cross sectional area, the gas cannot penetrate through the oxide into solution because of the solution / gas surface tension. It has been estimated (73) that a pressure of 150 atmospheres is necessary to force gas bubbles through a micropore 200 angstroms in diameter. The gas is thus trapped between the metal and oxide. As the gas pressure increases, the oxide is forced away from the metal surface and a blister is formed (Fig. 101b).

As immersion continues, oxide formation is occurring in the non-blistered regions of the surface. The metal beneath the blister (other than in the developing pit) is protected from oxidation, resulting in an promontory of blister-protected metal above the receding location of the remainder of the metal / oxide interface (Fig. 101c). Meanwhile, the blister continues to grow in diameter. Previous visual observations of oxide blister growth indicates that it proceeds in a stepwise fashion (74). The hydrogen gas source for the growing blister is from additional pits which form at the point where the blister separates from the metallic surface

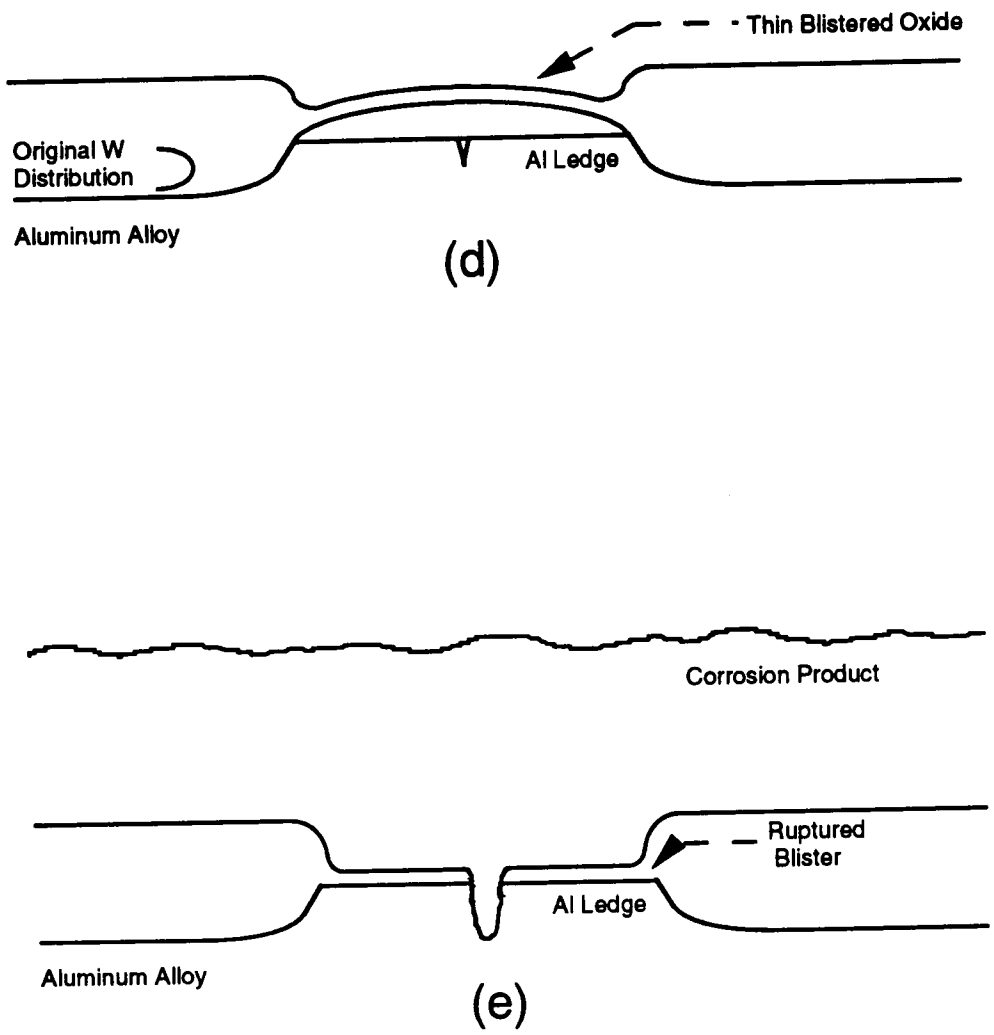

Figure 101. Model illustrating corrosion mechanisms on tungsten implanted aluminum in a NaCl solution.

(74). Eventually, the oxide growth in the non-blistered regions proceeds to the extent that all of the implanted W is lost to the solution, and the blister protected metal remains with a distinct ledge of unaffected material (Fig. 101d). Once in solution, the W species begins to catalyze the aluminum oxide precipitation. Upon rupture of the blister, localized corrosion starts to proceed at a much faster rate as the pit is fully exposed to the solution. However, the copious amount of aluminum oxide precipitate covering the entire surface at this point (Fig. 101e) acts to slow the pitting process.

The dramatically different blister morphologies that result from anodic polarization (Fig. 61) and immersion testing (Fig. 77) can be traced to the ubiquitous pit nucleation that occurs at high potentials during polarization. Blisters form at many sites on the surface and several are soon ruptured as the potential continues to increase. Little time is allowed for the blisters to grow in diameter before massive pitting dissolution begins at these sites. Conversely, the pits that form at the corrosion potential during immersion will nucleate at only a few of the most vulnerable oxide flaws. As pitting slowly proceeds at these points, each blister can grow significantly prior to rupture. Therefore, the immersion specimens show a few large blisters, while the polarized samples exhibit many smaller ones.

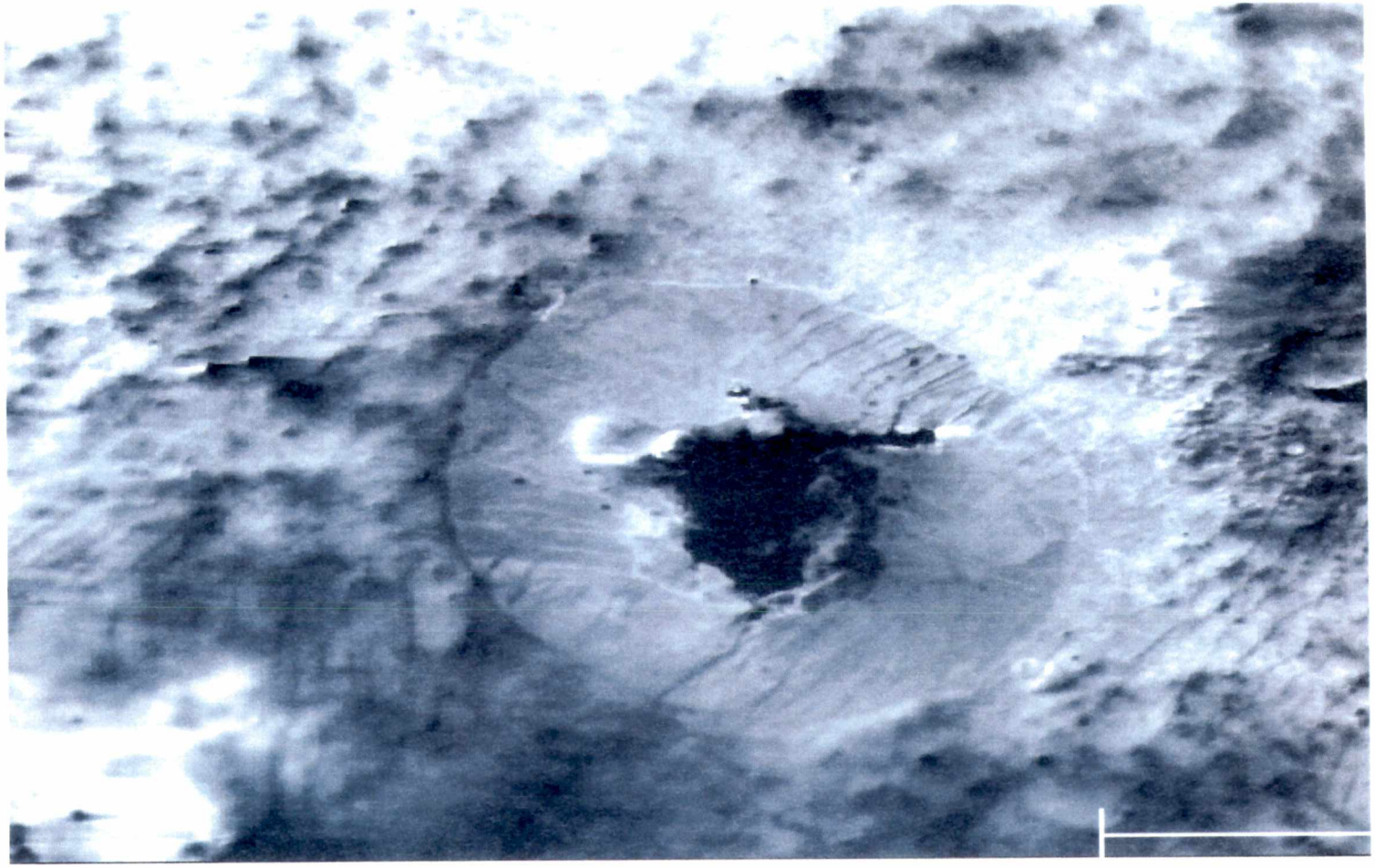

Figure 102. Surface of Al 1100 implanted with 60 kV 5.5 x 10^{16} W ions/cm^2, after immersion in aerated 3.5 wt% NaCl. Surface Ar sputtered for 3 minutes.

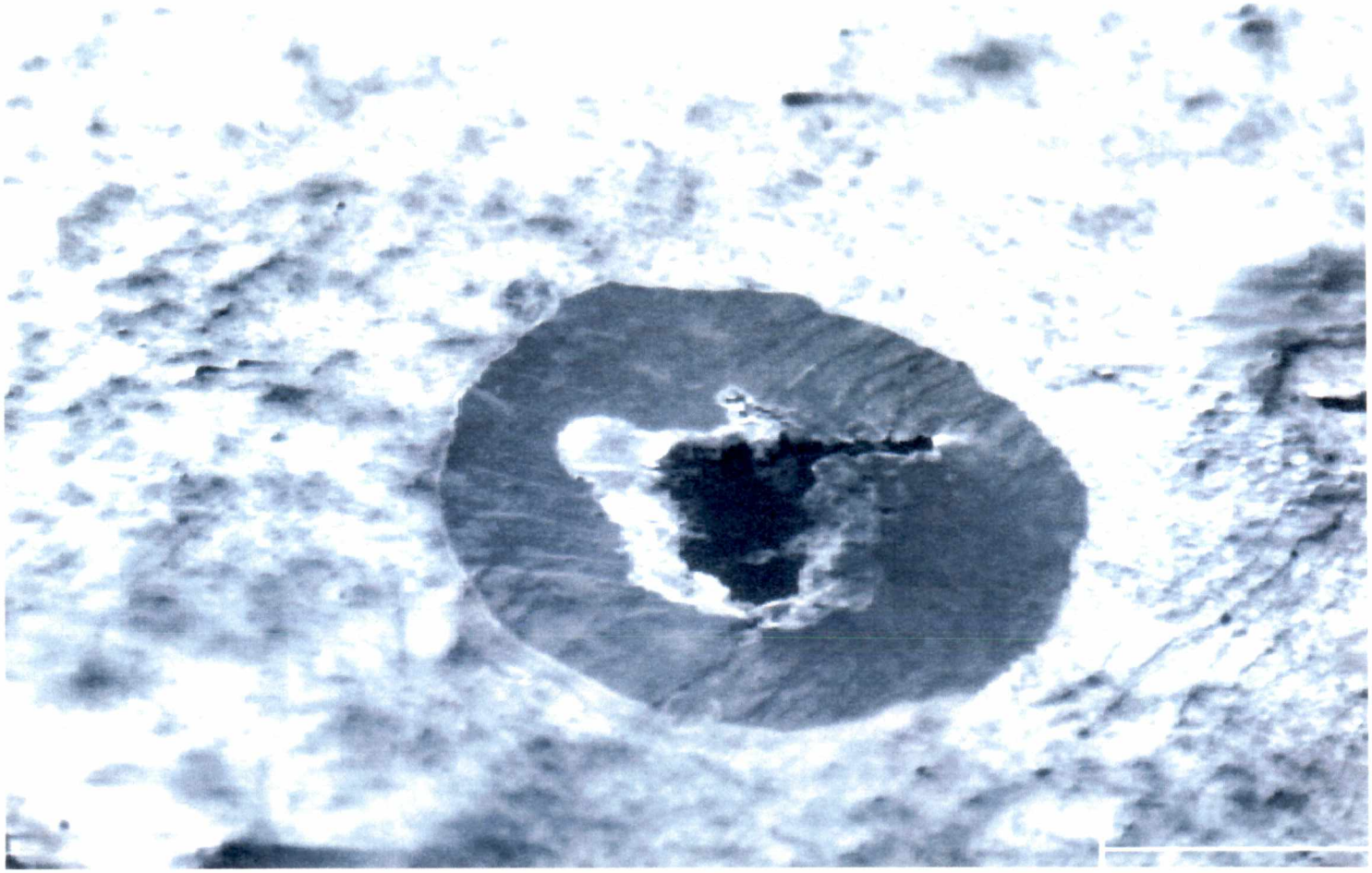

Figure 103. Surface of Al 1100 implanted with 5.5×10^{16} W ions/cm^2, after immersion in aerated 3.5 wt% NaCl. Surface Ar sputtered for 8 minutes.

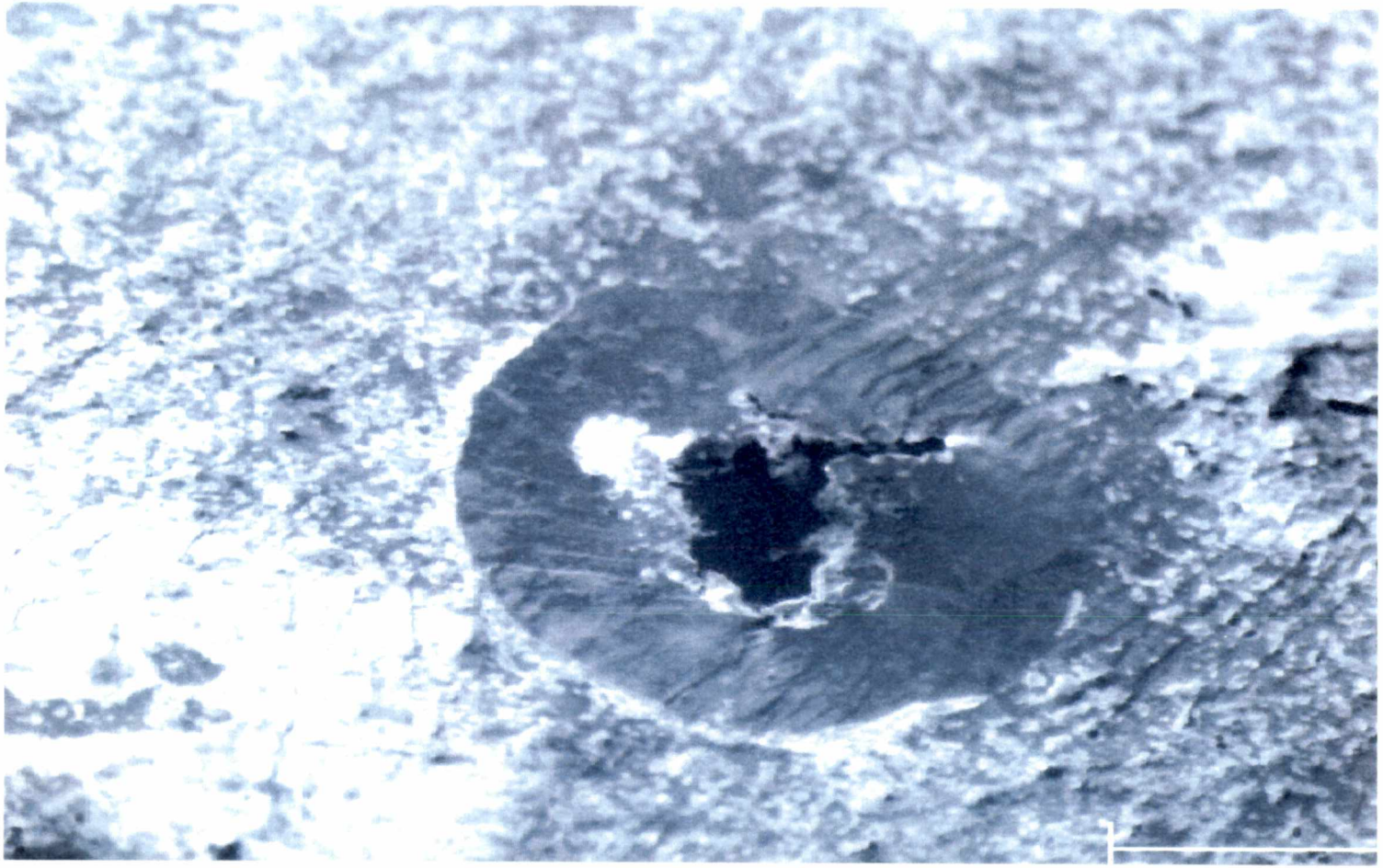

Figure 104. Surface of Al 1100 implanted with 5.5 x 10^{16} W ions/cm^2, after immersion in aerated 3.5 wt% NaCl. Surface Ar sputtered for 20 minutes.

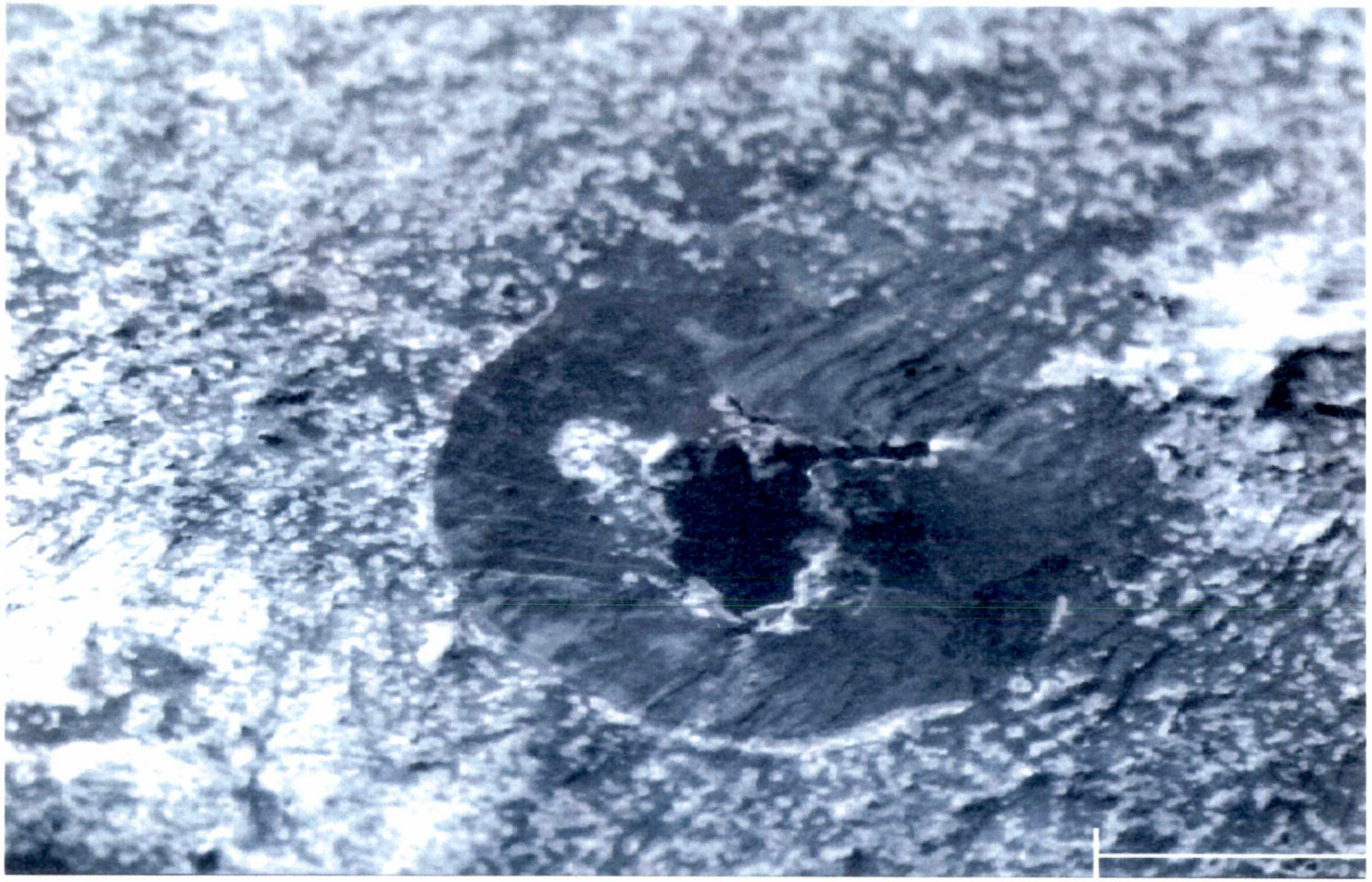

Figure 105. Surface of Al 1100 implanted with 5.5 x 10^{16} W ions/cm^2, after immersion in aerated 3.5 wt% NaCl. Surface Ar sputtered for 25 minutes.

SEM photographs of an immersion blister were taken as a function of Ar sputtering depth during Auger analysis. The blister is shown in Figures 102-105 after sputtering for 3, 8, 20, and 25 minutes. The original surface was shown in Figure 97. The substantial thickness of the oxide is again evident from its presence on a portion of the surface even after 25 minutes of sputtering. The appearance of the alloy beneath the blister region after only 8 minutes illustrates the projection of this area above the matrix metal-oxide interface.

The four closely spaced oxide blisters from Figure 94 are shown with AFM topographical line scans in Figure 106, which were generated along the lines superimposed on the photograph. Figure 95 is shown with corresponding line scans in Figure 107. These images clearly show that the oxide blister is recessed below the surface of the surrounding oxide. The sharp deviations in the linear topographical scans indicate the presence of deep pits (negative deviations) and corrosion product buildup next to the pit sites (positive deviations). Analyzing the elevation drop between the blister and matrix oxides shows that the largest blister in Figure 106 is approximately 19 nm below the surface, while the smaller blister in Figure 107 is approximately 17.5 nm below the surface. These values concur with the 15 nm difference in oxide depth as determined by Auger

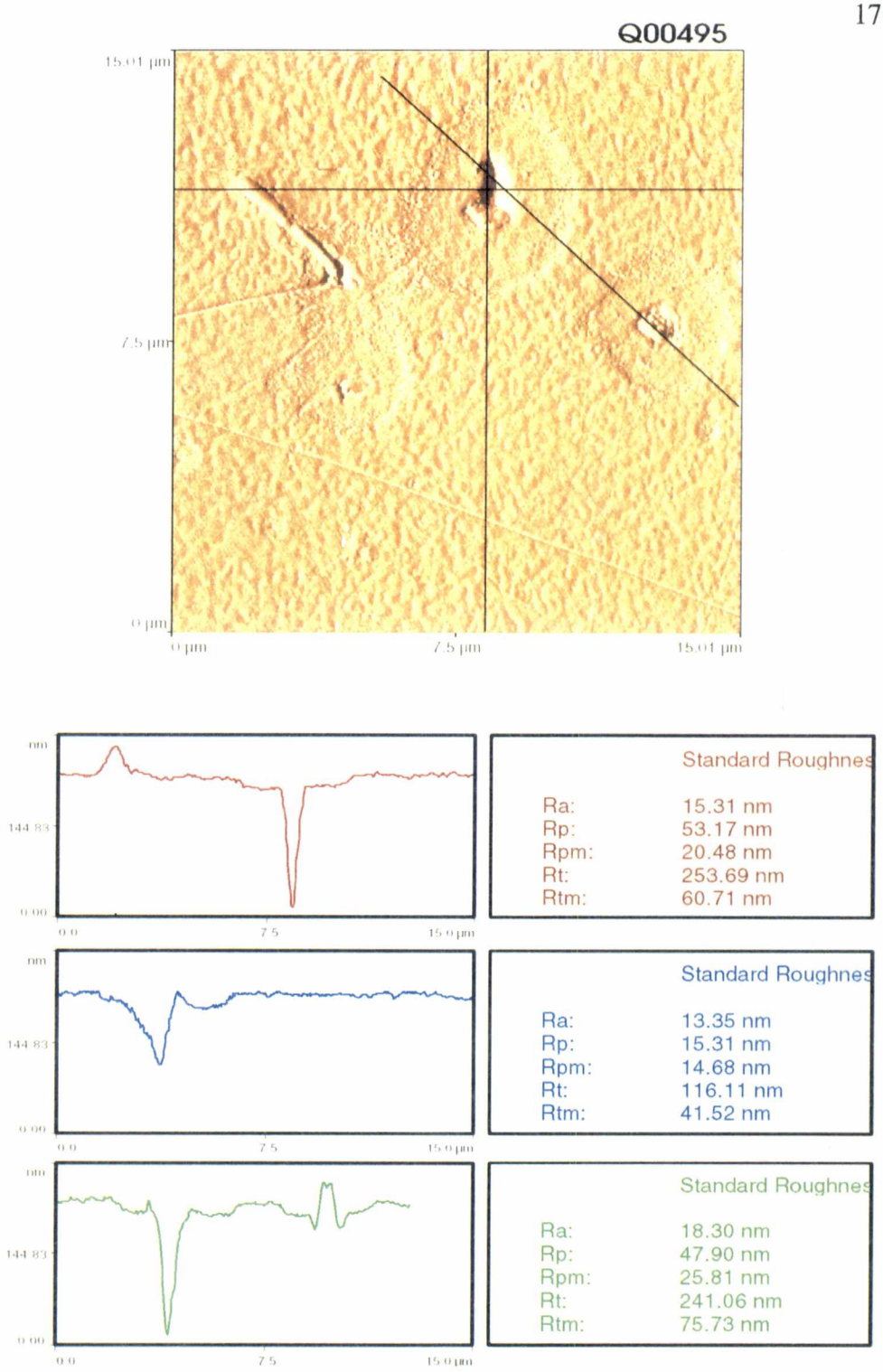

Figure 106. Topographical surface line scans of AFM image from Figure 94.

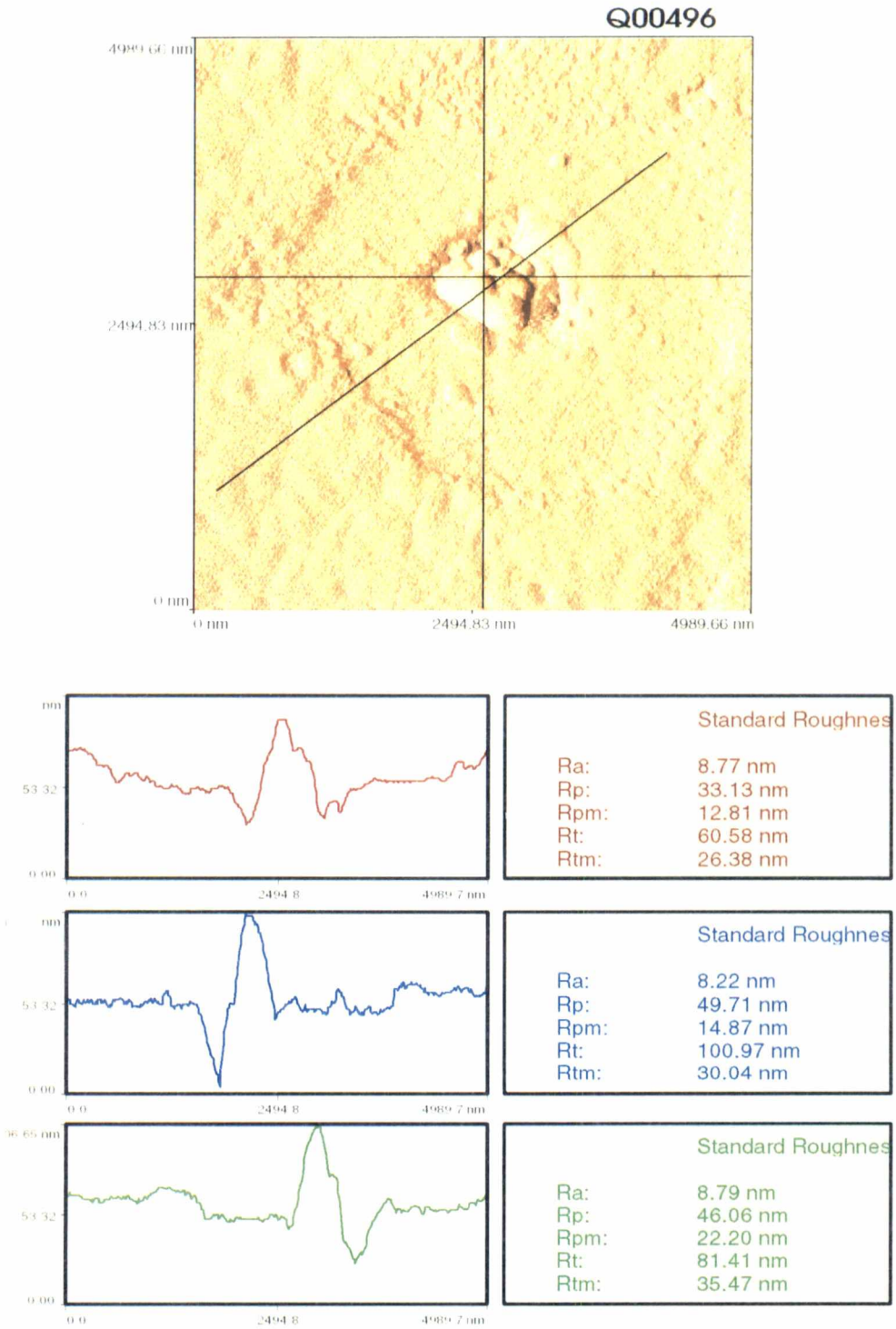

Figure 107. Topographical surface line scan of AFM image from Figure 95.

spectroscopy on a separate polarization sample. Each blister displays a center rupture with underlying pit growth. This is contradictory to the previous SEM evidence that anodic polarization blisters ruptured at the blister edge. The pitting potential measured on this specimen was only slightly elevated above the control E_p. Edge ruptures seem to be associated only with implanted, polarized surfaces which display elevated pitting potentials. Therefore, it is not possible to strictly delineate the blister fracture mode as a function of the type of corrosion test utilized.

Part II - Nitrogen Plasma Ion Implantation of 304L Stainless Steel

Experimental Difficulties Associated with Non-Uniformity of PII Dose Distribution and 304L Crevicing Tendency

A variety of plasma ion implantation parameters (sample holder shape, sample holder size, N dose, implantation energy, pulse frequency) and pre-corrosion specimen treatments (epoxy applications, nitric acid passivation, passive film removal, cathodic cleaning techniques) were applied during the study of the effects of nitrogen PII on the pitting corrosion of 304L stainless steel. This developmental work was done in an attempt to alleviate the irreproducibility that was observed in the measured pitting potentials. Inconsistent measurements could be attributed to non-uniformity of nitrogen coverage during the PII process and the crevice corrosion tendency of the 304L stainless alloy. Both the successful E_p enhancements and the difficulties in duplicating results will be discussed in terms of the successive experimental modifications which were undertaken to combat these two inherent difficulties.

304L Crevice Potential

The initial N PII implantations were applied to square 2 cm x 2 cm 304L specimens using the sample holder shown in Figure 40. Amercoat epoxy was applied to each surface after implantation and before corrosion testing in an attempt to minimize crevicing at the metal-PTFE sample holder knife edge. However, the susceptibility of this alloy to crevice corrosion resulted in crevice formation at the metal-epoxy interface in many cases. The potential at which localized film breakdown commences given a preexisting crevice (E_{crev}), is generally lower than the pitting potential on a given alloy. This is due to the preexisting site for formation of an occluded electrochemical cell, as opposed to the film breakdown and pit nucleation mechanisms required to initiate pitting corrosion.

The sensitivity of 304L stainless steel to preexisting crevice sites can be demonstrated by immersion testing in aggressive solutions. Two solutions used for this purpose were 10 wt. % $FeCl_3$ and a combination of 1 wt. % NaCl and 2 wt. % $KMnO_4$. An as machined 304L surface undergoes massive localized dissolution in 150 hours in the ferric chloride solution, and in 96 hours in the potassium permanganate solution. The scratches on the as machined surface result in a sufficient roughness to provide for crevice sites. Polished surfaces

(2400 grit) did not undergo any localized corrosion in either $FeCl_3$ or $KMnO_4$ in 333 and 502 hours, respectively. This is the surface condition of the 304L specimens prior to nitrogen PII. Therefore, the N-implanted 304L will be very susceptible to a preexisting crevice on the surface as a result of the sample holder or epoxy interfaces.

A comparison of E_{crev} as a function of the implanted dose shows that the nitrogen can act to increase or decrease E_{crev}, depending on the PII implantation energy (Fig. 108, Table 6). 20 kV implantations resulted in the crevicing potential decreasing with increasing dose, while the 10 kV implantations moderately increased E_{crev} by as much as 100 mV at a dose of 4×10^{15} N. Typical polarization behaviors are illustrated in Figure 109 for 20 kV (5×10^{14} N dose) and Figure 110 for 10 kV (7×10^{14} N dose), each plotted along side an unimplanted control. Immediate passivation under anodic control was noted with an extremely low passive current density (i_{pass}) of 0.2 - 0.6 $\mu A / cm^2$, with i_{pass} increasing slowly with potential in the passive region. This behavior is typical of 304L stainless steel.

Figure 108 and Table 6 refer to implanted doses, not retained doses. RBS analyses and an ion implantation computer modeling code, PROFILE, were used

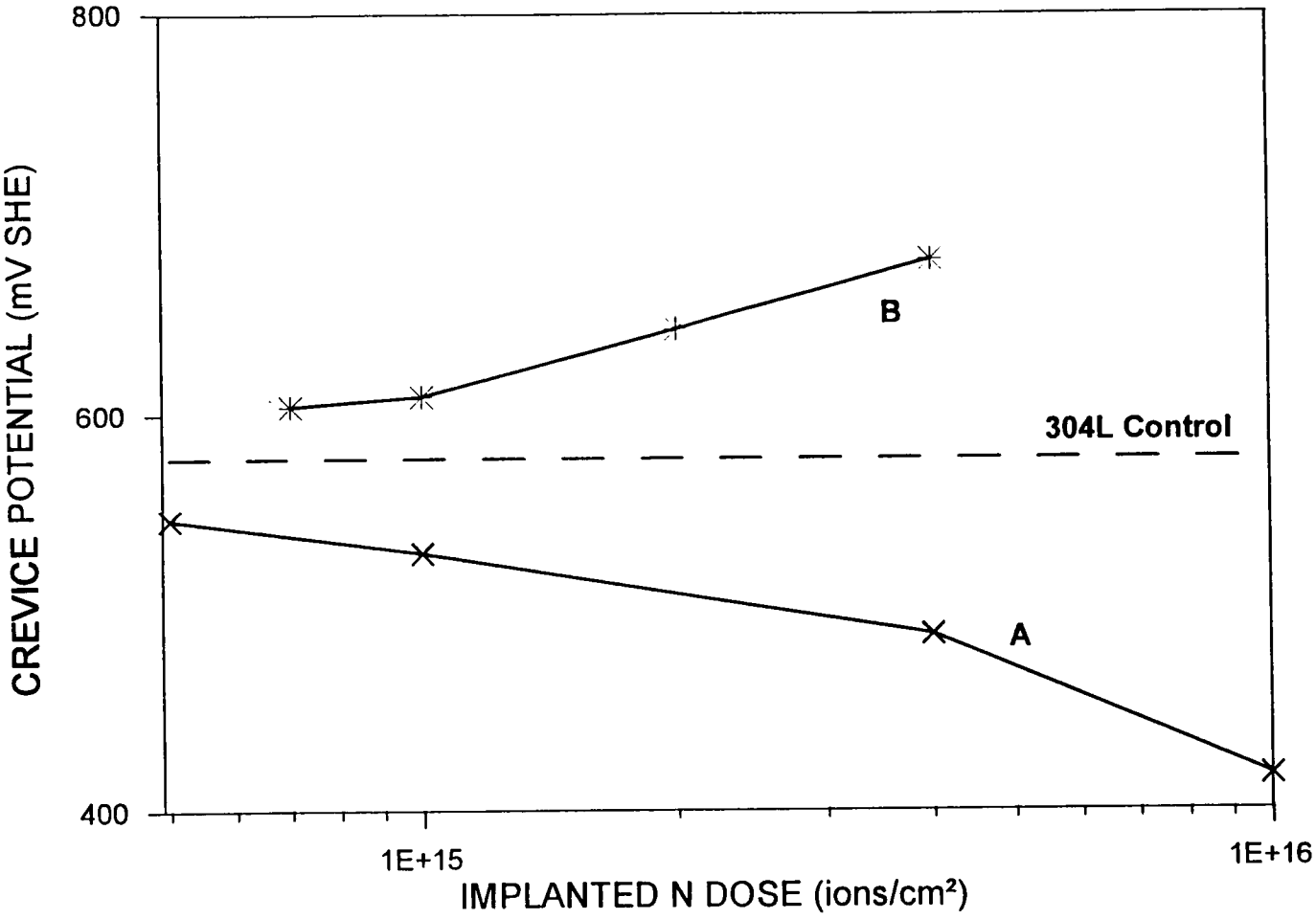

Figure 108. Crevice corrosion potentials of 304L stainless steel in deaerated 1 wt% NaCl as a function of applied N plasma ion implantation dose. [A - 20 kV implantation energy, B - 10 kV implantation energy]

Table 6

Crevice Potentials of PII N 304L Stainless Steel in Deaerated 1 wt% NaCl

N Implantation Energy and Dose	$E_{crev,1}$ (mV SHE)	$E_{crev,2}$ (mV SHE)	$E_{crev,3}$ (mV SHE)	$E_{crev,4}$ (mV SHE)
Control	574	529	627	
20 kV, 5e14	550	541		
20 kV, 1e15	585	472		
20 kV, 4e15	515	460		
20 kV, 1e16		417		
10 kV, 7e14		604		
10 kV, 1e15	605	586	606	639
10 kV, 2e15	643			
10 kV, 4e15	637	716		

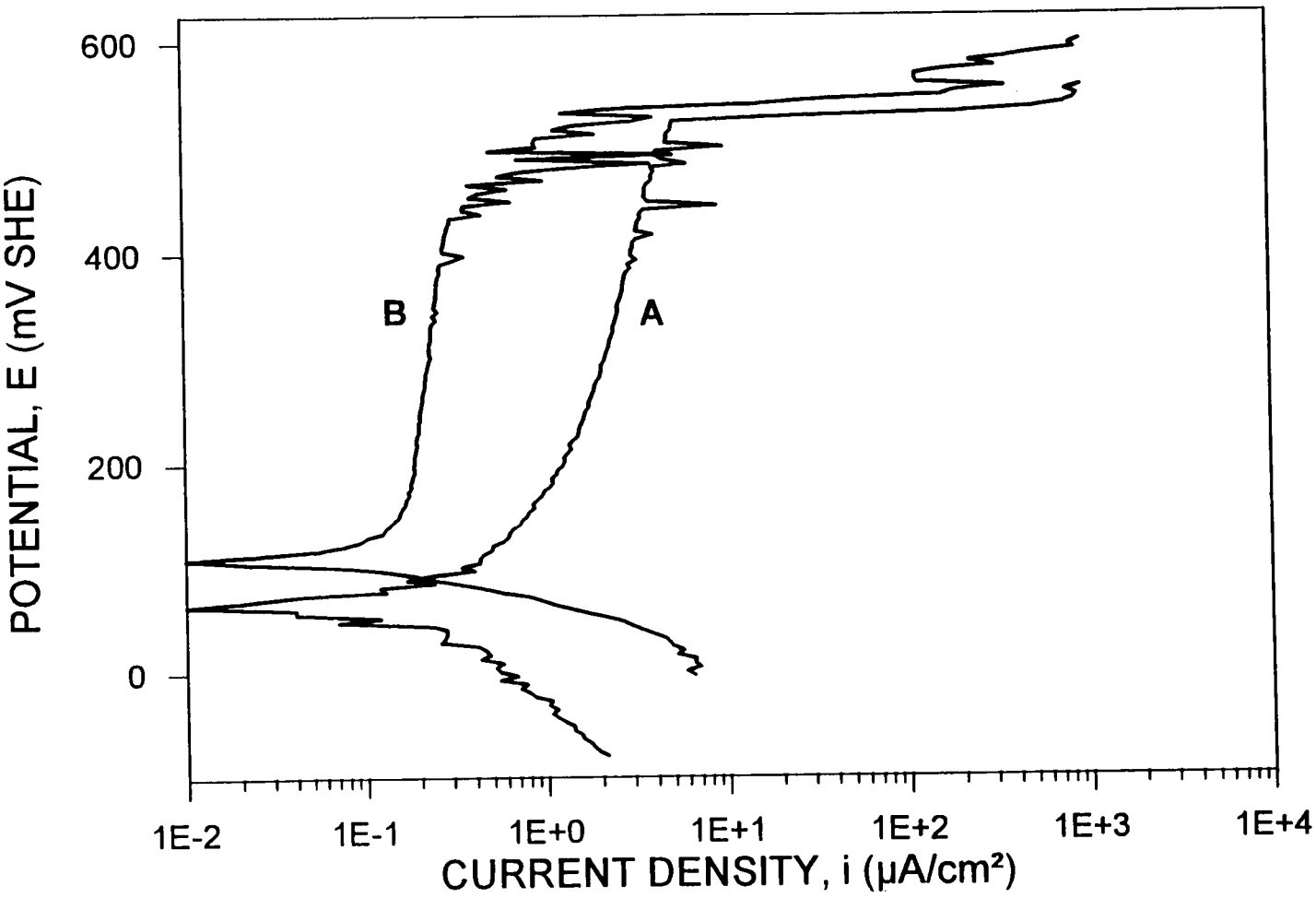

Figure 109. Anodic polarization in deaerated 1 wt% NaCl of (A) 304L and (B) 304L implanted with 5 x 10^{14} N ions/cm^2 at 20 kV.

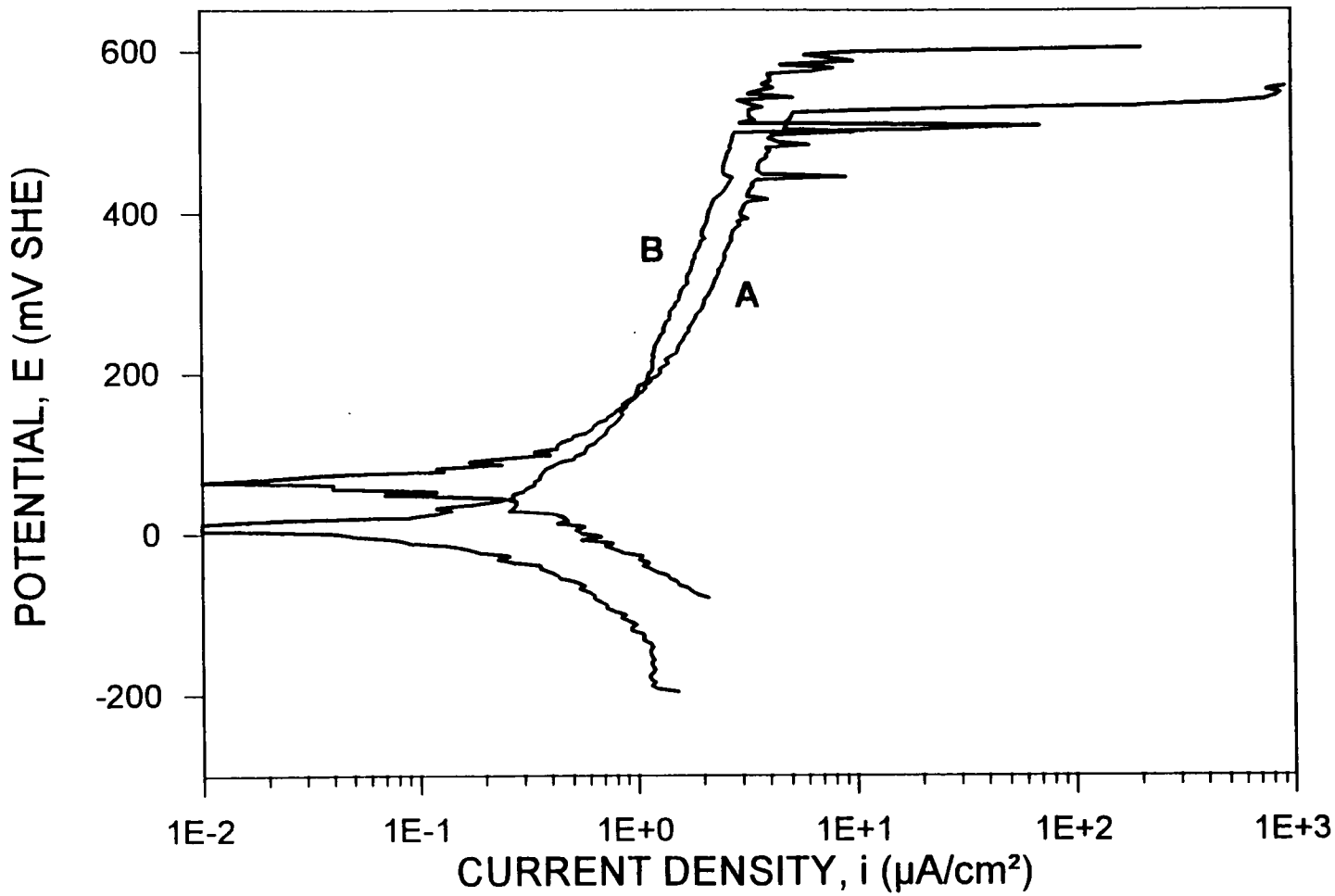

Figure 110. Anodic polarization in deaerated 1 wt% NaCl of (A) 304L and (B) 304L implanted with 7 x 10^{14} N ions/cm^2 at 10 kV.

to acquire a retained dose profile. For a 10 kV, 1 x 10^{18} implantation, assuming equal amounts of molecular (N_2^+) and atomic (N^+) nitrogen species, the PROFILE simulation indicated a retained dose of ~6 x 10^{16} ions / cm^2. This is shown in Figure 111, with peak separation for molecular and atomic nitrogen profiles, and assuming a sputtering coefficient of 1.80. This results in an excessive loss of dose due to the removal of 2100 angstroms via sputtering. Such losses are common for low implantation voltages and create an absolute limit on the retained dose at these accelerating potentials. RBS spectra of a nitrogen plasma ion implanted sample at 10 kV and 10^{18} ions / cm^2 indicated a similar retained dose value of 3 x 10^{16}. Furthermore, a nitrogen ion-beam implanted sample exhibited similar retained dose behavior to PII implants at an implanted dose of 1 x 10^{17} ions / cm^2.

Higher dose retention would be possible at greater implantation voltages; however, as the crevice potential results indicated and pitting potential evidence will indicate, passivity enhancements are more significant for a lower potential. Once developed, a corroding pit is difficult to repassivate due to autocatalytic conditions within the pit that accelerates the rate of corrosion penetration. Therefore, it is critical to improve the material's ability to resist the pit nucleation mechanism by modification of the passive film or the film / metal interface. At

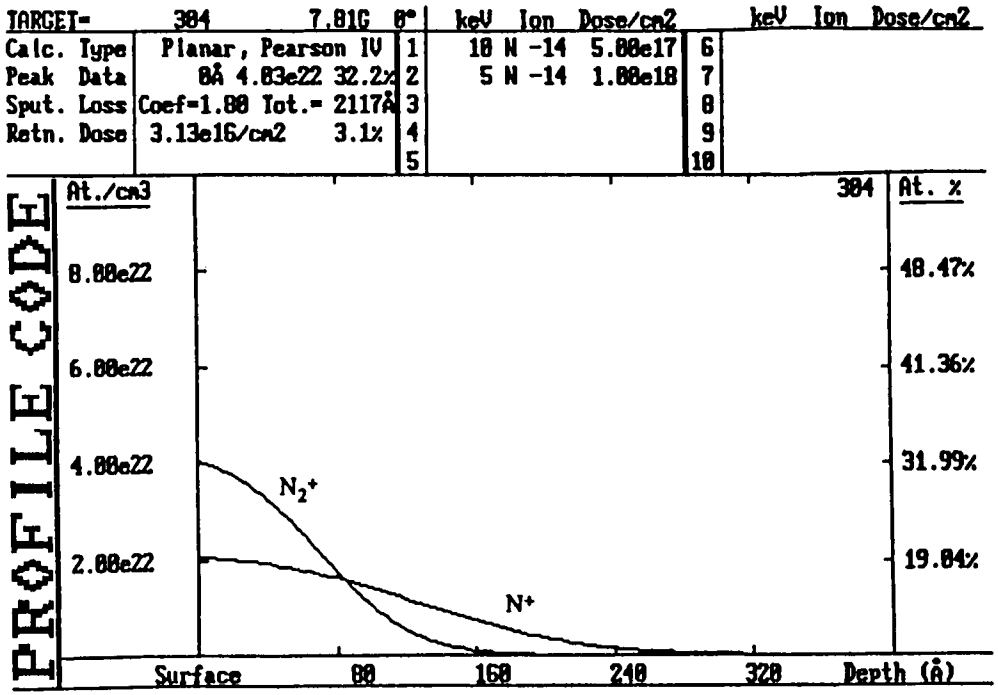

Figure 111. PROFILE code simulation of retained dose profile for 1 x 10^{18} ions/cm^2 N implanted into 304L stainless steel at 10 kV.

higher accelerating potentials, the nitrogen peak concentration is recessed below the surface and cannot modify the near surface region of the alloy and prevent pit nucleation. During pit growth, the nitrogen content may not be effective in repassivation due to pit acidification. It would then seem critical to attempt to increase the N surface concentration by decreasing the implantation energy. This can be seen in Figure 112, where the maximum retained N_2^+ concentration occurs within 80 angstroms of the surface at an accelerating potential of 10 kV. Our results indicate that crevice and pitting potential improvements of higher magnitude and consistency result from the 10 kV implantations as compared to those performed at 20 kV. One interesting aspect of plasma ion implantation is that the voltage is not constant over the length of the voltage pulse (Fig. 39a). This will cause the implantation depth to vary with the energy, and a somewhat non-Gaussian profile will result which is more uniform than for monoenergetic implantation.

Visual inspection of the surface of high-dose implantations on the 2 cm x 2 cm geometry show discoloration patterns indicating non-uniformity of nitrogen coverage. Depending on the applied dose, the specimen edges and diagonals displayed a noticeable darkening or lightening relative to the remainder of the surface. A typical pattern is sketched in Figure 113. This nonuniformity is

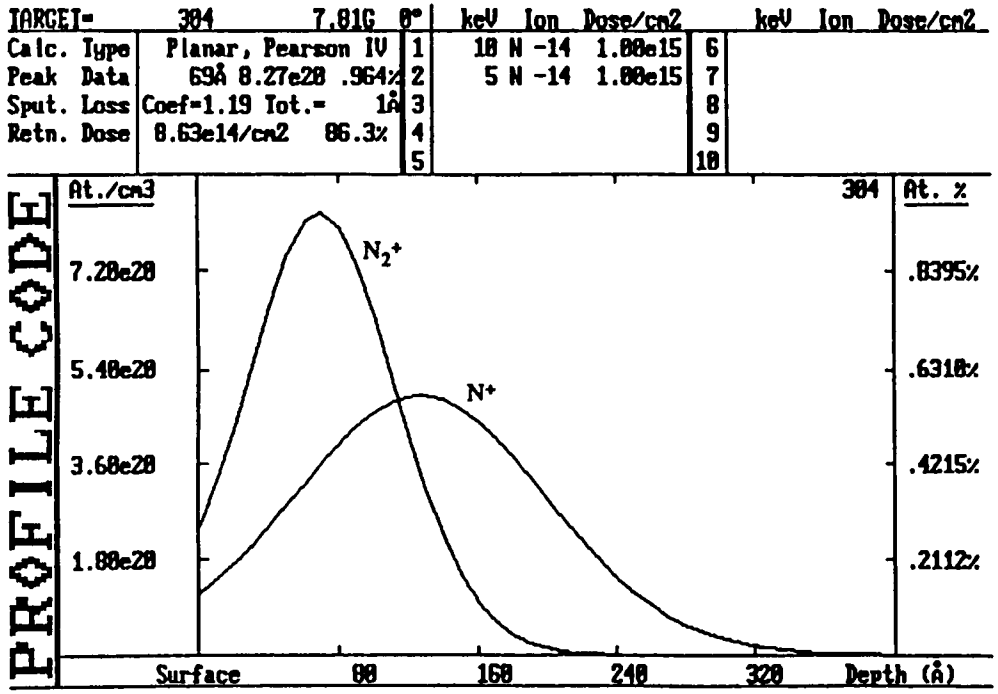

Figure 112. PROFILE code simulation of retained dose profile for 1 x 10^{15} ions/cm^2 N implanted into 304L stainless steel at 10 kV.

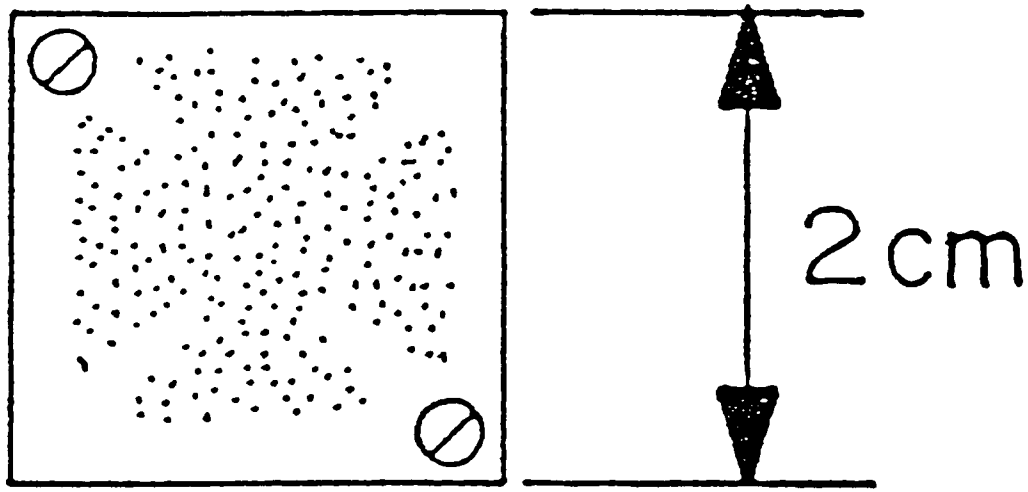

Figure 113. Discoloration pattern developed on 2 cm x 2 cm square sample holder during N PII.

believed to be caused by an electrostatic focusing of nitrogen ions onto specific regions of the sample during plasma ion implantation. The patterns may be a result of the combined effect of shadowing from the glass sleeve used to insulate the sample holder and electric field line concentration at the sample edges. The discoloration patterns were a strong function of the applied dose, increasing in nonuniformity with increasing nitrogen content. In an attempt to lessen the discoloration patterns, sharp edges and corners were avoided by grinding smooth radii on the 2 cm x 2 cm samples. However, the same patterns were still evident, although to slightly smaller extent.

304L Pitting Potential with 20 kV Nitrogen

A number of the 2 x 2 cm N-PII specimens did not undergo crevice corrosion at the epoxy / metal interface. For these samples, all implanted at an accelerating voltage of 20 kV, it is possible to directly determine the nitrogen effect on E_p. A comparison of E_p as a function of the implanted dose shows that the nitrogen acts to decrease the pitting potential for doses above 1 x 10^{15} nitrogen ions / cm^2 (Fig. 114, Table 7). As indicated in Figure 112, the maximum nitrogen concentration occurs near the oxide layer and is in the range of 1 at. % for this dose, after addition of the N_2^+ and N^+ ionic forms. This concentration parallels the optimum dose for pitting resistance improvements via other specimen preparation

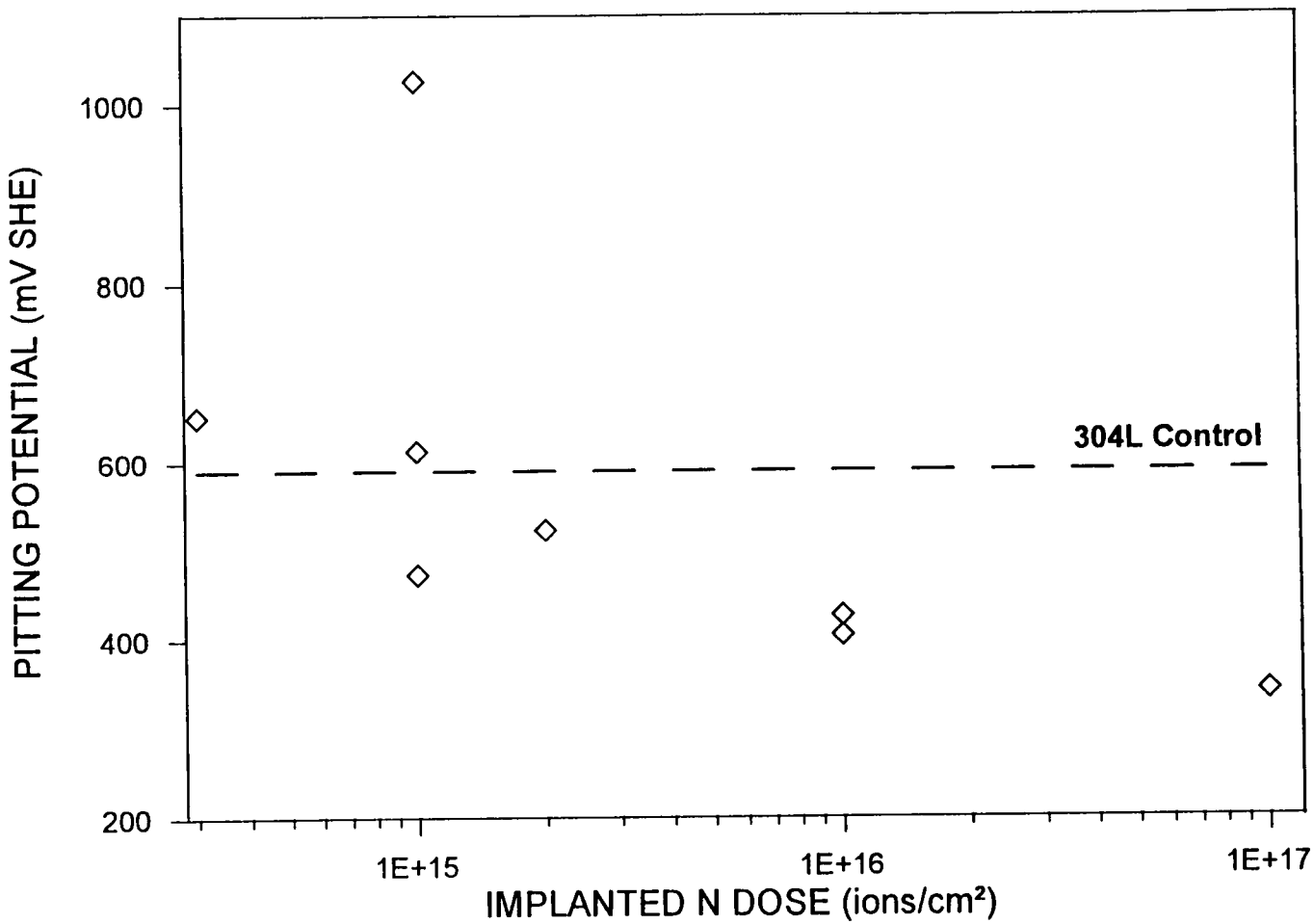

Figure 114. Pitting potentials of 304L stainless steel in deaerated 1 wt% NaCl as a function of applied N plasma ion implantation dose (20 kV implantation energy).

Table 7

Pitting Potentials of PII N 304L Stainless Steel in Deaerated 1 wt% NaCl

N Implantation Energy and Dose	$E_{p,1}$ (mV SHE)	$E_{p,2}$ (mV SHE)	$E_{p,3}$ (mV SHE)
Control	at least 577 (from Table 6)		
20 kV, 3e14	652		
20 kV, 1e15	472	613	1026
20 kV, 2e15	523		
20 kV, 1e16	426	404	
20 kV, 1e17	341		

procedures, as will be discussed. It also coincides with the concentration reported by Magdowski and Speidel (36), for which higher N contents lead to Cr_2N formation. Chromium nitride formation at doses above 1 x 10^{15} would have a seriously detrimental impact on the alloy's passivity, resulting in a successive lowering of E_p with additional nitrogen, as seen in Figure 114. The polarization behavior of a 20 kV 1 x 10^{17} ions / cm^2 implant exhibiting a reduced pitting potential is shown in Figure 115.

The non-uniform nitrogen coverage is manifested in two ways when analyzing these pitting results. First, post-pitting corrosion test microscopy indicated that several of the samples exhibited a pit location density that varied in the same systematic manner as seen in the surface discoloration. Usually, the center of the specimen area is pit free. This is the most homogenous area in terms of discoloration on the higher dose specimens. Therefore, the pitting distribution supports the evidence from surface discoloration that there is nonhomogenous dose coverage during implantation. Secondly, the pitting potential measured at a dose 1 x 10^{15} varies widely on duplicate specimens (Fig. 116). Since pitting develops at the point of least resistance to the passivity breakdown mechanism, any nonuniformity of dose will lead to irreproducible results due to the variable placement of the corrosion test area as determined by the exposed window in the

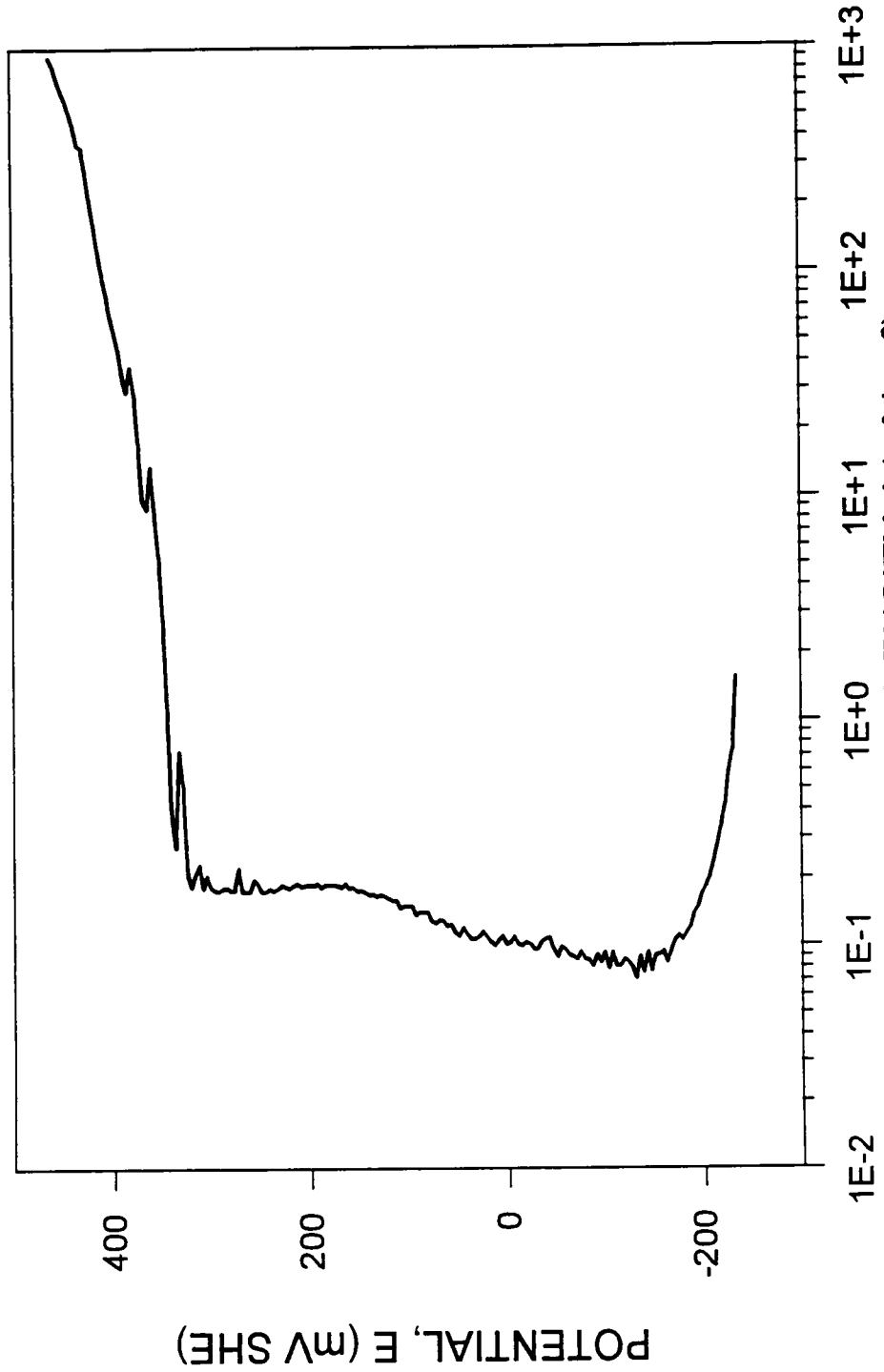

Figure 115. Anodic polarization behavior of 304L PII 1 x 10^{17} N ions/cm^2 in deaerated 1 wt% NaCl.

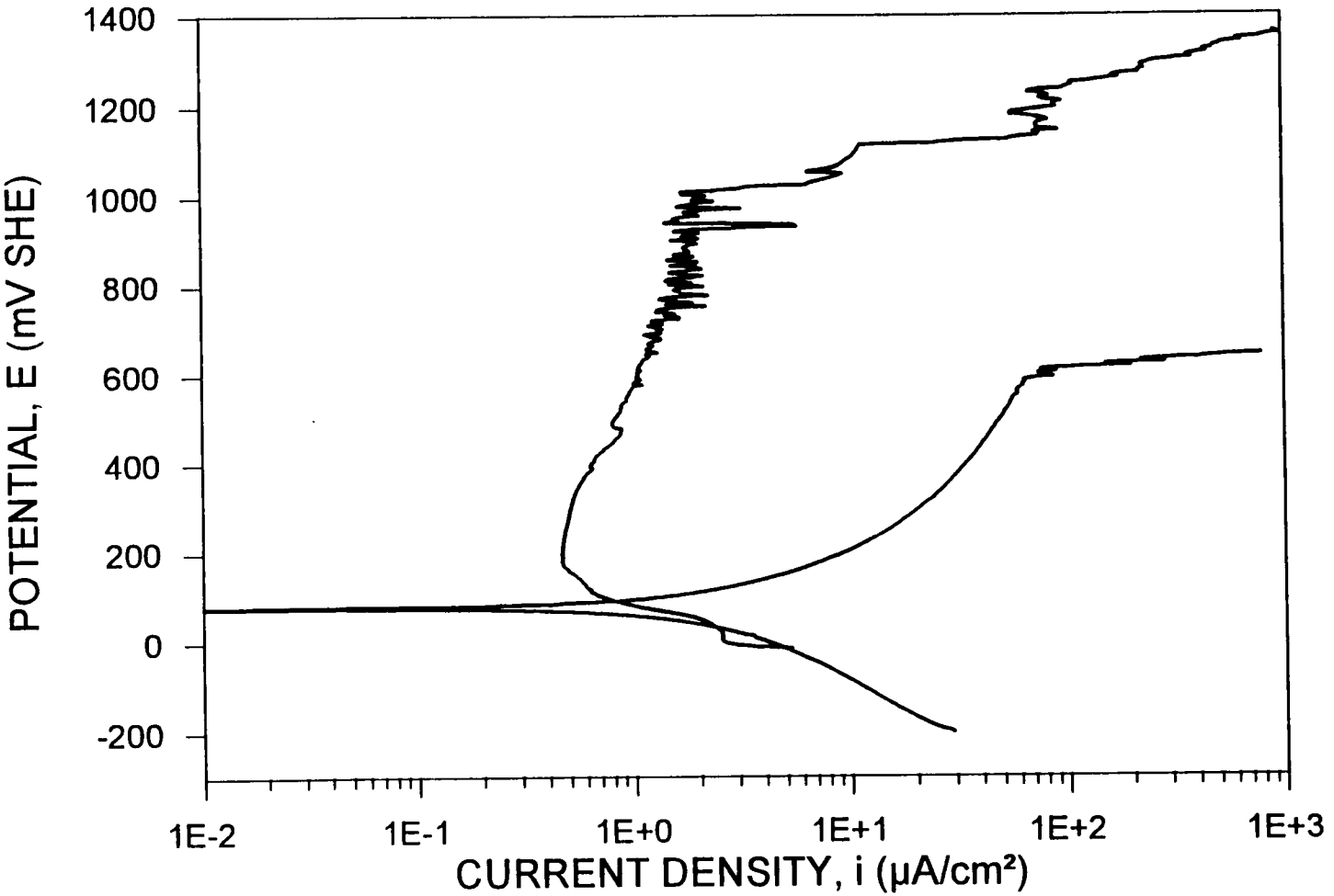

Figure 116. Two examples of the anodic polarization of 304L PII 20 kV 1 x 10^{15} N ions/cm^2 in deaerated 1 wt% NaCl.

epoxy mask. This irreproducibility is seen for other specimen preparation procedures, and is compounded by the crevicing tendency issue. However, Figure 116 does indicate that it is possible to enhance E_p with nitrogen implantation at 20 kV and a dose of 1 x 10^{15} or less.

304L Pitting Potential with Nitric Acid Passivation

In an effort to eliminate crevice corrosion at the metal / epoxy interface, specimens were prepassivated in a 50% HNO_3 + 50% H_2O bath at 55 °C for 30 minutes prior to application of the epoxy coating. Due to the highly oxidizing nature of the nitric acid, the free corrosion potential of 304L in this solution is well above the passivation potential. The passive film formed will restrict solution access to the crevice and limit the crevice effect on the breakdown potential. In an attempt to address the PII-N dose uniformity problem, a second sample holder (Fig. 41) was constructed. Inspection of the discoloration and pitting patterns generated when using the original sample holder indicated that a small area of uniform dose was generated in the center of the exposed specimens. The second sample holder was designed to take advantage of this condition by enlarging the surface area to 5.08 cm x 5.08 cm, thereby also enlarging the uniform area. The corrosion specimens were then mounted onto this central region as shown in Figure 41. The large backing plate was first implanted with a

nitrogen dose of 1 x 10^{18} N ions / cm^2. Figure 117 shows the discoloration pattern formed, which does indicate a large central uniform area.

Anodic polarization of these specimens shows that highly elevated pitting potentials can be achieved, both in the implanted and control states (Fig. 118). This augmentation of the passive behavior is a consequence primarily of the nitric acid passivation and not the redesigned PII sample holder. During the HNO_3 immersion of 304L, significant enrichment of chromium occurs in the oxide as a result of selective iron dissolution (109). As shown in Figure 119 for a 304L passivation treatment in 30 % HNO_3 for 1 hr at 60 °C, the oxide Cr content accounts for 66 % of the total cationic weight in the film, while the alloy Cr content is 18.4 w/o. This specimen preparation is similar to the nitric acid prepassivation used in the present study (50 % HNO_3, 30 min., 55 °C), and a comparable chromium enrichment should result. An increasing Cr oxide content leads directly to ennoblement of the pitting potential (Fig. 120) (109), which is seen by the increased E_p values for the unimplanted controls in Figure 118.

The magnitude of the larger shift in E_p for the nitrogen implanted specimens may partially be due to a synergistic effect between the N implantation and the nitric acid passivation. Since some evidence exists for N promoting the retention of Cr

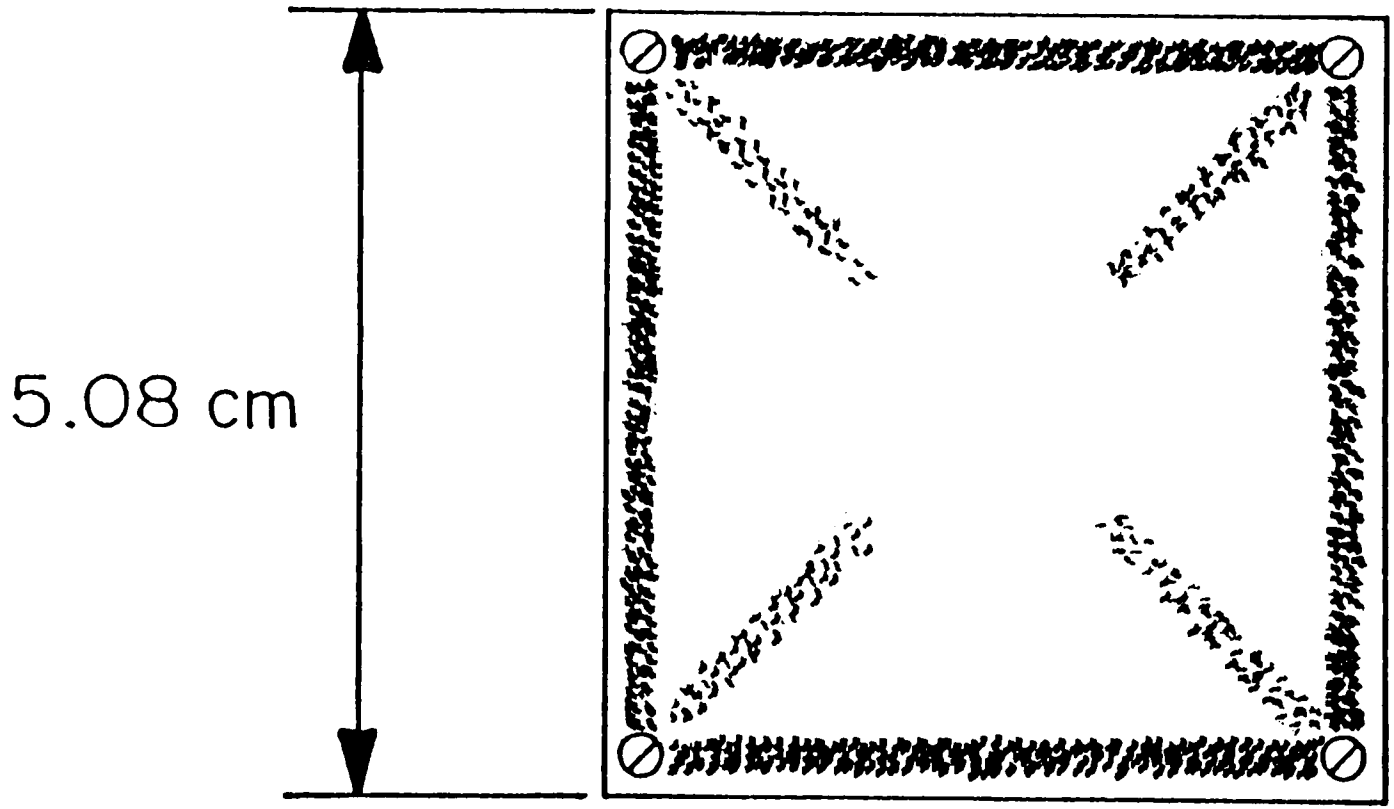

Figure 117. Discoloration pattern developed on 5.08 cm x 5.08 cm square sample holder during N PII.

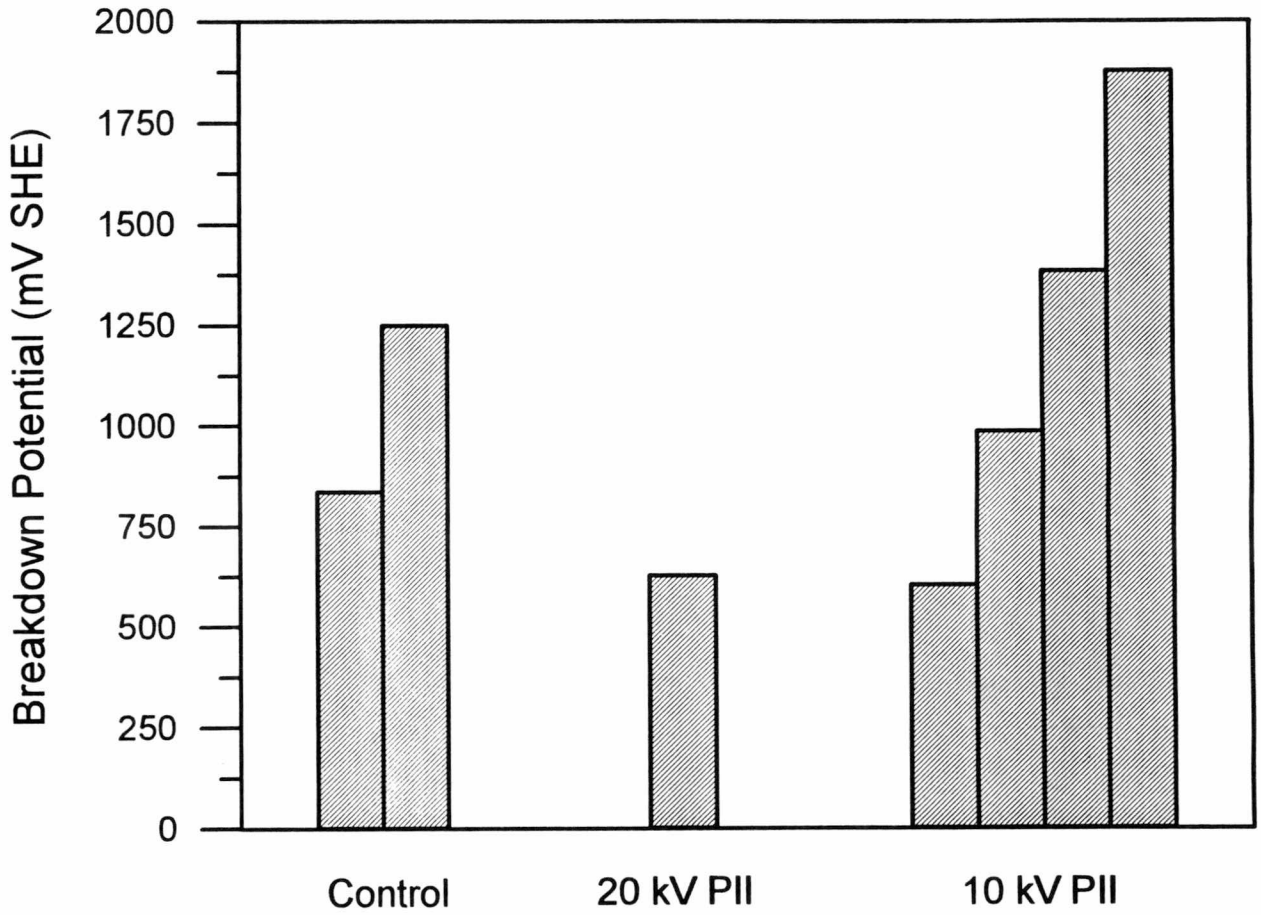

Figure 118. Breakdown potentials of 304L in deaerated 1 wt% NaCl after nitrogen implantation to 1x 10^{15} using the sample holder shown in Figure 41, and after applying the HNO_3 prepassivation treatment.

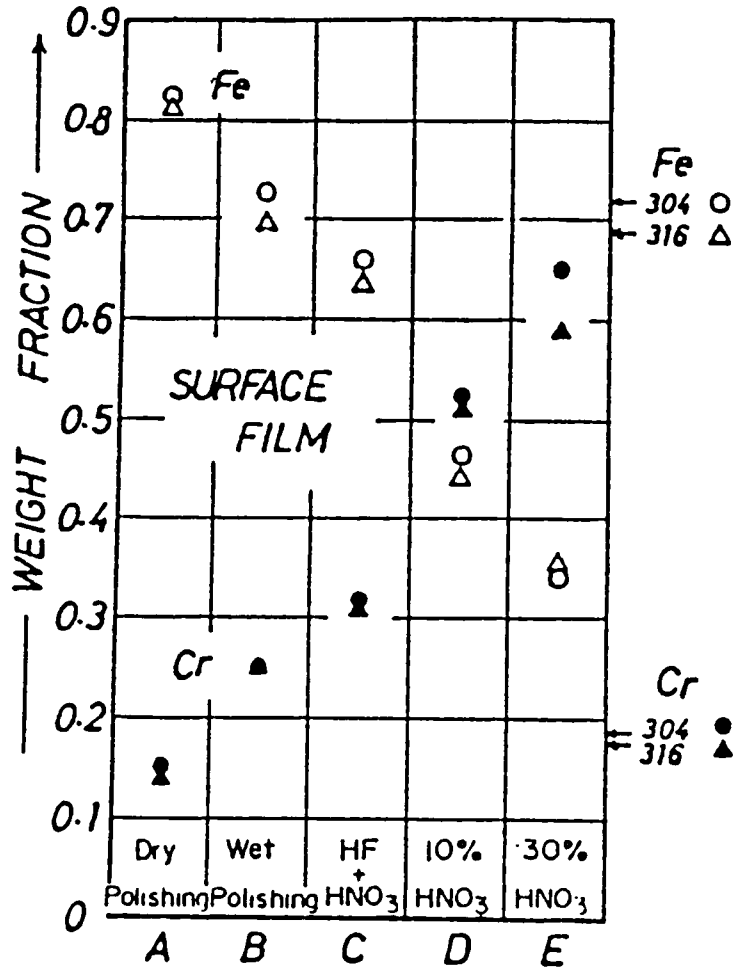

Figure 119. Weight ratios of Fe and Cr to the total weight of cations in 304 and 316 oxide films as a function of surface treatment. [(A) SiC 500 grit, (B) SiC 500 grit, (C) <5% HF + < 5% HNO_3 for 40-90 min. at 60 °C, (D) 10% HNO_3 for 1 hr at 60 °C, (E) 30% HNO_3 for 1 hr at 60 °C.

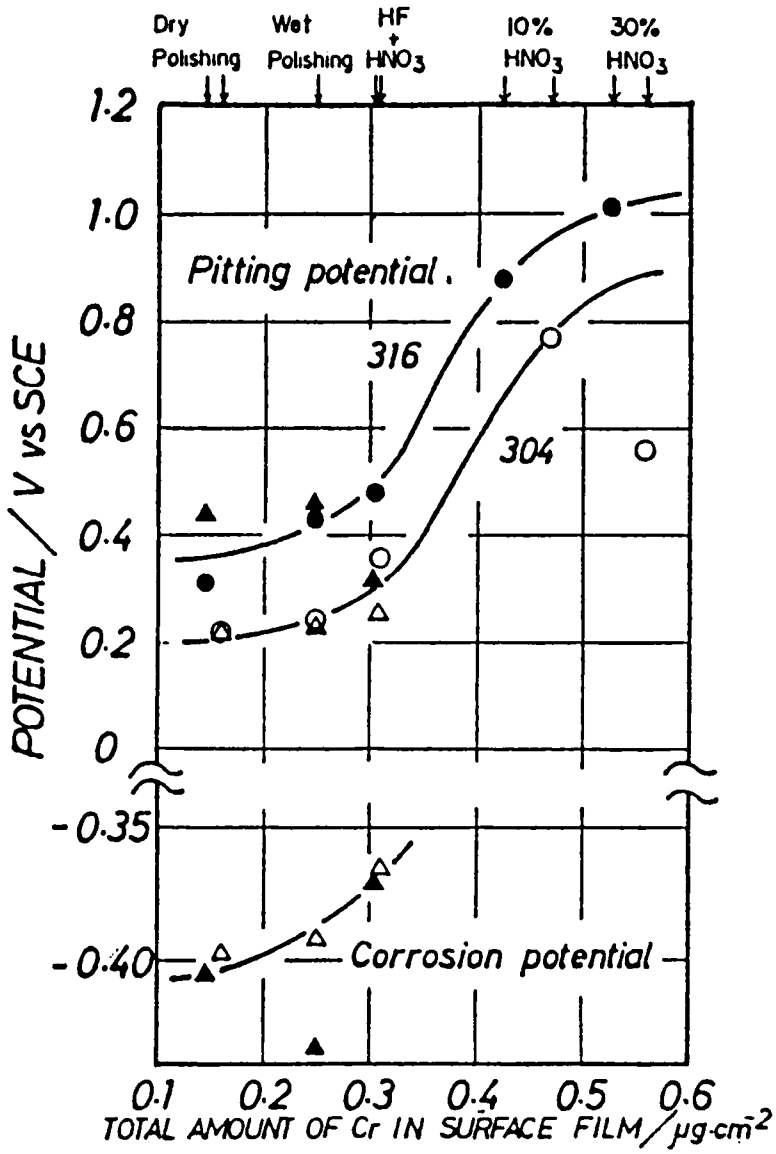

Figure 120. Relationship between the pitting potential of 304 and 316 stainless steels in 3.5 wt% NaCl solution and the total amount Cr in the oxide. [Black symbols are for 316, white for 304]

in the passive film (45,46), the implanted species may act to further increase the pitting potential by an additional elevation of the oxide chromium content. Alternatively, loss of base material to the oxide may result in elevating the N peak concentration nearer to the surface, enabling this region to more actively contribute N to the surface during passive corrosion conditions. The effect of surface Cr enrichment is demonstrated in Figure 121, where polarization scans of prepassivated alloys, with and without N implantation (curves A and B, respectively), are shown. The pitting potential of +1878 mV (SHE) for the N-implanted specimen is indicative of the cooperative effect between nitric acid passivation and nitrogen plasma ion implantation.

The wide variation in measured E_p values shown in Figure 118 can be traced to experimental variables involved in the implantation and prepassivation processes which are difficult to control precisely throughout multiple comparative tests. The remaining inhomogeneity in N dose distribution on the surface may lead to varying chromium oxide contents across the surface. Secondly, isothermal control of the warm nitric acid bath was difficult due to the method of heating utilized (hot plate). This can also lead to variations in the amount of Cr surface enrichment realized in different tests.

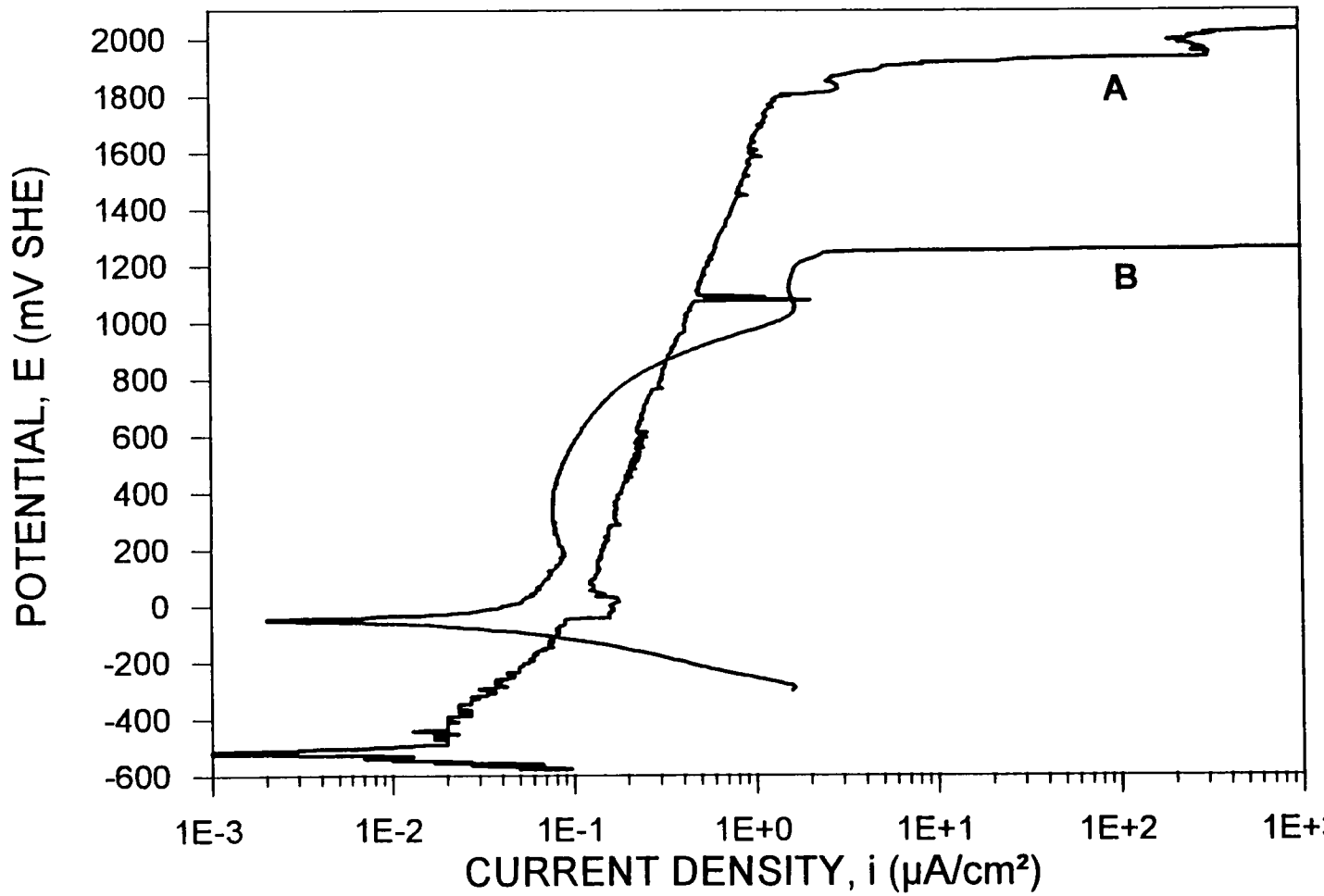

Figure 121. Anodic polarization behavior of (A) HNO_3-prepassivated PII 10 kV 1 x 10^{15} N ions/cm2, and (B) HNO_3-prepassivated control 304L.

304L Pitting Potential with Manual Oxide Removal

Anodic polarization of prepassivated 304L in deaerated 1 wt. % NaCl conveys the misleading proposition that pitting potentials as high as 1878 mV (SHE) are possible after nitrogen implantation. The pitting potential elevation which arises from increased oxide chromium content can be separated from the nitrogen effect by removal of the film prior to polarization testing. This must be achieved while maintaining the oxide at the epoxy / metal interface to protect against crevice corrosion. One method for manual oxide removal is to apply a fine abrasive to the surface such as 1 μm diamond paste after removal from the nitric acid solution.

A comparison of E_p as a function of the implanted dose for such manually polished samples (Fig. 122, Table 8) shows that a significant scatter remains, with pitting potentials varying by approximately 760 mV at a dose of 1 x 10^{15} ions / cm^2. However, the first reliable and repetitive evidence of significant passivity enhancement is noted with nitrogen additions. An example of the anodic polarization behavior of the unimplanted material is shown in Figure 123, for which an average pitting potential of 747 mV (SHE) was found. Confirmation of the possible formation of chrome nitrides at high doses is seen by the dramatic decrease in E_p to 349 mV (SHE) at a dose of 1 x 10^{18} (Fig.

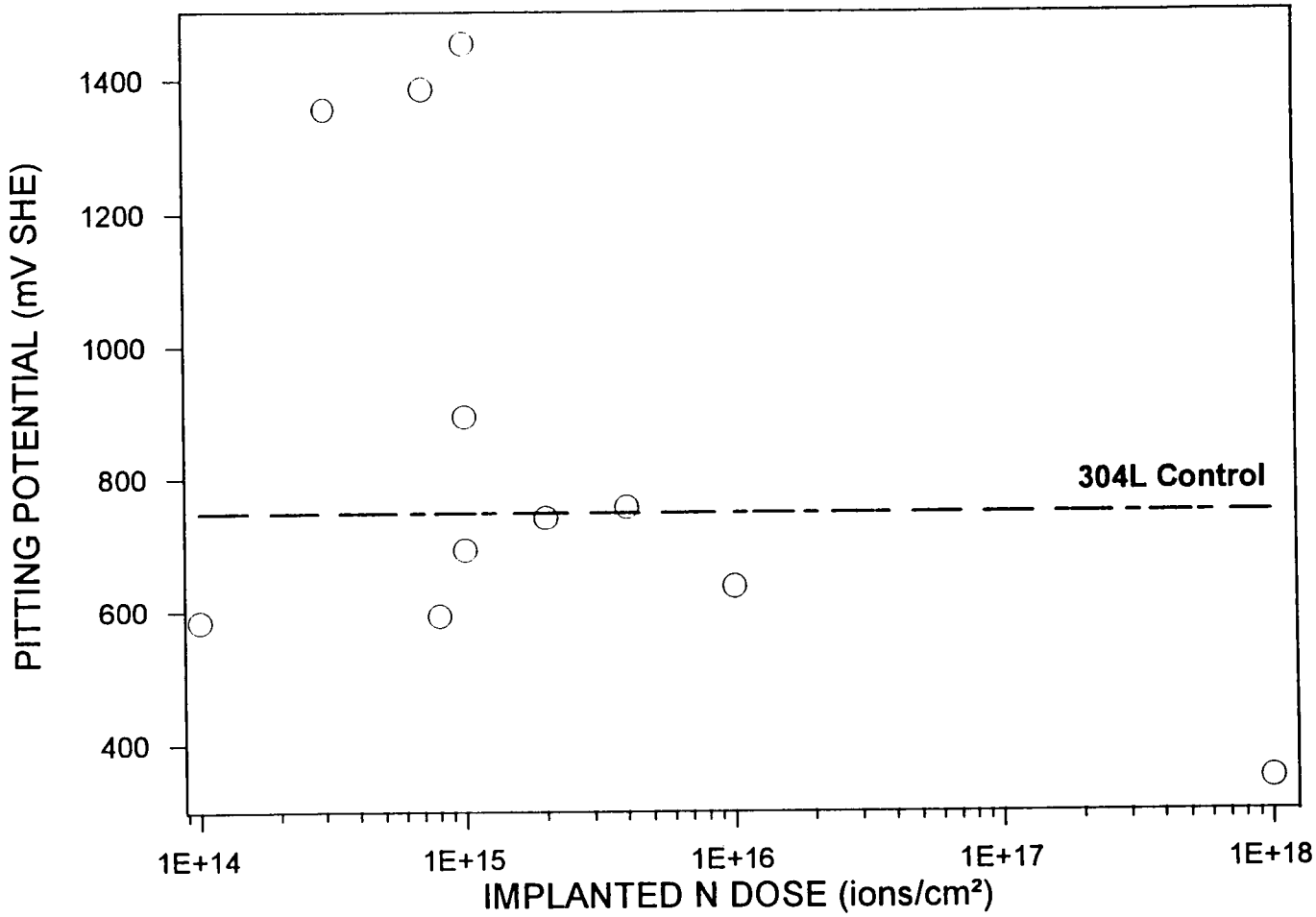

Figure 122. Pitting potentials of 304L stainless steel in deaerated 1 wt% NaCl as a function of applied N plasma ion implantation dose at 10 kV, after HNO_3 prepassivation and manual oxide film removal.

Table 8

Pitting Potentials of PII N 304L Stainless Steel in Deaerated 1 wt% NaCl with Manual Oxide Removal

N Implantation Energy and Dose	$E_{p,1}$ (mV SHE)	$E_{p,2}$ (mV SHE)	$E_{p,3}$ (mV SHE)	$E_{p,4}$ (mV SHE)
Control	638	766	782	802
10 kV, 1e14	584			
10 kV, 3e14	1357			
10 kV, 7e14	1386			
10 kV, 8e14	593			
10 kV, 1e15	691	893	1453	
10 kV, 2e15	740			
10 kV, 4e15	756			
10 kV, 1e16	636			
10 kV, 1e18	349			

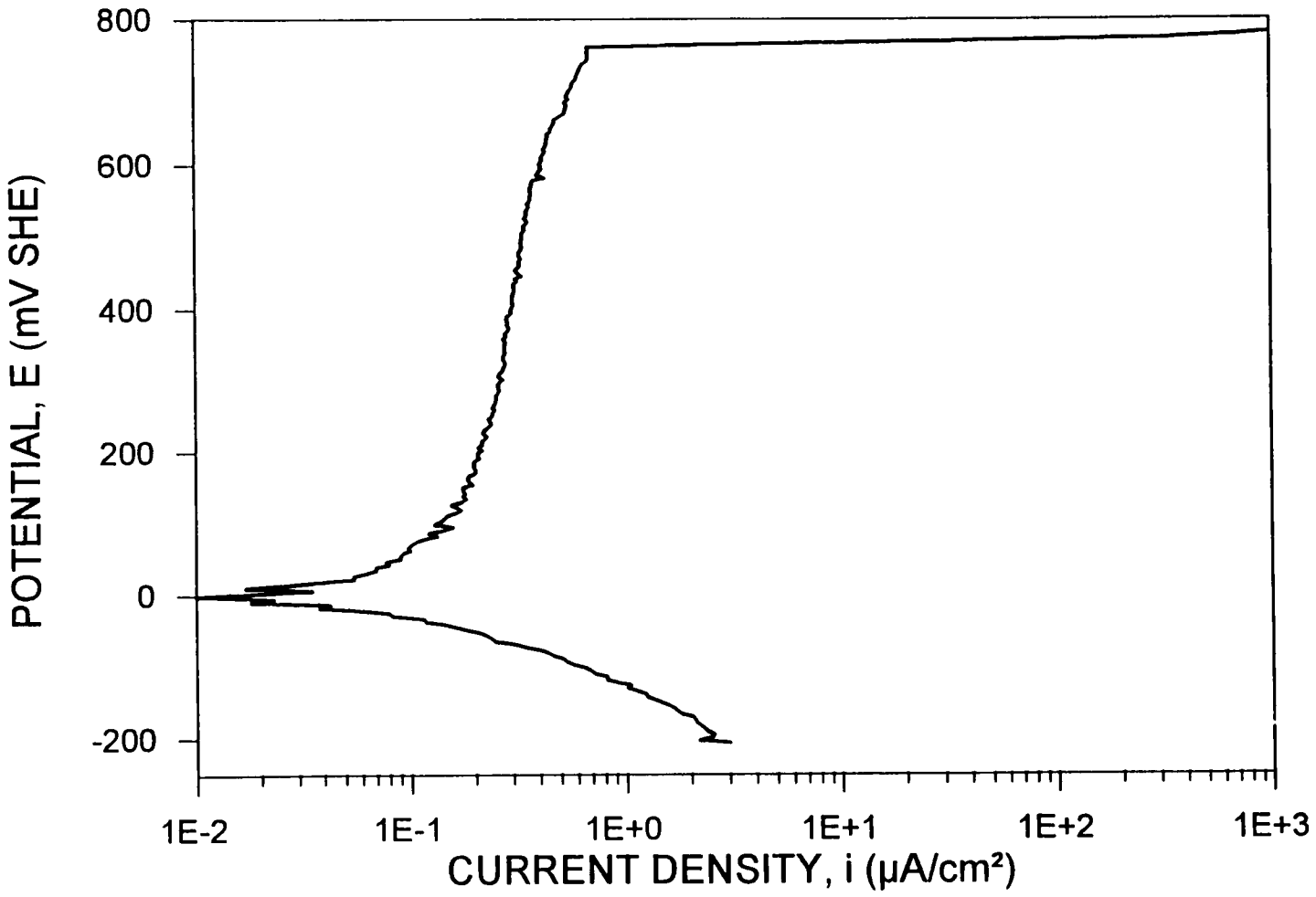

Figure 123. Anodic polarization of 304L in deaerated 1 wt% NaCl, after HNO_3 prepassivation and manual oxide film removal.

124). Several examples of positive increases of 600-700 mV are seen in the 3 x 10^{14} to 1 x 10^{15} ions / cm^2 dose range. This is consistent with the result from the non-passivated test in which an elevated E_p value was found for a dose of 1 x 10^{15}.

In Figure 125 is seen two examples of N-implanted alloys (3 x 10^{14} and 7 x 10^{14}) exhibiting elevated pitting potentials. Similar polarization behaviors are observed in that a somewhat smooth increase in current density is seen until around 500 mV (SHE), at which point a sudden increase is seen. At approximately 650 mV (SHE), a decrease in i_{pass} occurs. This lower passive current density, in the 10 μA / cm^2 range, demonstrates less stability than the passive region which precedes the current density surge. Finally, pitting commences at 1340 and 1380 mV (SHE). Such similarity in passive behavior between tests implies that it originates from a common physical process. The increase in pitting potential of ~600 mV is analogous to the effect found by Chyou and Shih for a low-alloy steel in an identical electrolyte (41). An order of magnitude increase in i_{pass} relative to the control behavior (Fig. 123) indicates that, although the alloys resistance to localized passivity breakdown has been increased, the corrosion penetration rate under passive conditions will also increase by nitrogen implantation. This can probably be linked to the high concentration of defects

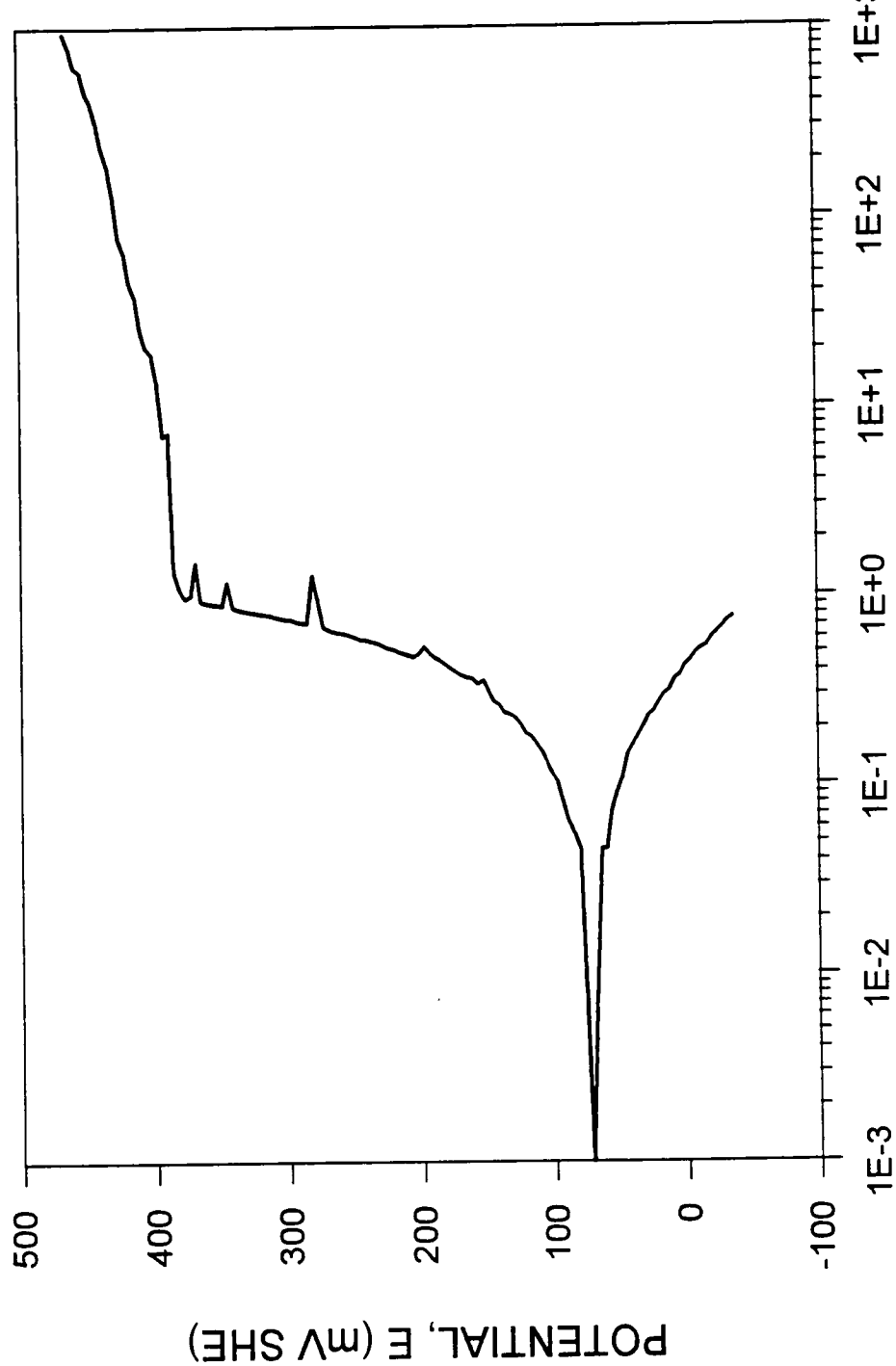

Figure 124. Anodic polarization of 304L PII 10 kV 1 x 10^{18} N ions/cm^2 in deaerated 1 wt% NaCl, after HNO_3 prepassivation and manual oxide film removal.

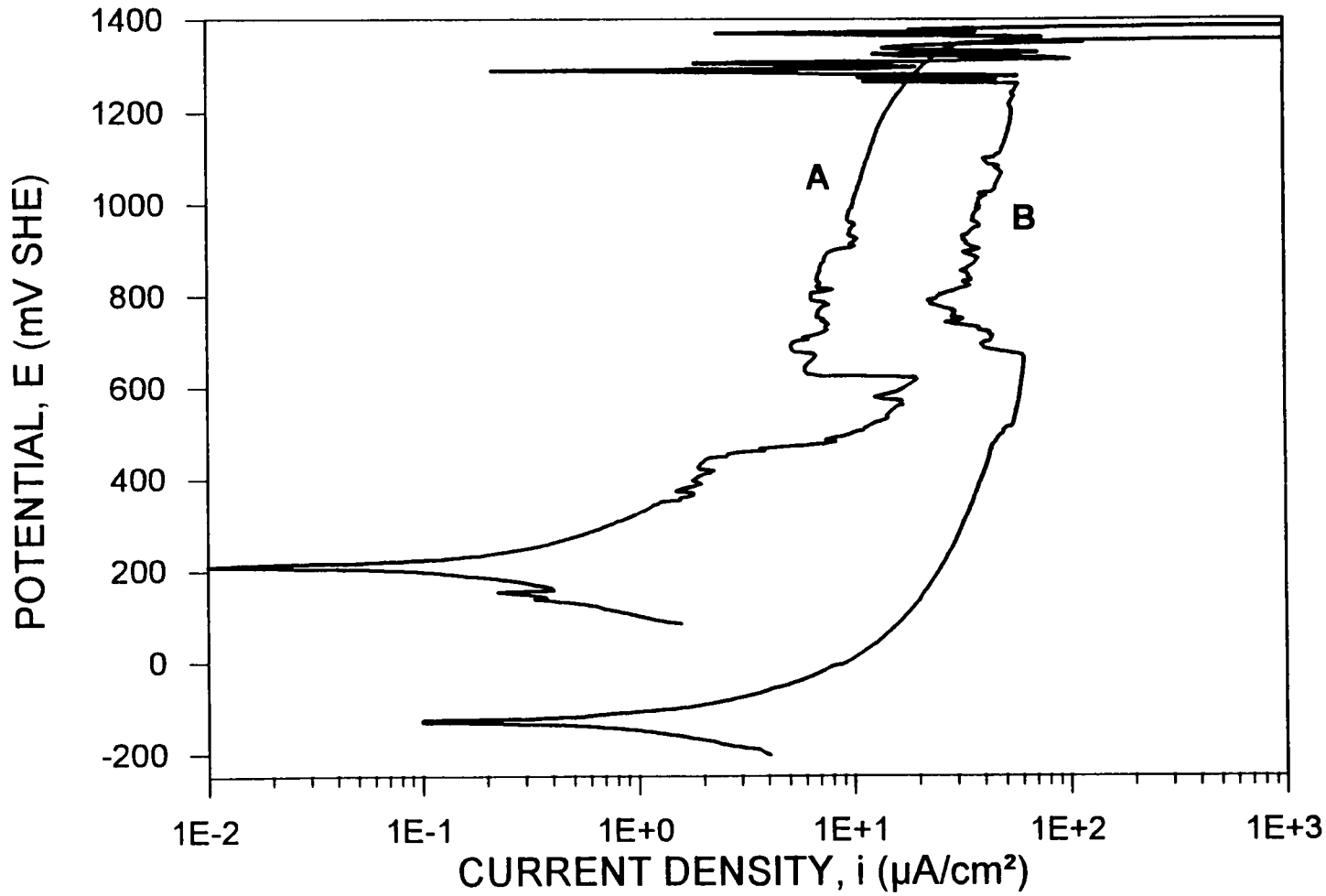

Figure 125. Anodic polarization of (A) 304L PII 10 kV 3 x 10^{14} N ions/cm^2 and (B) 304L PII 10 kV 7 x 10^{14} N ions/cm^2 in deaerated 1 wt% NaCl, after HNO_3 prepassivation and manual oxide film removal.

produced by ion implantation. However, this is a much more manageable in-service problem than that represented by the onset of pitting attack.

The source of the irreproducibility in the measurement of E_p can most likely be traced to a combination of the previously mentioned variables, nitric acid bath temperature regulation and continuing dose distribution nonuniformity, and also lack of control of the abrasion penetration depth during oxide removal. A rough estimate of the maximum material removal depth by an abrasive compound is 10% of the abrasive particle size. For 1 μm diamond paste, this corresponds to 1000 angstroms. From Figure 112, the nitrogen implantation depth is 300 angstroms for a 1×10^{15} dose. Therefore, even assuming that a light application of the diamond paste penetrates less than 1000 angstroms, it is seen that the entire N dose can be locally removed by the manual cleaning process. Since the pressure and length of time of the manual diamond paste application can be controlled with limited accuracy, a number of the specimens were likely affected in this way. As seen in Figure 122 and Table 8, these samples would then display a pitting potential matching the control value since pitting will initiate at sites of complete N removal.

304L Pitting Potential with Potentiostatic Etching

During implantation, the ion depth distribution assumes a nearly Gaussian profile assuming a constant accelerating potential. The surface of the alloy receives a relatively small dose as compared to the maximum concentration, which resides at some depth which is determined by the implantation energy, the implanted species, and the substrate. Although the nitric acid passivation removes layers of material by oxidation, further stripping of alloy layers should move the nitrogen peak closer to the surface. Enhancement of the surface N concentration enables this region to more actively contribute N to the oxide during passive corrosion conditions. One method for removing surface material is by potentiostatic etching, in which the alloy is held at a constant potential in an aggressive solution. The amount of metal removed can then be easily controlled and monitored by charge integration of the resulting current density. A convenient solution for etching 304L stainless steel is a combination of 1 N H_2SO_4 and 0.01 M KSCN. 304L actively corrodes with an extremely high anodic loop current density, which can be used to quickly etch the alloy surface. This solution forms the basis of the Electrochemical Potentiokinetic Reactivation (EPR) test (ASTM G108-92) on 304 stainless alloys for sensitization evaluation.

The potentiodynamic polarization of 304L in the deaerated sulfuric acid / potassium thiocyanate electrolyte is shown in Figure 126. The anodic current density quickly accelerates at potentials above E_{corr}, rising to a peak of 4 x 10^4 μA / cm^2. This current density would result in an excessively high etching rate. Therefore, a potential below the anodic peak (-104 mV (SHE)) was selected for potentiostatic control of the etching process. Under control at this potential, the current density on a 10 kV 1 x 10^{15} N implant typically rises to between 500 and 1500 $\mu A/cm^2$ in 1 to 4 minutes, an example of which is shown in Figure 127. This sample, upon current integration, is calculated to have undergone a corrosion penetration of 225 angstroms. Subsequent anodic polarization of the same sample in deaerated 1 wt. % NaCl (Fig. 128) shows an elevation of E_p to 1063 mV (SHE). Potentiostatic etching to greater depths resulted in pitting potentials in the vicinity of the control value (Table 9). From Figure 112, the implantation depth at this dose is limited to 300 angstroms, demonstrating that the lower pitting potentials are a result of the complete removal of all implanted nitrogen. The conclusion that the enhanced E_p value is not due to oxide chromium enrichment during potentiostatic etching can also be drawn. The enhanced passivity as a result of light etching was difficult to reproduce for the reasons discussed previously. However, its inclusion is important for continuation of the pattern of evidence in which pitting resistance enhancements

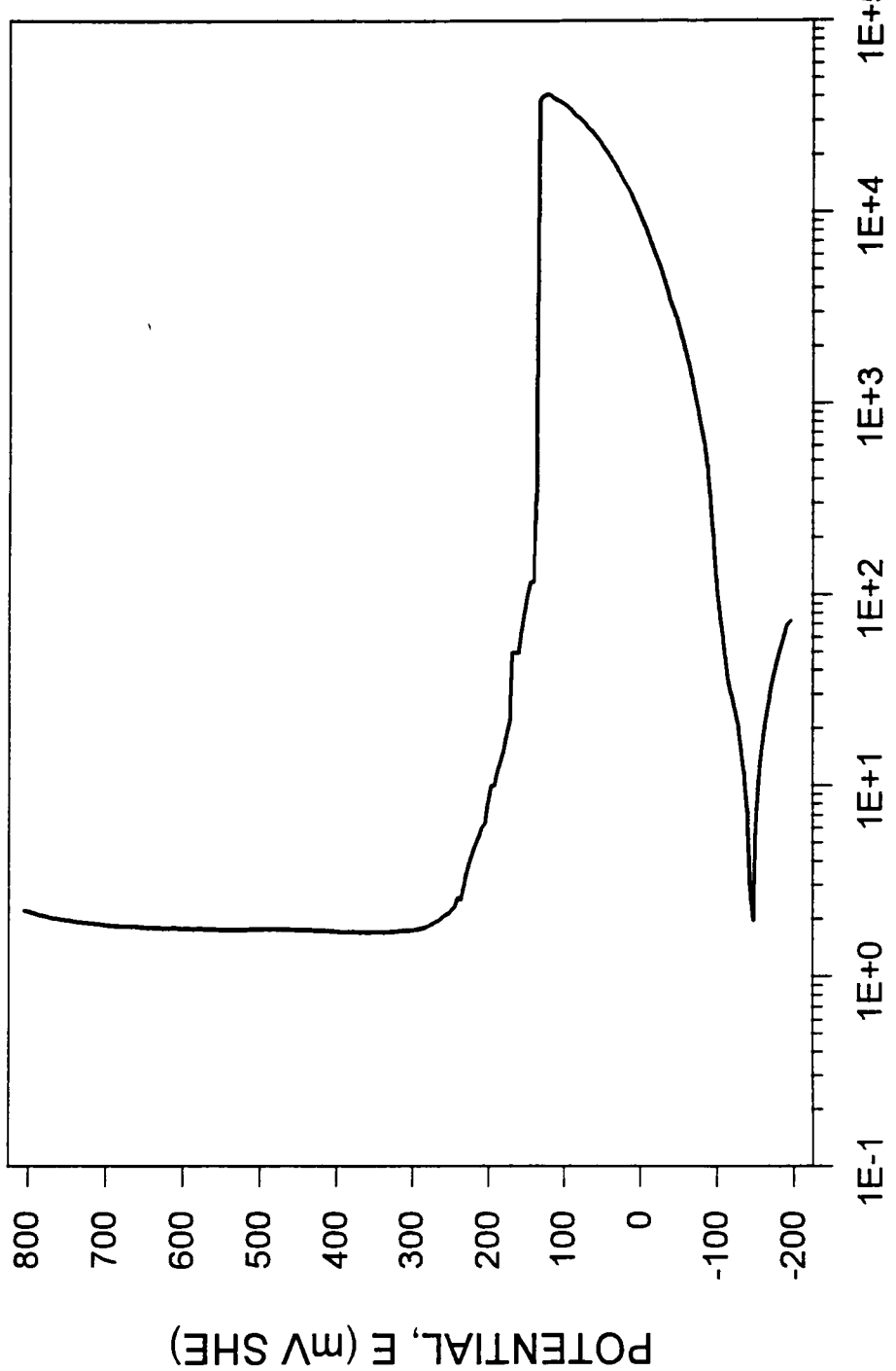

Figure 126. Anodic polarization of 304L in deaerated 1 N H_2SO_4 and .01 M KSCN.

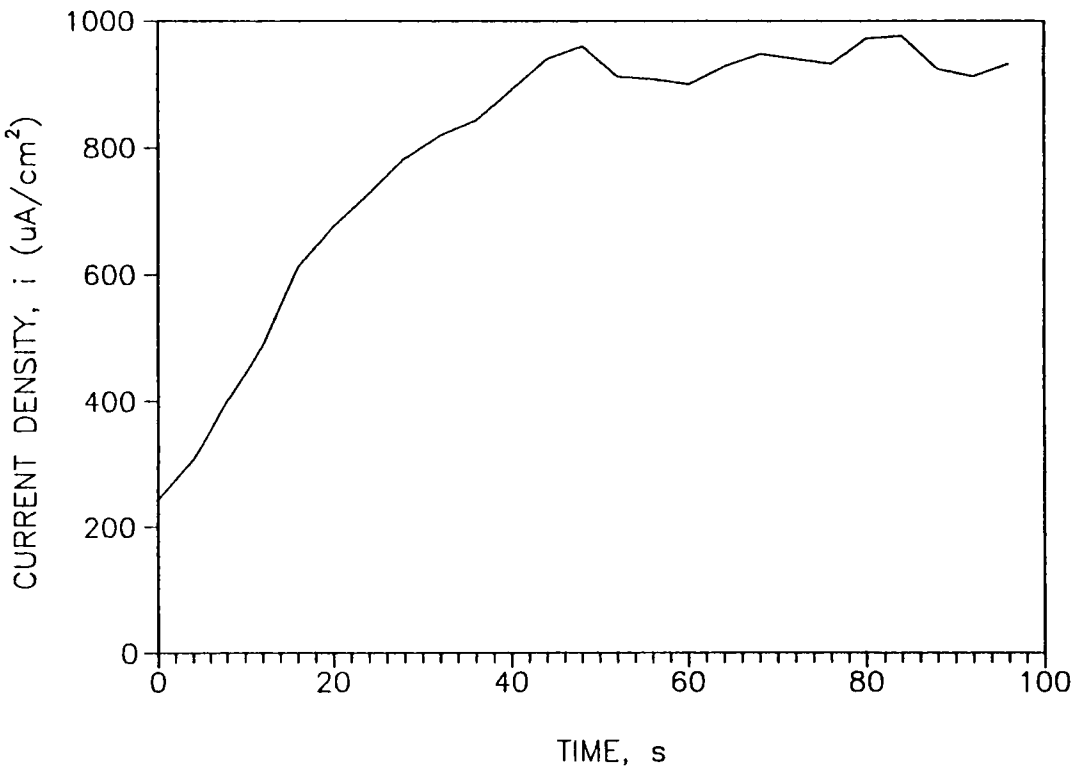

Figure 127. Current density behavior of 304L PII 1 x 10^{15} N ions/cm^2 during potentiostatic etching in deaerated 1 N H_2SO_4 and .01 M KSCN at -104 mV (SHE).

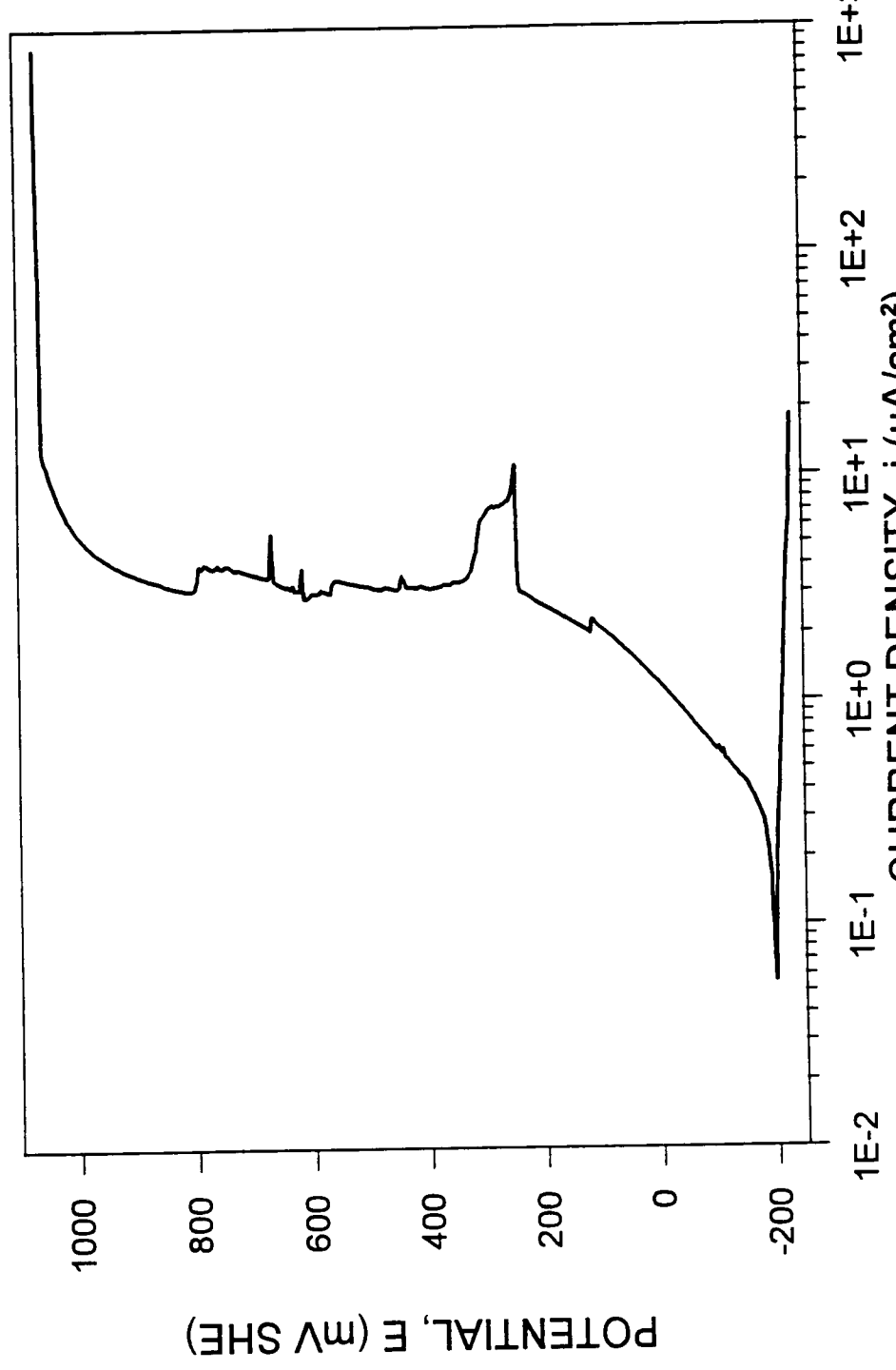

Figure 128. Anodic polarization behavior of 304L PII 10 kV 1 x 10^{15} N ions/cm^2 in deaerated 1 wt% NaCl after potentiostatic etching removal of 225 angstroms from the surface.

Table 9

Pitting Potentials of PII N 304L Stainless Steel in Deaerated 1 wt% NaCl after Potentiostatic Etching
20 kV Implantations, Dose of 1e15 N

Etch Depth (angstroms)	$E_{p,1}$ (mV SHE)	$E_{p,2}$ (mV SHE)
200	642	1063
400	604	652
800	626	

with N additions are found for a variety of specimen preparation procedures, while unimplanted alloys are always unaffected.

304L Pitting Potential with Modified PII Sample Holder

Further refinement of the plasma ion implantation sample holder design was pursued to deal with the surface discoloration nonuniformity at the specimen edges and diagonals, and the pitting potential measurement discrepancies that persist with the large square backing plate geometry. Co-workers of Dr. J. R. Conrad, inventor of the PII process, at the University of Wisconsin-Madison have indicated (105) that dose nonuniformity problems are encountered in the majority of plasma implantation processes. They have previously found that modification of the target to a circular geometry circumvents most of the dose distribution problem. However, concentric circles of non-uniformity can still result, mostly concentrated at the center and at the edges of the target.

A third PII sample holder (Fig. 42) was designed to capitalize on this geometry. A large diameter (8.35 cm) backing plate was used to increase uniformity and to provide multiple specimens from a single exposure. The samples were spatially arranged to avoid the center and edges of the exposed metal surface. The specimens were also recessed flush with the 304L backing plate to avoid the

projection of edges at which the electric field lines could concentrate. A circular backing plate was implanted with a nitrogen dose of 1 x 10^{17} N ions / cm^2. Figure 129 shows the discoloration pattern formed, which indicates significant nonuniformity near the periphery, but a large central uniform area. The concentric nature of the supposed N dose variation on a round sample is consistent with results found by other PII researchers (105).

Anodic polarization of the N-PII specimens implanted with this sample holder geometry was initially preceded by the nitric acid passivation and manual abrasive film removal treatments. A comparison of E_p as a function of the implanted dose (Fig. 130, Table 10) shows that large enhancements are achieved in the dose range around 1 x 10^{15} N ions / cm^2, although a significant scatter remains. This is the same dose range for which all previously discussed elevated pitting potentials were achieved. An electrochemical feature common to each of these specimens during polarization testing is a slight decrease in passive current density between 1025 mV (SHE) and E_p (Fig. 131). This characteristic seems to be a unique nitrogen signature. Among the proposed mechanisms of nitrogen-induced passivation, the decrease in i_{pass} at high potentials may support the proposition of N-Cr clustering increasing the chromium content in the passive film. In the 1 x 10^{15} to 5 x 10^{15} range, E_p is increased by at least 190 mV in

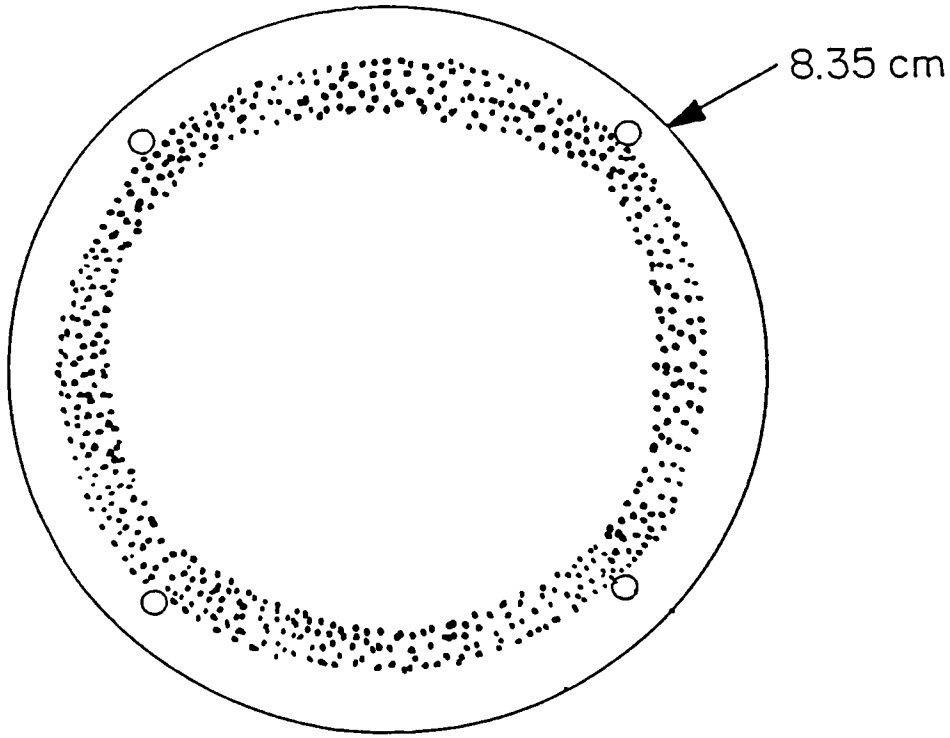

Figure 129. Discoloration pattern developed on 8.35 cm diameter round sample holder during N PII.

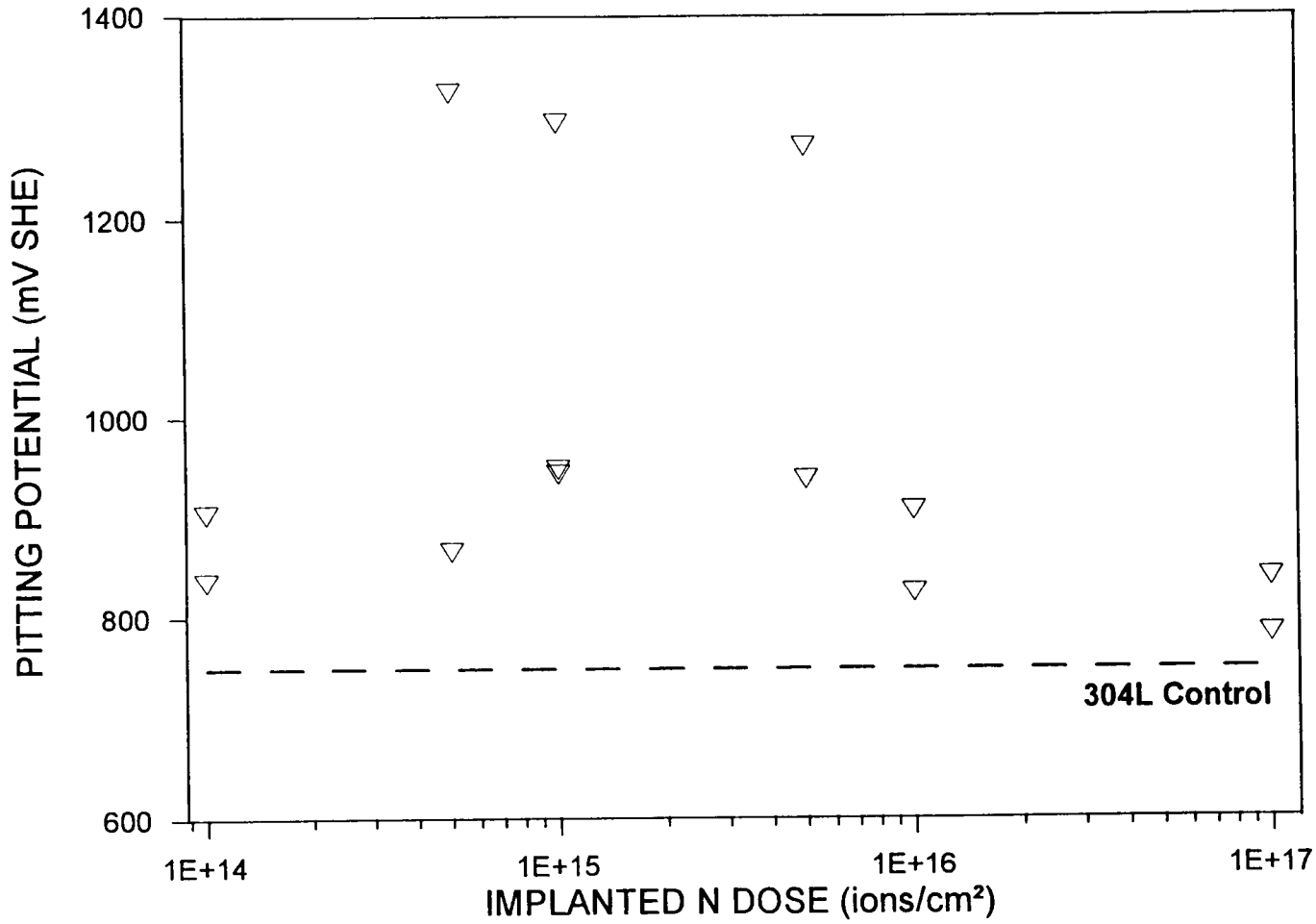

Figure 130. Pitting potentials of 304L stainless steel in deaerated 1 wt% NaCl as a function of applied N plasma ion implantation dose, after PII with large round sample holder (10 kV), HNO_3 prepassivation, and manual oxide film removal.

Table 10

Pitting Potentials of PII N 304L Stainless Steel in Deaerated 1 wt% NaCl
(Round Sample Holder)

N Implantation Energy and Dose	$E_{p,1}$ (mV SHE)	$E_{p,2}$ (mV SHE)	$E_{p,3}$ (mV SHE)
Control	747 (from Table 8)		
10 kV, 1e14	836	904	
10 kV, 5e14	866	1324	
10 kV, 1e15	943	948	1294
10 kV, 5e15	937	1270	
10 kV, 1e16	824	906	
10 kV, 1e17	781	838	

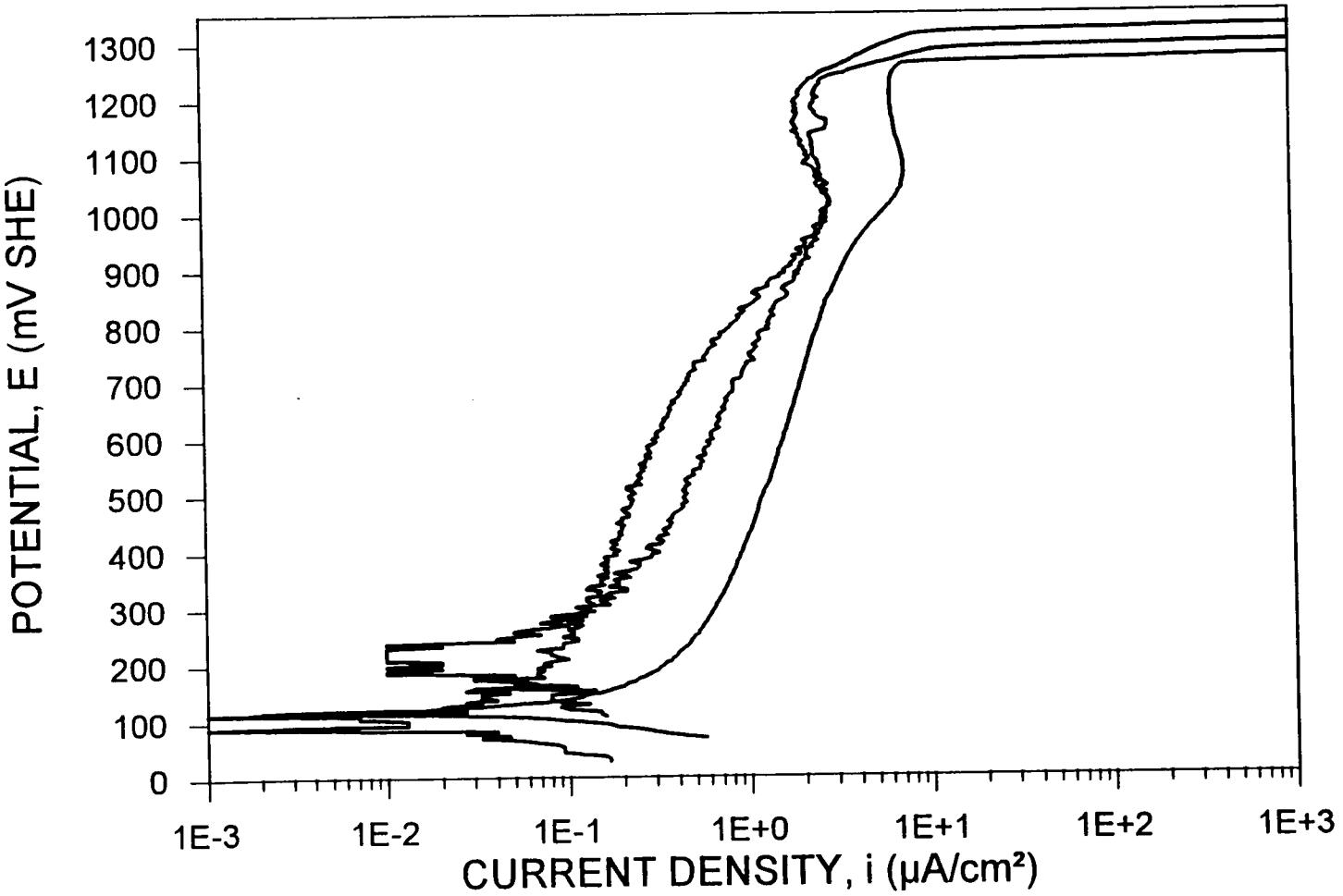

Figure 131. Three examples of anodic polarization of 304L, plasma ion implanted with N, in deaerated 1 wt% NaCl, after PII with large round sample holder (10 kV), HNO_3 prepassivation and manual oxide film removal. Doses correspond to the three highly elevated pitting potentials as seen in Figure 130.

each test. For all doses (10^{14} - 10^{17}) using the round, recessed sample holder geometry, E_p increases with nitrogen implantation.

Through successive modifications of the implantation process, it is thus shown that N implantation by PII is beneficial in enhancing the pitting corrosion resistance of 304L. However, the degree to which N bolsters 304L's pitting resistance is in question due to the remaining irreproducibility in the measured pitting potentials. The source of this discrepancy is thought to primarily be continuing limitations of the passivation / film removal processes, and not the non-uniformity of plasma ion implantation dose distribution.

304L Pitting Potential with Cathodic Cleaning Oxide Removal

An alternative method for removal of the high chromium nitric acid formed oxide was sought to address the remaining reproducibility problems. Cathodic cleaning, similar to that used in dissipating the passive film on Al 1100, was used in an attempt to remove the 304L oxide. Alloys held at -1259 mV (SHE) for 1 minute after nitric acid passivation did not disrupt the film formed, as seen by the subsequent rapid potential increase back to a passive E_{corr} (Fig. 132). Anodic polarization of these specimens all resulted in highly positive pitting potentials (Table 11) similar to those seen for alloys with no passive film removal. This

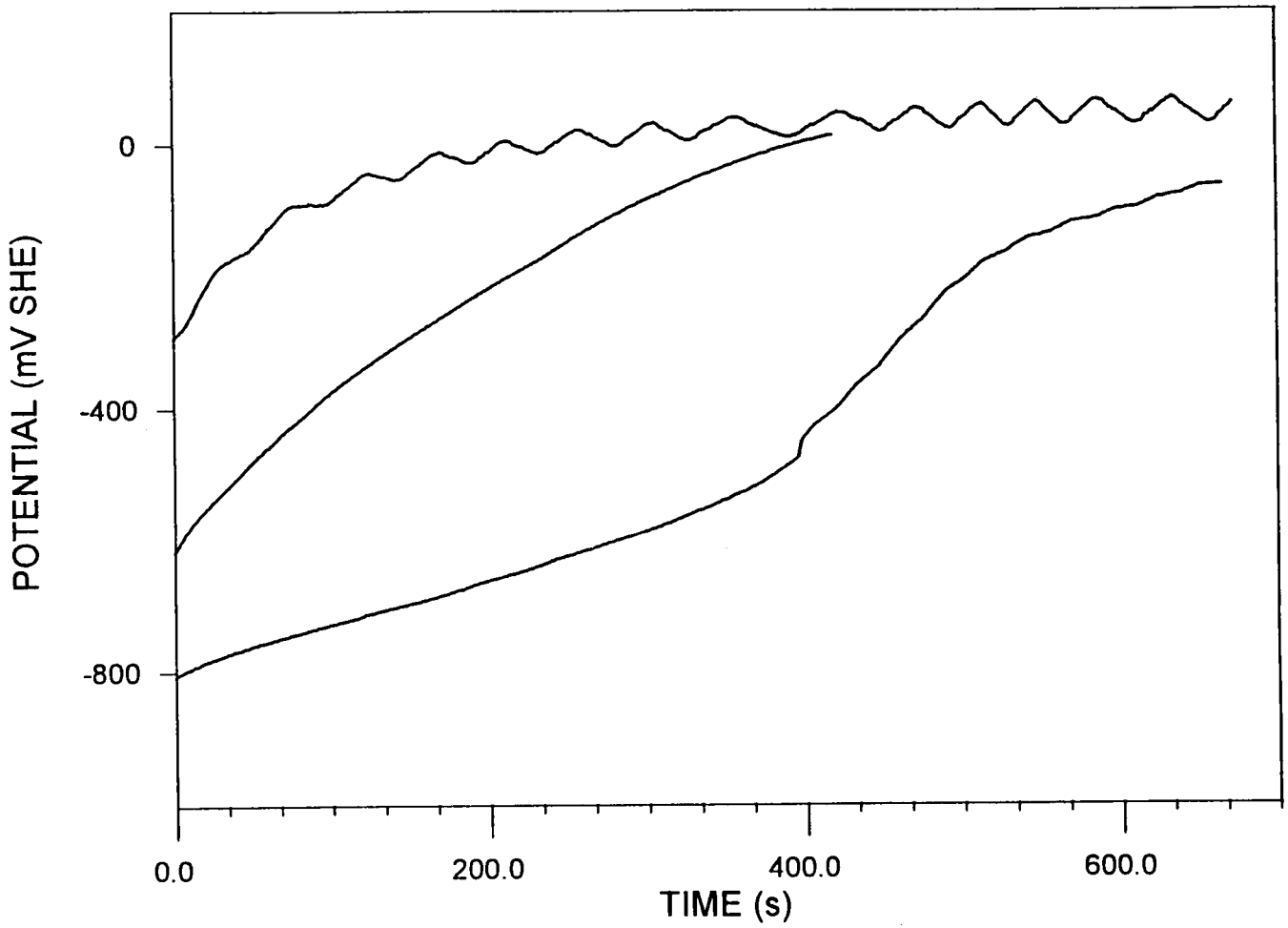

Figure 132. Three examples of the increasing corrosion potential of prepassivated 304L alloys after cathodic polarization at -1259 mV (SHE) for 1 minute.

Table 11

Pitting Potentials of PII N 304L Stainless Steel in Deaerated 1 wt% NaCl after Cathodic Cleaning at -1259 mV (SHE) for 1 minute

N Implantation Energy and Dose	$E_{p,1}$ (mV SHE)	$E_{p,2}$ (mV SHE)	$E_{p,3}$ (mV SHE)
Control	1231	1353	1373
10 kV, 2e15	1302	1388	1447

confirms that the nitric acid 304L oxide is undisturbed by cathodic cleaning at -1259 mV (SHE).

Lowering the potentiostatic control to -1509 mV (SHE) and holding for 20 minutes, however, does disturb the oxide. As seen in Figure 133, surfaces subjected to this treatment slowly increase in potential after release from cathodic control, and return to a more active steady state corrosion potential. Unfortunately, this more aggressive cathodic cleaning removes sufficient oxide from the epoxy / metal interface that crevice corrosion can again become a problem. Comparison of several control specimens showed that the breakdown potential does not depend on whether crevices or pits were formed (Fig. 134). Also, implanted alloys (10 kV, 2 x 10^{15} N ions / cm^2) which exhibited crevice formation showed that the E_{crev} corresponds to $E_{p,control}$. However, an implanted specimen which did not result in crevice formation had a much higher pitting potential. The anodic polarization behavior of this alloy (Fig. 135) mirrors that of the successful manually cleaned samples in the unique reduction of passive current density above 1000 mV (SHE). Once again, the pitting resistance of 304L is seen to be enhanced by nitrogen addition when crevice formation can be suppressed.

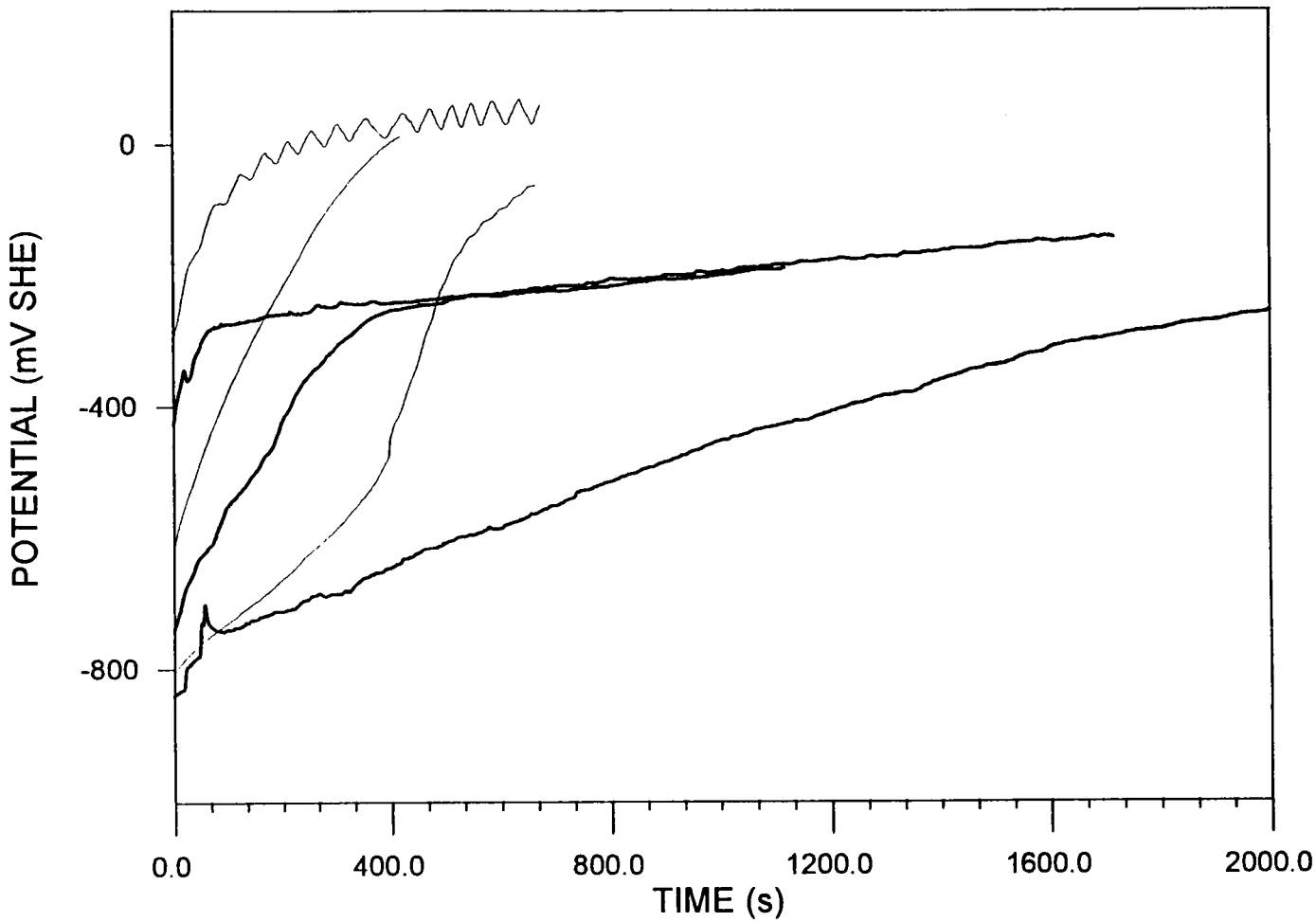

Figure 133. Three examples of the corrosion potential increasing to a more active E_{corr} on prepassivated 304L alloys after cathodic polarization at -1509 mV (SHE) for 20 minutes. Potential behaviors from Figure 132 are included with a lighter shading for comparison.

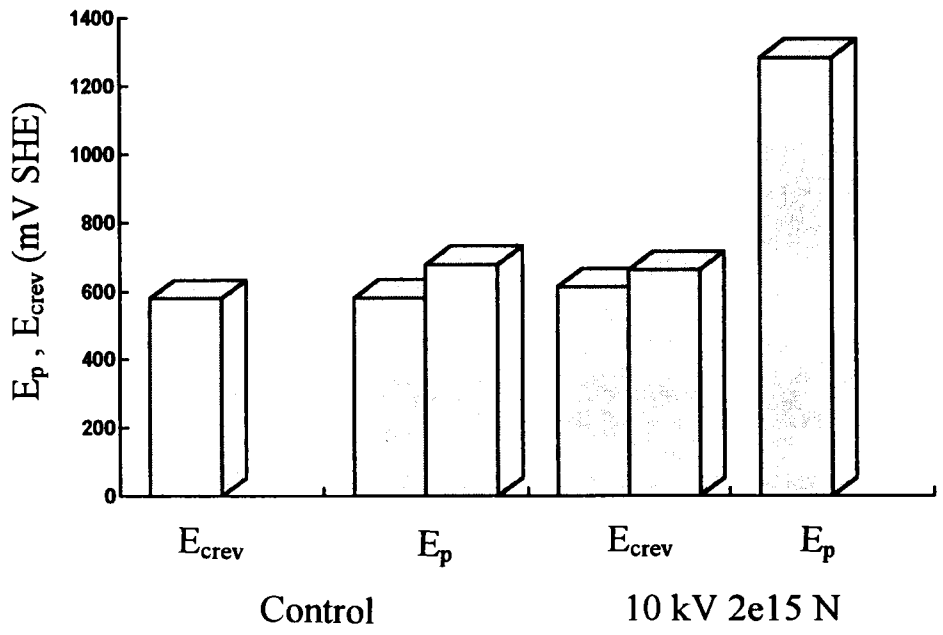

Figure 134. Comparison of breakdown potentials on 304L control and 304L PII N samples after cathodic cleaning at -1509 mV (SHE) for 20 minutes.

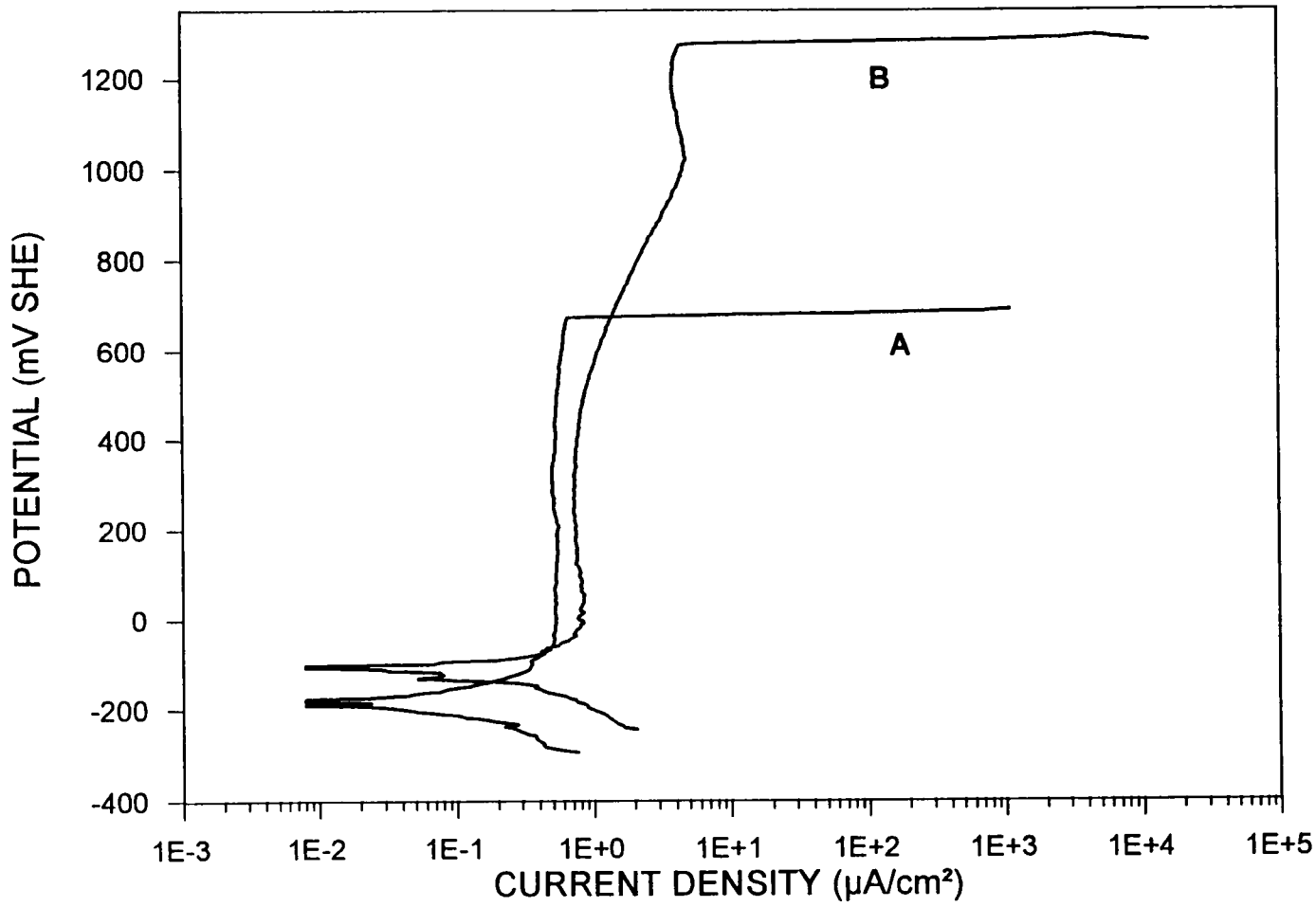

Figure 135. Anodic polarization of (A) 304L control and (B) 304L PII 2 x 10^{15} N ions/cm^2 in deaerated 1 wt% NaCl after cathodic cleaning at -1509 mV (SHE) for 20 minutes.

304L Anodic Polarization Summary

The inconsistency in producing an elevated pitting potential on 304L after the implantation of N raises a question concerning the origin of the increase in passivity for the successful anodic polarization tests. A variety of plasma ion implantation parameters and pre-corrosion specimen treatments were investigated during this study. These changes affected the polarization behavior of not only the implanted materials, but the control alloys as well. Therefore, in order to determine the change in E_p which can be attributed to N implantation without regard to the experimental procedures used, the control pitting potentials can be normalized to a baseline value. In Figure 136, all breakdown potentials from anodic polarization of the unimplanted alloy are set to zero, and the implanted specimens prepared by the same procedures are plotted as the positive or negative deviation in E_p (or E_{crev}) after implantation. It is immediately obvious that doses below 3×10^{14} and above 5×10^{15} N ions / cm^2 never result in large breakdown potential increases. Within this dose range, about half of the applied doses raise E_p by 400 - 700 mV. The grouping of potentials either around the control value or at a highly elevated value implies that the enhancement is a real effect limited in reproducibility by lack of experimental control of the many process variables that are involved during implantation, prepassivation, and corrosion. The overall results indicate that a nitrogen implantation dose in the vicinity of 1×10^{15} N

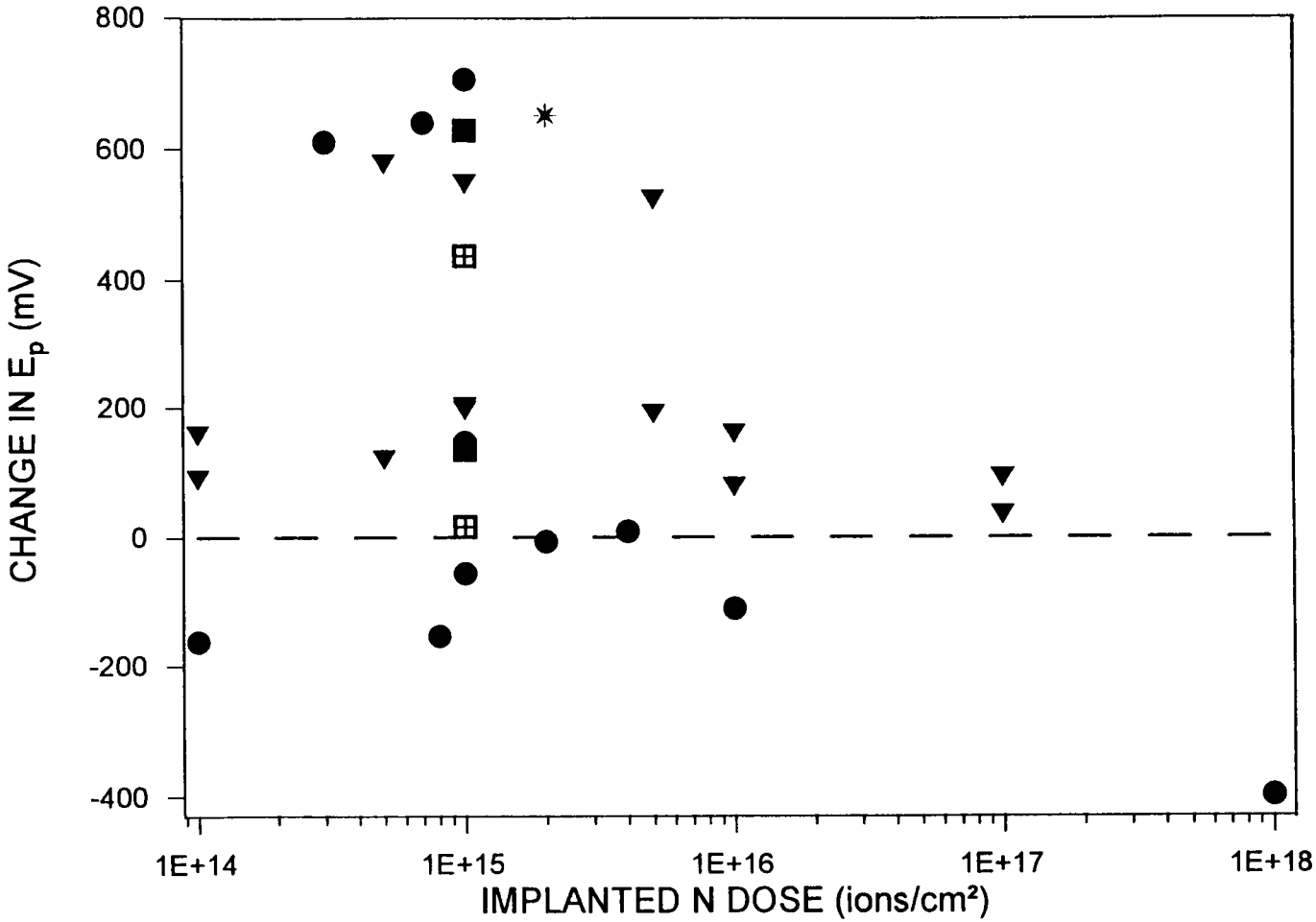

Figure 136. Change in the oxide film breakdown potential of 304L stainless steel due to nitrogen plasma ion implantation as a function of the applied dose. (● - manual oxide removal, ▼ - round sample holder, ⊞ - potentiostatically etched, ✳ - cathodically cleaned, ■ - no oxide removal)

ions / cm^2 can establish a highly elevated pitting potential. Nitrogen doses effective in improvement of wear properties (10^{17} - 10^{18} ions / cm^2) appear to be ineffective in enhancing localized corrosion resistance. Coincidental corrosion and wear resistance improvement can possibly be achieved by a two step implantation operation. A shallow implantation for corrosion mitigation would follow deposition of high dose, high energy N for wear prevention.

Several general comments about the nature of the anodic polarization tests should be noted here. Although improvements in the 304L pitting potential have been seen for a variety of experimental conditions, enhancement of the protection potential relative to the control material is not seen with nitrogen additions. Figure 137 illustrates a typical polarization behavior (for both implanted and control) including reversal of the potential scan at E_{1000}. Repassivation does not occur until 200 mV (SHE), or in near proximity to the original corrosion potential. This behavior was expected since an actively corroding pit bottom is well below the resident nitrogen depth. Therefore, the implanted species cannot affect repassivation.

A unique characteristic of the implanted alloys which exhibit large passive regions is that oxygen evolution is not seen above 800 mV (SHE). Anodic

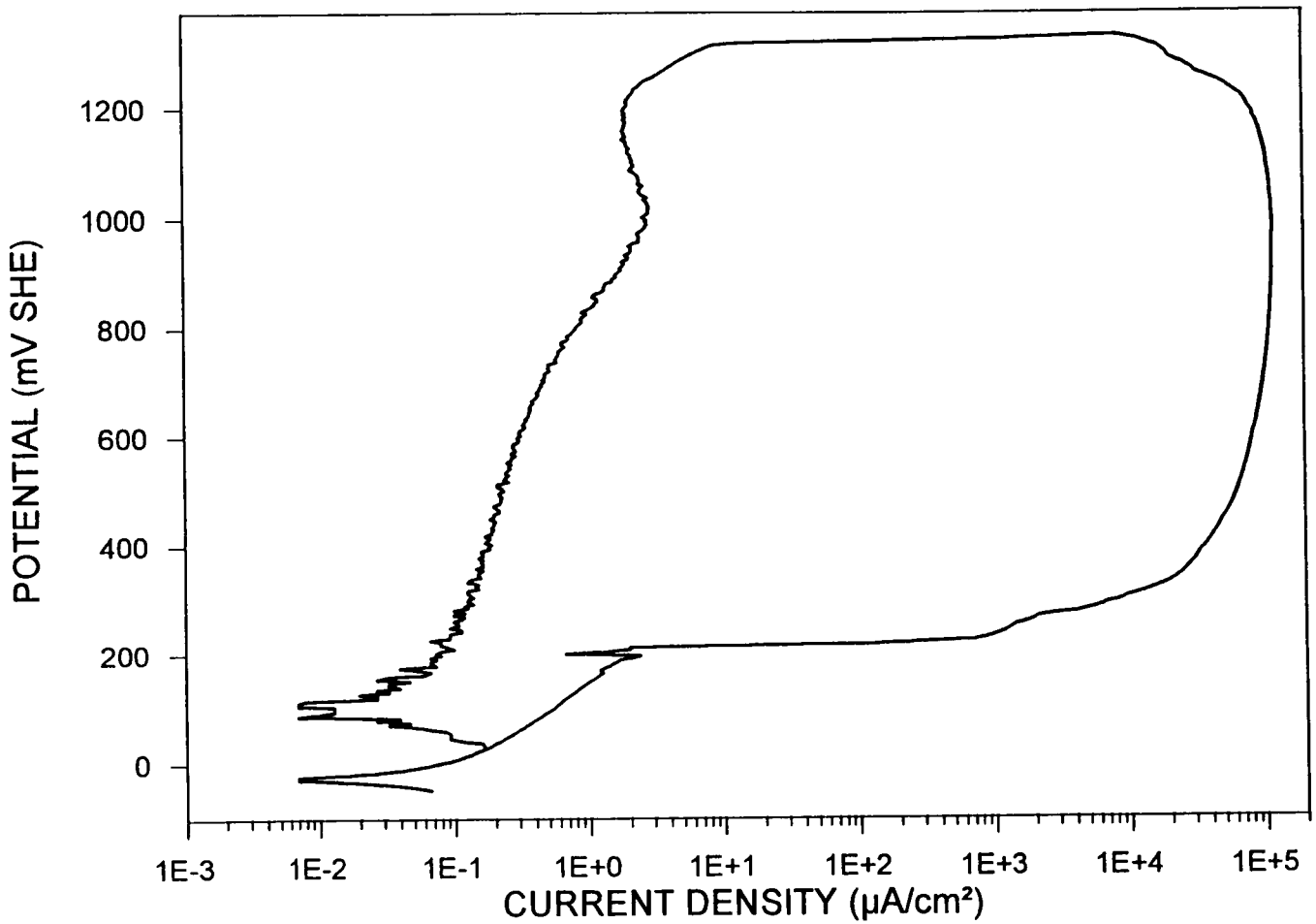

Figure 137. Anodic polarization of 304L PII 10 kV 5 x 10^{14} N ions/cm^2 in deaerated 1 wt% NaCl with potential reversal after reaching E_{1000}, showing large pitting hysteresis.

polarization of 304L above this potential should normally evolve O_2 by the dissociation of H_2O. This is manifested as an increasing current density ($2\ H_2O = O_2 + 4\ H^+ + 4\ e^-$) as shown in Figure 138. Ashworth and co-workers (26) have pointed out that implanted surfaces result in the growth of air formed films to greater thicknesses as a result of increased rates of diffusion and oxidation due to the high concentration of defects produced by ion implantation. As discussed below, Auger analysis indicates that the passive films formed on N-implanted specimens during polarization in 1 wt % NaCl are much thicker than those normally expected for a stainless steel. Since the oxygen reaction depends upon the surface for electron transport to the substrate, the thicker film may act to insulate the metal and prevent significant oxygen evolution.

An additional source of the E_p reproducibility problems may lie in lack of control of the PII pulse frequency. Implantation frequencies from 1 to 1000 Hz were used for various doses in order to facilitate rapid sample exposures. Some evidence exists of a correlation between lower pitting potentials and higher pulse frequencies. This could be attributed to inward thermal diffusion of the implanted species as the surface temperature rises.

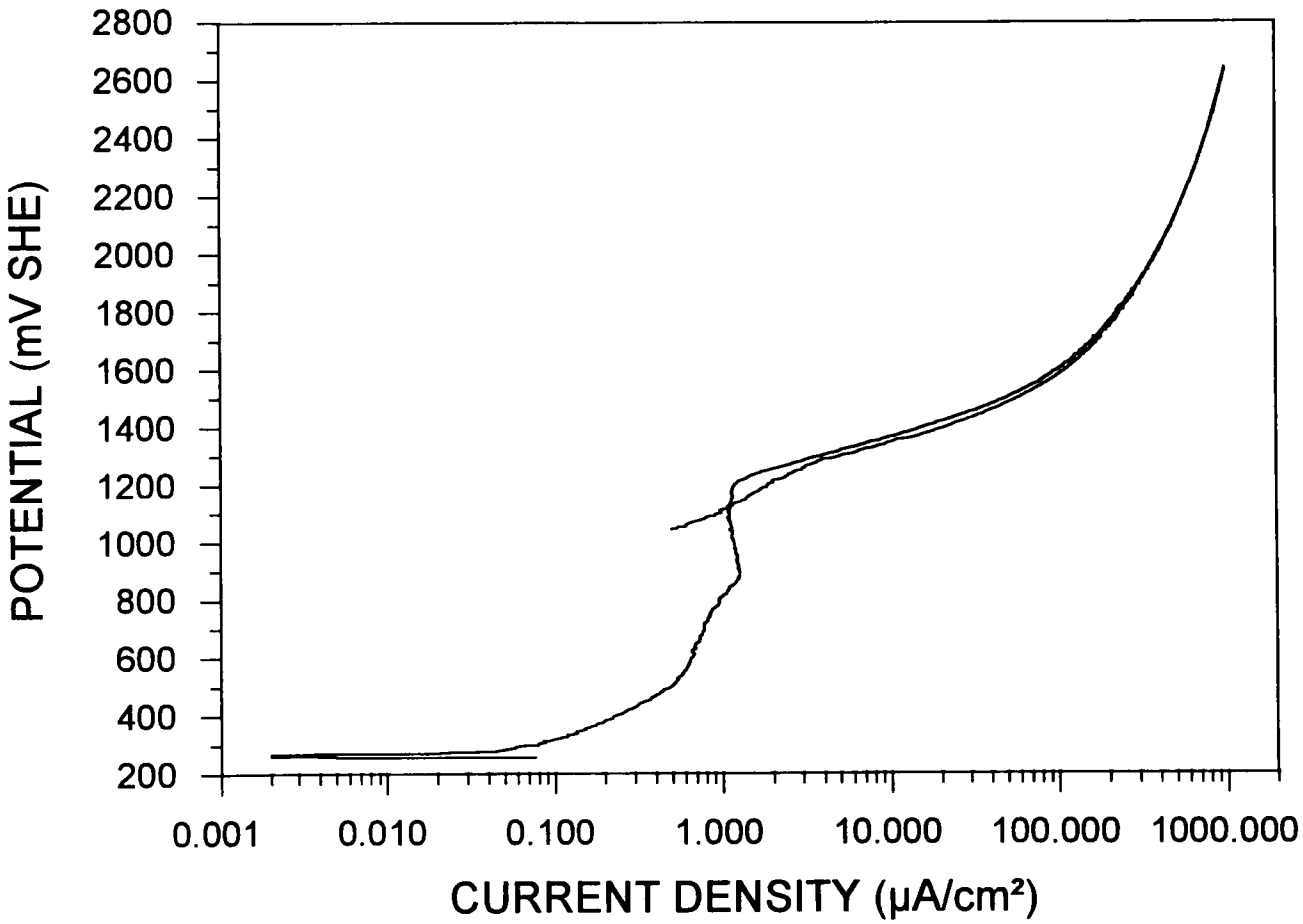

Figure 138. Anodic polarization of 304 stainless steel in tap water illustrating oxygen evolution.

Characterization of Dose Distribution by RBS / Auger Analyses

Auger electron and Rutherford backscattering spectroscopy analyses of the lateral distribution of the retained dose resulting from our nitrogen PII process were used to characterize any nonuniformity. Analysis was performed on implanted but non-corroded surfaces. RBS was carried out on a square 2 cm x 2 cm sample implanted to 1 x 10^{17} N using the original sample holder. Spectra were generated at four locations on the surface; near the corner, near the edge at the midpoint of one side, at the center, and between the center and the edge (Fig. 139). Light element backscattering is buried within the background generated by the heavier alloy elements (Fe, Ni, Cr). However, since the energy of each peak is known, qualitative information can be obtained from the size of small peaks, provided that they are present for each spectrum, and can be differentiated from the background noise. For example, in Figure 139, small rises in the spectra at 0.64 and 0.75 MeV could be mistaken for noise. However, they are repeated in each of the four spectra, and they correspond to the peak locations for nitrogen and oxygen. Eliminating the background and magnifying the portion containing the nitrogen peak results in Figure 140. A larger N peak area and higher maximum channel values can be seen for an analysis region near the corner of a 2 cm x 2 cm implanted specimen (Table 12). The nitrogen content decreases in order from the specimen corner to the specimen side, to the center, and finally, little or no

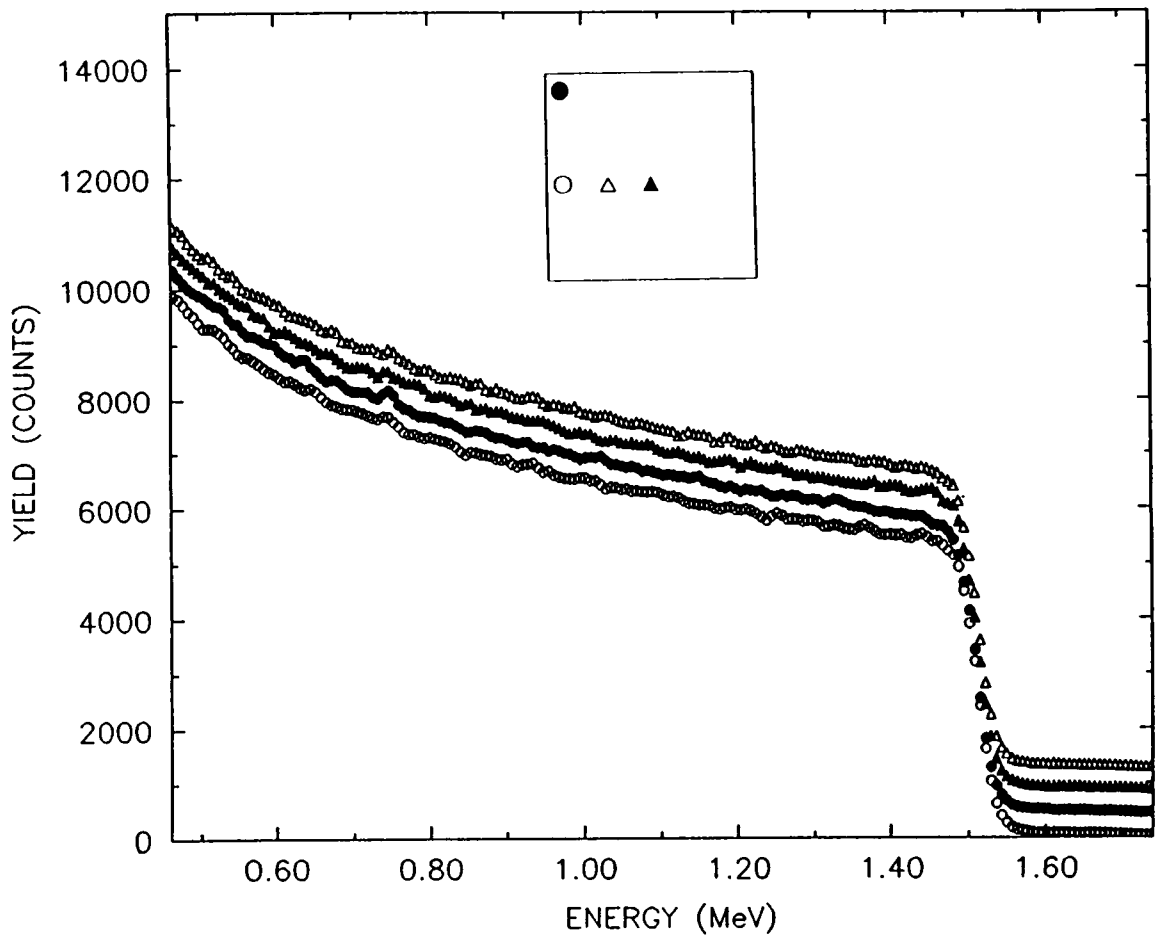

Figure 139. RBS spectra from 304L implanted to a dose of 1 x 10^{17} N ions/cm^2 on the 2 cm x 2 cm sample holder. Symbols indicate location on specimen from which spectra were generated.

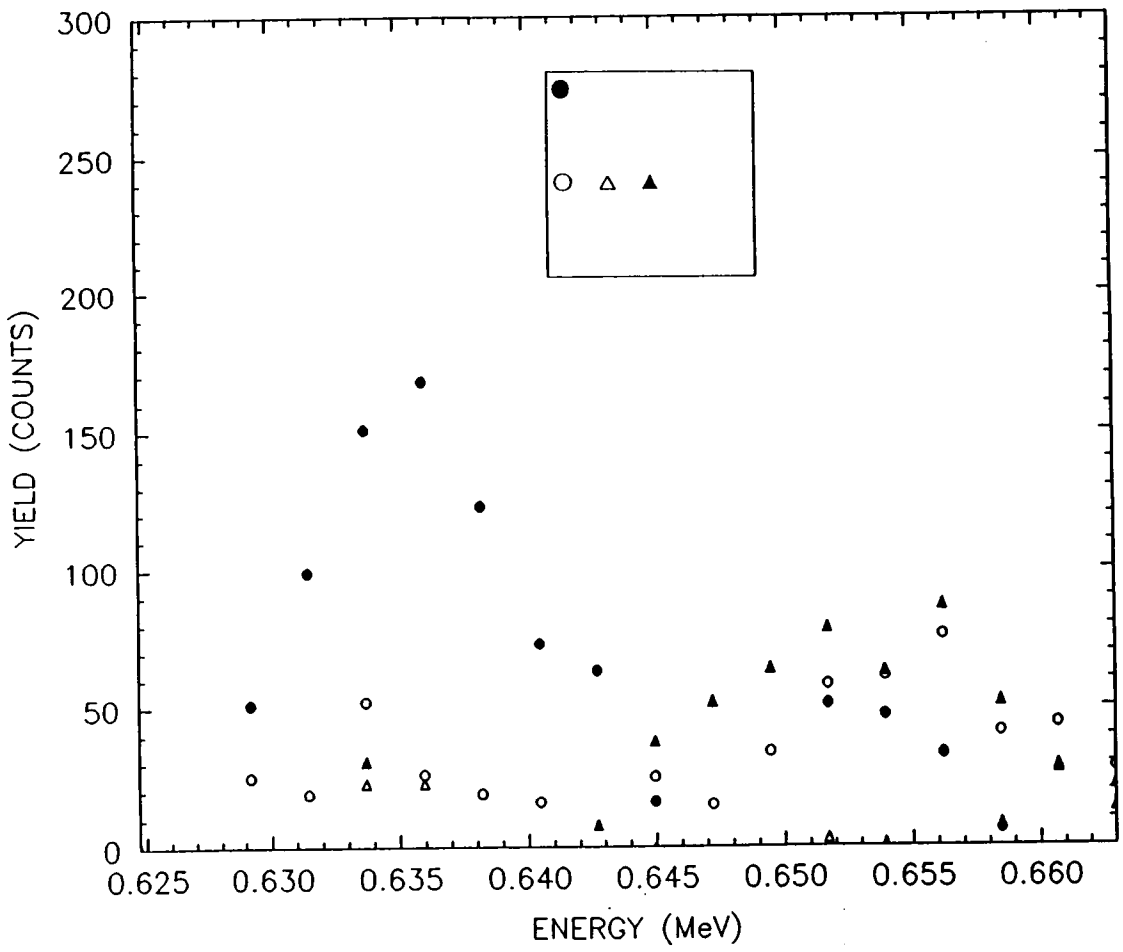

Figure 140. Magnification of the energy range containing N peak from RBS spectra in Figure 139.

Table 12

Qualitative RBS Nitrogen Content of 1e17 PII N 304L Stainless Steel
(2 cm x 2 cm square sample holder)

Location on Sample	Area Count	Maximum Channel Count
Corner	777	168
Center	415	86
Side	517	76
Off-center	0	27

nitrogen was observed at a point offset 0.5 cm from the center of the specimen. These observations correlate well with visual inspection of the surface of high-dose implantations, where discoloration patterns indicating non-uniformity have been seen near specimen edges and on specimen diagonals. A conclusion can therefore be drawn that the retained dose is higher at the specimen edges and along the specimen diagonals on the square samples, and the remaining areas retain a relatively low N dose.

A more quantitative analysis can be achieved with Auger electron spectroscopy since light elements (above He) are readily detectable by this technique. Auger was applied to a round specimen implanted to 5 x 10^{15} N using the third sample holder (Fig. 42). Beforehand, a depth profile was generated (Fig. 141), which indicates a Gaussian nitrogen distribution that peaks near the oxide / metal interface. The depth of implantation was reached after 110 seconds of sputtering, which from past experience with stainless steels (106), corresponds roughly to a 375 angstrom N penetration depth. This agrees with the PROFILE code simulation which predicts an implantation depth of 325 angstroms. This profile illustrates the successful placement of nitrogen at the oxide interface using a low implantation voltage of 10 kV. The thickness of the air-formed oxide can again

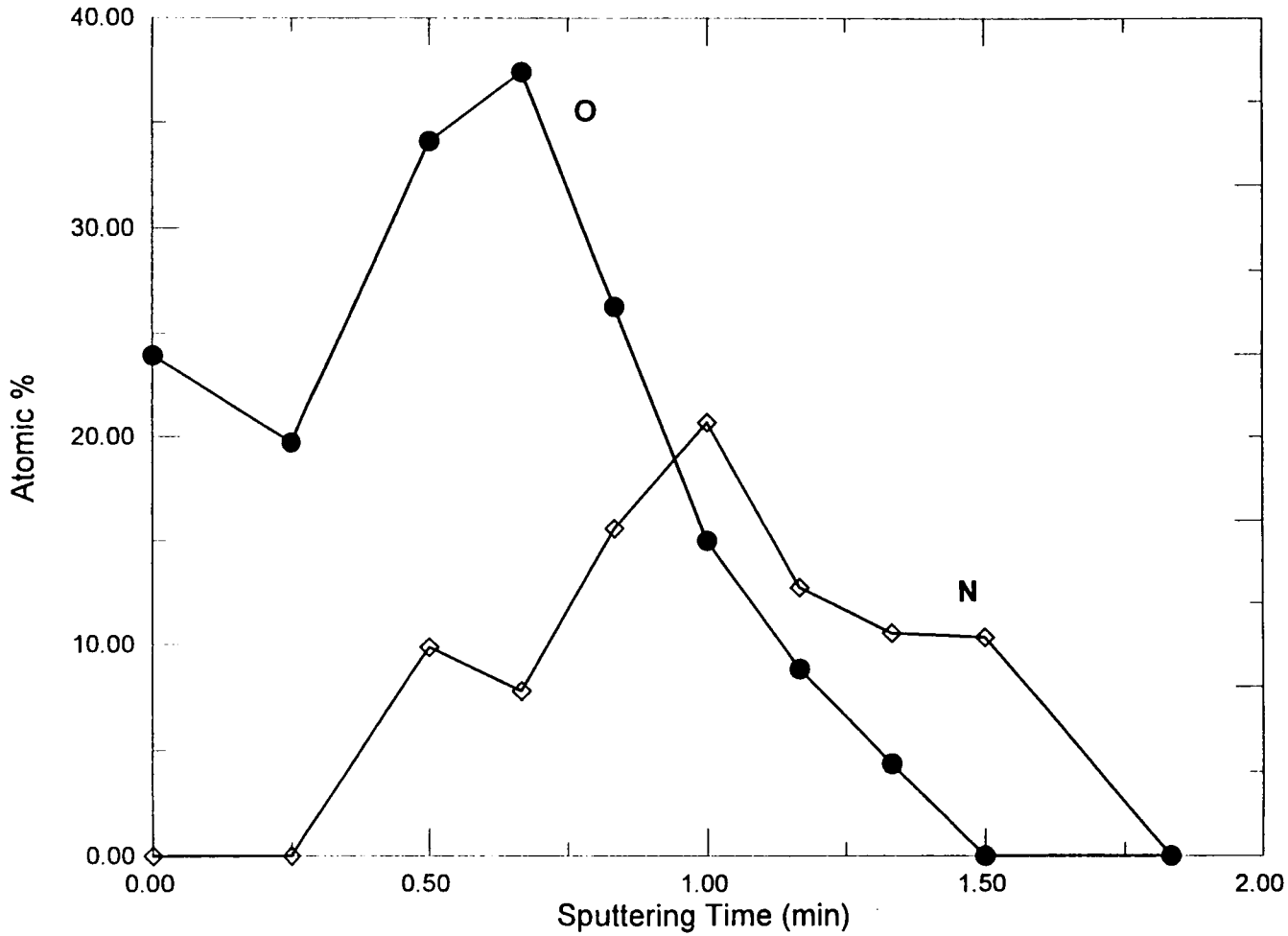

Figure 141. Auger depth profile of 304L implanted at 10 kV on round sample holder with a dose of 5 x 10^{15} N ions/cm^2.

be attributed to the increased rates of oxidation and diffusion on ion implanted surfaces.

Auger spectra were taken from seven points along the radius of the round sample, separated by 2.5 mm, after sputtering for one minute to locate the depth of maximum concentration. More closely spaced analysis points could not be used due to limitations on the reduction of the sputtering area. Figure 142 shows the nitrogen concentration along this radius. Some non-uniformity is seen as the N dose increases on the inner half of the specimen. However, this chemical information, along with the discoloration patterns, indicate that dose has become significantly more uniform as a result of modification of the PII sample holder. Although some inhomogeneity remains, the hypothesis that the major factor in the remaining irreproducibility of pitting potentials is due to the crevicing tendency is supported by the improvement in N distribution as noted by Auger analysis.

Auger spectroscopy was also applied to several specimens in an attempt to verify the chromium enrichment which results from nitric acid passivation (Figure 119). As seen in Figure 143, a significant Cr increase is noted at the surface of the passive film after treatment in the nitric acid bath. A nitrogen PII sample (Figure

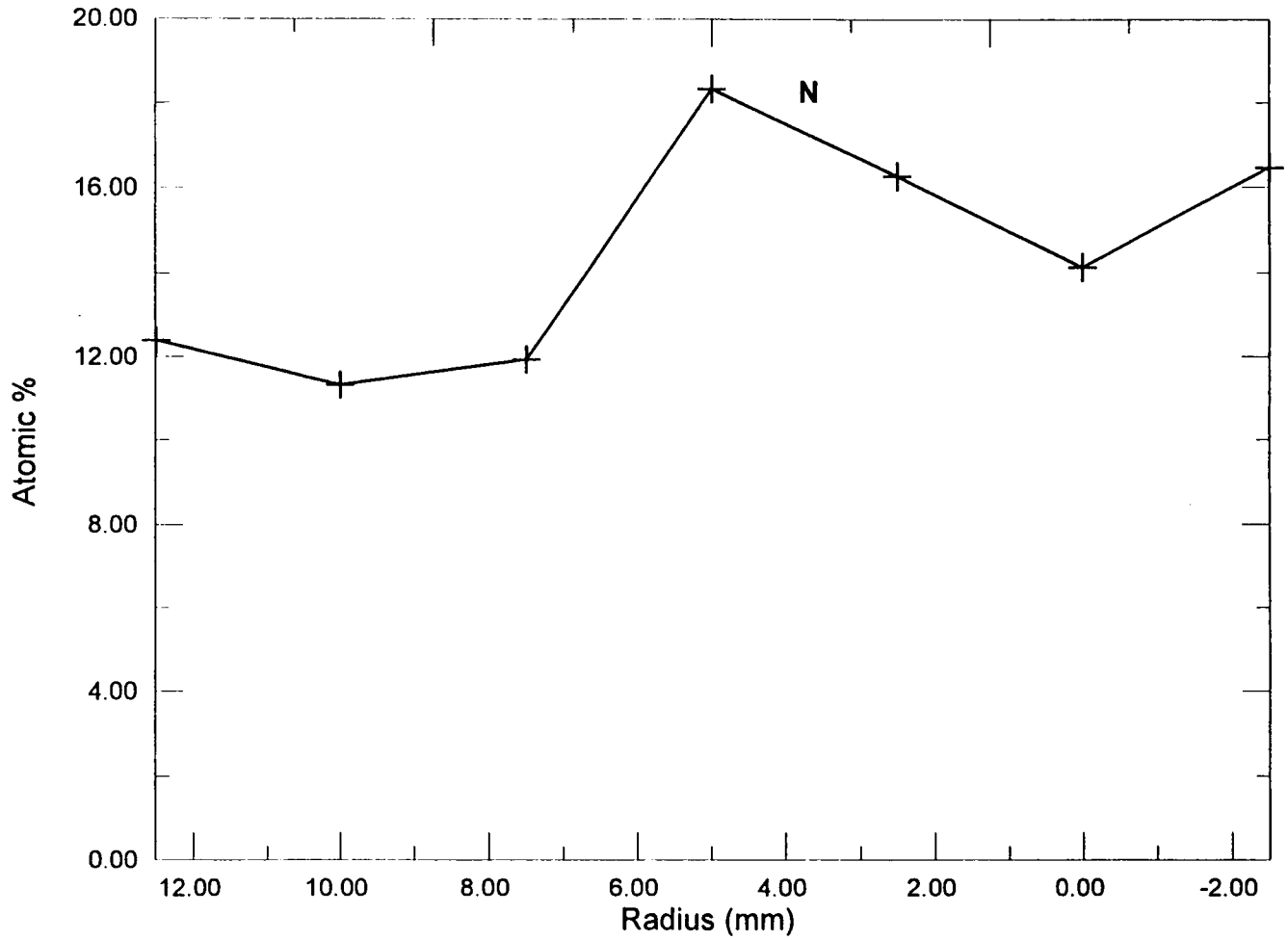

Figure 142. Auger nitrogen distribution on 304L implanted on round sample holder with a dose of 5 x 10^{15} N ions/cm^2. N content determined after sputtering surface for 1 minute.

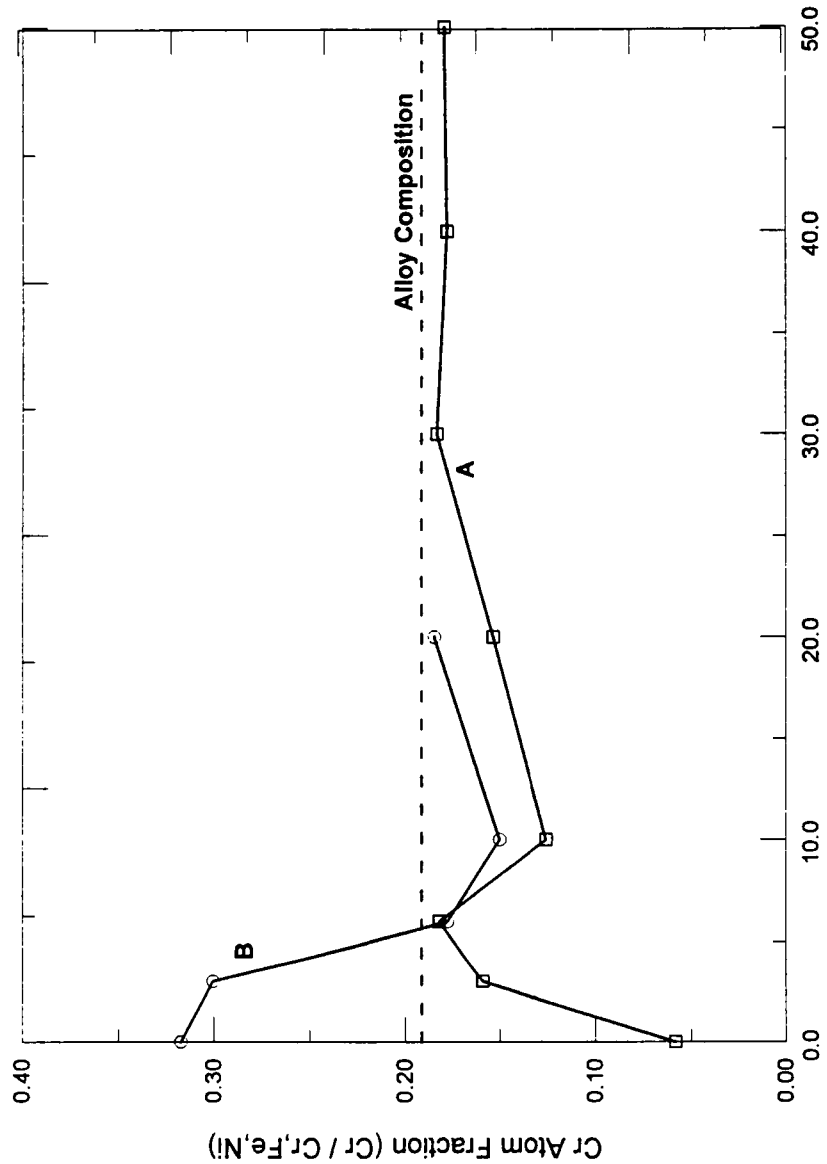

Figure 143. Chromium atom fraction (Cr / Cr + Fe + Ni) as determined by Auger spectroscopy as a function of depth on (A) control 304L with air formed oxide film, and (B) 304L, prepassivated in 50% HNO_3 for 30 minutes at 55°C.

144) shows no Cr content on the oxide surface, with slight enrichment deeper into the passive film. As seen for all implanted surfaces, the oxide is much thicker than the film formed on the unimplanted material. These results confirm the work of Asami and Hashimoto (109) that the highly elevated pitting potentials measured with the nitric acid formed passive film (both control and implanted) are the result of the oxide chromium enrichment. However, they also indicate that the N-induced increases in E_p cannot be attributed to the nitrogen causing further increases in the Cr content.

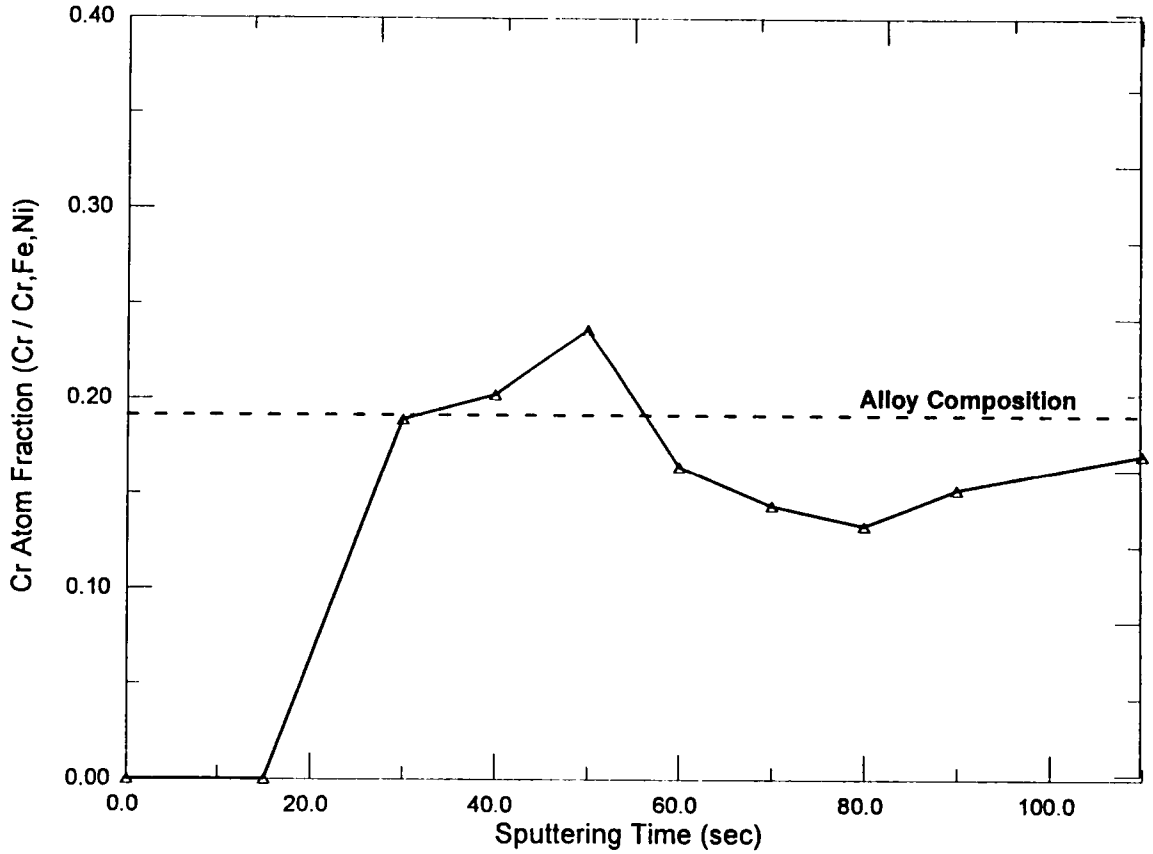

Figure 144. Chromium atom fraction (Cr / Cr + Fe + Ni) as determined by Auger spectroscopy as a function of depth on 304L PII 10kV 1e15 N after prepassivation in 50% HNO_3 for 30 minutes at 55°C.

5. CONCLUSIONS

Part I - Tungsten Ion Implantation of Aluminum 1100

1. Tungsten doses below 1 x 10^{16} ions/cm^2 do not alter the polarization behavior of Al 1100.
2. A tungsten dose of 4.9 x 10^{16} ions/cm^2 raised the pitting potential of Al 1100 in deaerated 1 wt% NaCl by 2240 mV. The polarization behavior of this alloy mirrors the extremely stable passivity previously found for W-Al sputtered thin films. However, the pitting potential of +1806 mV (SHE) was not reproduced in subsequent anodic polarization tests.
3. Tungsten ion implantation of aluminum always enhances its passivity, regardless of the substrate alloy (Al 1100, 99.9999 % Al), the solution aeration condition, or the applied dose (3 - 9 x 10^{16} ions/cm^2).
4. Oxide blisters form on the W-implanted surfaces during anodic polarization, confirming previous indications of their appearance on Al as a result of ion implantation.

5. Anodic polarization, potentiostatic, and immersion testing all indicate that the implantation of tungsten acts to significantly slow the propagation of pitting on Al 1100.

6. The first microstructural evidence of aluminum oxide blistering during a non-potentiostatically controlled test was found on both implanted and control Al 1100 surfaces.

7. Upon entering the chloride solution, the tungsten species catalyzes the formation of an aluminum oxide precipitate. This corrosion product acts to repassivate the surface and slow pitting propagation. Therefore, the implanted W performs the dual roles of promoting oxide blistering and forming a passivating precipitate oxide.

8. The oxide blister is much thinner than the surrounding oxide film. After the oxide is forced away from the metallic surface by the developing H_2 pressure, it cannot increase in thickness by further anodic reaction.

9. Confirmation was obtained of previous assertions that the blisters form at the pitting potential.

10. Tungsten is not found in the blistered oxide after anodic polarization or after immersion. Therefore, the mechanism behind the increase in pitting potential of Al 1100 cannot be traced to the W species improving the mechanical properties of the oxide film.

11. During immersion in aerated 1 wt% NaCl, an Al 1100 alloy implanted with tungsten develops a ledge of protected metal beneath the large oxide blisters. In one test, the non-blistered regions corroded almost 30 times as deeply as the area beneath a blister.

Part II - Nitrogen Plasma Ion Implantation of 304L Stainless Steel

1. Nitrogen ions have been successfully implanted into 304L stainless steel in a uniform microwave plasma for the purpose of pitting corrosion resistance improvements.
2. An increase in pitting potential of up to 700 mV was measured for a low dose range between 3×10^{14} and 5×10^{15} ions/cm^2 and an implantation voltage of 10 kV.
3. No improvement was noted for higher doses, indicating that nitrogen doses effective in improvement of wear properties are not effective in enhancing localized corrosion resistance.
4. The use of low accelerating potentials increases the N ion concentration in the near surface region, thereby modifying the passive film or the film / metal interface.
5. An amount of irreproducibility exists in the pitting potential measurements, mostly due to the inherent crevicing tendency of the 304L stainless alloy.

6. The lateral dose uniformity has been greatly improved through successive modifications of the plasma ion implantation sample holder geometry.

LIST OF REFERENCES

REFERENCES

1. ***Metals Handbook, Desk Edition***, ASM, Metals Park, OH (1985).

2. Z. Szklarska-Smialowska, ***Pitting Corrosion of Metals***, NACE, Houston (1986).

3. M. Pourbaix, ***Atlas of Electrochemical Equilibria in Aqueous Solutions***, NACE, Houston (1966).

4. R. T. Foley, ***Corrosion*** 42, No. 5, 277 (1986).

5. W. C. Moshier, G. D. Davis, J. S. Ahearn, H. F. Hough, ***J. Electrochem. Soc.*** 134, No. 11, 2677 (1987).

6. P. M. Natishan, E. McCafferty, and G. K. Hubler, ***J. Electrochem. Soc.*** 135, No. 2, 321 (1988).

7. S. Maitra, ***Ph. D. Dissertation***, University of Florida, Gainesville, FL (1974).

8. R. Galvele, S. M. deMicheli, I. L. Muller, S. B. Wexler, I. L. Alanis in ***Localized Corrosion; NACE-3***, R. Staehle, B. Brown, J. Kruger, and A. Agrawal, Eds., pp. 580-599, NACE, Houston (1971).

9. ***Metals Handbook***, 9th ed., Vol. 3, Metals Park, OH (1985).

10. R. S. Brown, ***Advanced Materials & Processes*** 145, No. 4, 20 (1994).

11. E. P. DeGarmo, J. T. Black, R. A. Kohser, ***Materials and Processes in Manufacturing***, 7th Ed., Macmillan Pub. Co., New York (1988).

12. G. Dearnaley in ***Ion Implantation and Plasma Assisted Processes***, R. F. Hochman, H. Solnick-Legg, K. O. Legg, Eds., pp. 1-7, ASM, Metals Park, OH (1988).

13. R. D. Granata and P. G. Moore, "Surface Modification," in ***Metals Handbook***, 9th ed., Vol. 13, Metals Park, OH (1985).

14. J. M. Williams, "High-Energy Ion Implantation of Materials," in ***Workshop on Surface Processing for Utilities and Transportation Industries***, Dec. 1991, Dearborn, MI.

15. R. F. Hochman in ***Ion Plating and Implantation Applications to Materials***, R. F. Hochman, Ed., pp. 1-6, ASM, Metals Park, OH (1986).

16. E. McCafferty, P. G. Moore, J. D. Ayers, and G. K. Hubler, in ***Corrosion of Metals Processed by Directed Energy Beams***, C. R. Clayton and C. M. Preece, Ed., TMS, Warrendale, PA (1982).

17. B. Holtkamp, ***Advanced Materials & Processes*** 144, No. 12, 45 (1993).

18. J. F. Ziegler, J. P. Biersack, and U. Littmark, ***The Stopping and Range of Ions in Solids***, Permagon Press, New York (1985).

19. N. G. Thompson and B. D. Lichter, ***Reviews on Coatings and Corrosion*** 4, No. 2, 156 (1981).

20. R. G. Wilson and G. R. Brewer, ***Ion Beams, with Applications to Ion Implantation***, John Wiley & Sons, New York (1973).

21. C. J. McHargue, ***International Metals Reviews*** 31, No. 2, 49 (1986).

22. L. E. Rehn, S. T. Picraux, and H. Wiedersich in ***Surface Alloying by Ion, Electron and Laser Beams***, L. E. Rehn, S. T. Picraux, and H. Wiedersich, Eds., ASM, Metals Park, OH (1987).

23. N. L. Lee, G. B. Fisher, and Y. T. Cheng in ***Environmental Degradation of Ion and Laser Beam Treated Surfaces***, G. S. Was and K. S. Grabowski, Eds., pp. 107-126, TMS, Warrendale, PA (1989).

24. C. R. Clayton in ***Environmental Degradation of Ion and Laser Beam Treated Surfaces***, G. S. Was and K. S. Grabowski, Eds., pp. 33-58, TMS, Warrendale, PA (1989).

25. J. M. Williams, G. M. Beardsley, R. A. Buchanan, and R. K. Bacon in ***Ion Implantation and Ion Beam Processing of Materials***, G. K. Hubler, O. W. Holland, C. R. Clayton, and C. W. White, Eds., pp. 735-740, North-Holland, New York (1984).

26. V. Ashworth, D. Baxter, W. A. Grant, and R. P. M. Procter, ***Corros. Sci.*** 17, 947 (1977).

27. E. McCafferty and G. K. Hubler, ***J. Electrochem. Soc.*** 128, 1892 (1978).

28. G. K. Wolf, J. Dressler, W. Ensinger, H. Ferber, A. Meger, and P. Munn in ***Fundamental Aspects of Corrosion Protection by Surface Modification***, E. McCafferty, C. R. Clayton, and J. Oudar, Eds., p. 42, Electrochem. Soc., Pennington, N. J. (1984).

29. C. R. Clayton, W. K. Chan, J. K. Hirvonen, G. K. Hubler, and J. R. Reed in ***Fundamental Aspects of Corrosion Protection by Surface Modification***, E. McCafferty, C. R. Clayton, and J. Oudar, Eds., p. 17, Electrochem. Soc., Pennington, N. J. (1984).

30. R. Wei, P. J. Wilbur, O. Ozturk, and D. L. Williamson, ***Nucl. Instrum. Methods*** B 59/60, 731 (1991).

31. J. J. Eckenrod and C. W. Kovach, ***ASTM STP 679***, pp. 17-41, ASTM, Philadelphia, PA (1979).

32. J. E. Truman, M. J. Coleman, and K. R. Pirt, ***Br. Corros. J.*** 12, 236 (1977).

33. C. L. Briant, R. A. Mulford, and E. L. Hall, ***Corrosion*** 38, 468 (1982).

34. J. R. Kearns and H. E. Deverell, ***Materials Performance***, June, 18 (1987).

35. ASM Handbook, Vol. 3, ASM International, Materials Park, OH (1992).

36. R. Magdowski and M. O. Speidel, 1993 Corrosion Research in Progress Symposium, New Orleans, LA, March, 1993 (unpublished).

37. V. Brusic, G. S. Frankel, B. M. Rush, A. G. Schrott, C. Jahnes, M. A. Russak, and T. Petersen, ***J. Electrochem. Soc.*** 139, 1530 (1992).

38. F. Cerney, M. Prazak, and J. Suchanek, ***Nucl. Instrum. Methods*** B 59/60, 762 (1991).

39. T. M. Wang, J. Shi, X. S. Zhang, ***Nucl. Instrum. Methods*** B 72, 55 (1992).

40. A. Singh, E. J. Knystautas, M. Elboujdaini, and E. Ghali, ***Nucl. Instrum. Methods*** B 35, 495 (1988).

41. S. D. Chyou and H. C. Shih, ***Corrosion*** 47, 31 (1991).

42. R. Sriram and D. Tromans, ***Corrosion*** 45, 804 (1989).

43. R. C. Newman and T. Shahrabi, ***Corr. Sci.*** 27, 827 (1987).

44. K. Osozawa and N. Okata, ***Passivity and its Breakdown on Iron and Iron Based Alloys***, pp. 135-139, NACE, Houston, TX (1976).

45. S. J. Pawel, E. E. Stansbury, and C. D. Lundin, ***Corrosion*** 45, 125 (1989).

46. Y. C. Lu and M. B. Ives, 1993 Corrosion Research in Progress Symposium, New Orleans, LA, March, 1993 (unpublished).

47. A. H. Al-Saffar, V. Ashworth, A. K. O. Bairamov, D. J. Chivers, W. A. Grant, R. P. M. Procter, ***Corrosion Science*** 20, 127 (1980).

48. P. M. Natishan, E. McCafferty, G. K. Hubler, ***Environmental Degradation of Ion and Laser Beam Treated Surfaces***, G. S. Was and K. S. Grabowski Eds., p. 167, TMS, Warrendale, PA (1988).

49. P. M. Natishan, E. McCafferty, G. K. Hubler, ***Nuclear Instruments and Methods in Physics Research*** B59/60, 841 (1991).

50. S. Venkatraman, M. R. Nair, D. C. Kothari, K. B. Lal, R. Raman, ***Nuclear Instruments and Methods in Physics*** Research B19/20, 241 (1987).

51. P. M. Natishan, E. McCafferty, and G. K. Hubler, ***Corr. Sci.*** 32, No. 7, 721 (1991).

52. J. M. Williams, A. Gonzales, J. Quintana, I. S. Lee, R. A. Buchanan, F. C. Burns, R. J. Culbertson, M. Levy, J. R. Treglio, ***Nuclear Instruments and Methods in Physics Research*** B59/60, 845 (1991).

53. A. Gupta, ***Master's Thesis***, University of Tennessee, Knoxville, TN (1991).

54. T. A. Mozhi, S. C. Jha, R. Ray, ***Corrosion*** 45, No. 10, 811 (1989).

55. M. Fass, D. Itzhak, D. Eliezer, F. H. Froes, ***J. Mat. Sci. Lett.*** 6, 1227 (1987).

56. W. C. Moshier, G. D. Davis, J. S. Ahearn, and H. F. Hough, ***J. Electrochem. Soc.*** ABC, p. 1063, May 1986.

57. G. S. Frankel, M. A. Russak, C. V. Jahnes, M. Mirzamaani, V. A. Brusic, ***J. Electrochem. Soc.*** 136, No. 4, 1243 (1989).

58. T. Heumann and N. Stolica, ***Electrochimica Acta*** 16, 643 (1971).

59. N. Bui, A. Irhzo, F. Dabosi, and Y. Limouzin-Maire, ***Corrosion*** 39, 491 (1983).

60. A. J. Sedricks, ***Corrosion*** 42, 376 (1986).

61. B. A. Shaw, T. L. Fritz, G. D. Davis, and W. C. Moshier, ***J. Electrochem. Soc.*** 137, No. 4, 1317 (1990).

62. B. A. Shaw, G. D. Davis, T. L. Fritz, B. J. Rees, W. C. Moshier, ***J. Electroch. Soc.*** 38, No. 11, 3288 (1991).

63. H. Yoshioka, H. Habazaki, A. Kawashima, K. Asami, K. Hasimoto, ***Corrosion Science*** 32, No. 3, 313 (1991).

64. H. H. Uhlig, ***Corrosion and Corrosion Control***, pp. 70-71, John Wiley and Sons, New York (1963).

65. A. K. Vijh, ***Corr. Sci.*** 11, 161 (1971).

66. P. M. Natishan, E. McCafferty, and G. K. Hubler, ***J. Electrochem. Soc.*** 133, No. 5, 1061 (1986).

67. W. C. Moshier, G. D. Davis, G. O. Cote, ***J. Electrochem. Soc.*** 136, No. 2, 356 (1989).

68. G. D. Davis, W. C. Moshier, T. L. Fritz, and G. O. Cote, ***J. Electrochem. Soc.*** 137, No. 2, 422 (1990).

69. G. D. Davis, W. C. Moshier, G. G. Long, D. R. Black, ***J. Electrochem. Soc.*** 138, No. 11, 3194 (1991).

70. Z. Szklarska-Smialowska, ***Corr. Sci.*** 33, No. 8, 1193 (1992).

71. R. B. Inturi, Z. Szklarska-Smialowska, ***Corrosion Science*** 34, No. 8, 1201 (1993).

72. G. D. Davis, B. A. Shaw, B. J. Rees, M. Ferry, ***J. Electrochem. Soc.*** 140, No. 4, 951, (1993).

73. C. B. Bargeron, R. B. Givens, ***J. Electroch. Soc.*** 124, No. 12, 1845 (1977).

74. C. B. Bargeron, R. B. Givens, ***Corrosion*** 36, No. 11, 618 (1980).

75. P. M. Natishan, E. McCafferty, G. K. Hubler, ***Environmental Degradation of Ion and Laser Beam Treated Surfaces***, G. S. Was and K. S. Grabowski Eds., p. 167, TMS, Warrendale, PA (1988).

76. Z. Szklarska-Smialowska, ***Pitting Corrosion of Metals***, Chapter 12, NACE, Houston (1986).

77. Z. Szklarska-Smialowska in ***Passivity of Metals***, R. Frankenthal, J. Kruger, Eds., p. 443, The Electrochemical Society, Princeton, NJ (1977).

78. V. S. Sastri, R. H. Packwood, V. E. Moore, and J. Bednar, ***Proceedings of the 6th European Symposium on Corrosion Inhibitors***, Suppl. No. 8, p. 741, Ann. Univ. Ferrara (1985).

79. R. C. McCune, R. L. Shilts, and S. M. Ferguson, ***Corr. Sci.*** 22, No. 11, 1049 (1982).

80. K. O. Legg, ***International Workshop on Plasma-Based Ion Implantation***, Madison, WI, August 1993 (unpublished).

81. ***Plasma Processing Of Materials: Scientific Opportunities and Technological Challenges***, Panel on Plasma Processing of Materials, Plasma Science Committee, Board on Physics and Astronomy, Commission on Physical Sciences, Mathematics, and Applications, National Research Council, National Academy Press, Washington D. C. (1991).

82. J. R. Conrad, R. A. Dodd, F. J. Worzala, X. Qiu, R. S. Post in ***Ion Implantation and Plasma Assisted Processes***, R. F. Hochman, H. Solnick-Legg, K. O. Legg, Eds., pp. 185-191, ASM, Metals Park, OH (1988).

83. J. R. Conrad, ***J. Appl. Physics*** 62, 777 (1987).

84. G. P. Meeker, J. R. Conrad, S. M. Baumann, and R. S. Post, ***Characterization of Plasma Source Ion Implanted Steels***, internal research at the University of Wisconsin, Madison, 1989, pp. 1-15 (unpublished).

85. F. J. Worzala, R. A. Dodd, J. R. Conrad, J. L. Radtke, "Ion Implantation of Tools and Punches - Laboratory Curiosity or Commercial Process," in ***Proceedings of the International Conference on Tool Materials***, Uddeholm Research Foundation, Chicago, IL (1987).

86. M. B. Abuzriba and R. A. Dodd, ***International Workshop on Plasma-Based Ion Implantation***, Madison, WI, August 1993 (unpublished).

87. J. Firmiss and J. R. Conrad, ***International Workshop on Plasma-Based Ion Implantation***, Madison, WI, August 1993 (unpublished).

88. S. M. Malik, K. Sridharan, R. P. Fetherston, A. Chen, and J. R. Conrad, ***J. Vac. Sci. Technol.*** B 12(2), 843 (1994).

89. K. C. Walter and J. R. Conrad, ***International Workshop on Plasma-Based Ion Implantation***, Madison, WI, August 1993 (unpublished).

90. E. C. Jones, W. En, S. Ogawa, D. B. Fraser, N. W. Cheung, ***J. Vac. Sci. Technol.*** B 12(2), 956 (1994).

91. A. Joshi, "Auger Electron Spectroscopy," in ***Metals Handbook***, Vol. 10, 9th ed., 566 (1987).

92. W. Chu, " Rutherford Backscattering Spectrometry," in ***Metals Handbook***, Vol. 10, 9th ed., 628 (1987).

93. W. Chu, J. W. Mayer, M. Nicolet, ***Backscattering Spectrometry***, Academic Press, Orlando, FL (1978).

94. J. Jahanmir, B. G. Haggar, and J. B. Hayes, ***Scanning Microscopy*** 6, No. 3, 625 (1992).

95. G. Binnig, C. F. Quate, and C. Gerber, ***Phys. Rev. Lett.*** 56, No. 9, 930 (1986).

96. S. A. C. Gould, B. Drake, C. B. Prater, A. L. Weisenhorn, S. Manne, H. G. Hansma, P. K. Hansma, J. Massie, M. Longmire, V. Elings, B. Dixon-Northern, B. Mukergee, C. M. Peterson, W. Stoeckenius, T. R. Albrecht, C. F. Quate, ***J. Vac. Sci. Technol.*** A 8(1), 369 (1990).

97. S. Alexander, L. Hellemans, O. Marti, J. Schneir, V. Elings, P. K. Hansma, M. Longmire, and J. Gurley, ***J. Appl. Phys.*** 65, 164 (1989).

98. R. M. Rynders, C. Paik, R. Ke, and R. C. Alkire, ***J. Electrochem. Soc.*** 141, No. 6, 1439 (1994).

99. S. G. Kamath, ***Master's Thesis***, University of Tennessee, Knoxville, TN (1994).

100. I. S. Lee, ***Master's Thesis***, University of Tennessee, Knoxville, TN (1994).

101. I. S. Lee, ***Ph. D. Dissertation***, University of Tennessee, Knoxville, TN (1994).

102. N. D. Greene, W. D. France, and B. E. Wilde, ***Corrosion*** 21, No. 9, 275 (1965).

103. I. S. Lee, E. E. Stansbury, and S. J. Pawel, ***Corrosion*** 45, No. 2, 134 (1989).

104. M. G. A. Khedr and A. M. S. Lashien, ***J. Electrochem. Soc.*** 136, No. 4, 968 (1989).

105. K. C. Walter, K. Sridharan, and M. Goeckner, private communication, ***1st International Workshop on Plasma-Based Ion Implantation***, Madison, WI (1993).

106. D. Brasky, private communication, ORNL High Temperature Materials Laboratory (1995).

107. C. B. Bargeron and R. C. Benson, ***J. Electrochem. Soc.*** 127, No. 11, 2528 (1980).

108. C. A. Jacobsen, ***Encyclopedia of Chemical Reactions***, Vol. 1, p. 37, Reinhold, New York (1946).

109. K. Asami and K. Hashimoto, ***Corrosion Science*** 19, 1007 (1979).

110. S. Kamath and J. R. Roth, ***20th IEEE International Conference on Plasma Science***, Vancouver, B. C., Canada (1993).

111. A. Gupta, ***Master's Thesis***, University of Tennessee, Knoxville, TN (1991).

112. P. F. Keebler, ***Master's Thesis***, University of Tennessee, Knoxville, TN (1990).

113. P. D. Spence, P. F. Keebler, M. S. Freeland, and J. R. Roth, ***10th International Symposium on Plasma Chemistry, Workshop on Industrial Plasma Applications and Engineering Problems***, August 10, 1991, Bochum, Germany.

114. J. E. Crowley, P. F. Keebler, and J. R. Roth, ***APS Bulletin***, 34, No. 9, 20 (1989).

115. P. F. Keebler, J. E. Crowley, and J. R. Roth, ***Proceedings of the 1989 IEEE International Conference on Plasma Science***, May 22-24, 1989, Buffalo, NY, IEEE Catalog #89 CH2760-7(1989), p. 149.

116. P. F. Keebler and J. R. Roth, ***Proceedings of the 1990 IEEE International Conference on Plasma Science***, May 21-23, 1990, Oakland Ca., IEEE Catalog #90 CH2857-1(1990), p. 161.

117. P. F. Keebler, M. S. Freeland, and J. R. Roth, ***APS Bulletin***, 35, No. 9, 2016 (1990).

118. P. D. Spence, M. S. Freeland, and J. R. Roth, ***Proceedings of the 1991 IEEE International Conference on Plasma Science***, Paper 2P9, ISBN: 07803-0147-1(1991), pp. 119-120.

119. S. Yu, S. Kamath, and J. R. Roth, ***Proceedings of the 1993 IEEE International Conference on Plasma Science***, June 7-9, 1993, Vancouver, B. C., ISBN D-7803-1360-7(1993), p. 213.

120. S. G. Kamath, J. R. Roth, P. P. Smith, and R. A. Buchanan, ***Proceedings of the 1st International Workshop on Plasma-Based Ion Implantation***, August 4-6, 1993, Madison, Wi.

121. J. R. Roth, S. G. Kamath, P. P. Smith, and R. A. Buchanan, ***Proceedings of the 1st International Workshop on Plasma-Based Ion Implantation***, August 4-6, 1993, Madison, Wi.

122. R. A. Buchanan, R. K. Bacon, J. M. Williams, and G. M. Beardsley, ***Transactions: Society for Biomaterials***, Vol. VI, 106 (1983).

123. J. M. Williams, R. A. Buchanan, G. M. Beardsley, and R. K. Bacon, ***Ion Implantation and Ion Beam Processing of Materials***, G. K. Hubler, O. W. Holland, C. R. Clayton, and C. W. White, eds., Elsevier, New York, pp. 735-740 (1984).

124. J. M. Williams and R. A. Buchanan, ***Materials Science and Engineering***, 69, 237-246 (1985).

125. J. M. Williams, R. A. Buchanan, and E. D. Rigney, Jr., ***Ion Plating and Implantation: Applications to Materials***, Metals/MaterialsTechnology Series 8504-008, American Society for Metals, Metals Park, Ohio, pp. 1-10, 1986.

126. R. A. Buchanan, E. D. Rigney, Jr., and J. M. Williams, ***Journal of Biomedical Materials Research***, Vol. 21, No. 3, 355-366 (1987).

127. R. A. Buchanan, E. D. Rigney, Jr., and J. M. Williams, ***Journal of Biomedical Materials Research***, Vol. 21, No. 3, 367-377 (1987).

128. I-S Lee, R. A. Buchanan, and J. M. Williams, ***Biomedical Materials and Devices***, Materials Research Society Symposium Proceedings, Vol. 110, MRS, Pittsburgh, PA, 687-695, 1988.

129. R. A. Buchanan, I-S Lee, and J. M. Williams, ***Ion Implantation and Plasma Assisted Processes***, ASM International, Metals Park, Ohio, 53-56, 1988.

130. J. M. Williams, R. A. Buchanan, and I-S Lee, ***Nuclear Instruments and Methods in Physics Research***, B37/38 (1989), 676-681, North-Holland, Amsterdam.

131. R. A. Buchanan, I-S Lee, and J. M. Williams, ***Journal of Biomedical Materials Research***, Vol. 24, 309-318 (1990).

132. J. M. Williams, A. Gonzales, J. Quintana, I-S Lee, R. A. Buchanan, F. C. Burns, R. J. Culbertson, M. Levy, and J. R. Triglio, ***Nuclear Instruments and Methods in Physics Research***, B59/60, 845-850 (1991).

133. P. P. Smith, R. A. Buchanan, J. R. Roth, and S. G. Kamath, ***Journal of Vaccum Science and Technology*** B 12(2), 940-944 (1994).

134. P. P. Smith, R. A. Buchanan, and J. M. Williams, "Tungsten Ion Implantation of Aluminum for Improved Resistance to Pitting Corrosion - Electrochemical Testing Results," accepted for publication in ***Scripta Metallurgica***, spring 1995.

135. P. P. Smith, R. A. Buchanan, and J. M. Williams, "Characterization of Blister Formation and Pitting of Tungsten Ion Implantated Aluminum," accepted for publication in ***Scripta Metallurgica***, spring 1995.

VITA

The author, Preston Paul Smith, was born in Memphis, Tennessee on May 19,1965. He attended Christian Brothers High School in Memphis, graduating in May, 1983. In September of that year, he was enrolled in the University of Tennessee at Knoxville in the College of Engineering on a National Merit Scholarship. During his undergraduate studies, he obtained industrial experience with Kimberly-Clark, Inc. and Richards Medical Co., both in Memphis. He received the Bachelor of Science Degree in Engineering Science and Mechanics, with a concentration in biomedical engineering, in December of 1987. Study towards the Master of Science in Metallurgical Engineering in the Materials Science and Engineering Department commenced in January of 1988. He was supported financially both as a Research Assistant (by NASA), and as a Teaching Assistant. This degree was awarded in August of 1990. The author's Master's Thesis was entitled "Morphological Modification and Fracture Toughness of the Niobium Aluminide Eutectic." His primary advisor for this work was Professor Ben F. Oliver. From June of 1990 until July of 1991, the author worked as a an Information Management Consultant for Andersen Consulting in Nashville, Tennessee. He reentered the University of Tennessee and the Materials Science and Engineering Department in August of 1991. He was supported financially

both by the Army Research Office and the UTK Center for Materials Processing as a Research Assistant, and as a Teaching Assistant. The Doctorate of Philosophy Degree in Metallurgical Engineering was awarded in May of 1995. His primary dissertation advisor was Professor Ray A. Buchanan.

The author married the former Mia Wren Creasman of Knoxville in August of 1992.

The author is a member of Tau Beta Pi, The American Society for Materials International, The Minerals, Metals, and Materials Society, and The National Association of Corrosion Engineers.